Atmospheric methane and its isotopic composition in a changing climate: A modeling study

Franziska Ilse Frank

Deutsches Zentrum für Luft- und Raumfahrt
Institut für Physik der Atmosphäre
Oberpfaffenhofen

Dissertation
der Fakultät für Physik
der Ludwig-Maximilians-Universität
München

F. I. Frank

Deutsches Zentrum
DLR   für Luft- und Raumfahrt

Atmospheric methane and its isotopic composition in a changing climate: A modeling study

Franziska Ilse Frank

Deutsches Zentrum für Luft- und Raumfahrt
Institut für Physik der Atmosphäre
Oberpfaffenhofen

Dissertation
der Fakultät für Physik
der Ludwig-Maximilians-Universität
München

204 Seiten
 87 Bilder
 24 Tabellen
283 Literaturstellen

Deutsches Zentrum
DLR für Luft- und Raumfahrt

Atmospheric methane and its isotopic composition in a changing climate: A modeling study

Franziska Ilse Frank

München 2018

Erstgutachter: Prof. Dr. habil. Martin Dameris
Zweitgutachter: Prof. Dr. Bernhard Mayer
Datum der Abgabe: 04.04.2018
Tag der mündlichen Prüfung: 29.05.2018

Atmospheric methane and its isotopic composition in a changing climate: A modeling study

Franziska Ilse Frank

Dissertation
an der Fakultät Physik
der Ludwig-Maximilians-Universität
München

vorgelegt von
Franziska Ilse Frank
aus München

München, den 04.04.2018

Atmosphärisches Methan und dessen isotopische Zusammensetzung in einem sich verändernden Klima:
Eine Modellstudie

Zusammenfassung:

Methan (CH_4) ist nach Kohlenstoffdioxid das zweitwichtigste anthropogene Treibhausgas und besitzt durch seine relative kurze atmosphärische Lebensdauer ein attraktives Mitigationspotential. Die Variabilität der Wachstumsraten von CH_4 ist allerdings noch nicht vollständig erklärbar. Das Ziel der vorliegenden Doktorarbeit ist, mithilfe eines Klima-Chemie-Modells das Verständnis bezüglich der Einflüsse und Rückwirkungen von CH_4 zu verbessern. Die Analyse umfasst dabei vier Aspekte, nämlich die Abbauprozesse (Senken), Quellen, globale Verteilung und den Klimaeffekt (in Form der Oxidationsprodukte) von CH_4.

Einführend werden die Abbauprozesse von CH_4 analysiert. Für diese Studie wurde die CH_4 Lebensdauer bezüglich des Hydroxylradikals (OH) von 16 Simulationen ausgewertet. Die durchschnittliche Lebensdauer von 8.11 ± 0.13 Jahre rangiert am unteren Ende der Werte ähnlicher Studien. Die Ergebnisse weisen darauf hin, dass die CH_4 Lebensdauer nicht konstant, sondern stark abhängig ist von OH und der Temperatur. Beide Parameter werden dabei von der Konfiguration des Modells und dem angenommenen Klimaszenario bestimmt. Des Weiteren zeigt sich, dass steigende Emissionen die CH_4 Lebensdauer verlängern, was jedoch zum Teil durch steigende Temperaturen kompensiert wird.

Im zweiten Teil wird ein, mithilfe eines "fixed-lag Kalman Filters" invers-optimiertes, Emissionskataster vorgestellt. Es wurde untersucht inwiefern das verwendete Modell und die angenommene OH Verteilung die Schätzung der inversen Optimierung beeinflussen. Die Ergebnisse zeigen, dass das optimierte Kataster die Übereinstimmung von simulierten und gemessenen CH_4 verbessert. Die Ergebnisse deuten auch darauf hin, dass das geschätzte Kataster stark durch die OH Konzentration bestimmt wird. Die atmosphärische Konzentration von OH kann jedoch noch nicht durch globale Messungen validiert werden. Eine weitere Vorwärtssimulation mit interaktiver Chemie und dem inverse optimierten Kataster enthüllt, dass sich das OH bezüglich des Emissionskatasters neu einstellt und dabei weitgehend unterbestimmt ist. Die Unsicherheiten der Senken von CH_4 limitieren die Genauigkeit der Schätzung von CH_4 Emissionen.

Der dritte Teil der Arbeit konzentriert sich auf die globale Verteilung von CH_4. Um Durchmischung und Transport von CH_4 von bestimmten Quellen zu untersuchen, wurde das Modell um die Simulation von CH_4 Isotopologen und deren Fraktionierungseffekte erweitert. Die Simulationsergebnisse wurden bezüglich des Vertikal- und Meridionalgradienten evaluiert. Die CH_4 Isotopologen wurden des Weiteren mit dem hydrologischen isotopischen Zyklus gekoppelt und frühere Ergebnisse bezüglich des isotopischen Gehalts von stratosphärischem Wasserdampf werden reproduziert.

Viertens, re-evaluiert die vorliegende Studie die Annahme, dass zwei H_2O Moleküle aus einem CH_4 Molekül entstehen. Diese systematische Analyse umfasst drei Ansätze, deren Ergebnisse dahingehend übereinstimmen, dass der Ertrag von H_2O durch die CH_4 Oxidation in der unteren Stratosphäre und oberen Mesosphäre kleiner ist als zwei. Der Ertrag nimmt außerdem, durch den Transport langlebiger Zwischenprodukte der Oxidationskette von CH_4, einen Wert größer als zwei in der oberen Stratosphäre und unteren Mesosphäre an. Daraus folgt, dass durch die Annahme von einem vertikal konstanten chemischen Ertrag von H_2O aus der CH_4 Oxidation, Variabilität in der chemischen Kinetik sowie der chemischen Abbau von H_2O vernachlässigt wird.

Die Ergebnisse der vorliegenden Arbeit heben die entscheidende Verbindung von Quellen und Senken von CH_4 sowie deren Unsicherheiten hervor. Die Arbeit stellt außerdem ein umfassendes Konzept für die globalen Simulation von CH_4 und dessen Isotopologe vor, um eben diese Unsicherheiten weiter zu analysieren.

Atmospheric methane and its isotopic composition in a changing climate: A modeling study

Abstract:

Methane (CH_4) is after carbon dioxide the second most important anthropogenically influenced greenhouse gas and offers, due to its relative short lifetime, an attractive mitigation potential. However, variations in CH_4 growth rates are still poorly understood. The main objective of this thesis is to provide an improved understanding of impacts of and feedbacks on CH_4 as a greenhouse gas with the help of a global Chemistry-Climate model. The analysis covers four aspects of atmospheric CH_4, namely its sinks, sources, global distribution and climate effect in form of its oxidation products.

First, the sink processes of CH_4 are studied by means of the main tropospheric sink reaction partner, the hydroxyl radical (OH). For this study, results of 16 simulations are analyzed concerning the CH_4 lifetime, which is defined by the reaction of CH_4 with OH. The derived average lifetime of 8.11 ± 0.13 a ranges at the lower end of similar studies. The results reveal that the tropospheric CH_4 lifetime is not constant and strongly relates not only to OH abundance, but also to temperature. Both, however, are influenced by the model configuration and the assumed future scenario of climate warming. It is found that increasing CH_4 emissions increase its lifetime. This is partly compensated by coherently rising temperatures in the atmosphere.

Secondly, an inverse optimized emission inventory derived by the fixed-lag Kalman Filter method is presented. It is investigated how the applied forward model and assumed OH distribution influence the estimates of the inverse optimization. The results show that the optimized inventory improves the agreement of simulated CH_4 to ground-based observations. The inventories are strongly determined by the applied OH abundance, which is in general poorly constrained. A forward simulation with interactive chemistry and the optimized emission inventory reveals that the OH distribution adjusts with respect to the emission inventory and is in general under-constrained. As a consequence, the uncertainty in the sink of CH_4 limits the certainty of estimated CH_4 emissions.

The third part of this thesis focuses on the global distribution of CH_4. In order to investigate mixing and transport of CH_4 from specific sources, the model is extended for the simulation of CH_4 isotopologues and its isotopic fractionation effects. The simulation results are evaluated concerning the representation of the vertical and latitudinal gradient. It is further coupled to the isotopologues in the hydrological cycle and previous results concerning the isotopic content in stratospheric water vapor are reproduced.

And fourth, the present study re-evaluates the common assumption that two water vapor (H_2O) molecules are produced per oxidized CH_4 molecule. The systematic analysis comprises three different approaches, focusing primarily on the tropical region. The results reveal that the yield of H_2O from CH_4 oxidation is smaller than two in the lower stratosphere and upper mesosphere. It also attains a value above two in the upper stratosphere and lower mesosphere due to transported long-lived intermediate molecules of the CH_4 oxidation chain. It is concluded that assuming a constant chemical yield of H_2O from CH_4 oxidation neglects vertical variations in the chemical kinetics as well as secondary chemical processes including the loss of H_2O.

In summary, this study comprises findings of the sinks, sources, global distribution and climate effective oxidation products of CH_4. This thesis emphasizes the decisive linkage of sources and sinks of CH_4 with respect to their uncertainties and provides a comprehensive framework for a global simulation of CH_4 and its isotopologues in order to analyze these uncertainties further.

Publications:

Parts of this thesis have been published in the following two articles.

- Frank, F., Jöckel, P., Gromov, S., and Dameris, M., Investigating the yield of H_2O and H_2 from methane oxidation in the stratosphere. Atmos. Chem. Phys. Discuss., 2018:1–29, 2018. doi: 10.5194/acp-2018-170. URL `https://www.atmos-chem-phys-discuss.net/acp-2018-170/`.

  F. Frank configured the model system, carried out the simulations, analyzed the results and wrote the paper. S. Gromov and P. Jöckel helped with the model configuration. S. Gromov, P. Jöckel and M. Dameris helped in formulating the paper. P. Jöckel supervised the study.

- Jöckel, P., Tost, H., Pozzer, A., Kunze, M., Kirner, O., Brenninkmeijer, C. A. M., Brinkop, S., Cai, D. S., Dyroff, C., Eckstein, J., Frank, F., Garny, H., Gottschaldt, K.-D., Graf, P., Grewe, V., , Kerkweg, A., Kern, B., Matthes, S., Mertens, M., Meul, S., Neumaier, M., Nützel, M., Oberländer-Hayn, S., Ruhnke, R., Runde, T., Sander, R., Scharffe, D., and Zahn, A. Earth System Chemistry integrated Modelling (ESCiMo) with the Modular Earth Submodel System (MESSy) version 2.51. Geosci. Model Dev., 9:1153–1200, 2016. doi: 10.5194/gmd-9-1153-2016. URL `http://www.geosci-model-dev.net/9/1153/2016/gmd-9-1153-2016.html`.

  In this article explicitely the Sections 4.1 and 4.4 are written by F. Frank. The presented results are based on analyses by F. Frank of the simulations conducted in the course of the in this article introduced Earth System Chemistry integrated Modelling (ESCiMo) project. P. Jöckel conducted the simulations and supervised the study. All other co-authors contributed to the particular simulations and/or to analyzing parts distinct to the indicated Sections 4.1 and 4.4 of the article.

Contents

Introduction

1.1 Motivation

Early and more recent scientific literature alike agree on the prime importance of methane (CH_4) as a greenhouse gas (GHG) together with carbon dioxide (CO_2) and water vapor (H_2O) [Fung et al., 1991, Hein et al., 1997, Wuebbels and Hayhoe, 2002, Sonnemann and Grygalashvyly, 2014, Dalsøren et al., 2016, Bergamaschi et al., 2017]. Additionally to its direct greenhouse warming potential CH_4 contributes to climate change via its oxidation products. Among others, it influences stratospheric water vapor [Revell et al., 2016], has an effect on the depletion of ozone [Johnston and Kinnison, 1998] and acts as a sink of the hydroxyl radical (OH) in the troposphere [Nisbet et al., 2016].

The overall strong interest of climate research in CH_4 is motivated, on the one hand, by its strong radiative forcing as well as its secondary climate effects (production of other GHGs), and, on the other hand, by its relative short lifetime of approximately less than 10 years [Prather et al., 2012] offering an attractive mitigation potential. In other words, CH_4 is a decisive driver of climate warming, but cutting down its emissions could limit the CH_4 burden and already make a difference in the medium term climate change [Dlugokencky et al., 2011].

It is known that since the preindustrial era surface CH_4 more than doubled from about 700 nmol mol^{-1} in 1750 to a todays value of more than 1800 nmol mol^{-1} [IPCC, 2013] (based on surface observations). In addition, ice core records show that CH_4 variations are closely related to temperature changes in the atmosphere, but the strong increase during the industrial era is unprecedented in the history of the Earth [Wuebbels and Hayhoe, 2002, Petit et al., 1999]. This strong increase is most likely related to the emerging role of anthropogenic CH_4 emissions by agriculture, production of fossil fuels and biomass burning during the industrial era. Facing the challenge of satisfying the energy thirst and managing the global food crisis as the world's population grows it is likely that CH_4 emissions from these sources will increase even further. Moreover, due to the predicted global warming methanogenesis from wetlands could be enhanced [Wuebbels and Hayhoe, 2002]. Also, currently trapped CH_4 could be released from thawing permafrost soils [Christensen et al., 2004] and from destabilized CH_4 hydrates in shallow sediments of the ocean [Ruppel and Kessler, 2017], which store very high amounts of CH_4 (i.e. > 100 times of the current total atmospheric budget).

However, variations in the recent evolution of surface CH_4 mixing ratio based on observations (shown in Fig. 1.1a) currently give rise to questions concerning the variability of the CH_4 budget. The growth rate of surface CH_4 (see Fig. 1.1b) shows that the strong increase of CH_4 during the 20th century slowed down and nearly came to a halt around the year 1999. After 2006 the trend increased again and reached the value of the early 1980s by 2015.

The leveling off between 1999 and 2006 is, for example, interpreted by Dlugokencky et al. [2003, 2011] as an approach to a steady state, assuming constant CH_4 emissions and lifetime. However, other studies found an increase of anthropogenic emissions in this time period [Bousquet et al., 2006] and the reduced growth rate is attributed to variations in OH, which is the main sink of CH_4 [Karlsdóttir and Isaksen, 2000, Fiore et al., 2006, McNorton et al., 2016, Rice et al., 2016]. It is still unclear whether the renewed growth after 2007 is mainly driven by wetlands, anthropogenic sources or variations in
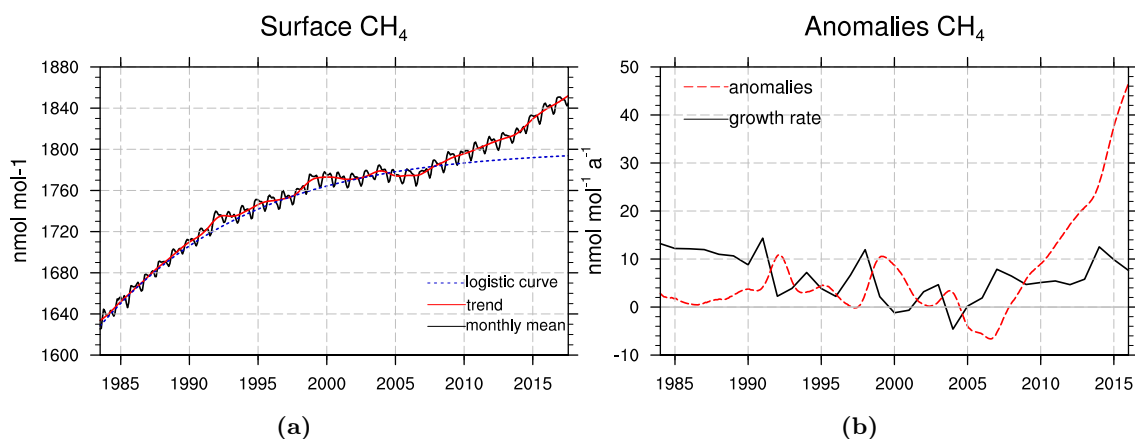
Figure 1.1: (a) The global mean surface CH_4 in [nmol mol^{-1}] based on observations shown as monthly means (black line) and as a 12 months running average or trend (red line). The blue dotted line indicates a fit of a logistic function, which assumes a constant lifetime of 10 years. (b) The black line shows the growth rate and the red dashed line the anomalies towards the logistic curve shown in (a) in [nmol mol^{-1} a^{-1}]. Globally averaged marine surface monthly mean data retrieved from `www.esrl.noaa.gov/gmd/ccgg/trends_ch4/` [Dlugokencky et al., 1994, 2015b].

the CH_4 sink and is recently much debated [Dlugokencky et al., 2011, Sussmann et al., 2012, Gosh et al., 2015, Dalsøren et al., 2016, Schwietzke et al., 2016, Schaefer et al., 2016, Nisbet et al., 2016, Poulter et al., 2017, Saunois et al., 2016b, Rigby et al., 2017, Turner et al., 2017].

This controversy emphasizes that variations of and impacts on CH_4 are still quite uncertain. Emission inventories of CH_4, for example, differ by 30–310 Tg CH_4 a^{-1} depending on the estimation method (e.g. Top-Down or Bottom-Up) [IPCC, 2013, Saunois et al., 2016a]. Furthermore, the major sink of CH_4, the OH radical, which cannot be constrained by global observations yet, varies in different Chemistry-Climate models (CCMs) by as much as 80% [Nicely et al., 2017].

Since global observations of OH are challenging, comprehensive state-of-the-art CCMs are needed to reduce these uncertainties. This motivates the present modeling study, which aims towards an exhaustive assessment of the atmospheric burden of CH_4 in such a CCM. The thesis includes the investigation with respect to virtually all factors determining the budget of CH_4: Sinks, sources and atmospheric distribution. It also implicates the consideration of potential effects on the climate by the oxidation products of CH_4.

Furthermore, a powerful and common method in the investigation of CH_4 burden is the study of CH_4 isotopologues. Production and reduction of CH_4 cause fractionation effects, which lead to distinct isotopological compositions in the atmosphere. These isotopic signatures provide potentially additional insights into the role of certain CH_4 sources and depleting reactions and are already widely used in the context of CH_4 [Hein et al., 1997, Fletcher et al., 2004, Monteil et al., 2011, Rigby et al., 2012, Nisbet et al., 2016, Schaefer et al., 2016]. In the course of the present study, CH_4 isotopologues are included into the applied CCM to be able to follow the isotopic trace of CH_4 from its source to the sink products.

Summarizing, estimates of both, sources, and sinks of CH_4 are still associated with large uncertainties. This motivates the present study to gain a deeper knowledge concerning effects on and feedback of atmospheric CH_4 by using a CCM and simulating CH_4 on global scale.

1.2 Scientific Questions

It is essential in the global modeling of atmospheric CH_4 to understand all determining factors of the CH_4 budget. This includes the sources, the sinks, and the atmospheric distribution of CH_4. Since the oxidation of CH_4 produces climate relevant compounds, these potential climate impacts should be addressed as well to enable a comprehensive view of the atmospheric trace gas CH_4.

The following scientific questions result from these four points in the order: sinks, sources, atmospheric distribution, and oxidation products, and are the key aspects addressed in the present study:

1. What are influencing factors onto the lifetime of atmospheric CH_4 and how does the lifetime change in a changing climate?

2. What kind of challenges can be expected in the CH_4 emission estimation?

3. How does knowledge about the isotopological signature of atmospheric CH_4 benefit the estimation of the global CH_4 budget?

4. How much water vapor is introduced into the stratosphere by CH_4 oxidation?

1.3 Investigation Strategy

The used methodology and outline of this study to answer the scientific questions given in the section above is described in the following.

Altogether, to investigate the CH_4 life-cycle concerning sources, sinks, and climate effect in a CCM, the ECHAM/MESSy Atmospheric Chemistry (EMAC) model [Jöckel et al., 2010] is used (i.e. the 5th generation European Centre Hamburg general circulation model (ECHAM5) combined with the Modular Earth Submodel System (MESSy)). In EMAC CH_4 can be simulated in two ways. One is to use the comprehensive interactive chemical mechanism of Module Efficiently Calculating the Chemistry of the Atmosphere (MECCA) [Sander et al., 2011a] and the other one is to use the computational cheap submodel CH4. The submodel CH4 allows to compute the chemical reactions of CH_4 in a simplified manner with respect to emission fluxes and prescribed fields of oxidation reaction partners. This submodel is further extended in the course of this study to simulate fractionation processes of CH_4 isotopologues as well as age and emission classes for additional information on the temporal and spatial evolution of CH_4.

In addition, the auxiliary submodel TRacer SYNChronization (TRSYNC) is introduced in this thesis. It closes the gap in EMAC between the chemical and physical fractionation of water vapor. It synchronizes the chemical tracer for deuterated water vapor (HDO) with its physical counterpart produced by the H_2O ISOtopologues (H2OISO) submodel [Eichinger et al., 2015a], which accurately simulates the physical fractionation of water vapor isotopologues in the troposphere. An achievement of this development is that it allows a more precise estimation of water vapor production and chemical sub-processes in the stratosphere.

The first part of the presented results (Chapter 4) investigates the variability in the sink processes of CH_4. A widely used indicator for the depletion of CH_4 is the CH_4 lifetime. In order to investigate influencing factors on the CH_4 lifetime and a potential climate sensitivity, various simulations of the Earth System Chemistry integrated Modelling (ESCiMo) project are analyzed. This also includes the discussion of possible feedbacks of a predicted CH_4 trend in the future, following the Representative Concentration Pathways (RCP) Scenario 6.0 [Meinshausen et al., 2011].

In order to be able to constrain the oxidation capacity of the atmosphere, in former chemistry-climate simulations using EMAC, CH_4 has been fixed to surface mixing ratios based on observations. Thus, a key development of this work is to establish an EMAC setup with prescribed emission fluxes in contrast to a prescribed lower boundary condition. This novel setup, including the CH4 submodel extension of age and emission classes, is further used in Chapter 5 for the application of an inverse optimization method (the fixed-lag Kalman Filter). The newly derived emission estimates are evaluated with respect to potential impacts of the used model system and assumed CH_4 sink. The inverse optimized emission inventory is additionally used together with a fully interactive chemistry setup applying MECCA, which provides further insight into the interactive linkage of CH_4 emissions and its sinks.

In Chapter 6 the isotopological content of atmospheric CH_4 is studied. As mentioned before, the MESSy submodel CH4 is extended and used in this study to simulate optionally the isotope signature of CH_4. Thus, kinetic isotope effects are implemented and appropriate isotopic signatures are assigned to the distinct emission sources. The simulations use thereby the inverse optimized emission inventory, which is a result of the previous chapter to potentially diminish CH_4 source uncertainties. This chapter also includes the analysis of a simulation carried out with the comprehensive simulation of isotopologues of species beyond CH_4 and H_2O. This is possible by applying the kinetic chemistry tagging technique (MECCA-TAG) [Gromov et al., 2010]. Results of both, the simulation using the simplified CH4 submodel, and the simulation applying MECCA-TAG are analyzed and compared in this chapter. The chapter ends with a discussion of the closed gap between chemical and physical fractionation concerning HDO.

Finally, Chapter 7 addresses the question how much H_2O is produced via CH_4 oxidation in the stratosphere. The stratospheric water vapor (SWV) is mostly determined by stratosphere-troposphere exchange (STE), but also produced by chemical reactions. Especially CH_4 is an important precursor of SWV. Hence, previous studies assume that two H_2O molecules are produced per one oxidized CH_4 molecule. However, there is evidence that this is not true at all altitudes. In this chapter this assumption is re-evaluated using both, box model, and global model simulations. The chapter also discusses processes, which should be considered in a potential simplified parameterization of the chemical production of SWV in General Circulation models (GCMs).

The appendices at the end of this thesis give further details on the model developments and comprise technical and theoretical information supporting the scientific outline presented in this study.

Scientific Background

This chapter provides an overview of the essential scientific background of this thesis. It includes a collection of general information about atmospheric chemistry, methane (CH_4), isotopologues, the hydroxyl radical (OH), and stratospheric water vapor (SWV). For fundamental physical equations used in this work consider Appendix B.

A short note on units used in this thesis: Chemical tracers are traditionally declared in SI base units of one mole of the chemical tracer per one mole of dry air (mol mol^{-1}). Synonymous and commonly used are the notations of parts per billion volume (ppbv) for nmol mol^{-1} and parts per million volume (ppmv) for μmol mol^{-1}. Water vapor is often declared in kg of the species per kg of dry air or per kg of moist air (kg kg^{-1}). While for mol mol^{-1} the reference is usually dry air, kg kg^{-1} can indicate both kg of the species per dry or per moist air, which makes a substantial difference. For a detailed clarification of the terms see Appendix B.

2.1 Atmospheric Chemistry

Chemical processes in the atmosphere are major players in the climate system. Chemical constituents are an important factor in the Earth system at all layers of the atmosphere, with the key members water vapor (H_2O), carbon dioxide (CO_2), methane (CH_4) and ozone (O_3).

The atmospheric chemistry is responsible that harmful gases are reduced and removed from the atmosphere, but is also the reason that other ones are formed. A prominent example for the role of atmospheric chemistry are the chlorofluorocarbons (CFCs), which were emitted by anthropogenic sources and have negatively influenced the ozone layer. After the strict reduction of CFC sources as a result of the Montreal Protocol in 1987 and amendments, the abundances of the CFCs declined and the ozone layer recovers, which is quite recently confirmed by Strahan and Douglass [2018].

In addition to long-lived greenhouse gases (GHGs), atmospheric radicals (e.g. OH, hydroperoxyl (HO_2)) are highly relevant as well [Seinfeld and Pandis, 2006]. These species, often identified as the HOx-family, have very low abundances ($<$ 1 nmol mol^{-1} [Griffith et al., 2013]), short atmospheric lifetimes and are highly variable in space and time. Nevertheless, they can be visualized as the engine of the atmospheric chemistry, as they are extremely reactive and part of most chemical cycles (e.g. HOx-NOx-cycle) and reaction chains. Especially OH is a pivotal part of the present study as it is the main oxidant of tropospheric CH_4 and is described in detail in Section 2.5.

In the work at hand, the focus is on both, tropospheric, and stratospheric chemistry. Troposphere and stratosphere cover in sum about 95% of the atmospheric mass and are seperated by the tropopause, which is defined by the temperature inversion between these two atmospheric layers (representing a cold point). Most emissions take place at Earth's surface, hence primarily influence the troposphere and reach the stratosphere via transport eventually, if their lifetime is sufficiently long. In general the troposphere is described as polluted, quite humid and with rapid and turbulent mixing, while the rather dry, but O_3 enriched, stratosphere exhibits a rather slow vertical motion [Fueglistaler

and Haynes, 2005]. This shapes two rather distinct – but similar interesting – chemical regimes above and below the tropopause.

In the present study the focus is on the atmospheric chemical compound CH_4 in its role as a GHG in the troposphere and stratosphere and is introduced in the next section.

2.2   Methane as a Greenhouse Gas

Methane (CH_4) is one of the most important GHGs after CO_2 and H_2O and is, furthermore, also the most abundant organic trace gas in the atmosphere [Wahlen, 1993, Wuebbels and Hayhoe, 2002, Saunois et al., 2016a]. In the following, the budget and variability of atmospheric CH_4, its role in atmospheric chemistry, as well as its effect on Earth's climate is introduced.

As already stated in the introduction, todays global surface mixing ratio being 1858.8 ppbv (estimate of October 2017[1]) is more than twice the value in 1750 (700 ppbv) [Wuebbels and Hayhoe, 2002] and is unprecedented in Earth's history [Petit et al., 1999].

The CH_4 growth reached values of up to 15 nmol mol^{-1} per year (a^{-1}) during the 20th century but growth rates decreased in the 1990s below 10 nmol mol^{-1} a^{-1}. There was also a short period of a enhanced growth in 1998 and 1999 (> 10 nmol mol^{-1} a^{-1}), probably influenced by the strong El Niño [Dlugokencky et al., 2011], before growth rates nearly diminished and even showed negative values between 1999 and 2006 (cf. Fig. 1.1b). After this period, however, growth rates increased again substantially and recently reached comparable values of the 1980s.

As mentioned before, Dlugokencky et al. [2003] explains the reduction of the CH_4 growth rate between 1999 and 2000 as an approach to a steady state. Assuming such an approach during the early 2000s, results in the blue dashed line in Fig. 1.1a, which represents the fit of a logistic curve with a limit of 1800 ppbv and a constant atmospheric lifetime of 10 years. I.e.

$$f(t) = \frac{1800.}{(1 + \exp(-0.1 * (t - 1961)))} \quad t \in [1984, ..., 2017]. \tag{2.1}$$

In Fig. 1.1b the anomalies, hence the difference of the observed annual mean surface CH_4 mixing ratio and the logistic curve $f(t)$, are shown as the red dashed curve. At about 2007 the increase of the anomalies strongly emphasizes the renewed growth rate and gives evidence that emissions must have increased substantially or sink processes have strongly decreased in 2007. Moreover, the persistence of the positive growth rate suggests that the renewed growth of CH_4 is not a short term anomaly [Dlugokencky et al., 2015b], but reasons are still highly uncertain and much debated as pointed out in the introduction.

For a general overview on the CH_4 distribution consider Fig. 2.1a, displaying the NOAA/ESRL GHG Marine Boundary Layer (MBL) Reference of CH_4 surface mixing ratios retrieved from `ftp://aftp.cmdl.noaa.gov/data/trace_gases/ch4/flask/surface/` (Accessed: 10 January 2018) [Dlugokencky et al., 2015a]. The overall global distribution of CH_4 has a significant north-south gradient, with the largest mixing ratios of CH_4 found in the northern hemisphere (NH) reaching more than 1950 ppbv in 2016. Moreover, the zonal mean trend of CH_4 (see Fig. 2.1b) is partly stronger in the NH, which is likely due to anthropogenic CH_4 sources, but may also relate to northern hemispheric wetlands [Wahlen, 1993]. In this plot also the growth rate anomaly between 1999 and 2007 as described before becomes apparent. Note that the renewed growth in 2007 is fairly uniform with respect to latitude until 2014. Specifically in this year, the NH shows a stronger increase, which might be associated with increasing anthropogenic [Turner et al., 2017, Bergamaschi et al., 2013] as well as wetland emissions [Bousquet et al., 2011].

---

[1]retrieved from `www.esrl.noaa.gov/gmd/ccgg/trends_ch4/` [Dlugokencky et al., 1994]
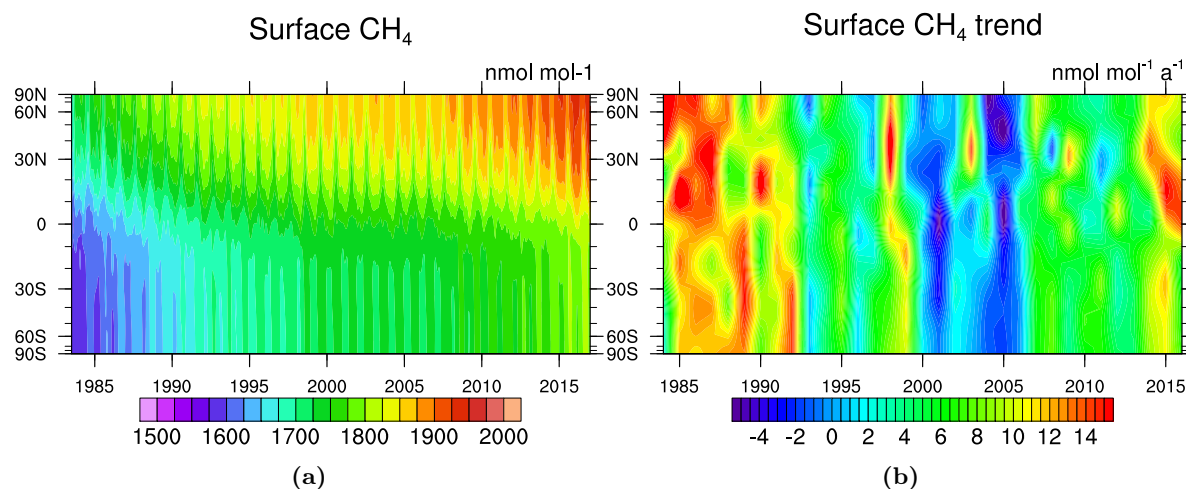
Figure 2.1: (a) National Oceanic and Atmospheric Administration/Earth System Research Laboratory (NOAA/ESRL) GHG Marine Boundary Layer (MBL) Reference of CH_4 surface mixing ratio in [nmol mol^{-1}]. (b) Yearly trend of MBL reference of CH_4 in [nmol mol^{-1} a^{-1}]. Data retrieved from `ftp://aftp.cmdl.noaa.gov/data/trace_gases/ch4/flask/surface/` (Accessed: 10 January 2018) [Dlugokencky et al., 2015a].

Another aspect of the north-south gradient becomes apparent in the seasonal cycle of the NH and southern hemisphere (SH), which is stronger in the NH than in the SH. Additionally, although emissions from aerobic fermentation in wetlands increase with temperature [Wuebbels and Hayhoe, 2002], lowest values of the CH_4 seasonal cycle are observed during the respective summer and autumn, which can be explained by the enhanced sink due to increased OH mixing ratios during the summer months [Wahlen, 1993].

Considering the climate effect of CH_4, a prominent physical property of this GHG is that it has a 34 times greater global warming potential (GWP) than a CO_2 equivalent on a time horizon of 100 years and more than twice this value for a time horizon of 20 years. Furthermore, although CH_4 has a 200 times smaller atmospheric concentration of about 1.8 ppmv compared to CO_2 (about 390.5 ppmv) its radiative forcing is 0.48($\pm$0.1) W m^{-2} for the industrial era. This is by itself more than a quarter of the radiative forcing of CO_2 (1.68($\pm$0.35) W m^{-2}). This, however, does not include secondary climate effects by the oxidation products of CH_4. Considering indirect effects of CH_4 onto other atmospheric compounds, such as ozone, SWV, and CO_2, adds an additional radiative forcing and consequently sums up to 0.97($\pm$0.23) W m^{-2} [IPCC, 2013].

Nonetheless, methane has, due to its shorter lifetime of 8–10 years compared to CO_2 (approx. 100 years), a more attractive mitigation potential, since emission reduction would yield a reduction of the climate effect on a shorter time horizon. Furthermore, it is relatively cheap to reduce emissions of CH_4. If leaking CH_4 is collected, it could for example be used as an energy source instead. Besides that, it often needs only minor adjustments in the industry, agriculture or waste management to reduce CH_4 emissions [Dlugokencky et al., 2011].

Methane is produced by sources at the surface, removed by soil-loss or in the atmosphere by the reaction with OH, excited oxygen (O(^{1}D)), chlorine (Cl) and via photolysis. The following sections give an overview about sources and sinks of CH_4.

2.2.1 Methane Sources

Methane is a GHG produced by both, natural, and anthropogenic sources. The sources are further distinguished by the formation process of CH_4: biogenic, fossil (thermogenic) or pyrogenic. Biogenic sources produce CH_4 by methanogenesis and fermentation, while fossil sources are related to leaks or the extraction from underground reservoirs of fossil CH_4 (also called natural gas) [Wuebbels and Hayhoe, 2002]. Incomplete combustion of organic matter (e.g. under low oxygen conditions) produces CH_4 as well, and is categorized as a pyrogenic source.

Natural sources represent about one third of the total CH_4 emissions and are primarily attributed to wetlands (60–70%). Most CH_4 is formed in anaerobic soils by methanogenic bacteria. Other sources are biological activity in freshwater, as lakes and rivers, wild animals (ruminants), geological sources (volcanoes onshore or mud volcanoes offshore), and termites. Rather small sources are wild fires, oceanic hydrates and permafrost soils. Despite their small emission, the latter two contain together most of the Earth's CH_4 reservoir of about 2–8 million Tg CH_4 and 530 000 Tg CH_4, respectively [IPCC, 2013]. Leaks of these reservoirs, however, become more likely in a warmer climate as permafrost thaws [Christensen et al., 2004] and hydrates in oceanic sediments become unstable [Ruppel and Kessler, 2017]. Ruminants and termites produce CH_4 through microbial fermentation in their rumen or gut, while volcanoes raise fossil CH_4 from underground reservoirs to the surface [Saunois et al., 2016a].

Anthropogenic sources are categorized into biomass burning, fossil fuel exploitation and agriculture and waste management. The latter includes the biogenic sources livestock ruminants, rice cultivation and landfills and waste. Any fossil fuel such as coal or oil commonly occurs together with CH_4. CH_4 is potentially released during the exploitation process and reaches the surface either unrestrained or is purposely transported to the surface, to protect against explosion hazard during mining. Last but not least, biomass burning combines all combustion of biomass as well as biofuel for anthropogenic purposes, as heating, cooking or agricultural related slash-and-burn land clearances [Wuebbels and Hayhoe, 2002].

Total Top-Down estimates of all CH_4 sources as an average for 2000–2009 yield 553 [526–569] [IPCC, 2013] and 552 [535–566] 10^{12} g CH_4 per year (Tg CH_4 a^{-1}) [Saunois et al., 2016a] respectively. Top-Down estimates are inversions based on statistical methods and are constrained by atmospheric observations, while Bottom-Up estimates use parameterizations of individual sources, which are scaled to global inventories. The emissions separated to the distinct source types and values for Top-Down and Bottom-Up inventories are presented in Table 2.1. Total Bottom-Up estimates differ strongly from Top-Down estimates and are mostly larger (by ca. 100–200 Tg CH_4 a^{-1} depending on the study and time period) [Kirschke et al., 2013, IPCC, 2013, Saunois et al., 2016a]. Since they are not constrained by the global CH_4 budget, they probably overestimate the sources due to double accounting, primarily in the case of natural emissions [Saunois et al., 2016a].

Note, when referring to the emission categories introduced in this section and in Table 2.1, throughout this thesis the term emission type is synonymously used.

Table 2.1: Global CH$_4$ emissions and sinks in Tg CH$_4$ a^{-1} from IPCC [2013] (left) and Saunois et al. [2016a] (right) for the years 1990–1999 (left column), 2000-2009 (middle column) and 2012 (right column). The values in italics refer to estimates of 2003-2009 [Saunois et al., 2016a]. Reported uncertainties are listed in parentheses.

	[IPCC, 2013] 1990–1999		[IPCC, 2013] 2000–2009		[Saunois et al., 2016a] 2000–2009		[Saunois et al., 2016a] 2012	
	Bottom-Up	Top-Down	Bottom-Up	Top-Down	Bottom-Up	Top-Down	Bottom-Up	Top-Down
Sources								
Natural sources	**336 [230-465]**	**182 [162-197]**	**347 [238-484]**	**218 [179-273]**	**382 [255-519]**	**234 [194-292]**	**386 [259-532]**	**211 [192-302]**
wetlands	206 [169-265]	150 [144-160]	217 [177-284]	175 [142-208]	183 [151-222]	166 [125-204]	187 [155-235]	172 [155-201]
other	130 [61-200]	32 [23-37]	130 [61-200]	43 [37-65]	*199 [104-297]*	68 [21-130]		49 [22-137]
freshwater	40 [8-73]		40 [8-73]		*122 [99-272]*			
wild animals	15 [15-15]		15 [15-15]		*10 [5-15]*			
wildfires	3 [1-5]		3 [1-5]		*3 [1-5]*			
termites	11 [2-22]		11 [2-22]		*9 [3-15]*			
geological[a]	54 [33-75]		54 [33-75]		*54 [35-76]*			
hydrates[b]	6 [2-9]		6 [2-9]		*2 [0-5]*			
permafrost soils	1 [0-1]		1 [0-1]		*1 [0-1]*			
Anthropogenic sources	**313 [281-347]**	**372 [290-453]**	**331 [304-368]**	**335 [273-409]**	**338 [329-342]**	**319 [255-357]**	**370 [351-385]**	**347 [262-384]**
agriculture & waste	187 [177-196]	239 [180-301]	200 [187-224]	209 [180-241]	190 [174-201]	183 [112-241]	197 [183-211]	200 [122-213]
ruminants	87 [82-91]		89 [87-94]		*103 [95-109]*		107 [100-112]	
landfills & waste	65 [63-68]		75 [67-90]		*57 [51-61]*		60 [54-66]	
rice	35 [32-37]		36 [33-40]		*29 [12-35]*		29 [25-39]	
fossil fuels	84 [66-96]	95 [84-107]	96 [85-105]	96 [77-123]	112 [107-126]	101 [77-126]	134 [123-141]	122 [90-137]
biomass burning	42 [38-45]	38 [26-45]	35 [32-39]	30 [24-45]	30 [26-34]	35 [16-53]	30 [25-36]	35 [28-51]
Sum sources	**649 [511-812]**	**554 [529-596]**	**678 [542-852]**	**553 [526-569]**	**719 [583-861]**	**552 [535-566]**	**756 [609-916]**	**568 [542-582]**
Sinks								
chemical loss	571 [521-621]	515 [491-554]	604 [483-738]	518 [510-538]		514		518
trop. OH	479 [457-501]		528 [454-617]					
trop. Cl	25 [13-37]		25 [13-37]					
strat. Loss (OH, O(^{1}D), Cl, hν)	67 [51-83]		51 [16-84]					
soil-loss	28 [9-47]	27 [27-27]	28 [9-47]	32 [26-42]		32 [27-38]		36 [30-42]
Sum sinks	**599 [530-668]**	**542 [518-579]**	**632 [592-785]**	**550 [514-560]**		**546**		**555**

[a] incl. on- and offshore sources
[b] oceanic hydrates

2.2.2 Methane Sinks

Chemical Sinks Methane is removed from the atmosphere by three photochemical reactions:

$$CH_4 + OH \xrightarrow{k_{CH_4+OH}} CH_3 + H_2O \tag{R 2.1}$$

$$CH_4 + O(^1D) \xrightarrow{k_{CH_4+O(^1D)}} CH_3 + OH \tag{R 2.2}$$

$$\longrightarrow CH_3O + H \tag{R 2.3}$$

$$\longrightarrow CH_2O + H_2 \tag{R 2.4}$$

$$CH_4 + Cl \xrightarrow{k_{CH_4+Cl}} CH_3 + HCl \tag{R 2.5}$$
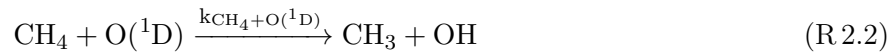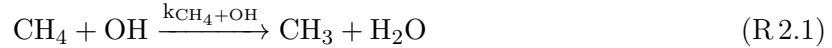
and is also depleted by photolysis:

$$CH_4 + h\nu \xrightarrow{k_{CH_4+h\nu}} products \tag{R 2.6}$$

with (R 2.1)–(R 2.5) from [Sander et al., 2011b] and (R 2.6) from [Sander et al., 2014].

More than 90% of the atmospheric CH_4 is removed via its chemical sink in the troposphere, accounting for 553 Tg CH_4 a^{-1} IPCC [2013]. The largest part is thereby the reaction with OH (95% of the tropospheric sink). The rest is attributed to the reaction with Cl in the MBL. The stratosphere accounts for a CH_4 sink of about 51 Tg CH_4 a^{-1}, which represents the sum of the reactions with OH, $O(^1D)$, Cl and through photolysis.

Soil-loss Another sink of CH_4 is the so called soil-loss at the Earths' surface. Methane is either depleted by methane eating bacteria (methanotrophs) or is removed from the air by diffusive transport into the soil, which is mostly influenced by soil water content [King, 1997]. Globally, the soil-loss accounts for approximately 28 Tg CH_4 a^{-1} IPCC [2013], which is about 5% of the total CH_4 sink.

2.2.3 Methane Observations

Current CH_4 budget inventories are constrained by global observations. This includes ground-based, balloon and airborne, as well as satellite measurements.

Measurements of atmospheric CH_4 are commonly done by retrieving flask samples from the ambient air, which are analyzed concerning CH_4 using gas chromatographs together with a flame ionization detector [Dlugokencky et al., 1995]. However, other emerging in-situ observation methods are using spectroscopy techniques (among others Cavity Ring Down Spectroscopy (CRDS) and Fourier transform infrared (FTIR) spectroscopy) [Zellweger et al., 2016].

Global networks of flask and in-situ observations enable the assimilation of the atmospheric CH_4 distribution, by taking care of a common calibration scale. For example, the NOAA/ESRL coordinates the Global Greenhouse Gas Reference Network (`https://esrl.noaa.gov/gmd/ccgg/index.html`), which collects observations of CH_4 mixing ratios at over 50 surface sampling sites, several tall towers, and aircraft flights around the world and provides the MBL Reference based on measurements of a subset of the NOAA/ESRL Cooperative Global Air Sampling Network. NOAA/ESRL is also partner of the Advanced Global Atmospheric Gases Experiment (AGAGE; `http://agage.eas.gatech.edu`) [Prinn et al., 2016]. Additionally, the World Meteorological Organization (WMO) Global Atmosphere Watch (GAW) gathers data from multiple networks, institutes and researchers all over the globe. Collected mixing ratios of CH_4 and various other GHGs are archived in the World Data Center for Greenhouse Gases (WDCGG) (`http://ds.data.jma.go.jp/gmd/wdcgg/`) operated by the Japan Meteorological Agency (JMA).

Fourier transform spectroscopy to detect CH_4 mixing ratios is likewise used for remote sensing activities. Vertical columns of CH_4 are, for example, provided by the ground-based Total Carbon Column Observing Network (TCCON) at currently over 25 locations using Fourier Transform Spectrometer (FTS) for the detection of near-infrared absorption spectra, while being directed towards the sun (a so called limb measurement) [Wunch et al., 2011].

Additionally, there are by now several remote sensing satellites launched or planned, which are designated to observe CH_4 mixing ratios from space [Jacob et al., 2016]. The instruments on board the satellites are detecting radiation of CH_4 either in shortwave infrared (SWIR) or thermal infrared (TIR) pointing towards the surface (i.e. nadir) or partly aslant through the atmosphere (limb). Among others the Scanning Imaging Absorption Spectrometer for Atmospheric Cartography (SCIAMACHY) on board ENVIronmental SATellite (ENVISAT) [Frankenberg et al., 2011], the Thermal And Near-infrared Sensor for carbon Observation - Fourier transform spectrometer (TANSO-FTS) on board the Greenhouse gases Observing SATellite (GOSAT) [Kuze et al., 2016] and the very recently launched Sentinel-5 Precursor satellite with the TROPOspheric Monitoring Instrument (TROPOMI) [Butz et al., 2012] measure the solar backscatter of the sun in the SWIR, while thermal emissions are detected e.g. by the Atmospheric Infrared Sounder (AIRS) [Xiong et al., 2008] and the Infrared Atmospheric Sounding Interferometer (IASI) [Xiong et al., 2013].

Despite the fact that recently several satellites using passive observation methods detecting radiation in the SWIR with high precision were launched, they, however, lack the ability to measure CH_4 at high latitudes during the polar night. The active remote sensing operation with the MEthane Remote LIdar missioN (MERLIN) (whose launch is planned for 2023) equipped with a LIght Detection And Ranging (LIDAR) instrument [Kiemle et al., 2014, Ehret et al., 2017] will be able to provide these additional constraints for global atmospheric CH_4, since it is independent of the radiation of the Sun.

2.3 Introduction to Isotopologues

The study of isotopes and isotopologues, used as biomarkers or tracers, is a popular tool in various science disciplines (e.g. geochemistry, ecology or astrophysics). In the Earth System Sciences stable isotopologues are commonly used to determine transport pathways and to separate sources of atmospheric trace gases [Gros et al., 2004]. This section and the following one give an overview on the basic principles of the study of isotopologues.

The nucleus of an atom consists of protons and neutrons. The distinct chemical elements in the periodic table differ by their number of protons in the nucleus. However, isotopes are types of one specific element (having the same amount of protons), but varying in their numbers of neutrons in the nucleus (see Fig. 2.2). While protons are positively and electrons negatively charged, neutrons are neutral, but contribute to the total mass of an element. Isotopes with extra neutrons have therefore a larger atomic mass and are commonly described as heavier.

Isotopologues are to molecules, as isotopes are to atoms.

Isotopologues and molecules have the same relationship as isotopes and atoms. Isotopologues of a specific molecule contain the same chemical elements, but one or more atoms in the molecule are substituted by a corresponding isotope. This results in distinct compound combinations of the same molecule, called isotopologues. Substituting an element with a heavier isotope results in a heavy isotopologue.

For example, each hydrogen atom ^1H in H_2O can be substituted by its stable isotope with one neutron instead of none: ^2H (i.e. deuterium (D)), which results in the stable water isotopologues: H_2O, HDO, and D_2O.
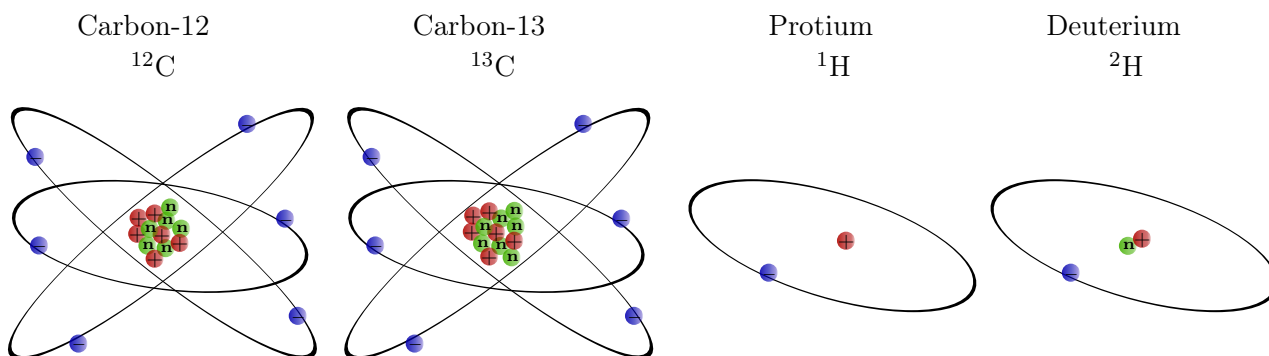
Figure 2.2: Stable isotopes of carbon and hydrogen sketched in the Bohr atom model. Red dots with plus symbol, blue dots with minus symbol and green dots with the character n represent protons, electrons and neutrons, respectively.

The isotopologue containing solely the most abundant isotopes of the included atoms, are generally also the most abundant isotopologues. Isotopologues, which are substituted by only one rare isotope are the most common ones after the abundant isotopologue. Higher substituted isotopologues are scarcer, as the probability for the isotopes to meet in one molecule decreases quadratically.

The compounds with rare isotopes are called rare isotopologues. One chemical element can have various isotopes. Moreover, several substitution variations of an element might be possible in a molecule (i.e., if the corresponding element occurs in the molecule multiple times). This results in multiple distinct isotopologues for one molecule. Additionally, if the position of the isotopes in the molecule is distinguishable, the variant isotopologues are called isotopomers.

Isotopologues of the same molecule have slightly different physical and kinetic characteristics [Fry, 2006] described as mass- and non-mass-dependent isotope effects, leading to the fractionation of heavy and light isotopologues. Since rare isotopologues can be detected and differentiated from their abundant counterpart, it is possible to track them and to investigate the isotopic pattern, which forms due to the varied characteristics of the isotopologues. Moreover, sources of atmospheric trace gases can be distinguished by their isotopic signature. Consequently, it is possible (to some extent) to relate the isotopic compositions of trace gases in the atmosphere to their origin and to use the isotopic signature as an additional information to estimate the contribution of distinct sources to the atmospheric budget.

2.3.1   The δ-Notation

Atmospheric amounts of rare isotopologues are usually quite small. For reasons of readability the so called δ-notation after McKinney et al. [1950] is widely used. The δ-value is the ratio of a specific samples' isotopic ratio with respect to a reference isotopic ratio given in ‰:

$$\delta \;=\; \left(\frac{R_{sample}}{R_{ref}} - 1 \right) \cdot 1000 \,. \tag{2.2}$$

R_{sample} and R_{ref} are the isotopic ratios of the sample and the reference, respectively. R_{ref} is an internationally accepted reference value for the isotopic ratio of a specific isotope. The standard values of Vienna Standard Mean Ocean Water (VSMOW) for hydrogen and PeeDee Belemnite (PDB) for carbon are used in this work and are listed in Table 2.2. From a relative point of view, low δ-values correspond to isotopically depleted or light samples, whereas conversely, high δ-values indicate isotopically enriched or heavy samples.

Table 2.2: International standard references for isotopic ratios. Values are taken from Fry [2006].

			Isotope abundances	
Reference name	Element	Value	Heavy	Light
Vienna Standard Mean Ocean Water (VSMOW)	$^2H/^1H$	0.00015576	0.015574	99.984426
PeeDee Belemnite (PDB)	$^{13}C/^{12}C$	0.011180	1.1056	98.8944

Isotopic ratios are calculated as the fraction of the number of rare to the number of abundant isotopes:

$$R = \frac{I_{rare}}{I_{abundant}}, \tag{2.3}$$

with I_{rare} being the number of rare and $I_{abundant}$ the number of abundant isotopes in the considered probe. Note that for isotopic ratios isotopes, hence atoms, are counted – not molecules.

For a specific molecule Φ and isotope Ψ_j of element Ψ the isotopic ratio is defined as,

$$R_{\Psi_j}(\Phi) := \frac{\sum_{i=0}^{q} i \cdot \Phi_i}{\sum_{i=0}^{q} (q-i) \cdot \Phi_i} \tag{2.4}$$

with q being the number of elements Ψ in molecule Φ. Φ_i denotes the isotopologues, where i positions of the element Ψ in molecule Φ are occupied with the (rare) isotope Ψ_j.

For example, the isotopic ratio of a sample of CH_4 with respect to D is calculated as:

$$R_D(CH_4) = \frac{[CH_3D] + 2 \cdot [CH_2D_2] + 3 \cdot [CHD_3] + 4 \cdot [CD_4]}{4 \cdot [CH_4] + 3 \cdot [CH_3D] + 2 \cdot [CH_2D_2] + [CHD_3]}$$

with $[\Phi]$ being the number of molecules Φ in the sample.

The abundances of isotopologues substituted with more than one rare isotope are in general neglected in the calculation of $R_{\Psi_j}(\Phi)$, since these are usually smaller than other uncertainties, e.g. in the measurement method:

$$R_{\Psi_j}(\Phi) \simeq \frac{\Phi_1}{q \cdot \Phi_0 + (q-1) \cdot \Phi_1}. \tag{2.5}$$

For further simplification, the abundance of the first rare isotope Φ_1 (e.g. deuterated methane (CH_3D)) in the denominator is sometimes neglected as well. This, however, is not always advisable, as in some cases, where the sample is highly enriched by the rare isotopologue (e.g. deuterated water vapor (HDO) in ice clouds) the thereby applied bias becomes significant.

2.3.2 Isotopologues of Methane

Focusing again on the principal species of this thesis, leads over to the introduction of CH_4 isotopologues.

Fundamentally, the isotopologues of CH_4 form with respect to the stable isotopes of hydrogen and of carbon. The stable isotopes of hydrogen are ^1H and D, and for carbon, carbon-12 (^{12}C) and
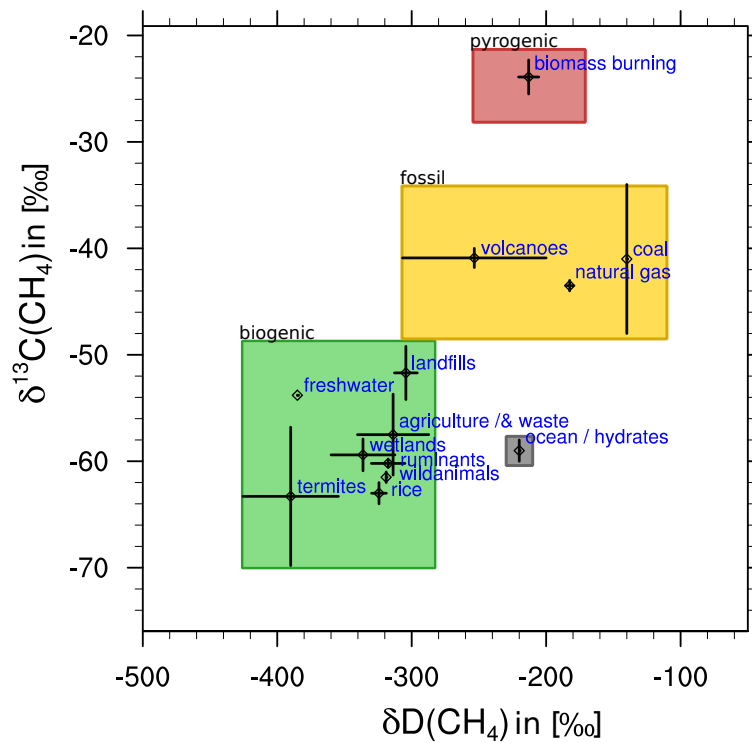
Figure 2.3: Signatures of CH$_4$ sources in [‰] with respect to ^{13}C and D plotted against each other. The colored boxes indicate the corresponding emission processes either biogenic (green), fossil (yellow) or pyrogenic (red). Hydrates are seperated in the grey box. Values are taken from Table 2.3.

carbon-13 (^{13}C) (see Fig. 2.2). This results in the stable isotopologues ^{12}CH$_4$ and ^{12}CH$_3$D, and ^{12}CH$_4$ and ^{13}CH$_4$, respectively.

Methane isotopologues are foremost utilized as additional characteristics of CH$_4$ sources [Hein et al., 1997, Quay et al., 1999, Gros et al., 2004, Fletcher et al., 2004, Whiticar and Schaefer, 2007] and have recently been used to investigate the prominent variations in CH$_4$ growth between 1999 and today [Nisbet et al., 2016, Schaefer et al., 2016]. Particularly, since biogenic, fossil and pyrogenic sources have quite distinct isotopic signatures (see Fig. 2.3), it is possible to associate atmospheric isotopic compositions with flux variations of certain emission types. In particular, the joint investigation of the delta value concerning ^{13}C of CH$_4$ (δ^{13}C(CH$_4$)), and the delta value concerning D of CH$_4$ (δD(CH$_4$)), provides an even more precise indication of the source composition. It is, however, not possible by the isotopic signature alone to distinguish natural from anthropogenic sources, since wetlands, ruminants and rice cultivation, are biogenic sources and do not differ substantially in their isotopic signatures.

In general, biogenic sources are the most depleted ones with mean signatures of δ^{13}C(CH$_4$)$= -59$‰ and δD(CH$_4$)$= -324.5$‰. Fossil sources have a median value of δ^{13}C(CH$_4$)$= -41.8$‰, while pyrogenic sources are relatively enriched in ^{13}C with δ^{13}C(CH$_4$)$= -23.9$‰. However, by means of δD(CH$_4$), fossil (-192.0‰) and pyrogenic sources (-213.0‰), are not very well distinguishable. For further distinct signatures of CH$_4$ sources and corresponding references see Table 2.3.

The global annual mean isotopic composition of atmospheric CH$_4$ is -47.3 ± 0.04‰ in case of δ^{13}C(CH$_4$) and -86 ± 3‰ in case of δD(CH$_4$) [Quay et al., 1999]. Similar to atmospheric CH$_4$, the isotopic composition of CH$_4$ has a meridional and vertical gradient. The NH is generally isotopically

depleted (lower delta value) compared to the SH. $\delta D(CH_4)$ has thereby a larger north-south difference (SH: $-81 \pm 3‰$, NH: $-91 \pm 5‰$) than $\delta^{13}C(CH_4)$ (SH: $-47.15 \pm 0.08‰$, NH: $-47.41 \pm 0.14‰$) [Quay et al., 1999]. Atmospheric CH_4 is isotopically most enriched near the surface and $\delta^{13}C(CH_4)$ and $\delta D(CH_4)$ decrease with altitude [Röckmann et al., 2011]. The measurements of CH_4 isotopologues, which are the basis for these estimates, are, for example, done by gas chromatography and isotope ratio mass spectrometry (IRMS), or by using a quantum cascade laser absorption spectroscopy (QCLAS) instrument [Röckmann et al., 2016a].

For the present study, solely the abundant and first rare, hence second most abundant, isotopologues are considered. The so called clumped CH_4 isotopologues (CH_4 molecules with two or more deuterium or with deuterium and heavy carbon combined) are neglected for their even smaller probability to form. Nevertheless, clumped CH_4 isotopologues gain more attention in current literature [Eiler, 2007, Stolper et al., 2014, Wang et al., 2015, Röckmann et al., 2016b, Whitehill et al., 2017] and are expected to serve as an additional information carrier in future.

Moreover, next to stable isotopes, hydrogen and carbon also have unstable isotopes. The carbon isotope ^{14}C, with a half-life of 5715 ± 30 years [Holden, 1990], is strictly speaking another candidate for an isotopologue, and is for example, in conjunction with carbon monoxide (CO), used to determine OH abundances of the atmosphere [Brenninkmeijer et al., 1992]. Furthermore, other isotopes of carbon (e.g. ^{11}C) have half-lifes of less than 20 min and do not occur naturally. The same applies for tritium (i.e. ^3H with a half life of 12.33 years [Enghag, 2004]), which is produced during nuclear bomb tests. However, the present study focuses on stable isotopes only.

Distinct isotopologues have different physical and kinetic properties, which are summarized as isotope fractionation effects. These effects are the reason for distinct source signatures and the particular meridional and vertical gradients in the CH_4 isotopic content described above and are introduced in the following section.

2.4 Isotope Fractionation Effects

In general, isotope fractionation occurs with respect to physical and chemical processes. Physical fractionation happens mostly with respect to diffusion and transport (heavier isotopologues are "slower") as well as phase transitions [Fry, 2006, Gat, 2010], while chemical fractionation becomes evident by altered reaction or turnover rates in chemical and biochemical processes. Another minor isotope effect is the nuclear spin isotope effect, which is based on the nuclear structure of different isotopes [Michener and Lajtha, 2007].

2.4.1 Physical Fractionation Effects

The theory of physical isotopic fractionation distinguishes fractionation under equilibrium conditions, in closed and in open systems, as well as fractionation by transport [Mook, 2000, Gat, 2010].

The isotopic fractionation due to transport in the atmosphere originates directly from the higher mass of heavy isotopologues, as more energy is needed to achieve the same velocity as of the light isotopologue and results in different diffusion of the distinct isotopologues [Mook, 2000].

The equilibrium fractionation in closed systems assumes an equilibrium between substrate and product during the whole process, as well as mass conservation [Fry, 2006]. Light and heavy isotopologues are transferred back and forth in the considered process(es) and are fractionated with respect to the Equilibrium Isotope Effect (EIE) of the whole system.

In the concept of an open system, formed products are extracted from the system, which leads to an irreversibility of the process and is often described using the Rayleigh model [Gat, 2010]. The

Table 2.3: Flux in [Tg CH$_4$ a^{-1}] and signatures in [‰] of CH$_4$ sources. Flux values are taken from the [IPCC, 2013] bottom-up estimate for 2000-2009. Signatures of bulk source types (other natural, agriculture & waste, and fossil fuel) are averages weighted by the individual flux strength contributions.

		δ^{13}C(CH$_4$)			δD(CH$_4$)			
source	flux	δ-value	$\pm$	ref.	δ-value	$\pm$	ref.	type
wetlands	**217**	**-59.4**	**1.5**	1,2,3,4,6	**-336.2**	**23.8**	3,4,6	biogenic
other natural	**126**	**-50.3**	**8.9**		**-313.3**	**88.9**		
freshwater	40	-53.8	/	3	-385.0	/	3	biogenic
wildanimals	15	-61.5	0.5	1	-319.0	/	5	biogenic
termites	11	-63.3	6.5	1,2,3	-390.0	35.5	3	biogenic
volcanoes	54	-40.9	0.9	1,2	-253.4	53.4	3,7	fossil
ocean/hydrates	6	-59.0	1.0	1,2,3	-220.0	/	3	biogenic
agriculture & waste	**200**	**-57.5**	**3.8**		**-313.8**	**26.5**		
ruminants	89	-60.2	0.3	3,4,6	-317.5	12.5	3,4	biogenic
landfills	75	-51.7	2.5	3,4,6	-304.3	8.5	3,4,6	biogenic
rice	36	-63.0	1.0	1,2,3,4,6	-324.3	5.5	3,4,6	biogenic
fossil fuel	**96**	**-41.8**	**7.5**		**-154.2**	**2.5**		
natural gas	32	-43.5	0.5	3,6	-182.5	2.5	3,6	fossil
coal	64	-41.0	7.0	3,6,8	-140.0	0.0	3,6	fossil
biomass burning	**35**	**-23.9**	**1.6**	1,2,3,4,6	**-213.0**	**7.5**	3,4,6	pyrogenic
biogenic		-59.0			-324.5			
fossil		-41.8			-192.0			
pyrogenic		-23.9			-213.0			

references: [1] [Monteil et al., 2011] [2] [Fletcher et al., 2004] [3] [Whiticar and Schaefer, 2007] [4] [Snover and Quay, 2000] [5] [Rigby et al., 2012] [6] [Quay et al., 1999] [7] [Kiyosu, 1983] [8] [Zazzeri et al., 2015]

physical isotope effect in open systems is sometimes called Kinetic Isotope Effect (KIE), which is, however, in recent literature reserved for chemical and biochemical fractionation [Gat, 2010] and will be discussed in the next section.

As stated before physical isotope effects can occur during phase transitions. Some of the most prevalent phase transitions in the atmosphere are those of the hydrological cycle (i.e. ice $\longleftrightarrow$ liquid $\longleftrightarrow$ vapor). Fractionation processes take place during evaporation, condensation, desublimation and freezing, at the surface (land or waters), as well as in clouds. They are partly assigned to equilibrium fractionation in closed systems (evaporation, condensation, freezing in clouds and formation of rime), if transport can be neglected, and partly to fractionation in open systems (desublimation in clouds and formation of dew), if it can be assumed that produced particles are removed sufficiently fast [Eichinger, 2014].

2.4.2 The Kinetic Isotope Effect

The chemical fractionation is based on the fact that isotopologues of the same molecule have different reaction rates, i.e. they react with different speed or probability. This difference in reaction rates is described as the so called Kinetic Isotope Effect (KIE).

The KIE becomes apparent during the chemical reaction of a specific molecule X:

$$X_L + E \xrightarrow{k_L} P$$

$$X_H + E \xrightarrow{k_H} P$$
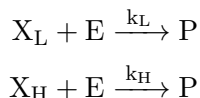
with X_L being its light and X_H its heavy isotopologue. E and P denote the reaction partner(s) and product(s) of the reaction, respectively.

The reaction rates k_L and k_H vary slightly, due to the different mass of the included isotopes in X_L and X_H. The mass of the atoms influence the vibrational energy of the molecules, to which the molecular bonding, defined as the force holding atoms together, is directly proportional [Baskaran, 2011].

The value of the KIE is thereby defined as the ratio of the reaction rates [Bigeleisen, 2005]:

$$KIE := \frac{k_L}{k_H} \tag{2.6}$$

and the inverse of the KIE is called the fractionation factor α:

$$\alpha := \frac{1}{KIE} \ .$$

The KIE does not have to be constant and can, as the reaction rates, depend on temperature, pressure or other parameters.

Heavy isotopologues have lower vibrational energy (slower vibration), which results in stronger bonds in the heavy isotopologue [Michener and Lajtha, 2007]. Therefore, usually the heavier isotopologue has a slower reaction rate, which results in a KIE greater than 1 [Fry, 2006]. The KIE and the resulting fractionation can be pictured in the sense, that lighter isotopologues are favored in the reaction. Molecular bonds between light isotopes have a priori more potential energy than their with heavy isotopes substituted counterpart. Therefore, it is more difficult for the heavier isotopologue to reach a certain energy level to break the bonds between the atoms in the molecule. Consequently, as more lighter isotopes reach the product, the latter is isotopically enriched compared to the substrate.

For equilibrium reactions (under the assumption of a closed system), where isotopes are exchanged back and forth, the KIEs of the forward and backward reaction combine to an EIE [Michener and Lajtha, 2007]. In this case, usually, the molecule with strongest bonds gets enriched with the heavy isotope [Fry, 2006].

Table 2.4: Temperature dependent KIEs used for the sink reactions of CH_4 calculated as KIE $=$ A $\cdot$ exp(B$/T$). The KIEs are valid in the given temperature range (T in [K]).

reaction	A	B	T	reference
$KIE^{OH}_{^{13}CH_4}$	1.0039	0.0	–	[Saueressig et al., 2001]
$KIE^{O(^1D)}_{^{13}CH_4}$	1.013	0.0	223–295	[Saueressig et al., 2001]
$KIE^{Cl}_{^{13}CH_4}$	1.043	6.455	223–297	[Saueressig et al., 1995]
				[Crowley et al., 1999]
$KIE^{OH}_{CH_3D}$	1.097	49.0	–	[Saueressig et al., 2001]
$KIE^{O(^1D)}_{CH_3D}$	1.060	0.0	224–295	[Saueressig et al., 2001]
$KIE^{Cl}_{CH_3D}$	1.278	51.31	223–295	[Saueressig et al., 1996]

2.4.3 Fractionation Effects in the Sink Reactions of Methane

The KIEs of the reactions of CH_4 isotopologues with its sink reactants OH, $O(^1D)$ and Cl have been, among others, determined by Saueressig et al. [1995, 1996, 2001] and Crowley et al. [1999] in laboratory measurements. The KIEs used throughout this thesis for the sink reactions of CH_4 ((R 2.1)-(R 2.5)) are listed in Table 2.4.

Since the KIEs of CH_4 isotopologues are partly temperature dependent, the KIEs are given by two parameters A and B and are calculated as

$$KIE = A \cdot \exp(B/T), \tag{2.7}$$

with T being the temperature in [K].

The largest KIE and therefore strongest fractionation effect is found for the reaction with Cl, which especially influences the isotopic composition of CH_4 in the middle and upper stratosphere [Saueressig et al., 1996, Bergamaschi et al., 1996]. Conversely, the lowest KIE is attributed to $O(^1D)$, which furthermore does not show any temperature dependence [Saueressig et al., 2001].

Nair et al. [2005] estimated the rate coefficients of the photodissociation of CH_4 and its major isotopologues for planet Mars. They calculated the zero point vibrational energy differences of the isotopologues and estimated that CH_3D shifts its absorption cross-section relative to CH_4 by 0.9 nm blue-ward. Methane containing ^{13}C ($^{13}CH_4$) shifts it only by 0.4 nm. This results in a calculated KIE$= 1.005$ for CH_3D and a negligible isotopic fractionation for the ^{13}C isotopologue [Nixon et al., 2012]. Nevertheless, since the KIE related to photolysis of CH_3D is small and removal of CH_4 by photolysis becomes significant above the stratopause only [Röckmann et al., 2011], it is neglected in the current study.

There is, especially for deuterium, a non-negligible fractionation during the soil-loss for CH_4 [Snover and Quay, 2000, Maxfield et al., 2008]. Measurements over grassland and forestry areas suggest a KIE_{CH_3D} of 1.099 ± 0.030 and 1.066 ± 0.007, respectively [Snover and Quay, 2000]. Since the implementation of the CH_4 soil-loss in ECHAM/MESSy Atmospheric Chemistry (EMAC) currently does not account for distinct land categories an overall KIE for soil-loss is calculated. Grassland and forest cover both about the same percentage of the worlds land cover [Holmgren, 2006], resulting in an overall $KIE^{soil}_{CH_3D}$ of 1.0825, i.e. the average for both categories. For $KIE^{soil}_{^{13}CH_4}$ the literature reports values of 1.0181 ± 0.0004 and 1.0219 ± 0.0011 for forest and woodland areas respectively, and, 1.0173 ± 0.0010 and 1.0211 ± 0.020 for grasslands [Snover and Quay, 2000, Maxfield et al., 2008]. This results in an average value of $KIE^{soil}_{^{13}CH_4)} = 1.0196$ of the overall soil-loss.

Table 2.5: KIEs used in this study besides the KIEs for the sink reactions of CH_4. Some reaction products are shown as net products assuming fast reaction of intermediates with molecular oxygen (O_2).

reaction		KIE[a]	reference
$HCHO + h\nu$	$\longrightarrow H_2 + CO$	$\frac{500. + 2.5 \cdot 10^{-2} \cdot p}{500. + 1.34 \cdot 10^{-2} \cdot p}$	[Nilsson et al., 2010]
$HCHO + h\nu$	$\longrightarrow H + CO + HO_2$	1.63	[Röckmann et al., 2010]
$HCHO + OH$	$\xrightarrow{O_2} CHO + H_2O$	1.28	[Feilberg et al., 2004]
$HCHO + Cl$	$\longrightarrow HCl + CO + HO_2$	1.201	[Feilberg et al., 2004]
$HCHO + NO_3$	$\xrightarrow{O_2} HNO_3 + CO + HO_2$	1.78	[Feilberg et al., 2004]
$HCHO + Br$	$\xrightarrow{O_2} HBr + CO + HO_2$	3.27	[Feilberg et al., 2004]
$CH_3OH + OH$	$\xrightarrow{O_2} 0.85\,HCHO + 0.85\,HO_2$ $+ 0.15\,CH_3O + H_2O$	1.119	[Feilberg et al., 2008]
$H_2 + O(^1D)$	$\longrightarrow H + OH$	$1.100 \cdot \exp(\frac{130.0}{T})$	[Zahn et al., 2006]
$H_2 + OH$	$\longrightarrow H_2O + H$	1.130	[Zahn et al., 2006]
$CH_3Cl + OH$	$\longrightarrow H_2O + Cl + L_H + L_C$[c]	3.9	[Gola et al., 2005]
$CH_3CHO + h\nu$	$\xrightarrow{O_2} CH_3O_2 + HO_2 + CO$	1.26	[Nilsson et al., 2009]

[a] p := pressure in [Pa]; T := temperature in [K]
[c] $L_{H/C}$ surrogates for neglected hydrogen and carbon compounds

Besides that, biochemical fractionations are to a lesser extent considered in this thesis. Nevertheless, it should be noted that there is also evidence that fractionation due to methanotrophy varies in thawing permafrost soils. During the temperature rise, the composition of specific methane eating and producing bacteria changes, and the respectively prevalent type determines the isotope fractionation factor, which therefore varies with time and temperature [McCalley et al., 2014].

2.4.4 Further Chemical Fractionation Effects in the Atmosphere

All chemical fractionation effects presented so far solely relate to the sink reactions of CH_4. This is sufficient for a simplified CH_4 chemistry description, where only sink reactions of CH_4 are relevant. However, in the EMAC model as used in this study further chemical fractionation effects need to be considered when a more comprehensive kinetic set-up is applied.

In Table 2.5 these additional KIEs used in a comprehensive chemical mechanism within EMAC are presented. For further information on the chemical mechanism with and without isotopologues see Section 3.4 and the following ones. Note that only fractionation effects with respect to D are considered in the complex chemical set-up.

The value of the KIE indicates the differences in the reaction rates with respect to the involved isotopologues. However, isotope fractionation effects in chemical reactions are also evident on the product side of the reaction. For example, D in CH_3D either stays connected to the carbon and reaches the product deuterated methyl (CH_2D) or is detracted by the reactant OH to form HDO. Indeed, the so called isotopic composition transfer describes, how the isotopes of the educts are passed to and distributed among the products by accounting for mass and isotopic conservation.

The isotopic composition of the products is determined (1) by the branching ratios of the reaction channels and (2) by the transfer probabilities of the isotope during the reaction towards the products.

Some photochemical reactions form different product channels given the same educts (e.g. Reaction

(R 2.2)). The probability of a certain product channel to form is called the branching ratio. These branching ratios can be altered in presence of isotopologues inducing an additional isotope effect [Kaye, 1992].

During the reaction process the atoms of the educt molecules are distributed among the product molecules. Isotopic transfer probabilities indicate whether the isotope of the involved isotopologue X_H is passed to product P or to Q, if both include the element of the isotope.

In order to explain the origin of isotope influenced transfer probabilities, consider the exemplary reaction of the methoxy radical (CH_3O) with O_2 [Hu et al., 2012],

$$CH_3O + O_2 \longrightarrow HCHO + HO_2 \cdot \tag{R 2.7}$$
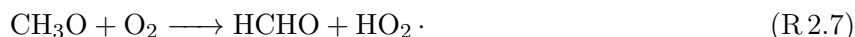
For deuterated CH_3O (CH_2DO) it is possible, that the D either stays connected to the carbon and forms formaldehyde (HCHO) or is stripped off by O_2 and forms HO_2. I.e.

$$CH_2DO + O_2 \longrightarrow HCDO + HO_2 \tag{R 2.8}$$
$$\longrightarrow HCHO + DO_2 \tag{R 2.9}$$
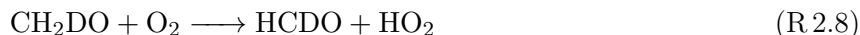
However, the channels (R 2.8) and (R 2.9) are not equiprobable. The hydrogen abstraction process is influenced by the bond reactivity of the C–D and C–H bond, respectively. Since, as stated before, heavy isotopologues in general strengthen the molecular bond, it is no surprise that the reactivity of the C–D bond is 1/8 of the C–H bond [Nilsson et al., 2007]. Therefore the products of (R 2.8) are favored over (R 2.9). Hu et al. [2012] also shows that the (R 2.9) channel is further suppressed for lower temperatures, indicating a temperature dependency.

Another vivid example for the non-stochastic isotopic transfer are the reactions of atmospheric species with the radicals OH and HO_2, which usually result in H_2O through hydrogen abstraction from the reactant. If the reacting radical is carrying D (i.e. DO, DO_2) it will be included in the resulting water molecule as well, determining the isotope transfer towards HDO.

Summarizing, the combination of KIE, isotopic branching ratios and isotope transfer probabilities is shaping the chemical isotopic fractionation of the reaction products.

2.5   The Hydroxyl Radical

The hydroxyl radical (OH) is the most important cleansing oxidant in the atmosphere [Spivakovsky et al., 2000, Lawrence et al., 2001, Lelieveld et al., 2004] and is often referred to as the oxidation (alternatively oxidizing or self-cleansing) capacity of the atmosphere [Montzka et al., 2011, Nicely et al., 2017, Lelieveld et al., 2016, 2004]. Metaphorical speaking it is the detergent of the atmosphere by reacting with a large variety of organic and inorganic compounds (CH_4, CO, nitrogen dioxide (NO_2), non-methane hydrocarbons (NMHCs) etc., to name only a few). Among others, it oxidizes harmful greenhouse gases and is also a crucial participant in the HOx-NOx-cycle (odd hydrogen (HO_x) and nitrous oxides (NO_x)). The average tropospheric lifetime of OH is 1.5 s, with, locally, being approximately less than 1 s in the boundary layer (BL), and up to 20 s around the tropical tropopause [Lelieveld et al., 2016].

Due to the importance of OH as a sink reaction partner, additionally to the mere atmospheric OH concentration, the oxidation capacity is often represented with respect to the sink reactions of certain atmospheric species (e.g. methylchloroform (CH_3CCl_3), CO or CH_4) in terms of the so called atmospheric lifetimes [Dentener et al., 2003, Lawrence et al., 2001, Fiore et al., 2006, Naik et al., 2013, Bell et al., 2003].

The main source of OH is the photolysis of O_3 at a wavelength of $\lesssim 336$ nm, resulting in $O(^1D)$, which further reacts with H_2O [Finlayson-Pitts and Pitts, 2000]:

$$O_3 + h\nu \xrightarrow{j_{O_3 \to O(^1D)}} O(^1D) + O_2 \tag{R 2.10}$$

$$O(^1D) + H_2O \xrightarrow{k_5} 2\,OH \quad \cdot \tag{R 2.11}$$
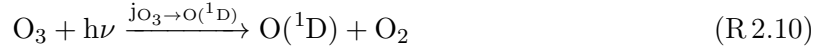
Furthermore, $O(^1D)$ can also return to its ground state by the following reaction:

$$O(^1D) + M \xrightarrow{k_6} O + M \tag{R 2.12}$$

with M being either N_2 or O_2.

The production rate of OH can approximately be calculated with respect to O_3 and H_2O concentrations:

$$P_{OH} \quad = \quad \frac{2 j_{O_3 \to O(^1D)} k_6}{k_5} \frac{[H_2O]}{[M]} [O_3] \tag{2.8}$$

after Seinfeld and Pandis [2006], with $j_{O_3 \to O(^1D)}$ being the photolysis rate of Reaction (R 2.10) and k_5 and k_6 the reaction rates of Reactions (R 2.11) and (R 2.12), respectively:

$$k_5 \quad = \quad 1.63 \cdot 10^{-10} \cdot \exp(60/T) \tag{2.9}$$

$$k_6(M = O_2) \quad = \quad 3.3 \cdot 10^{-11} \cdot \exp(55/T) \tag{2.10}$$

$$k_6(M = N_2) \quad = \quad 2.15 \cdot 10^{-11} \cdot \exp(110/T). \tag{2.11}$$

with T being temperature in K.

In the present study OH is mostly of interest due to its role as a sink for CH_4. It is thereby responsible for up to 90% of the CH_4 removal in the atmosphere [Gosh et al., 2015].

2.6 Stratospheric Water Vapor

Atmospheric water vapor is most abundant in the troposphere. In the global hydrological cycle, water vapor is introduced into the atmosphere by evaporation. It underlies convection and transport, condenses and rains out.

The present study highlights the chemical production of stratospheric water vapor (SWV), which is by itself an influential driver of climate change. Enhanced SWV, for example, negatively influences the stratospheric ozone concentration [Stenke and Grewe, 2005, Revell et al., 2016], cools the stratosphere [Revell et al., 2012, Forster and Shine, 1999, Maycock et al., 2014] and causes a positive radiative forcing [Solomon et al., 2010]. It is a mostly natural produced GHG, but there is also a non-negligible chemical contribution to SWV, mostly by oxidation of CH_4 and hydrogen gas (H_2). These gases are still abundant above the tropopause to act as significant in-situ photochemical sources of SWV, which therefore experiences a potential anthropogenic influence. Metaphorical speaking, the trace gases CH_4 and H_2 serve as the "Trojan horse" for SWV [Brenninkmeijer, 2009]. In the present study this impact on SWV is used as an example for the secondary climate effect of CH_4.

The water vapor abundance in the stratosphere is mainly controlled by the cold point at the tropopause. Particularly low temperatures at the cold point reduce the humidity of the air, since less water vapor can be carried (the air is freeze dried) [Fueglistaler and Haynes, 2005]. This process is responsible for the strong H_2O gradient between troposphere and stratosphere (see Fig. 2.4) and reduces the water vapor mixing ratio by several orders of magnitude from 10×10^4 ppmv in the BL to 5–10 ppmv in the stratosphere [Hall et al., 2016].
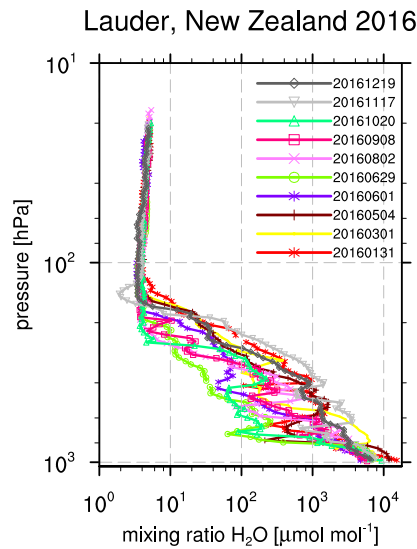
Figure 2.4: Vertical profiles of water vapor in 2016 over Lauder (New Zealand) of 10 balloon borne measurements with a frost point hygrometer. Data retrieved from `ftp://aftp.cmdl.noaa.gov/data/ozwv/WaterVapor/Lauder_New/` (Accessed: January 2018, contact: Dale Hurst) [Hall et al., 2016].

Changes in SWV are driven by stratosphere-troposphere exchange (STE), e.g., through deep convection in the tropics [Fueglistaler and Haynes, 2005] or transport by eddy motion on isentropic surfaces from the subtropics towards higher latitudes [Holton et al., 1995, Ploeger et al., 2013]. A prominent example of the variations in SWV is the so called tape recorder signal in the tropical stratosphere, first reported by Mote [1995]. It displays the alternating transport of primarily dry and moist air into the stratosphere, during boreal winter and summer, respectively. The signal is then propagated upward by the Brewer-Dobson circulation (BDC), shaping a distinct wave-like pattern.

Altogether, SWV likely increases due to climate warming [Dessler et al., 2013], but strong variations of the SWV are also driven by temporary events like the El Niño-Southern Oscillation and La Niña events [Brinkop et al., 2016].

The Chemistry Climate Model EMAC

In the following the model system and technical tools used in the present study are introduced. This chapter should serve as a reference for certain definitions and general setups of simulations carried out in the course of this thesis.

The conducted simulations use the ECHAM/MESSy Atmospheric Chemistry (EMAC) model. "It is a state-of-the art numerical chemistry and climate simulation system that includes submodels describing tropospheric and middle atmosphere processes and their interaction with oceans, land and human influences [Jöckel et al., 2010]. It uses the second version of the Modular Earth Submodel System (MESSy) to link multi-institutional computer codes. The core atmospheric model is the 5th generation European Centre Hamburg general circulation model (ECHAM5) [Roeckner et al., 2006]."

For the present study EMAC (ECHAM5 version 5.3.02, MESSy version 2.52 and 2.53) is applied in the T42L90MA- or T42L47MA-resolution, "i.e. with a spherical truncation of T42, which corresponds to a quadratic Gaussian grid of approx. 2.8 by 2.8 degrees in latitude and longitude, and includes 90 or 47 vertical hybrid pressure levels, respectively, up to 0.01 hPa" (model description taken from `http://www.messy-interface.org`).

The EMAC model is highly flexible and can be configured in several operational modes, which is possible due to the incorporated Modular Earth Submodel System (MESSy) described below.

3.1 The Modular Earth Submodel System (MESSy)

The framework of MESSy is based on the idea to modularize a climate model in a way, that single components can be switch on and off depending on the desired set-up, meeting the demands of current Earth System Modeling in terms of flexibility and computational performance. The modularization enables the user to pick suitable submodels or expand the model easily with new ones.

The so called base model is the atmospheric core of the model system. It is responsible for the parameterization of physical processes in the atmosphere (e.g. vertical diffusion, convection, clouds). Some routines of ECHAM5 have been adopted by MESSy submodels and were partly extended [Jöckel et al., 2016], which further emphasizes the flexibility of the MESSy framework.

MESSy is constructed in several layers from the Base Model Layer (BML) over the Base Model Interface Layer (BMIL) and the Submodel Interface Layer (SMIL) to the Submodel Core Layer (SMCL) (sketched in Fig. 3.1). The base model and submodels solely communicate over the interfaces layers (BMIL and SMIL), which makes the submodels independent from the base model. Generic submodels on the BMIL provide common subroutines, control interfaces and a joint infrastructure for data handling (e.g. import and output) [Jöckel et al., 2010]. Among those are, for example, CHANNEL for memory and meta-data management and data export [Jöckel et al., 2010] and TRACER for management of data and meta-data of constituents [Jöckel et al., 2008].

The independence of SMCL and BML makes it also possible to switch the base model. At the moment, besides ECHAM5, as used for EMAC, also the base models Community Earth System Model (CESM) and Consortium for Small-Scale Model (COSMO) are available. For the present study, however, only EMAC is used.
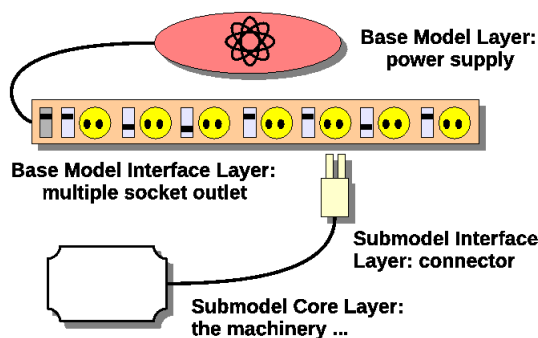
Figure 3.1: Schematics, displaying the four main layers of MESSy. The Base Model Layer (BML) is connected via Base Model Interface Layer (BMIL) and Submodel Interface Layer (SMIL) to the Submodel Core Layer (SMCL).

Individual namelists for the submodels enable the user to construct the EMAC set-up tailor-made according to the research objective. An overview of the MESSy submodels used for the simulations presented in this study are listed in Table 3.1. In the following the most relevant operational modes, submodels and corresponding model developments are described in more detail.

3.2   Operational Modes of EMAC

As stated before, MESSy allows the configuration of EMAC in several operational modes. The two basic ones are the General Circulation model (GCM) set-up without chemistry and the Chemistry-Climate model (CCM) set-up with fully interactive chemistry, using, among other components, the Module Efficiently Calculating the Chemistry of the Atmosphere (MECCA). However, MESSy provides also a manifold of additional alternatives. An excerpt of the modes applied in the simulations presented in this thesis, is presented in the following.

Most important for the present study is the inclusion of the simplified CH_4 chemistry in a GCM mode by using the submodel CH4, which is described in more detail in the next section. A crucial part of this thesis is the comparison of this pseudo CCM to the fully interactive CCM (including MECCA).

Another presented mode includes the coupling with an ocean model (e.g. MPIOM, [Pozzer et al., 2011]), which improves the Earth system simulation regarding climate change, since it considers potential ocean-atmosphere feedbacks and accounts for the relative long time scale of climate adaptation of the oceans [Dameris and Jöckel, 2013]. The combination of this coupled ocean with a CCM set-up further enables to study interactions of atmospheric chemistry and climate change in an Atmosphere-Ocean Chemistry-Climate model (AO-CCM).

Furthermore, EMAC can either be conducted in a "free running" mode, without constraints on meteorological reference data, or with specified dynamics. The latter indicates that a Newtonian relaxation (so called "nudging") to meteorological reference data is applied, in order to represent realistic meteorological conditions of the simulated time periods. In EMAC nudging is performed with the prognostic variables divergence, vorticity, temperature and (logarithm of) surface pressure. A different form of nudging is also applied in EMAC to constrain selected tracers by using the submodel TNUDGE [Kerkweg et al., 2006b]. This is usually done in CCM mode simulations for CO_2, CH_4 and nitrous oxide (N_2O), which are prescribed at the lowest model layer to be consistent with atmospheric observations.

The various simulations presented in the four chapters of this thesis represent individual configura-

Table 3.1: Overview of the applied MESSy process and diagnostic submodels. The submodels highlighted in the upper section are in particular modified, uniquely configured or newly implemented for this study.

submodel	description	reference
CAABA[a]	atmospheric chemistry box model	[Sander et al., 2011a]
CH4[a]	simplified methane chemistry	[Eichinger et al., 2015a] and this work
H2OISO[a]	water isotopologues	[Eichinger et al., 2015a]
MECCA[b]	tropospheric and stratospheric chemistry	[Sander et al., 2011a]
MECCA-TAG[b]	kinetic chemistry tagging technique	[Gromov et al., 2010]
MSBM[a]	multi-phase stratospheric box model	[Jöckel et al., 2010]
TRSYNC[c]	tracer synchronization for HDO	this work
AEROPT	aerosol optical properties	http://www.messy-interface.org
AIRSEA	air-sea exchange	[Pozzer et al., 2006]
CLOUD	ECHAM5 cloud scheme	[Roeckner et al., 2006, Jöckel et al., 2006]
CLOUDOPT	optical properties of clouds	[Dietmüller et al., 2016]
CONTRAIL	potential contrail and contrail cirrus coverage	[Jöckel et al., 2016]
CONVECT	convection parameterization	[Tost et al., 2006b]
CVTRANS	convective tracer transport	[Tost, 2006]
DDEP	dry deposition	[Kerkweg et al., 2006a]
DRADON	^{222}Rn as a diagnostic tracer	[Jöckel et al., 2010]
E5VDIFF	ECHAM5 vertical diffusion	http://www.messy-interface.org
GWAVE	non-orographic gravity waves	[Baumgaertner et al., 2013]
JVAL	photolysis rate coefficients	[Sander et al., 2014]
LNOX	lightning NO_x	[Grewe et al., 2001, Tost et al., 2007]
O3ORIG	ozone origin diagnostics	[Grewe, 2006]
OFFEMIS	offline emissions	[Kerkweg et al., 2006b]
ONEMIS	online emissions	[Kerkweg et al., 2006b]
ORBIT	Earth's orbit around the Sun	[Dietmüller et al., 2016]
OROGW	orographic gravity waves and low level drag	http://www.messy-interface.org
PTRAC	additional tracers beyond the chemical mechanism	[Jöckel et al., 2008]
QBO	assimilation of the quasi-biennial oscillation (QBO)	[Giorgetta et al., 2002, Jöckel et al., 2006]
RAD	radiation scheme	[Roeckner et al., 2006, Jöckel et al., 2006, Dietmüller et al., 2016]
S4D	sampling in four dimensions	[Jöckel et al., 2010]
SATSIMS	satellite simulators	[Jöckel et al., 2016]
SCALC	simple algebraic calculations	[Kern, 2013]
SCAV	scavenging and wet deposition of aerosol and trace gases	[Tost et al., 2006a]
SCOUT	stationary column output	[Jöckel et al., 2010]
SEDI	sedimentation of aerosol particles	[Kerkweg et al., 2006a]
SORBIT	sampling along sun-synchronous satellite orbits	[Jöckel et al., 2010]
SURFACE	surface processes	[Jöckel et al., 2010]
TNUDGE	Newtonian relaxation of tracers	[Kerkweg et al., 2006b]
TREXP	decay and release of additional tracers	[Jöckel et al., 2010]
TROPOP	tropopause diagnostics	[Jöckel et al., 2006]
VISO	iso-surfaces and maps	[Jöckel et al., 2010]

[a] submodel modified for this study
[b] extensive, novel, and unique configurations applied
[c] newly implemented

tions with respect to the desired analysis outline. Due to this fact, an overview of these simulations including their specific configurations are not given at this point. Instead, the individual set-ups are presented in the following chapters, close to the corresponding analyses.

3.3 The Submodel CH4

The focus of the present study with EMAC is on atmospheric methane and its isotopologues. However, simulations with CCMs are, due to the large number of involved chemical species computationally demanding.

The basic concept of the MESSy submodel CH4 is to reduce the chemical mechanism to the loss-processes of methane. This simplified chemistry uses predefined fields of the reaction partners OH, $O(^1D)$ and Cl, from either earlier fully interactive chemistry simulations with EMAC, or from other data sources (e.g. reanalyses). If CH4 is included in a CCM simulation, the CH4 submodel can also be coupled to the reactant fields, which are on-line calculated during the same simulation by the chemical mechanism. The same applies for the photolysis rate of CH_4, which is on-line calculated by the submodel JVAL.

Current GCMs include CH_4 foremost for its influence on SWV (e.g. [Monge-Sanz et al., 2013, ECMWF, 2007, Austin et al., 2007, Boville et al., 2001, Mote, 1995]). The CH4 submodel is likewise equipped with an optional feedback onto H_2O, to account for the secondary climate feedback of CH_4. It is thereby assumed that two molecules of H_2O are produced per oxidized CH_4 molecule, which is a rough approximation based on le Texier et al. [1988]. For further discussion on this assumption, see Chapter 7.

First simulations using the CH4 submodel are presented in studies of Eichinger et al. [2015a,b] and it was exemplarily included in the simulations of the Earth System Chemistry integrated Modelling (ESCiMo) project [Jöckel et al., 2016]. The submodel CH4 is confined solely to the four degradation reactions of CH_4 (e.g. Reaction (R 2.1)–(R 2.6)). Thus, it is considerably computationally cheaper, compared to a fully interactive chemistry simulation using MECCA, which represents (depending on the chosen set-up) several hundred reactions (e.g. 224 in the base simulations of ESCiMo). For example, a reference set-up with MECCA requires about 250 node-h[1] per simulated year, while a set-up with the CH4 submodel without MECCA requires only 30 node-h per year (these numbers are calculated for simulations conducted on the high performance computer (HPC) Mistral at the *Deutsches Klimarechenzentrum* (DKRZ)).

Figure 3.2 visualizes the conceptual differences between the MESSy submodel CH4 (left) and a CCM simulation with MECCA (right). MECCA simulates the entire chemical mechanism and therefore also includes the feedback onto the reaction partners of CH_4. Additionally, there is also a secondary feedback by the products from the CH_4 sink reactions. Conversely, the CH4 submodel uses the predefined fields of the reactant species to calculate the CH_4 loss. This loss is included in the CH_4 tracer of the CH4 submodel (`CH4_fx`) but does not feedback onto the sink fields or any other chemical species, except H_2O, in the case when the hydrological feedback of CH_4 oxidation is switched on.

Although higher frequencies are technically possible, monthly mean sink fields are used in the present set-up. Monthly mean fields smooth the diurnal cycle, which is especially strong in OH. However, the aim of the application in the present study is to investigate long-term global climatological trends of CH_4, which, as stated before, has a tropospheric lifetime of 8–10 years. Variations on time scales of less than one month are therefore negligible and monthly mean fields are assumed to suffice for the sought application.

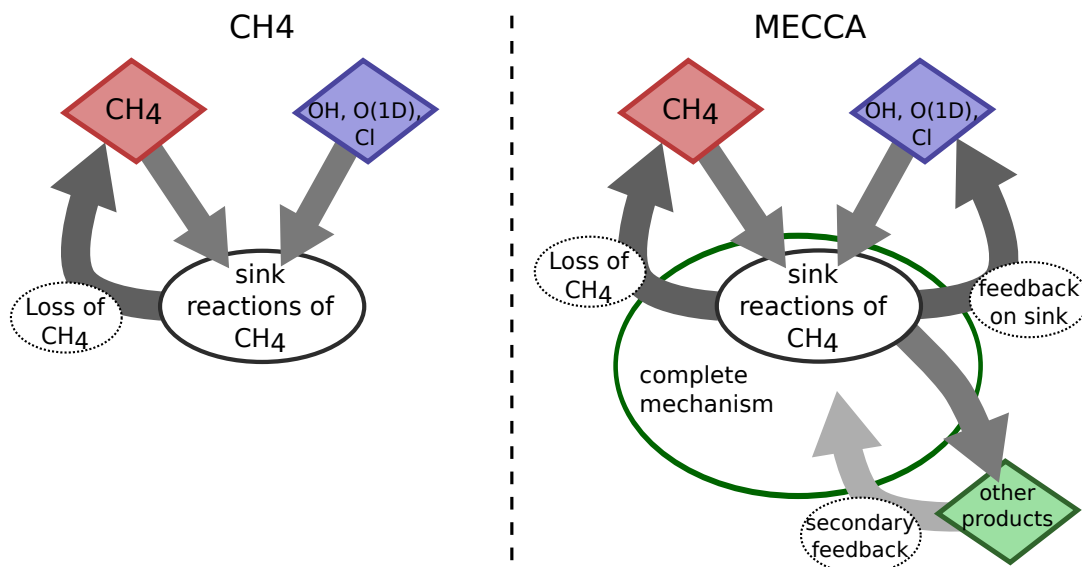[1]node-h: required wall-clock hours times applied HPC nodes.

Figure 3.2: Sketch visualizing the concepts of parameterizing CH_4 sink reactions in the MESSy submodels CH4 (left) and MECCA (right).

For further information consider the technical documentation of the CH4 submodel in the Appendix C.

3.3.1 The Isotopologue Extension in the CH4 submodel

Additional to the basic CH_4 parameterization, the submodel CH4 is further extended for the present study to allow for the simulation of methane isotopologues, which are a potent diagnostic tool in the source and sink attribution. In this extension, the reaction rates of CH_4 with its reaction partners are adjusted with respect to the KIE factors, e.g.:

$$\text{KIE} = k_{CH_4+OH}/k_{CH_3D+OH} \tag{3.1}$$

$$k_{CH_3D+OH} = k_{CH_4+OH} * \text{KIE}^{-1} . \tag{3.2}$$

The submodel CH4 is able to simulate the abundant and first rare isotopologues and defines these as tracers additional to the master tracer `CH4_fx` of the submodel. Higher substituted isotopologues are neglected. The user can choose, whether isotopologues are simulated with respect to carbon (methane containing ^{12}C ($^{12}CH_4$) and $^{13}CH_4$), or hydrogen (CH_4 and CH_3D, with CH_4 including ^1H isotopes only), or both. The abundant and rare isotopologues are thereby simulated in parallel. During the simulation it is taken care that both sum up to the master tracer `CH4_fx`. Moreover, the isotopic signatures of CH_4 emission sources are simulated with OFFEMIS [Kerkweg et al., 2006b]. Sources are distinguished by their emission type (see Table 2.3), however, for the moment, no regional variations in the source signatures are included.

The oxidation of CH_3D produces to a certain extent HDO. If the feedback of CH_4 oxidation onto the hydrological cycle is switched on, an additional tracer for HDO is created and filled by the produced HDO from CH_3D oxidation. There are two options available: (1) one oxidized CH_3D produces one

HDO molecule or (2) the tendency of the HDO tracer is calculated by Eq. 3.3 [Eichinger et al., 2015a]:

$$\frac{\partial(HDO)}{\partial t} = \frac{-\frac{\partial(CH_3D)}{\partial t} + 6.32 \times 10^{-5} \cdot \frac{\partial(CH_4)}{\partial t}}{\frac{M_{air}}{M_{HDO}} \left(\frac{1}{1-HDO}\right)^2} \ . \tag{3.3}$$

with M_{air}/M_{HDO} being the molar masses of air (28.987 g mol^{-1}) and HDO (19.02 g mol^{-1}), respectively.

This equation accounts for the D, which stays in deuterated hydrogen gas (HD), as it builds up to an equilibrium with HDO via the HOx-cycle.

3.3.2   CH4 Submodel with Age and Emission Classes

As mentioned before, current estimates of CH_4 emission inventories still include large uncertainties. In order to reduce these, new estimates of inventories must be able to represent temporal and spatial resolutions in greater detail (e.g. seasonal cycle, distinct regions). One statistical method to estimate CH_4 emission strengths is the fixed-lag Kalman Filter, which performs an inverse optimization by comparing simulated and observed mixing ratios of a trace gas. This "off-line" inversion algorithm requires data from a forward simulation including temporal and spatial information of the simulated CH_4 tracer.

In EMAC this additional information is provided by the extension of the CH4 submodel concerning age and emission classes. These classes enable a precise distinction between selected CH_4 source categories and/or regions, as well as further insight into the CH_4 distribution over time. The term emission class denotes thereby a methane-like tracer in the extension of the CH4 submodel and is subject to the emissions of a combination of an emission type (like wetlands, rice, etc.) and region (e.g. continents or countries). The tracer emis01, for example, could thus trace anthropogenic methane emitted from Africa. These additional diagnostic tracers are transported identical to the master CH_4 tracer of the CH4 submodel and also experience the same sink reactions.

The time period represented by one age class can be chosen by the user. The default and used configuration in this work is that one age class represents one month. How the age and emission classes evolve over time in this default configuration is depicted in Fig. 3.3. Methane of each emission class is propagated through a specific number of age classes (in the applied case: 5). The emitted CH_4 of one month of a specific emission class is added to its first age class. After one month all CH_4 of one class is moved to the next "older" age class, hence, the CH_4 of the first age class moves after one month into the second and after another month into the third and so on. In the last age class the CH_4 gets accumulated, since it does not proceed further. This age class is also acknowledged as the background CH_4.

The assignment of the emission classes to the emission sources is done in the submodel OFFEMIS, where each emission class tracer is filled by its own emission source. In order to avoid numerical biases, the age and emission classes are, moreover, continuously constrained (i.e. in each model time step) to sum up to the master tracer `CH4_fx` and scaled appropriately if the sum deviates.

3.4   The Chemical Processes in EMAC

The Module Efficiently Calculating the Chemistry of the Atmosphere (MECCA) [Sander et al., 2005] represents the chemical core of EMAC. It defines the underlying chemical reaction mechanisms for gas-phase chemistry in various domains (e.g. troposphere, stratosphere). MECCA provides a
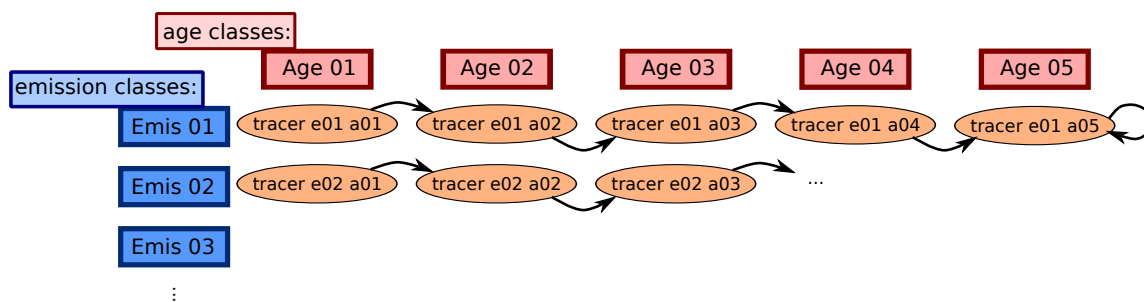
Figure 3.3: Sketch picturing the advancing of the age classes in the CH4 submodel. Each tracer represents one specific emission and age class. After one month the age classes proceed to the next "older" age class. The last class (Age 5) is the accumulative class representing the background CH_4.

comprehensive mechanism, combining state of the art reactions and rate coefficients recommended by Sander et al. [2011b] and partly by other references (see Appendix E).

The kinetic preprocessor (KPP) used in MECCA translates the chemical mechanism into source code for solving the corresponding differential equations and includes appropriate numerical solvers for the latter [Sander et al., 2005, Sandu and Sander, 2006].

Photolysis rate coefficients are for instance on-line calculated by the submodel JVAL [Sander et al., 2014]. The basic mechanism includes the chemistry of O_3, CH_4, HO_x, NO_x, NMHC (up to four carbon atoms plus isoprene), Cl, bromine (Br), jodine (I) and sulfur. Recent developments of the chemical mechanism extended the basic chemistry also towards detailed isoprene, terpenes and aromatics chemistry (i.e. Mainz Organic Mechanism (MOM)) and there are several other chemical mechanism available within MECCA [Sander et al., 2018].

Usually, subsets of reactions are selected from the comprehensive available chemical mechanism. This makes it possible to construct a custom-made chemical mechanism, according to the desired set-up and computational constraints [Sander et al., 2005]. The chemical mechanism, applied in the presented simulations of this study, is based on selected reactions, which, for example, were used and evaluated with the base simulations in the ESCiMo project [Jöckel et al., 2016] (for further details on this project see chapter 4). The mechanism at hand was further extended to resolve specific intermediates in the $CH_4 \longrightarrow H_2O$ reaction chain, resulting in slightly more comprehensive chemical kinetics. The full chemical mechanism as used in ESCiMo is published in the supplement of Jöckel et al. [2016]. The additional and changed reactions, respectively, for the present study including the corresponding references are listed in Appendix E.

For the sake of completeness, the submodels SCAV [Tost et al., 2006b] and MSBM [Jöckel et al., 2010] are responsible for chemical processes beyond the chemical mechanism of MECCA. The submodel SCAV describes the aqueous-phase chemistry and wet-deposition of trace gases and aerosols, hence their removal by clouds and precipitation. The stratospheric heterogeneous chemistry is simulated by the submodel MSBM. This includes the generation of sulfuric acid aerosols and particles, responsible for the formation of polar stratospheric clouds (PSCs).

3.5 The Kinetic Chemistry Tagging Technique

The kinetic chemistry tagging technique (MECCA-TAG) [Gromov et al., 2010] enables the user to tag certain chemical elements, without modifying the underlying standard chemical mechanism of MECCA. It can either be applied for simulating isotopologues of trace gases with respect to selected isotopes or used to investigate elemental exchange between the species of interest. For example, model

studies were carried out focusing on carbon (C) and atomic oxygen (O) isotope composition of CO [Gromov et al., 2010, 2017]. Note that for the application of MECCA-TAG including MECCA in the model set-up is mandatory.

In the simulations of the present study, MECCA-TAG is applied for simulating hydrogen isotopes. This involves particularly the isotopologues of CH_4 and H_2O and enables the investigation of the pathways of D from CH_3D towards HDO. In order to do so, counterparts of the species of interest (e.g. those containing atomic hydrogen (H)) are created in an isolated doubled set of studied reactions (e.g. CH_4 oxidation chemistry) in the same chemical mechanism simulated. These compounds in MECCA-TAG are representing the abundant and rare isotopological content, resulting in two additional tracers per tagged chemical species, which are further constrained to add up to the corresponding master compound. To account for the chemical fractionation additional KIEs are implemented according to Table 2.5. Furthermore, certain branching ratios and transfer probabilities are set for reactions, which include molecules containing hydrogen. If no particular branching ratios or transfer probabilities are known, probabilities based on stochastic assumptions are applied [Gromov, 2014].

Furthermore, in the present study the tagging technique (in the so called fractional mode) is also used to investigate the pathways of H transfer from the source CH_4 to H_2O via all simulated intermediates. By doing so, it is possible to quantify the fraction of molecules (hence their H content) stemming from CH_4 oxidation only, as well as their production and loss rates. Furthermore, the latter has been improved by quantifying production and loss of H_2O with recycled H in the given reactions.

In this particular case, the H_2O molecules created from CH_4 oxidation pathways are counted, enabling the differentiation of H from CH_4 to H from other sources (e.g. H_2, NMHCs, hydrochlorofluorocarbons (HCFCs) etc.). However those species, which further break down to other HOx compounds (and subsequently produce H_2O again) are counted separately. This is the on-line approximation of the technique used by Lehmann [2004] and helps to avoid double-counting issues of production terms of H_2O. Ultimately, the fraction of H atoms populating the species of the complete $(CH_4 \longrightarrow H_2O \, / \, H_2 \longleftrightarrow HO_x)$-cycle can be quantified, including their fractions recycled via H_2O.

3.6   The Submodel H2OISO

The H_2O ISOtopologues (H2OISO) submodel [Eichinger, 2014, Eichinger et al., 2015a] simulates the stable water isotopologues with respect to H and D, as well as ^{16}O and ^{18}O. Overall, it represents a second hydrological cycle, which includes water isotopologues in their three phases: gas, liquid and ice. H2OISO accounts for fractionation processes during vertical diffusion, evaporation from the ocean, advection and large scale as well as convective clouds, while the surface processes of evaporation from bare soil, plants or snow are considered not to have an influential fractionation.

In former versions of H2OISO [Eichinger et al., 2015a] the chemical production of H_2O was included by using the production of H_2O from the CH4 submodel. The tendency of the production of HDO from the oxidation of CH_3D was parameterized according to Eq. 3.3 by introducing an additional CH_3D tracer. This tracer was set below 500hPa to a value constrained by the current abundance of the master tracer CH_4 to represent a constant climatological $\delta D(CH_4)$ of $-68‰$ as estimated by Ridal and Siskind [2002].

For the sake of consistency, in consecutive updates of the H2OISO submodel during the present study, the calculation of chemical induced changes of H_2O and its isotopologue tracers are moved to the chemical submodels CH4 and MECCA. Both simulate the isotopologues of CH_4 explicitly, driven by surface emissions and replace the constrained lower boundary of the former CH_3D tracer in the H2OISO submodel. This however, results in distinct H_2O isotopologue tracers for the physical
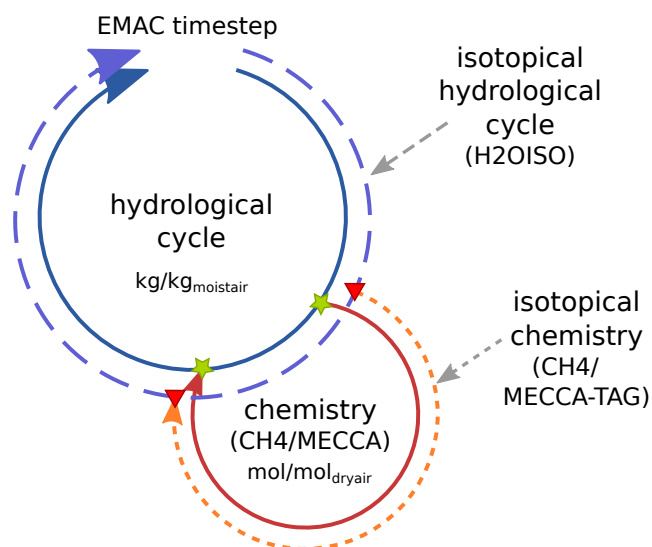
Figure 3.4: Sketch picturing the coupling of the hydrological cycle and the chemistry (either CH4 or MECCA) with respect to H_2O isotopologues in one time step of EMAC. Green stars indicate the points of the hydrological cycle, where chemical tendencies as added onto the water vapor master tracer. Red triangles indicate the synchronization points of the corresponding isotopical tracers with TRacer SYNChronization (TRSYNC). Synchronization of the isotopological cycles cares for the appropriate unit conversion and accounts for the filter of chemistry only processes on top of the fractionation in the hydrological cycle.

and chemical fractionation processes of the hydrological cycle within EMAC.

The resulting necessary technical coupling of the physical and chemical isotopological water tracers to obtain a coherent isotopical hydrological cycle is described in the following section.

3.7 Coupling of Physical and Chemical Water Tracers

The previous sections introduced three different submodels dealing with isotopologues of H_2O in the vapor phase. The CH4 submodel and MECCA-TAG are treating the chemical fractionation, while H2OISO is responsible for the physical fractionation. All three create independent tracers, which need to be synchronized to be able to combine physical and chemical fractionation effects onto H_2O. The chemical fractionation is thereby considered either from MECCA-TAG or from CH4, although both submodels can be included in the carried out simulation at the same time and compute the isotopic fractionation independently.

In principal, if EMAC is applied in a GCM mode, only the master hydrological cycle is present (see Fig. 3.4, inner solid blue cycle). Adding MECCA or CH_4 to the set-up expands the model to a CCM or a quasi CCM, respectively (red solid circle). The chemistry uses water vapor as a chemical tracer (first green star) and calculates a feedback (second green star). This chemical feedback onto water vapor was already implemented as an option in previous EMAC versions. By including the isotopological submodels into the set-up, H2OISO doubles the hydrological cycle for the water isotopologues and CH4 and MECCA-TAG create the chemical tracers of the water isotopologues. This results in several physical and chemical H_2O isotopologue tracers. While the master chemical processes could add their feedback directly to the specific humidity of the hydrological cycle (there

is no need for a chemical water tracer), the synchronization of the physical isotopological tracers in the isotopic hydrological cycle and the chemical isotopological tracer needs to be done via the auxiliary submodel TRSYNC. Since isotopological water vapor tracers of MECCA-TAG and the HDO tracer created by CH4 are transported in EMAC in the same way as every other tracer, they are subject to some of the physical processes but not to all hydrological fractionation effects. At the first synchronization point the chemical tracer is synchronized to represent the current value of the physical tracer. In the following, chemical tendencies inclusive fractionation effects are calculated and are added via the second synchronization point to the physical tracer as well. By doing so, the tendencies of the chemical tracers are adjusted to represent the chemical tendencies on top of the previous physical fractionations in the current time step. Potential physical processes influencing the chemical isotopological tracers are therefore filtered.

Note that physical tracers of water vapor (regarding ECHAM5 and H2OISO) are defined in one kg of the tracer per one kg of moist air (kg $\text{kg}^{-1}_{\text{moist air}}$), while the chemical tracers are defined in mol $\text{mol}^{-1}_{\text{dryair}}$. This also holds for the corresponding isotopologue tracers. Parameterizations of physical processes in ECHAM5 traditionally rely on specific humidity (per moist air). Conversely, chemical reactions are actually calculated with species concentrations ideally independent from the remaining air content. This justifies the individual chemical and physical isotopologue tracers, which have distinct units, and motivated the development of the auxiliary submodel TRSYNC in order to be able to synchronize these tracers accordingly and in a common way for CH4 and MECCA-TAG, respectively.

Additional to that, the application of MECCA-TAG creates the basis to investigate the course of life of various isotopes in the interactive chemical mechanism, making its way from isotopologue to isotopologue. While CH4 feedbacks on H_2O with respect to hydrogen isotopes only, MECCA-TAG can also be used to simulate oxygen isotopes (^{16}O, ^{17}O and ^{18}O) in the chemical mechanism. It is therefore also possible to couple MECCA-TAG with oxygen isotopes to the corresponding isotopologue tracers in H2OISO. Last but not least, for MECCA-TAG tracer names are not standardized. Therefore, the namelist of the submodel TRSYNC can be adjusted according to the actual tracer names in MECCA-TAG.

For further information, a technical documentation of the TRSYNC submodel is provided in Appendix D.

Lifetime of Methane in EMAC

The results of this chapter have partly been published as the Sections 4.1 and 4.4 (written by F. Frank) in Jöckel et al. [2016].

The present study focuses especially on the influence of the OH abundance onto CH_4. Although, there is evidence that OH is in general well-buffered to inter-annual variations [Lelieveld et al., 2002, Montzka et al., 2011], it is shown by McNorton et al. [2016] that already small variations in OH are enough to significantly contribute to the growth rate of CH_4. Both, Turner et al. [2017] and Rigby et al. [2017], likewise attribute changes in CH_4 growth in the last 20 years (being nearly constant in 1999–2007 and showing a renewed strong growth after 2007) to OH variations.

The oxidation capacity of the atmosphere, namely the abundance of OH, is one of the most important as well as most debated parts of atmospheric chemistry, as became evident at a workshop held in Boulder, Colorado in 2005 [Lelieveld et al., 2006]. OH plays a vital role in many atmospheric chemical reactions, but estimates of OH concentration and its variations over time still imply large uncertainties [Manning et al., 2005, Patra et al., 2014, Gosh et al., 2015]. Although efforts are undertaken measuring OH on local scale (e.g. [Finlayson-Pitts and Pitts, 2000, Heard and Pilling, 2003, Smith et al., 2006, Bloss et al., 2007, Lelieveld et al., 2008, Elshorbany et al., 2012]) and techniques do improve in terms of reduced uncertainty, measurements on global scale are basically still unavailable. Due to its strong reactivity and high variability spatio-temporal observations of OH remain considerably challenging. For example, the OH mixing ratio from shady (cloudy) to sunny conditions varies within seconds by orders of magnitude. Global distributions of OH are therefore mostly inferred in-directly via measurements of CH_3CCl_3 or carbon monoxide containing radio carbon (^{14}CO) [Brenninkmeijer et al., 1992, Jöckel et al., 2002, Manning et al., 2005, Prinn et al., 2005, Krol et al., 2008, Krol and Lelieveld, 2003, Patra et al., 2014, Montzka et al., 2011]), since the main sink of both molecules is the reaction with OH.

However, there has been decent debate about the OH concentration and distribution in the troposphere, since various studies – especially measurement based and model based studies – vary strongly in their conclusion about the OH estimate. For example, Montzka et al. [2011] concludes that OH has small inter-annual variations, while Manning et al. [2005] provides evidence for short-term variations of about 10%, but no trend. In contrast, Prinn et al. [2005] as well as Dentener et al. [2003], derived certain trends in OH. Furthermore, Lelieveld et al. [2002] suggests that relative constant OH concentrations may be fortuitous and most of the variations in OH are compensated by increasing emissions. The multiple opposing views give the impression that the life-cycle of OH is not fully resolved yet, and also shows the importance to investigate OH further as a crucial factor in the composition of the atmosphere. This lead to the discussion to establish new methods, which could be used, additional to the estimation of OH based on CH_3CCl_3 or ^{14}CO, including, for example, the release of artificial tracers as proposed by Jöckel et al. [2003]. Moreover, particularly, in the chemistry-climate modeling the global OH field is a decisive factor for the realistic representation of various chemical species. Thus, it is essential (not only) on the modelers side that current state-of-the-art CCMs accurately describe the OH budget in the atmosphere to reduce uncertainties in the simulated chemical mechanisms and

Table 4.1: Overview of tropospheric $\tau_{CH_4}(OH)$ estimates in literature.

Reference	$\tau_{CH_4}(OH)$ in [a]	uncertainty	time-period
measurement based			
[Prather et al., 2012]	11.2	± 1.3	
[Prinn et al., 2005]	10.2	$+0.9/-0.7$	
[Krol et al., 1998]	9.2	$+1.7/-0.8$	1978
	8.6	$+1.6/-0.8$	1993
model based			
[Dentener et al., 2003]	9.0	± 0.13	1979–1993
[Voulgarakis et al., 2013]	9.8	± 1.6	2000
[Naik et al., 2013]	9.7	± 1.5	2000
[Nicely et al., 2017]	9.3	(8.0–11.6)	2008
[Fiore et al., 2006]	10.23		
[Karlsdóttir and Isaksen, 2000]	8.4	± 0.5	
[Gosh et al., 2015]	9.0	± 0.09	
[Jöckel et al., 2006]	8.02		
[von Kuhlmann, 2001]	8.7		
[Hein et al., 1997]	8.3		
[Righi et al., 2015]	8.3	(7.9–9.1)	1999–2009
[Lelieveld et al., 2016]	8.5		
[Dalsøren et al., 2016]	9.6		1970
	8.8		2012
this study	8.11	± 0.13	2000–2010

in particular motivates the investigation of the oxidation capacity carried out in this chapter.

In general, model based OH levels are higher than estimates reported from measurements, which is attributed by Bell et al. [2003] to unresolved processes in the simulated chemical mechanisms. Consequently, model-based estimates of the lifetime of CH_4 with respect to OH ($\tau_{CH_4}(OH)$), varying from 8.3 year (a) [Hein et al., 1997] to 10.23 a [Fiore et al., 2006], are generally lower than observation-based estimates of $\tau_{CH_4}(OH)$ derived from CH_3CCl_3 abundance, e.g. by Prather et al. [2012] and Prinn et al. [2005] with 11.2 ± 1.3 a and $10.2(+0.9/-0.7)$ a, respectively, with the exception of Krol et al. [1998] (max. $9.2(+1.7/-0.8)$ a). The wide range of lifetimes of CH_4 (τ_{CH_4}) (cf. Table 4.1) is mainly caused by different methods of calculation and applied weighting [Lawrence et al., 2001], whereas varying included vertical layers due to different tropopause definitions have a minor impact (see also [O'Connor et al., 2014]). The table also includes the averaged value derived in this study for the year 2000–2010 as the multi simulation mean (MSM) of the analyzed simulations.

In this study $\tau_{CH_4}(OH)$ and airmass weighted OH concentration ($[OH]_{AW}$), as widely used and accepted indicators of the oxidation capacity of the atmosphere, are used to compare several simulations of the ESCiMo project [Jöckel et al., 2016]. This study follows thereby the recommendation of Lawrence et al. [2001] regarding comparable global mean OH concentrations and methane lifetime. Similar analyses have, for example, been done by Naik et al. [2013], Voulgarakis et al. [2013] and Nicely et al. [2017]. These studies compared different CCMs with various process parameterizations or meteorological parameters. In contrast, the current study presents investigations of variations in

τ_{CH_4}(OH) and [OH]$_{AW}$ within the same CCM with respect to different model configurations. For the evaluation of τ_{CH_4}(OH) and the oxidation capacity the main focus is on long-term trends, hence mostly annual means and inter-annual variations of specific variables are considered.

In the first section of this chapter the consortial project ESCiMo is introduced, on which the evaluation study in this chapter is based. An overview of the ESCiMo reference simulations used for the study is also given, including a description of the various set-ups and a short basic analysis of temperature, CH$_4$ mixing ratio and OH concentration in the various simulations. Additionally, a study concerning extreme methane enhancements is introduced, which gives an overview on large scale trends of the oxidation capacity with respect to CH$_4$ emissions. The subsequent sections define the used methods to calculate methane lifetime. Variations between the simulations with respect to methane lifetime and in the projections onto future climates are analyzed. Additional conclusions are drawn by analyzing sub-compartments of [OH]$_{AW}$ and lifetime of CH$_4$ (τ_{CH_4}). At last, the impact of minor numerical factors in the lifetime calculation are discussed.

Figures in this chapter are produced with the aid of the ESMValTool 1.0 [Eyring et al., 2016].

4.1 The Consortial Project ESCiMo

The project "Earth System Chemistry integrated Modelling (ESCiMo)" was conducted by the MESSy Consortium and includes several reference and sensitivity simulations carried out with the EMAC model [Jöckel et al., 2016]. The project aims at a deeper understanding of chemistry-climate interactions and provides a comprehensive dataset to study dynamics and chemistry in the atmosphere.

The excerpt of the ESCiMo simulations analyzed in this study are listed in Table 4.2. The comprehensive simulation experiments include hindcast (RC1-* and RC1SD-*) and projection (RC2-*) simulations within the years 1950–2100 on variable time periods. They differ with respect to vertical resolution (i.e. 47 or 90 levels), the applied sea surface temperatures (SSTs) (observed, nudged to ERA-Interim or simulated) and are either free-running or with specified dynamics (indicated by SD in RC1SD), which means that nudging to meteorological reference data is performed with respect to divergence, vorticity, temperature and (logarithm of) surface pressure. Particularly the simulations RC1SD-base-07/08 are notable as they are additionally mean temperature nudged, which further corrects temperature biases in the EMAC model.

Up to now the ESCiMo simulations served as the data basis for several studies on the dynamical and the chemical part. To name but a few, exemplary are the study of Löffler et al. [2016] about the variations in stratospheric water vapor after major volcanic eruptions as the El Chichon in 1982 and Mount Pinatubo in 1992, and the study concerning the water vapor drop at the millennium by Brinkop et al. [2016]. In Bacer et al. [2016], for example, the North Atlantic Oscillation is investigated and how it effects tracer transport.

The data of the simulations will become publicity available in the Climate and Environmental Retrieval and Archive (CERA) database and are part of the Chemistry-Climate Model Initiative (CCMI) project.

4.1.1 Temperature Profiles and Time Series

For the assessment of the simulated air temperatures, the results of the ESCiMo simulations are compared with ERA-Interim data [Dee et al., 2011]. The reanalysis ERA-Interim is chosen as the temperature reference, since it is also used in the simulations with specified dynamics, thus represents the overall reference meteorology in the ESCiMo simulations. Furthermore, for an overall consistency check, the temperature profiles are also compared to reanalysis data from NCEP/NCAR [Kalnay

Table 4.2: Overview of the analyzed ESCiMo simulations [Jöckel et al., 2016]. The numbers in the parentheses indicate the corresponding time period covered by the simulation.

SSTs resolution	observed SSTs	Specified Dynamics ERA-Interim SSTs	simulated SSTs
	RC1-	RC1SD-	RC2-
T42L90MA	base-07 (1950-2011) base-07a (1990-2011)[a] aero-06 (1950-1997)[b] aero-07 (1990-2011)[b] aecl-01 (1958-1971)[c] aecl-02 (1965-2011)[c]	base-07 (1979-2013)[d] base-10 (1979-2013) base-10a (2000-2014)[e]	base-04 (1950-2099)
T42L47MA	base-08 (1950-2011) base-08a (1990-2019)[a]	base-08 (1979-2013)[d] base-09 (1979-2013)	base-05 (1950-2099) oce-01 (1950-2100)[f]

[a] with stratospheric aerosol optical properties corrected
[b] with interactive tropospheric aerosol
[c] with interactive tropospheric aerosol and aerosol-cloud coupling
[d] additional mean temperature (wave 0) nudged
[e] with road traffic emissions and stratospheric aerosol optical properties corrected
[f] with interactively coupled ocean model

et al., 1996] (not shown). Differences between the two reanalyses ERA-Interim and NCEP/NCAR are marginal. NCEP/NCAR is solely in the upper tropical troposphere between $150 - 100$ hPa about $2 - 4$ K warmer. Therefore, also the differences of the ESCiMo simulations to NCEP/NCAR are similar to the differences to ERA-interim shown in this section.

The period 2000–2010 is chosen for the evaluation, as it is covered by most of the simulations. The presented differences are, however, consistent with respect to longer time periods as well (i.e. in simulations where those are available).

Multi-annual climatologies of zonally averaged temperature profiles of selected simulations for the period 2000–2010 are shown in Fig. 4.1, together with a climatological tropopause as defined in Eq. (B.8). All simulations are regridded for the purpose of the comparison to the grid of the ERA-Interim data. The data is first monthly, then annually averaged and the values of ERA-Interim are subtracted from the simulation results. For the discussion, the simulations with basically identical characteristics concerning the temperature, can be put into three categories: First, the nudged simulations including nudged global mean temperature: RC1SD-base-07 and RC1SD-base-08. Second, the nudged simulations (without global mean temperature nudging): RC1SD-base-09 and RC1SD-base-10. Third, the free-running simulations: RC1-base-07/07a/08, RC1-aecl-02, RC1-aero-07, RC2-oce-01, and RC2-base-04 (excerpt of all free-running simulations).

The simulations in the first category with global mean temperature nudging perform best, as expected, compared to ERA-Interim with minor differences of mostly less than ± 1 K. Furthermore, there are only minor differences visible comparing the two different vertical resolutions of the simulations. There are also only small seasonal variations evident in this category (see Fig. F.4–F.7 in the Appendix). Solely, in the NH winter the simulations show a particular warm bias in the north polar region.

The simulations in the second category without global mean nudging show a cold bias, which moreover has an obvious vertical structure. However, the vertical patterns of the simulations in this category differ significantly between the two applied resolutions. The maximum of the cold bias in the RC1SD-base-09 simulation is at around 70 hPa with more than -4 K. Between 100 and 150 hPa this simulation shows a bias minimum of -1 to -1.5 K. In the RC1SD-base-10 simulation, with a higher vertical resolution, the maximum of the cold bias is located lower, at about 200 hPa and is less above 50 hPa. The differences in the patterns are an effect of the vertical resolution, but – although significant – the nudging of the model has a much larger impact on the temperature distribution (compare e.g. RC1SD-base-10 with RC1base-07 in Fig. 4.1). Concerning the seasonal variations, the two simulations in this category show a similar behavior, as the temperature bias in December, January, and February (DJF) is the smallest in the Arctic, while it is overall mostly negative (seasonal variations are shown in Appendix Figs. F.4–F.7).

The free-running simulations in the third category show a cold bias of more than 6 K around the tropopause and show a warm bias of 2–4 K in the SH above 100 hPa, as also analyzed in previous EMAC simulations by Righi et al. [2015]. In this region the bias is smallest in the RC2-oce-01 simulation, but the profile shows a larger cold bias below the tropical ($30°$ S–$30°$ N) tropopause at around 250 hPa. This region, however, has a smaller bias in the free-running simulation on 47 levels RC1-base-08 and the aerosol-cloud coupled simulation RC1-aecl-02. Since these simulations represent different resolutions and aerosol parameterizations, this is likely a coincidence with two separate reasons. The lower bias as in RC1-base-08 is also pronounced in RC2-base-05 (not shown) and in the nudged simulation RC1SD-base-09, which suggests that this is a feature of resolution. In the aerosol-cloud-coupled RC1-aecl-02 the lower bias can possibly be attributed to the different cloud model, which in this case is a two moment cloud microphysical scheme to explicitely calculate interactions of aerosol, cloud and radiation. In the tropical troposphere at 200–400 hPa the aerosol-cloud-coupled simulations exhibit an enhanced cloud optical thickness and cloud cover (Holger Tost, pers. communication, 2018), which tends to result in a cooling above and a warming below [Ackerman et al., 1988, Sherwood et al., 1994]. The free-running simulations also show a more pronounced seasonal cycle of the bias than the nudged simulations. The warm bias above the tropopause around $60° - 30°$ S, which is seen in the annual climatology as well, is strongest in SH winter (more than 6 K). Around this time there is also a strong cold bias of up to 10 K in the tropics above the tropopause. Solely the ocean coupled simulation RC2-oce-01 performs better in that regard.

Besides the temperature profile, the time series of the pressure weighted global mean temperature of the troposphere gives an overview of the temperature variation and evolution of the ESCiMo simulations. Notable is that the projection simulations RC2-base-04/05 predict a temperature rise of the global mean temperature (see Fig. 4.2) of about 3.05 K (0.04 K a^{-1}) from present day (2010) to the end of the 21st century with respect to the applied Representative Concentration Pathways (RCP) scenario (RCP6.0), whilst the ocean coupled simulation indicates a smaller increase of 1.81 K (0.02 K a^{-1}) (for trends in different time periods consider Table 4.4).

Again, as expected, the simulations RC1SD-base-07/08 perform best with respect to ERA-Interim, but are still about 0.7 K colder in the global mean. This corresponds to the temperature profile, where in the free troposphere a low but significant cold bias of < 2 K is visible. Even though the mean temperature is nudged, the model still has a certain degree of freedom concerning the temperature due to the relaxation time of 24 h resulting in this small bias.

Furthermore, the global mean tropospheric temperature of the specified dynamics simulations RC1SD-base-10/10a are the lowest ones. It must be noted that the cold bias in the free-running simulations is mostly above the climatological tropopause, hence not contributing much to the global mean tropospheric temperature, whilst the minimum of the cold bias in RC1SD-base-10 (cf. Fig. 4.1)
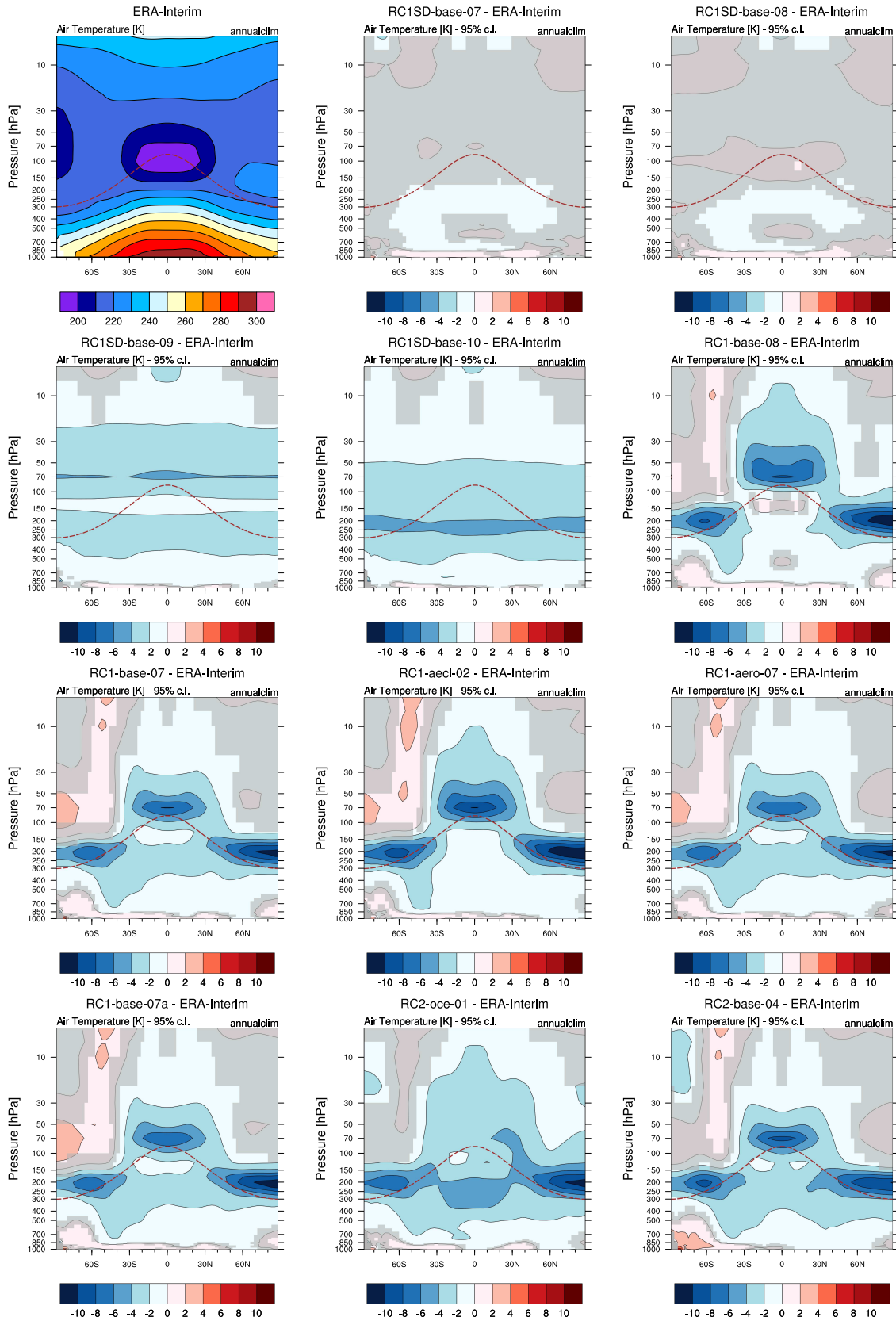
Figure 4.1: (a) Climatology of total dry air temperature of ERA-Interim in Kelvin. The data is monthly and zonally averaged for the period 2000 - 2010. (b)–(h) dry air temperature differences of selected ESCiMo simulations compared to ERA-Interim data. The unshaded areas in the difference plots are significant on a 95% confidence level according to a two-sided Welch's test. The dashed brown line indicates the height of the climatological tropopause.
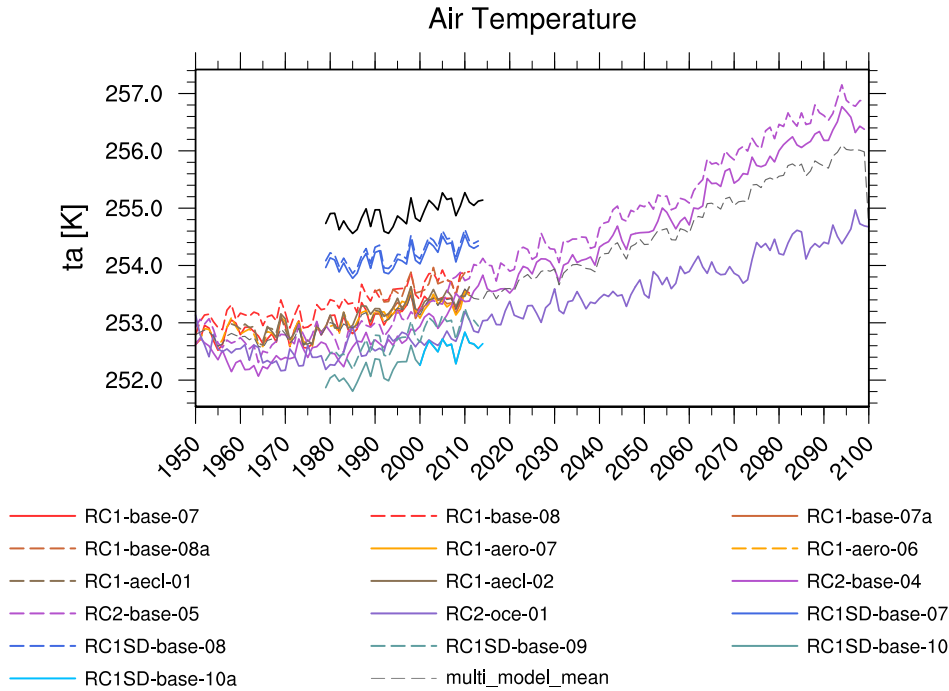
Figure 4.2: Area and pressure weighted global mean tropospheric temperature of the considered ESCiMo simulations.

is far below the tropopause in the tropics, certainly reducing the global mean tropospheric temperature.

Overall, in the time period from 1980 to 2010, which is covered by most simulations, increases the MSM by 0.55 K and has a trend of 0.018±0.001 K a^{-1}. This is comparable to estimates from the Intergovernmental Panel on Climate Change (IPCC) for the upper air global mean temperature of the lower troposphere (0.128–0.162 ±0.49 K a^{-1}) [IPCC, 2013]. Although, estimates of the IPCC are based on satellite measurements and results of the retrieval algorithms likely differ to the global mean tropospheric temperature calculation used in this study, the good agreement gives evidence that the simulation results are within reasonable boundaries.

4.1.2 Simulated Methane in ESCiMo

All presented ESCiMo simulations make use of the interactive chemistry of MECCA. Methane mixing ratios are thereby prescribed by Newtonian relaxation (i.e. *nudged*) at the lower boundary. The pure hindcast simulations (RC1(SD)-*) follow observations of surface mixing ratios from observation sites of the Advanced Global Atmospheric Gases Experiment (AGAGE; `http://agage.eas.gatech.edu`) and National Oceanic and Atmospheric Administration/Earth System Research Laboratory (NOAA/ESRL; `http://www.esrl.noaa.gov`), while the projection (RC2-*) simulations are following the CCMI RCP6.0 scenario based on Meinshausen et al. [2011] and Eyring et al. [2013], but do not differ much during the hindcast time period (see Fig. 4.3). Since the historical parts of both data sets are based on ground-based observations, the global averaged tropospheric mixing ratios of methane of the simulations agree expectably well with the observed surface mixing ratio (see Fig. 4.4 (left)). While tropospheric mixing ratios of the simulations are close by each other, due to the nudging at the lower boundary, they start to differ slightly in the stratosphere with respect to the simulation dependent methane sinks (see Fig. 4.4 (right)).

The various simulation set-ups additionally include the MESSy submodel CH4 in its basic config-
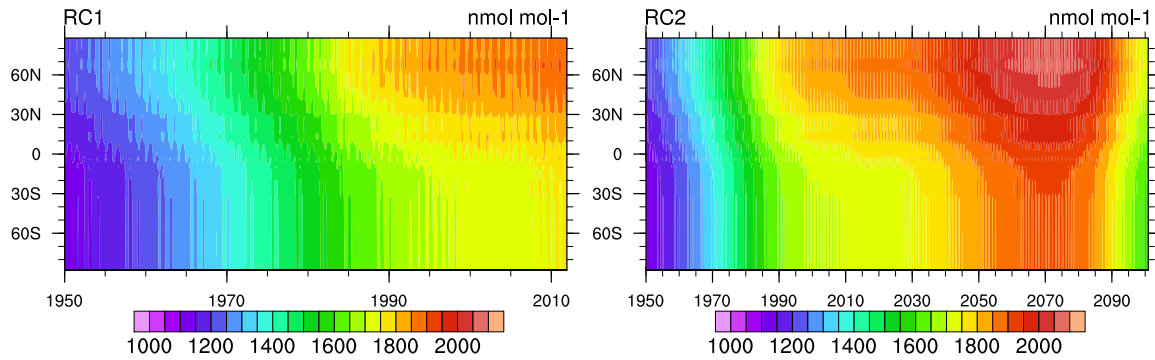
Figure 4.3: Lower boundary conditions of methane (in nmol mol^{-1}) used for the RC1(SD)-* (left) and RC2-* (right) simulations.
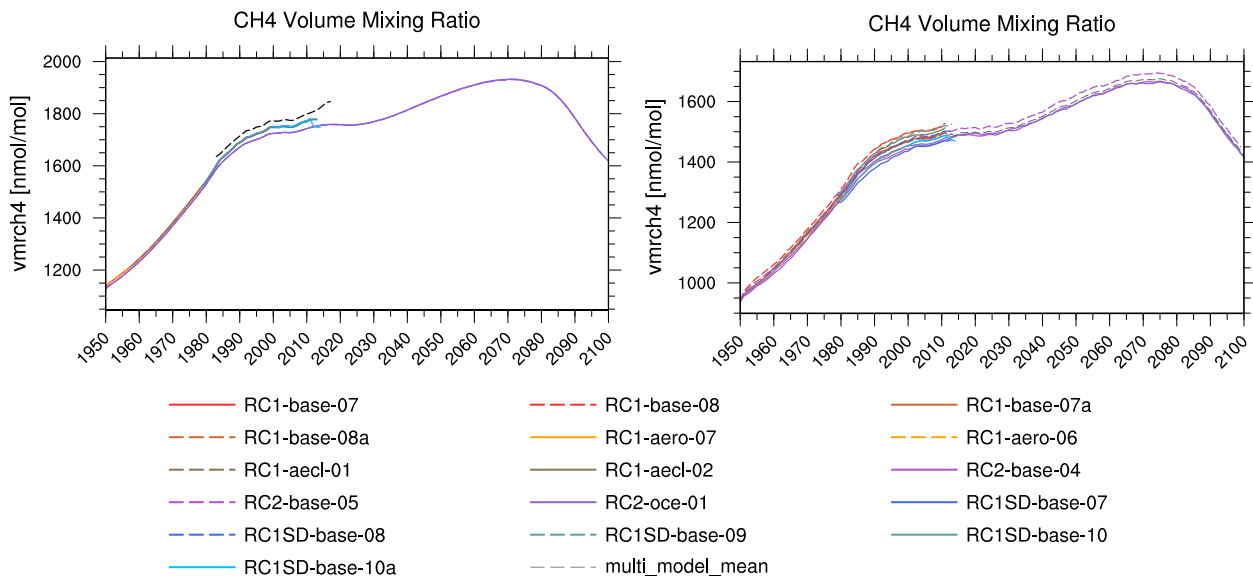

Figure 4.4: Global mean tropospheric (left) and stratospheric (right) CH$_4$ mixing ratio of the considered ESCiMo simulations. The dashed black line in the left plot shows the surface mixing ratio based on stationary observations. Data retrieved from `www.esrl.noaa.gov/gmd/ccgg/trends_ch4/` [Dlugokencky et al., 1994].

uration (for more details see Section 3.3). This means, that two different methane tracers exist in the simulation output, one tracer from the standard chemistry and one – purely diagnostic, thus no feedback on H$_2$O is applied – from the submodel CH4 (i.e. `CH4_fx`). Instead of prescribed lower boundary conditions, emission fluxes are used for the tracer `CH4_fx`. This tracer, however, is not used for the analysis in this chapter, but will be of interest in the following chapters of this thesis.

4.1.3   Profile of OH

The concentration of OH is, like temperature, analyzed with respect to its vertical profile. Zonal means in Fig. 4.5 are produced similar to the temperature profiles (Fig. 4.1), except that the panels show relative differences and the pressure axes are plotted only up to 100 hPa for a better representation of the troposphere. Since no observational based reference is available for OH, a MSM of all simulations in the specific time period is chosen as reference. This MSM agrees with earlier findings concerning the OH profile using EMAC [Jöckel et al., 2006], displaying two local OH maxima. One peak is in

the lowermost tropical troposphere and the other one between 200 and 150 hPa.

Again, the ESCiMo simulations can be put into the previously used categories concerning the dynamics specifications: nudging with mean temperature nudging, standard nudging, and free-running.

The first category of simulations, which are nudged and additionally mean temperature nudged, show a negative deviation in the tropical upper troposphere, which is stronger for RC1SD-base-07 (up to -30%) than for RC1SD-base-08 (up to -15%). In contrast, the standard nudged simulations in the second category show a positive deviation of up to 10%, which is for RC1SD-base-09 (lower vertical resolution) around 300 hPa and for RC1SD-base-10 (higher vertical resolution) at 150 hPa. Compared to the temperature profiles, it seems that OH concentrations are lower at higher temperatures in certain areas, probably linked to enhanced reaction rates favoring OH depletion.

Most of the free running simulations in the third category, namely RC1-base-07/07a, RC1-aero-07 and RC2-base-04, show nearly similar properties, with a high positive deviation from the MSM in the uppermost tropical troposphere and an overall negative deviation in the southern hemisphere, except in the polar region, which is only a feature of the relative differences. Absolute values of OH are very low during the polar night, hence also in the annual climatology at the poles. This can result in large relative differences, but represents actual small absolute variations (see Fig. F.3). The positive deviation in the uppermost tropical troposphere, however, is not evident in RC1-base-08 and exceptional is also the strong negative deviation of up to -35% in the upper tropical troposphere in RC1-aecl-02. Moreover, the ocean coupled simulation RC2-oce-01 reacts conversely to that, as it shows a positive deviation of up to 15% in the same region. It is unlikely that most of the OH differences are solely caused by varied temperature biases in the considered simulations, but rather are secondary effects. OH variations are foremost induced by ozone, which in turn is strongly related to NO_x produced from lightning activity (LNO_x), which is one of the most variant parameter among the nudged and free-running simulations and will be further discussed in detail later in this chapter.

Summarizing, the zonal mean temperature in the ESCiMo simulations varies mostly with respect to the applied or not-applied (mean) temperature nudging. Free running and standard nudged simulations tend to be overall colder than the mean temperature nudged ones. However, although some simulation exhibit an almost similar zonal mean temperature, the zonal mean OH still differs strongly. This indicates a rather weak connection between the temperature profile and the OH distribution. Nevertheless, zonal mean OH varies with respect to the specific simulation set-up. Particularly, it seems that the vertical profile of OH is sensitive to cloud and convective processes.

4.2 Simulating Extreme Methane Enhancements with EMAC

In the past, several studies were carried out concerning the climate impact of doubled atmospheric CO_2 (among others Sigmond et al. [2004], Rind et al. [1990] and Dietmüller et al. [2014]). Moreover, some studies investigated the effect of a doubled CH_4 climate, with respect to radiative forcing with a one-dimensional radiative-convective climate model [Owens et al., 1982, MacKay and Khalil, 1991] or with respect to a limited regional area (e.g. strongly increased emissions over China [Shang et al., 2015]).

However, current literature is lacking studies similar to the doubled CO_2 climate concerning the chemical impact of CH_4 in a state-of-the-art three-dimensional CCM. The purpose of the study by Tanalski [2017] was to investigate the effects in a climate with extremely enhanced methane.

The used data basis consists of three simulations with the EMAC model (see Table 4.3) in a CCM mode based on the ESCiMo base set-ups (resolution T42L90MA). The first simulation serves as a

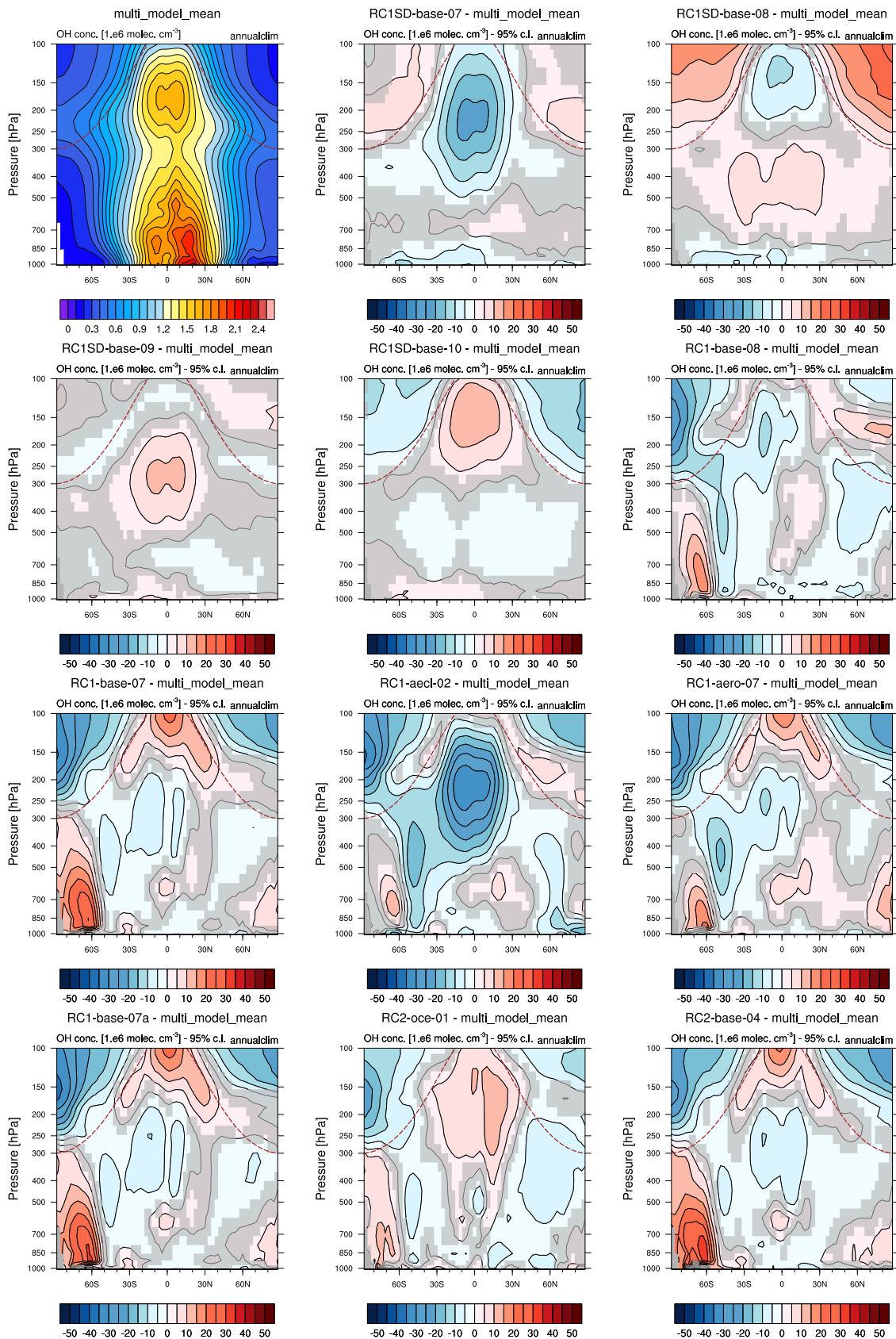**Figure 4.5:** (a) Climatology of concentration of OH of the MSM. The data is monthly and zonally averaged for the period 2000 - 2010. (b)–(h) OH concentration relative differences of selected ESCiMo simulations compared to the MSM. The unshaded areas in the difference plots are significant on a 95% confidence level according to a two-sided Welch's test. The dashed brown line indicates the height of the climatological tropopause.

Table 4.3: Extreme methane scenarios carried out with EMAC, with respect to a fixed lower boundary condition (LBC). The table includes the main results of Tanalski [2017]. The values in the columns of stratospheric (strat.) Temperature (T), SWV, tropospheric (trop.) O_3 and strat. O_3 denote the (relative) difference to the reference.

Simulation	scenario	avg. LBC [ppmv]	strat. T [K]	SWV [%]	trop. O_3 [%]	strat. O_3 [%]	RF [Wm^{-2}]	avg. τ_{CH_4} [a]
R1EME-01	reference	1.8						8.02
S1EME-02	2×CH_4	3.6	-5	+40	+20	+10	0.62	10.35
S2EME-02	5×CH_4	9.0	-10	+110	+40	+15	1.77	15.56

reference and is performed with lower boundary conditions similar to the RCP 6.0 scenario (i.e. R1EME-01). The other two simulations contain a lower boundary condition for CH_4, which is doubled (S1EME-02) and quintupled (S2EME-02), respectively with respect to the reference simulation. All three represent time-slice experiments over 20 years with 10 years spin up and fully interactive chemistry. Monthly SST and sea ice concentration (SIC) are repeatedly prescribed, representing a climatological mean of the years 2000–2009 based on global analyses of Rayner et al. [2003].

The main results of this study are that strongly intensified CH_4 emissions lead to lower stratospheric temperatures, due to the strong increase of the H_2O content in the stratosphere. O_3 increases, both in the troposphere and in the stratosphere. This is mostly caused by a reduced OH concentration as more OH is reduced due to the prevalent reaction with CH_4. Furthermore, the radiative forcing (RF) in the 2×CH_4 scenario, which equates to a growth of ~1800 ppbv, is estimated to be 0.62 W m^{-2} at the top of the atmosphere and is comparable to the value presented in IPCC [2013] of 0.48 W m^{-2} for the CH_4 increase from the preindustrial era (i.e. a growth of ~1100 ppbv). Additional results of this study concerning the CH_4 lifetime as a probe of the atmospheric oxidation capacity are shown in Section 4.3.2.

These results emphasize the strong influence of CH_4 on atmospheric chemistry. Despite the fact that by prescribing the SSTs and SIC no final conclusions about the climate effect can be drawn, it already gives a first hint on the outcome of a potential extreme CH_4 intrusion into the atmosphere. It should be noted here that more than enough CH_4 for such an event is currently stored in permafrost soil and CH_4 hydrates.

Additional, to this fundamental study, further studies with a mixed-layer ocean CCM are planned in future to investigate the climate effect in a doubled/quintupled CH_4 atmosphere incorporating a modeling concept for determining the effective climate forcing as suggested by Ponater et al. [1999].

4.3   Calculation of the Lifetime of Methane

The simulated lifetime of atmospheric CH_4 at time t with respect to OH, as a measure for the oxidizing power of the atmosphere is calculated according to Jöckel et al. [2006] as

$$\tau_{CH_4}(t) = \frac{\sum\limits_{b \in B} M_{CH_4}(b,t)}{\sum\limits_{b \in B} k_{CH_4+OH}(T(b,t)) \cdot c_{air}(T(b,t),p(b,t),q(b,t)) \cdot OH(b,t) \cdot M_{CH_4}(b,t)} \quad (4.1)$$

with $M_{CH_4}(b,t)$ being the mass of methane in kg, $k_{CH_4+OH}(T(b,t))$ the reaction rate of the reaction $CH_4 + OH \longrightarrow$ products in s^{-1}, $c_{air}(T(b,t),p(b,t),q(b,t))$ the concentration of air in molecules

(molec.) cm^{-3} and $OH(b,t)$ the mole fraction of OH in mol mol^{-1}$_{\text{dry air}}$ in the grid box $b \in B$ with B being the set of all considered grid boxes, e.g. all boxes which lie below the tropopause.

The reaction rate $k_{CH_4+OH}(T(b,t))$ is dependent on the temperature T (in Kelvin) at time t in the specific grid box b. The reaction rate applied in MECCA and CH4 is Eq. (B.1) [Atkinson, 2003], which is a three parameter function for a better resolving of the temperature dependency of the CH$_4$ + OH reaction. For a consistent calculation of τ_{CH_4} this rate is applied in Eq. (4.1) throughout this study if not indicated otherwise.

Concentration of air in one box is calculated as a function of pressure p, temperature T and specific humidity q, all dependent on time t and grid box b:

$$c_{air}(T,p,q) = \frac{N_A}{10^6} \cdot \frac{p(b,t)}{R_{gas} \cdot T(b,t) \cdot (1 + (\frac{M_{air}}{M_{H2O}} - 1) \cdot q(b,t))} \tag{4.2}$$

with $N_A = 6.02214129(27) \times 10^{23} \frac{1}{mol}$ being the Avogadro's constant, $R_{gas} = 8.3145 \frac{J}{K\,mol}$ being the universal gas constant and M_{air} and M_{H2O} being the molar masses of air (28.987 g mol^{-1}) and H$_2$O (18.01 g mol^{-1}), respectively.

The mass of CH$_4$ ($M_{CH_4}(b,t)$) serves as a weighting factor to account for variant global distributions of OH and CH$_4$. Boxes with low CH$_4$ abundances are therefore weighted less, taking into account that τ_{CH_4} is only well defined under presence of CH$_4$.

In this study the lifetime of methane is defined solely with respect to OH, although, basically all reaction partners (i.e. OH, O(^{1}D) and Cl) can serve individually or combined as the considered sink reaction and the term can also be extended to loss via soil and photolysis. A lifetime, which includes all sink reactions is often referred to as the total lifetime. This section, however, concentrates on the oxidation capacity of the atmosphere in terms of OH and, hence, investigates the lifetime only with respect to OH.

4.3.1 Tropospheric Lifetime and Inter-Simulation Variability

Figure 4.6 shows the tropospheric τ_{CH_4}(OH) for all simulations, calculated using Eq. (4.1). The set of boxes chosen includes all boxes below a climatological tropopause, while boxes intersected by the tropopause are added proportionally to their part below the tropopause in terms of pressure. The model output of 10 hourly instantaneous values is, furthermore, monthly averaged and interpolated onto pressure levels before applying the formula. Afterwards, for reasons of clarity, values are averaged annually.

As already stated by Jöckel et al. [2010], τ_{CH_4}(OH) of all included simulations is foremost not constant and increases between 1950 and 1975, and decreases afterwards more or less with the same trend. The projection simulations RC2-base-04 (orchid solid) and RC2-base-05 (orchid dashed) also predict a decrease in the future of -0.77 a between 2010 and 2100 with a mean slope of -0.008 a a^{-1}. The lifetime of RC2-oce-01 (purple), with the interactively coupled ocean model, stays nearly constant with only a small positive slope after 2013 until approximately 2075 and decreases as well after that (-0.51 a in 2010–2100 with a mean slope of -0.003 a a^{-1}). The ocean coupled simulation (RC2-oce-01) prognosticates a lower reduction, due to the lower temperature increase in this simulation (1.81 K instead of 3.04 K in RC2-base-04). The reason for that is that heat, generated by radiative forcing induced by the emissions of the RCP 6.0 scenario, is partly stored in the ocean. Due to the vivid variations in τ_{CH_4}(OH) of the various simulations over time, it is concluded that τ_{CH_4}(OH) is not constant over time, as is frequently assumed in inverse modeling approaches for constraining CH$_4$ emissions [Hein et al., 1997, Quay et al., 1999, Monteil et al., 2011, Bergamaschi et al., 2013].

The mean tropospheric lifetime of CH$_4$ of the MSM in the period 2000–2010 is 8.11 a, with the

included simulations varying by a relative standard deviation of 1.6 months. This value is at the lower end of lifetime ranges as calculated by comparable studies (see Table 4.1), but overall agrees in terms of uncertainty. It must be further noted that, while the given estimate in this study is explicitly calculated over the time period 2000–2010, the values given by the indicated studies in Table 4.1 represent different or unspecified time periods. Since the key message of Fig. 4.6 with the notable trend of τ_{CH_4} is that the lifetime is not constant, a comparison of different studies is quantitatively only possible if similar time periods are used.

The mean $[\mathrm{OH}]_{AW}$ of the same time period is $1.18 \pm 0.02 \times 10^6$ molec. cm^{-3}. This is comparable to the mean tropospheric OH concentrations of $0.88 - 1.26 \times 10^6$ molec. cm^{-3} in Lawrence et al. [2001], although they do not represent a particular time period.

Altogether, the simulation with nudging of the global mean temperature (RC1SD-base-08) predicts together with the interactive tropospheric aerosol simulation (RC1-aero-06) the shortest lifetime. The longest lifetime is calculated for the simulation with aerosol-cloud coupling (RC1-aecl-02) during the years 1970–1980. Afterwards, it still has one of the longest lifetimes, but alternates with the projection simulations RC2-base-04/05 in the following years.

Mean temperature nudging leads to a higher temperature in basically all vertical layers compared to the simulations without this nudging (see Fig. 4.2). This accelerates the oxidation of CH$_4$ by OH (given the temperature dependent reaction rate Eq. B.1) and also has a positive impact on the OH production (through enhanced tropospheric humidity). It is confirmed for the mean temperature nudged simulation RC1SD-base-08 (47 levels) in Fig. 4.7, which shows $[\mathrm{OH}]_{AW}$ for the considered ESCiMo simulations. RC1SD-base-08 has one of the highest values of $[\mathrm{OH}]_{AW}$, which together with the comparable high temperature yields the lowest lifetime.

In contrast, the lifetime in the other mean temperature nudged simulation RC1SD-base-07 (90 levels) is longer than e.g. RC1SD-base-09 (standard nudging), although average temperatures are higher. This results from a fairly lower OH concentration in RC1SD-base-07 (see Fig. 4.7), mainly in the tropical upper tropopause (see Fig. 4.5), and compensates the impact of the temperature onto the OH abundance.

The longest lifetime is simulated in the aerosol-cloud coupled simulation RC1-aecl-02, which shows the largest cold bias of all simulations in the profile, but global mean tropospheric temperatures are comparable to the other free-running simulations near the MSM. Remarkable is, however, the substantially low $[\mathrm{OH}]_{AW}$ of both aerosol-cloud coupled simulations RC1-aecl-01/02 which is also evident in mean temperature nudged RC1SD-base-07. These low values in the aerosol-cloud coupled simulations, in contrast to the behavior in RC1SD-base-07, are not compensated by higher temperatures, which consequently results in a rather long CH$_4$ lifetime.

Altogether, the differences in the projection simulations towards the end of the 21st century can be purely explained by different global mean temperatures of the projection simulations RC2-base-04/05 versus the ocean coupled RC2-oce-01, since $[\mathrm{OH}]_{AW}$ of theses simulations are basically identical.

The simulations differ by means of temperature and by OH concentration. However, the reasons for the variations in OH also vary from simulation to simulation and depend on various precursors. Equation (2.8) indicates the dependence of OH onto the phololysis rate of $O_3 \rightarrow O(^1D)$ $(j_{O_3 \rightarrow O(^1D)})$ and the abundances of H$_2$O and O$_3$, which will be investigated in the following. The idea is, that fluctuations in these parameters can be used to explain the variations in $[\mathrm{OH}]_{AW}$. Tropospheric O$_3$ is for example driven by stratosphere-to-troposphere exchange and by the NO$_x$-cycle, and is therefore, among others, dependent on LNO$_x$, while O$_3$ production via photolysis is relatively low in the troposphere. Furthermore, a strong dependence of OH production onto temperature via the reaction rates is not expected. The reaction rates (Eq. (2.9)-(2.11)) have only a low temperature dependency, which is further reduced by the ratio of k$_2$ and k$_3$ in Eq. (2.8). The tropospheric humidity,
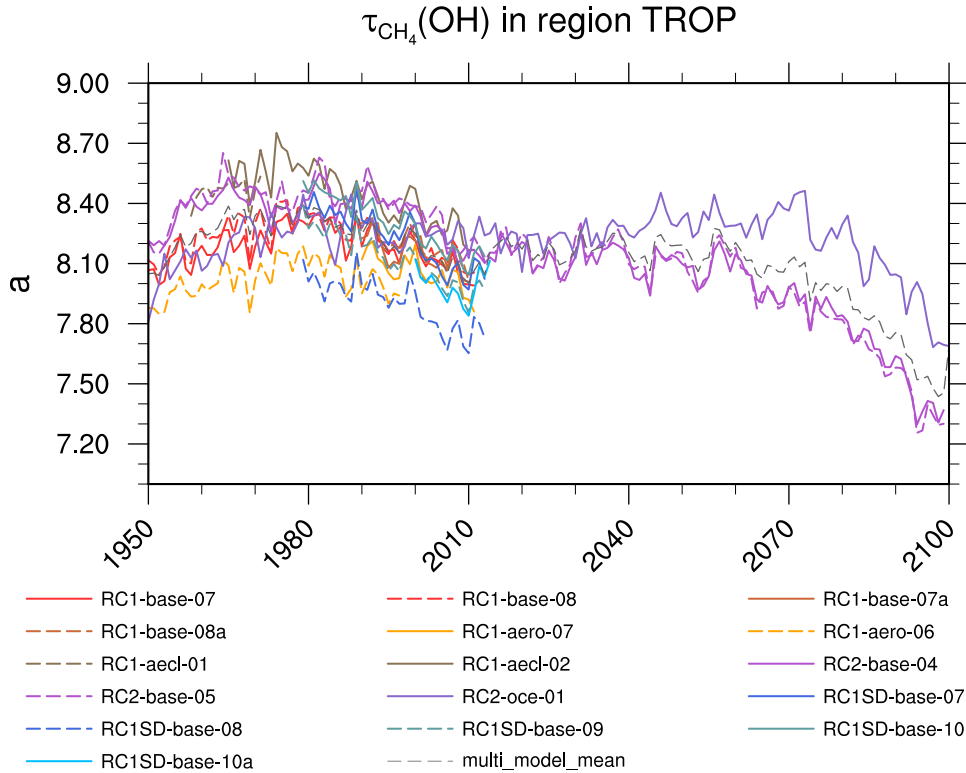
Figure 4.6: Tropospheric $\tau_{CH_4}(OH)$ of the various ESCiMo simulations calculated with formula (4.1) using a climatological tropopause level. Input values are monthly averaged before applying the formula. The lifetime is plotted in years and is yearly averaged for reasons of clarity.

however, as already stated above, is strongly related to temperature and introduces a certain climate impact onto the abundance of OH. Precisely, OH is via specific humidity related to temperature.

To begin with, aerosol-cloud coupled RC1-aecl-01/02 and mean temperature nudged RC1SD-base-07 exhibit a high specific humidity and high $j_{O_3 \to O(^1D)}$ compared to the other simulations. Nevertheless, the low bias of $[OH]_{AW}$ in RC1-aecl-01/02 and RC1SD-base-07 is caused by low tropospheric O_3 (see Fig. 4.8d) due to likewise small LNO_x (see Fig. 4.8c). RC2-oce-01, on the other hand, has high LNO_x and therefore high O_3, albeit a low specific humidity and $j_{O_3 \to O(^1D)}$, which results in a relatively high $[OH]_{AW}$.

The other temperature mean nudged RC1SD-base-08 has – as RC1SD-base-07 and RC1-aecl-01/02 discussed above – high specific humidity and $j_{O_3 \to O(^1D)}$, with O_3 being a bit higher than in RC1-aecl-01/02 and RC1SD-base-07, but lower than in the other simulations. Still RC1SD-base-08 is one of those simulations with highest $[OH]_{AW}$, suggesting that in this case the rather low O_3 (but not as low as RC1-aecl-01/02 and RC1SD-base-07) is compensated with the high specific humidity and $j_{O_3 \to O(^1D)}$.

Another interesting aspect of the $[OH]_{AW}$ variability is given by the standard nudged RC1SD-base-10a (90 levels), which follows its predecessor RC1SD-base-10 (identical set-up except for corrected road traffic emissions) in temperature, specific humidity, $j_{O_3 \to O(^1D)}$ and LNO_x. However, $[OH]_{AW}$ is a bit higher than in RC1SD-base-10 and (considering Fig. 4.8d) the time series of RC1SD-base-10a is on the level of the line of RC1SD-base-09 (standard nudged, 47 levels). The higher O_3 in this simulation is not caused by LNO_x, but by an exceptional higher NO_x mixing ratio due to the corrected emissions from road traffic (see Fig. 4.8e).
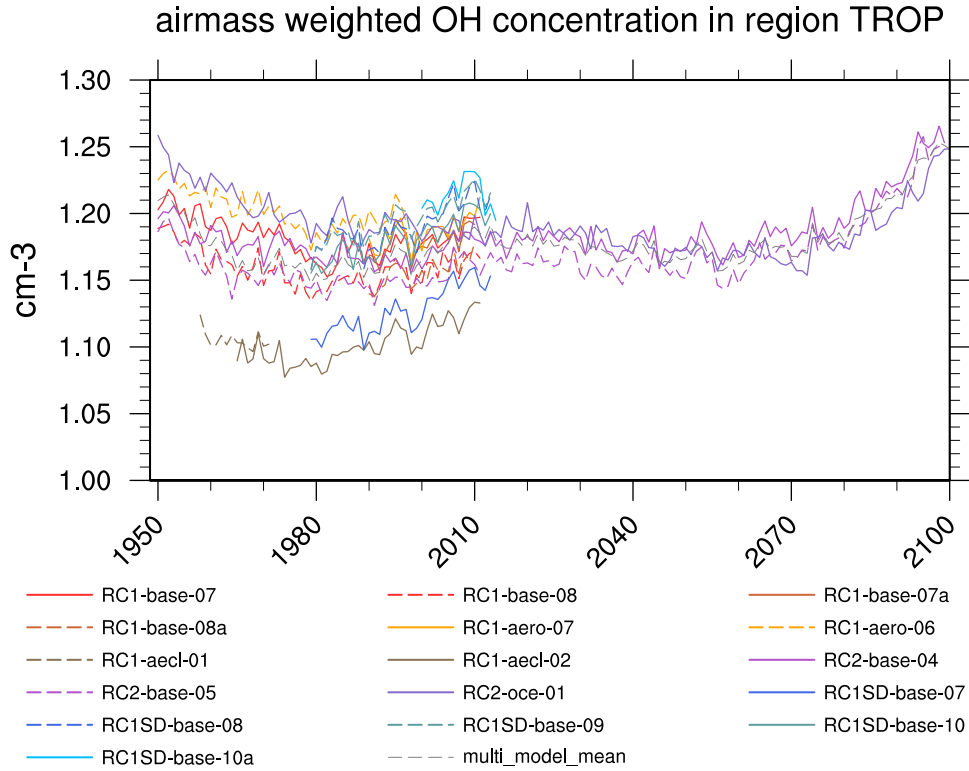
Figure 4.7: The annual tropospheric mean airmass weighted OH concentration in [10^6 molec. cm^{-3}] of the various ESCiMo simulations.

A unique behavior is detected in interactive tropospheric aerosol simulations RC1-aero-06/07. These simulations are comparable in all three precursors, nevertheless, have higher $[OH]_{AW}$ than e.g. the free-running simulations RC1-base-07/08. This indicates that there are further factors controlling $[OH]_{AW}$, probably via the heterogeneous chemistry and NO_y species influenced by the aerosol compounds (Holger Tost, pers. communication, 2018). A detailed investigation of these simulations with the rather novel aerosol submodel is, however, beyond the scope of this thesis.

4.3.2 Sensitivity of the Lifetime of Methane with respect to OH and Temperature

The lifetime τ_{CH_4} is by definition determined by the abundance of OH, by the applied reaction rate k_{OH} (being the same for all ESCiMo simulations) and by temperature, since the reaction rate for $CH_4 + OH$ depends on temperature.

For example, consider the application of a simplified version of Eq. (4.1), where the grid space is reduced to one global mean box and one value for each global mean temperature as well as OH concentration is used. This yields that varying the global mean temperature at 255 K by 1 K changes τ_{CH_4} by 0.35 a. Moreover, a variation of 0.1×10^6 molec. cm^{-3} of a global mean OH concentration at 1.0×10^6 molec. cm^{-3} changes τ_{CH_4} by 0.75 a.

In reality, of course, not only the differences in the mean parameters have impact on τ_{CH_4}, but the corresponding distributions in the whole troposphere, since τ_{CH_4} is calculated by evaluating every grid box separately. Therefore, trends can not be analyzed by this simple example alone. Instead, the following analysis is used to investigate the change in τ_{CH_4} with respect to the trends in the $[OH]_{AW}$ and temperature fields towards the end of the 21st century regarding the applied specific RCP scenario.

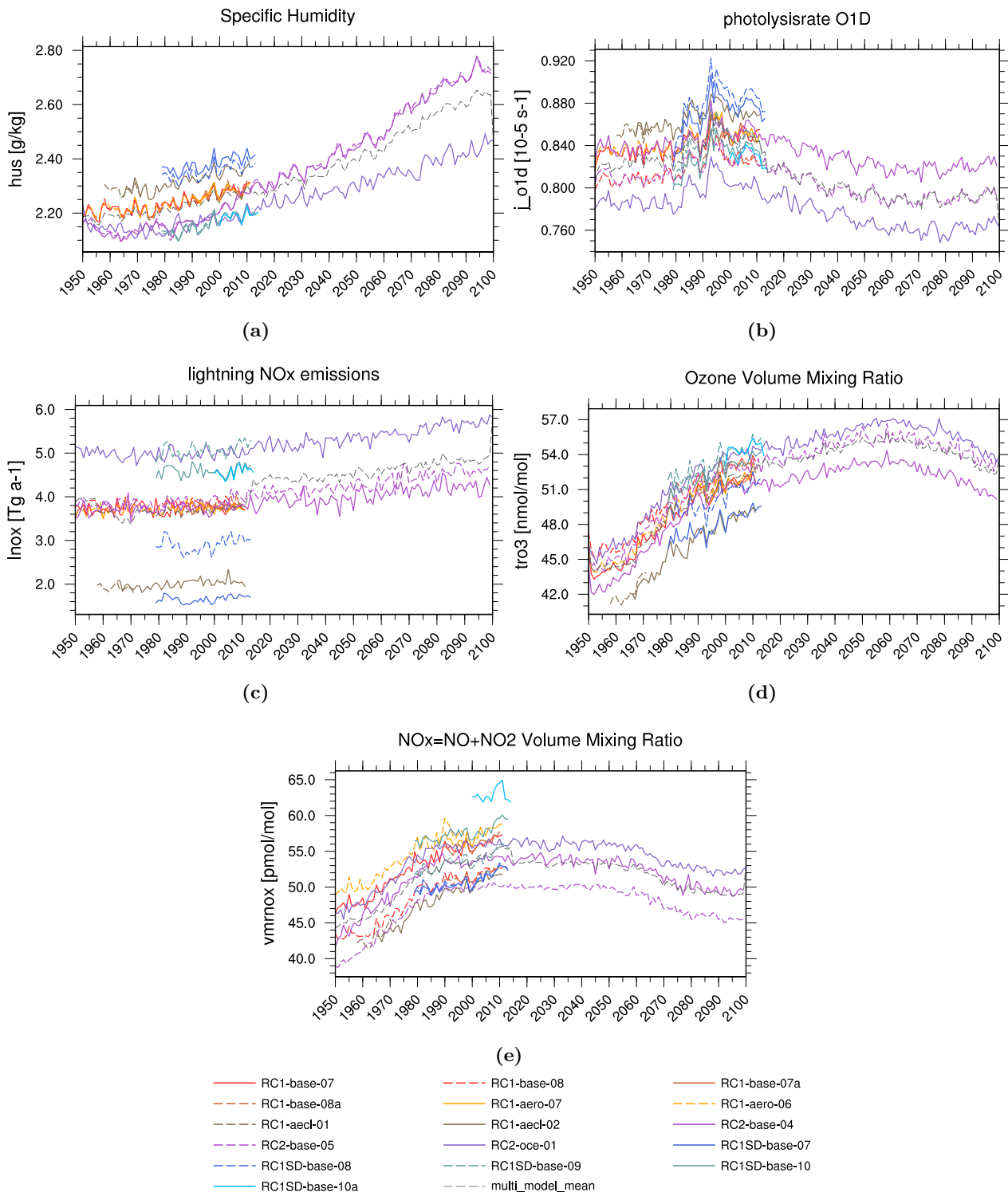**Figure 4.8:** (a) Global mean tropospheric specific humidity in [g kg^{-1}]. (b) Global mean tropospheric photolysisrate of O$_3$ →O(^{1}D) in [10^5 molec. s^{-1}] (c) Annual total emissions of LNO$_x$ in [Tg(N) a^{-1}]. (d) Global mean tropospheric O$_3$ mixing ratio in [nmol mol^{-1}]. (e) Global mean tropospheric NO$_x$ mixing ratio of all ESCiMo simulations.
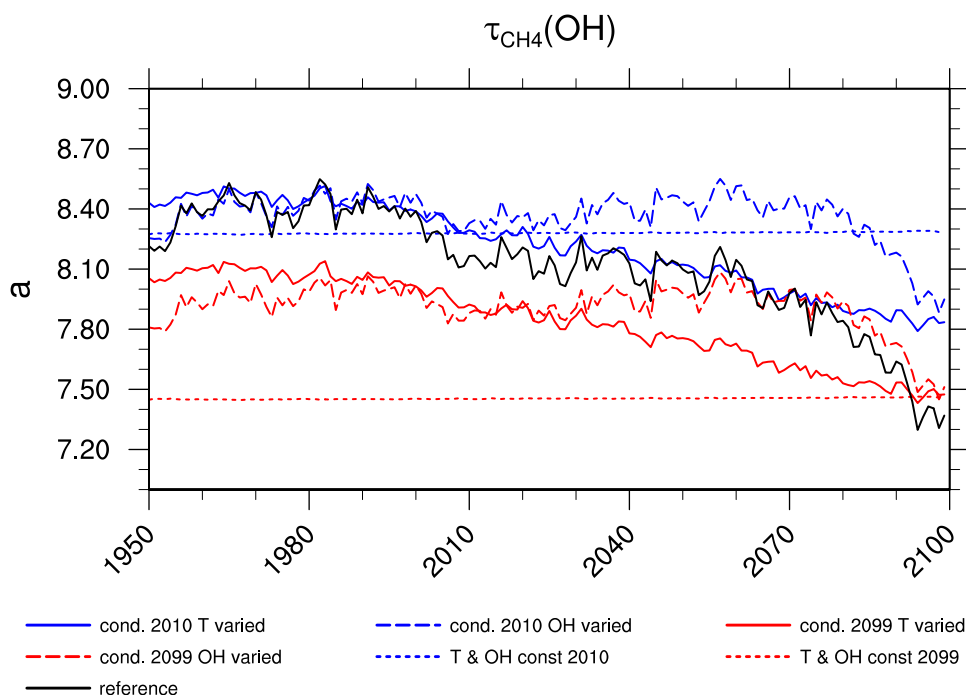
Figure 4.9: The plot shows $\tau_{CH_4}(OH)$ in [a] of the projection simulation RC2-base-04 (black). Solid colored lines indicate $\tau_{CH_4}(OH)$ with temperature varied according to the time series and OH, specific humidity and CH_4 are set to a constant annual mean value. Dashed colored lines, indicate $\tau_{CH_4}(OH)$ with OH varied according to the time series and temperature, specific humidity and CH_4 are set to a constant annual mean value. Dotted lines indicate the lifetime with both, OH and temperature, being constant at the respective annual means, while specific humidity and CH_4 are varied according to their time series. The blue and red lines indicate the reference for the applied constant annual mean to be the year 2010 and 2099, respectively.

Altogether, as stated before, the projection simulations RC2-* overall show a negative trend concerning τ_{CH_4} towards the end of the 21st century. Figure 4.9 gives evidence that this trend can partly be attributed to temperature and partly to OH changes. The figure shows the original lifetime of RC2-base-04 as a reference (black) and the lifetime calculated with fixed conditions of 2010 (blue) and 2099 (red) with respect to specific humidity and CH_4 as constant annual means. In addition, either OH is assumed to be a constant annual mean of that year and temperature is varied with respect to its time series (solid) or vice versa (dashed). The dotted lines are the lifetimes, where both, temperature and OH, are at the constant level of the respective years and the other two parameters, i.e. specific humidity and CH_4, are varied with respect to their time series. The very small trend (< 0.0001 a a^{-1}) of the dotted line indicates that the trend of $\tau_{CH_4}(OH)$ can mostly be explained by the trends of OH and temperature, confirming that the trend of CH_4 and specific humidity, which solely impacts the concentration of air, is, as expected, basically unimportant for this analysis.

In those cases where only temperature varies and $[OH]_{AW}$, humidity and CH_4 are kept constant, the lifetimes have an approximately linear negative trend corresponding to the temperature increase (-5.58×10^{-3} a a^{-1}), whilst in those cases with constant temperature, τ_{CH_4} increases a little bit after 2010 (2.13×10^{-3} a a^{-1}) and decreases later but stronger (18.9×10^{-3} a a^{-1}). A similar behavior is also detected in the lifetime of the ocean coupled RC2-oce-01 projection simulation (see Fig. 4.6). This simulation also shows a smaller trend in global mean temperature (see Fig. 4.2) since some of the

induced heat is stored in the ocean, but it also shows an OH trend comparable to RC2-base-04, which suggests that due to the lower temperature in RC2-oce-01 the trend of OH becomes more apparent in τ_{CH_4}.

One must be aware, that CH_4 itself changes the OH abundance through oxidization. Increasing CH_4 emissions and therefore higher abundances of CH_4 (see Fig. 4.4) hence potentially counteract the positive trend of OH through most of the 21st century. As stated before, Lelieveld et al. [2002] claim that potentially increasing emissions of sink species of OH possibly compensate its increase. Moreover, the study of extreme methane simulations, with double and fivefold LBCs compared to the reference LBC as in the ESCiMo simulations, further emphasizes the link of CH_4 and its sink OH [Tanalski, 2017] (recall Section 4.2). In these simulations a nearly linear relationship of the increasing CH_4 mixing ratios and the lifetime is detected (see Fig. 4.10) nearly exclusively caused by OH decrease, since these simulations are performed with prescribed SST, which basically suppresses any climate relevant temperature changes in the troposphere. In a true climate sensitivity simulation the SST need to adapt to the GHG forcing, and thus increasing emissions of CH_4 (in its role as a GHG) would lead to higher temperatures in the troposphere, which in turn enhances the tropospheric humidity, potentially increasing the OH concentration and reducing τ_{CH_4}. This is, however, dampened with respect to the positive trend of CH_4, which partly reacts with the additional OH. Hence, in the real atmosphere, the sink OH is both, enhanced and reduced by CH_4 itself.

Figure 4.9 indicates with the solid blue line the decrease of τ_{CH_4} with respect to temperature and with the dashed blue line the decrease of τ_{CH_4} with respect to OH. This implies that the lifetime decrease from present day (2010) until the end of the 21st century can be explained by the temperature increase by approximately 57.5% and by 47.4% by the OH increase respectively. The two numbers do not add up to 100% because of the small impact of humidity and CH_4. Comparably, Fiore et al. [2006], for example, attributed 65% of the negative trend in τ_{CH_4}(OH) between 1990 and 2004 to OH increase and the rest to temperature increase. Yet, Nicely et al. [2017] attributed most of the lifetime differences between the considered models to variations in the chemical mechanism, $j_{O_3 \rightarrow O(^1D)}$ and O_3, and proposed that variations in τ_{CH_4}(OH) are only marginally temperature driven. The reason for this result, however, is that the considered models in the study of *Nicely et al.* use the same temperature fields of a meteorological analysis, hence do not vary much with respect to temperature.

Furthermore, lifetime responses to OH and temperature variations are derived by calculating a linear regression coefficient of the indicated time periods. This results in a lifetime response to OH variations of 5.5±0.15 a per 1×10^6 molec. cm^{-3} (see Table 4.5). The response to temperature is 0.16±0.01 a K^{-1}. These numbers differ from the simplified approach above, however, note that the latter is a simplification treating the troposphere as one box, while the calculation of τ_{CH_4} actually is preformed with respect to the model grid, so that regional variations in temperature and OH are also taken into account.

Voulgarakis et al. [2013] derived the so called climate penalty factor as 0.31±0.14 a K^{-1}, which is larger than the derived value in the work at hand. The lifetime response from temperature changes in the present analysis can not be separated from the temperature induced change in OH by e.g. increase of specific humidity or any other OH precursor. A total temperature impact onto τ_{CH_4}(OH) would require additional sensitivity time slice experiments with climate parameters set to the conditions of 2099 while keeping O_3 precursor emissions (primarily NO_x) at present day values, similar to experiments carried out by Voulgarakis et al. [2013]. This, however, is beyond the scope of the current analysis, and for that reason, impact of temperature and [OH]$_{AW}$ are considered separately for now.

To summarize, τ_{CH_4}(OH) is anti-correlated with temperature and [OH]$_{AW}$. Furthermore, the lifetime of CH_4 is likely to decrease in the RCP6.0 scenario towards the end of the 21st century,

Table 4.4: Differences and trends of $\tau_{CH_4}(OH)$, temperature and $[OH]_{AW}$ in the indicated time periods of the projection simulations RC2-base-04 and RC2-oce-01.

	$\Delta\tau_{CH_4}(OH)^a$ [a]			ΔT^b [K]		
	1950–1980	1980–2010	2010–2099	1950–1980	1980–2010	2010–2099
RC2-base-04	0.201	-0.284	-0.772	-0.093	0.978	3.046
RC2-oce-01	0.278	-0.034	-0.509	-0.245	0.469	1.806
	ΔOH^c [10^6 cm^{-3}]					
	1950–1980	1980–2010	2010–2070	2070–2099		
RC2-base-04	-0.030	0.012	0.004	0.070		
RC2-oce-01	-0.045	-0.008	-0.021	0.075		
	$\delta\tau_{CH_4}(OH)/\delta t^d$ [a a^{-1}]			$\delta T/\delta t^e$ [K a^{-1}]		
	1950–1980	1980–2010	2010–2099	1950–1980	1980–2010	2010–2099
RC2-base-04	0.004	-0.010	-0.008	0.002	0.031	0.037
RC2-oce-01	0.011	-0.002	-0.003	-0.011	0.013	0.020
	$\delta OH/\delta t^f$ [10^6 cm^{-3} a^{-1}]					
	1950–1980	1980–2010	2010–2070	2070–2099		
RC2-base-04	-0.001	<0.001	<0.001	0.003		
RC2-oce-01	-0.002	<0.001	<0.001	0.003		

[a]−[c]: Values are derived by first applying a 10 years running average and then calculating the difference between the start and end years of the indicated time periods.
[d]−[f]: Trends are derived by calculating a linear regression coefficient of the values in the indicated time periods.

almost evenly based on temperature and $[OH]_{AW}$ increases. The positive trend of $[OH]_{AW}$ is likely damped by enhanced CH_4 emissions, so that the impact of $[OH]_{AW}$ onto τ_{CH_4} is smaller than that of temperature in the first three quarters of the 21st century. With potentially decreasing CH_4 emissions, $[OH]_{AW}$ catches up, due to the enhanced tropospheric humidity, and leads to an intensified reduction of $\tau_{CH_4}(OH)$.

4.3.3   Lifetime and Airmass Weighted OH in Sub-Compartments

Comparing the tropospheric lifetime of CH_4 and $[OH]_{AW}$ between different studies is challenging, since there is a certain freedom in chosen domain and weighting as explained by Lawrence et al. [2001]. Instead of one total tropospheric value, Lawrence et al. [2001] therefore suggests, together with defining the tropospheric domain up to a climatological tropopause, to divide the troposphere into specific sub-compartments as depicted in Fig. 4.11 and precisely itemized in Table F.1. This enables to a certain degree to assess the role of the vertical and horizontal structure of $[OH]_{AW}$ in the troposphere. The analysis in this section follows this recommendation and is applying the sub-domains to $\tau_{CH_4}(OH)$ and $[OH]_{AW}$.

Overall, as indicated by the MSM in Table 4.6, the domains in the upper troposphere show the longest mean lifetime, while the shortest lifetime is calculated in the lower tropical troposphere. It is also obvious that higher latitudes have a longer τ_{CH_4} compared to the tropical regions at the same vertical layer. This is also reflected by the MSM $[OH]_{AW}$, which is longest in the middle and lower troposphere and decreases towards higher latitudes and higher altitudes. The same applies horizontally, as tropical domains have higher OH in the annual mean than at mid and high latitudes. This occurs, since the outer domains include the polar region, where during the polar night no photolysis driven OH production is happening.

Furthermore, the absolute magnitude of the inter-annual variations (not shown) correlates with the

Table 4.5: Differences and trends of $\tau_{CH_4}(OH)$, temperature and $[OH]_{AW}$ in the indicated time periods of the projection simulations RC2-base-04 and RC2-oce-01.

	$\delta\tau_{CH_4}(OH)_{\text{varied T only}}/\delta t^{(a)}$ [a a^{-1}]			$\delta\tau_{CH_4}(OH)_{\text{varied OH only}}/\delta t^{(a)}$ [a a^{-1}]			
	1950–1980	1980–2010	2010–2099	1950–1980	1980–2010	2010–2070	2070–2099
RC2-base-04	0.00013	-0.00545	-0.00558	0.00445	-0.00486	0.00213	-0.01892
RC2-oce-01	0.00118	-0.00220	-0.00311	0.00972	0.00022	0.00533	-0.01865

	$\delta\tau_{CH_4}(OH)_{\text{T and OH const.}}/\delta t^{(a)}$ [a a^{-1}]		
	1950–1980	1980–2010	2010–2099
RC2-base-04	-0.00003	0.00007	0.00012
RC2-oce-01	-0.00010	0.00001	0.00006

	$\delta\tau_{CH_4}(OH)_{\text{varied T only}}/dT^{(b)}$ [a K^{-1}] 1950–2099	$\delta\tau_{CH_4}(OH)_{\text{varied OH only}}/d[OH]_{AW}^{(b)}$ [a (10^6 cm^{-3})$^{-1}$] 1950–2099
RC2-base-04	-0.155	-5.464
RC2-oce-01	-0.160	-5.548

[a]: Trends are derived by calculating a linear regression coefficient of the time series in the indicated time periods.
[b]: Trends are derived by calculating a linear regression coefficient of lifetime versus temperature and $[OH]_{AW}$ respectively in the indicated time periods.
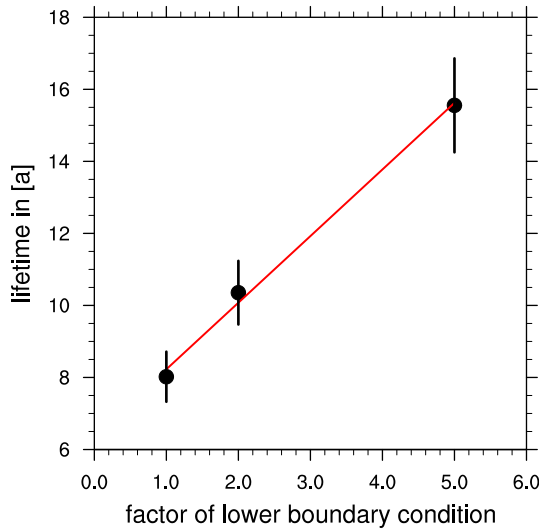

Figure 4.10: $\tau_{CH_4}(OH)$ in years versus the factor multiplied with the reference lower boundary condition. The black lines indicate the standard deviation of the dominant annual cycle and the red line follows the regression function $y = 6.378 + 1.849 \cdot x$ (with modifications taken from Tanalski [2017]).
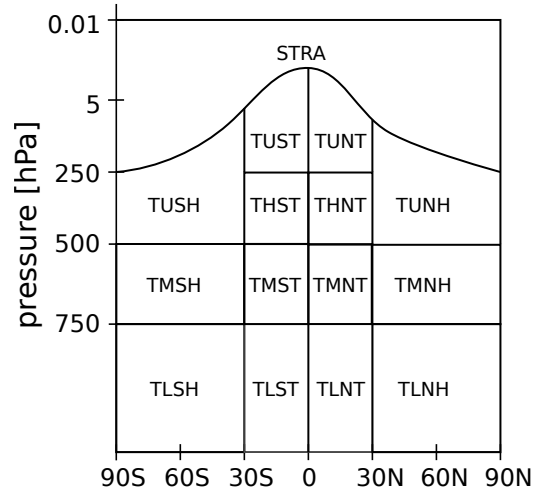

Figure 4.11: Schematics of the sub-compartments for calculating the zonal lifetimes and $[OH]_{AW}$.

Table 4.6: The table shows the MSM lifetime in [a] averaged over the time period 2000-2010 in sub-domains as indicated in Fig. 4.11. The standard deviation of the inter annual variation (upper) and inter simulation variation (lower) is given in [a] by the number in parentheses.

	SH	ST	NT	NH
STRA		$49.662^{(\pm 0.279)}_{(\pm 4.018)}$		
TROP		$8.112^{(\pm 0.069)}_{(\pm 0.129)}$		
	SH total $10.164^{(\pm 0.1)}_{(\pm 0.196)}$		NH total $8.260^{(\pm 0.077)}_{(\pm 0.157)}$	
TU	$57.285^{(\pm 0.743)}_{(\pm 3.604)}$	$39.943^{(\pm 0.663)}_{(\pm 2.491)}$	$37.437^{(\pm 0.546)}_{(\pm 2.071)}$	$50.577^{(\pm 0.668)}_{(\pm 2.239)}$
TH		$13.204^{(\pm 0.22)}_{(\pm 0.529)}$	$11.766^{(\pm 0.191)}_{(\pm 0.426)}$	
TM	$32.001^{(\pm 0.418)}_{(\pm 1.529)}$	$6.267^{(\pm 0.075)}_{(\pm 0.189)}$	$5.316^{(\pm 0.062)}_{(\pm 0.219)}$	$28.676^{(\pm 0.389)}_{(\pm 1.009)}$
TL	$26.060^{(\pm 0.359)}_{(\pm 0.881)}$	$4.420^{(\pm 0.034)}_{(\pm 0.191)}$	$3.582^{(\pm 0.032)}_{(\pm 0.151)}$	$18.883^{(\pm 0.256)}_{(\pm 0.626)}$

mean of the lifetime, hence, large variations correspond to large mean lifetimes. Except, however, for the stratosphere, where the inter-annual variation is the lowest of all domains. Although inter-annual variation is low in the stratosphere, the inter-simulation variation is exceptionally large, which can be explained by the quite steep increase of $[OH]_{AW}$ in the nudged simulations in the stratosphere (see Fig. 4.12). In contrast to the free-running simulations, the nudged ones show no cold bias above the tropopause. This enhances the transport from the troposphere, reduces the dehydration and leads to an increased stratospheric humidity, which in turn positively affects the OH concentration, despite unchanged O_3 levels. Additionally, the relative inter-annual variation of the lifetime is largest in the higher and upper tropical region, which suggests that these regions are most sensitive for meteorological variations. In contrast, the lowest relative standard deviation is found in the middle and lower tropical region.

In the stratosphere $[OH]_{AW}$ is substantially lower than at higher latitudes of the troposphere (compare STRA with SH* and NH* in Table 4.7), which explains that although most of the stratosphere is colder than the troposphere and pressure is low, the stratosphere has a mean lifetime, which is shorter than the maximum τ_{CH_4} at higher latitudes in the troposphere. Furthermore, the stratospheric lifetime is with 49.7 a substantially shorter than observation based estimates (e.g. 93 ± 18 a [Volk et al., 1997]).

The lifetime τ_{CH_4}, calculated in the specific domains, is shown in Figs. 4.13-4.15. Prominent is that the lifetimes of the aerosol-cloud coupled RC1-aecl-01/02 simulations are exceptionally long in the higher and upper troposphere at all latitudes. The corresponding values of this simulation are partially more than twice a standard deviation of the inter-annual variation larger than the next lower mean value of the other simulations (e.g. in TUSH: 65.847 ± 0.709 a (RC1-aecl-02) > 61.947 ± 0.777 a (RC1-aero-07, interactive trop. aersol)). This also applies throughout all layers of the southern hemisphere and becomes less evident in the northern hemisphere. Moreover, RC1-aecl-02 has with 1.28 the largest NH/SH OH ratio. Although, aerosols have usually a higher abundance in the NH and one would consequently expect also a larger impact in the very same region, the analysis of the specific domains and OH profiles suggests that instead of increased values of OH in the NH, OH is reduced in the SH. This can be explained by the different cloud scheme used for the interactive aerosol and
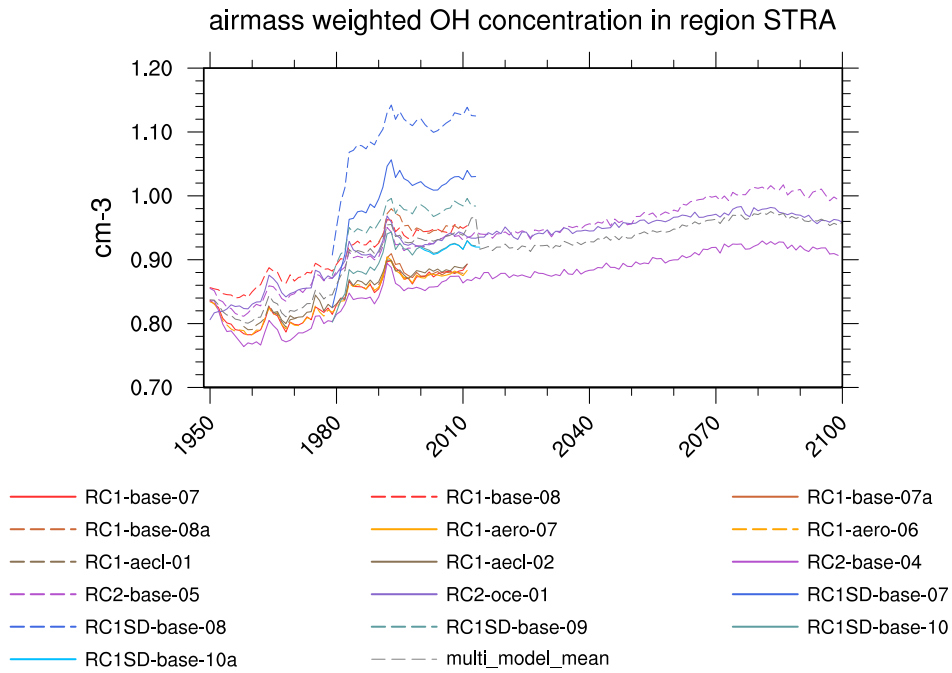
Figure 4.12: Stratospheric $[OH]_{AW}$ of the various ESCiMo simulations above a climatological tropopause level.

Table 4.7: The table shows the MSM airmass weighted OH concentration in $[10^6$ molec. cm$^{-3}]$ averaged over the time period 2000-2010 in sub-domains as indicated in Fig. 4.11. The standard deviation of the inter annual variation (upper) and inter simulation variation (lower) is given in $[10^6$ molec. cm$^{-3}]$ by the number in parentheses.

STRA			0.935	($\pm$0.005) ($\pm$0.063)			
TROP			1.178	($\pm$0.008) ($\pm$0.025)			
	SH total	1.057	($\pm$0.008) ($\pm$0.03)		NH total	1.287	($\pm$0.01) ($\pm$0.022)

	SH		ST		NT		NH	
TU	0.658	($\pm$0.006) ($\pm$0.021)	1.185	($\pm$0.016) ($\pm$0.098)	1.257	($\pm$0.011) ($\pm$0.095)	0.820	($\pm$0.008) ($\pm$0.019)
TH			1.186	($\pm$0.013) ($\pm$0.055)	1.327	($\pm$0.014) ($\pm$0.041)		
TM	0.651	($\pm$0.005) ($\pm$0.016)	1.388	($\pm$0.011) ($\pm$0.032)	1.617	($\pm$0.014) ($\pm$0.054)	0.846	($\pm$0.008) ($\pm$0.022)
TL	0.534	($\pm$0.004) ($\pm$0.013)	1.432	($\pm$0.008) ($\pm$0.051)	1.693	($\pm$0.013) ($\pm$0.056)	0.843	($\pm$0.007) ($\pm$0.022)

cloud coupling. The applied cloud scheme used in the two aerosol-cloud coupled simulations RC1-aecl-01/02 is more sensitive to low aerosol abundances as evident in the southern hemisphere. This results in relatively more clouds in this area, which additionally decreases OH (Holger Tost, pers. communication, 2018).

This strong effect of the interactive aerosol and aerosol-cloud coupling suggests that aerosol is an influential factor in the atmospheric chemistry with respect to OH as has been evident in the OH profiles in Section 4.1.3. However, the smaller cold bias in temperature, hence higher temperatures than in the other free-running simulations in the upper and higher tropical troposphere, potentially counteracts the lifetime increase (higher temperature lead to lower τ_{CH_4}). This suggests that the chemistry component itself, which is induced by the aerosols on the OH abundance, would result in an even longer lifetime.

The shortest lifetimes in the various domains are shown by the four specified dynamics simulations (RC1SD-*). This indicates that the low OH concentrations in the uppermost tropical troposphere in the mean temperature nudged simulations RC1SD-base-07/08 (cf. Fig. 4.5) are compensated by the overall higher temperature of these simulations and, likewise, the low temperature bias in the standard nudged RC1SD-base-09/10 is compensated by the relatively high OH concentrations in the same region.

As a last point, the lifetime in the southern hemisphere is longer than their counterpart in the northern hemisphere, giving evidence for an OH gradient with higher OH in the northern hemisphere. This has previously been observed in CCMs [Patra et al., 2011, Naik et al., 2013] and is also found in this study with a NH/SH ratio of $[OH]_{AW}$ of 1.22. Yet, estimates of the interhemispheric OH ratio based on measurements by ^{14}CO suggest that the ratio is more likely near or less than one [Brenninkmeijer et al., 1992]. This, however, is under debate, since Jöckel et al. [2002] claims that the ^{14}CO tracer is not safe to be used for the estimation of the OH asymmetry, as it is also dependent on the STE, which is also not hemispherically symmetric. Moreover, Krol et al. [2008] also argues that OH inferred from ^{14}CO is highly sensitive to transport and measurement location. Nevertheless, work by Patra et al. [2014] results in a comparable conclusion to Brenninkmeijer et al. [1992] using CH_3CCl_3 and reopens the debate, arguing that a NH/SH ratio greater than one in CCMs could, for example, indicate that emissions of OH removing substances in the northern hemisphere are currently underestimated.

The CH_4 mixing ratio of all simulations in ESCiMo reproduces by construction surface observations. CH_4 is, of course, not the only sink of OH and is only prescribed at the surface. A correct reproduction of the OH field is, however, a three dimensional problem and depends on several species of the atmospheric chemistry. It is beyond question, that this is a challenging part of the chemistry-climate modeling, and further studies of the presented kind are necessary to closer investigate the OH distribution in CCMs.

4.3.4 Influence of Post-processing, applied Tropopause Height and Reaction Rates

Next to the major influencing factors of τ_{CH_4}, namely the OH and temperature fields, some additional minor factors (bias of $< 1.5\%$) are impacting the variations of τ_{CH_4} and must be considered as well. These sensitivities are displayed in Fig. 4.16 exemplarily for the simulations RC2-base-04 (free-running, projection, 90 levels) and RC1SD-base-08 (mean temperature nudged, 47 levels).

The data used to calculate the lifetimes shown in Fig. 4.6 are post-processed, hence, interpolated from model levels onto pressure levels and reduced to monthly means. In contrast, Fig. F.2 displays the lifetime, calculated with the same formula and the same climatological tropopause height, yet
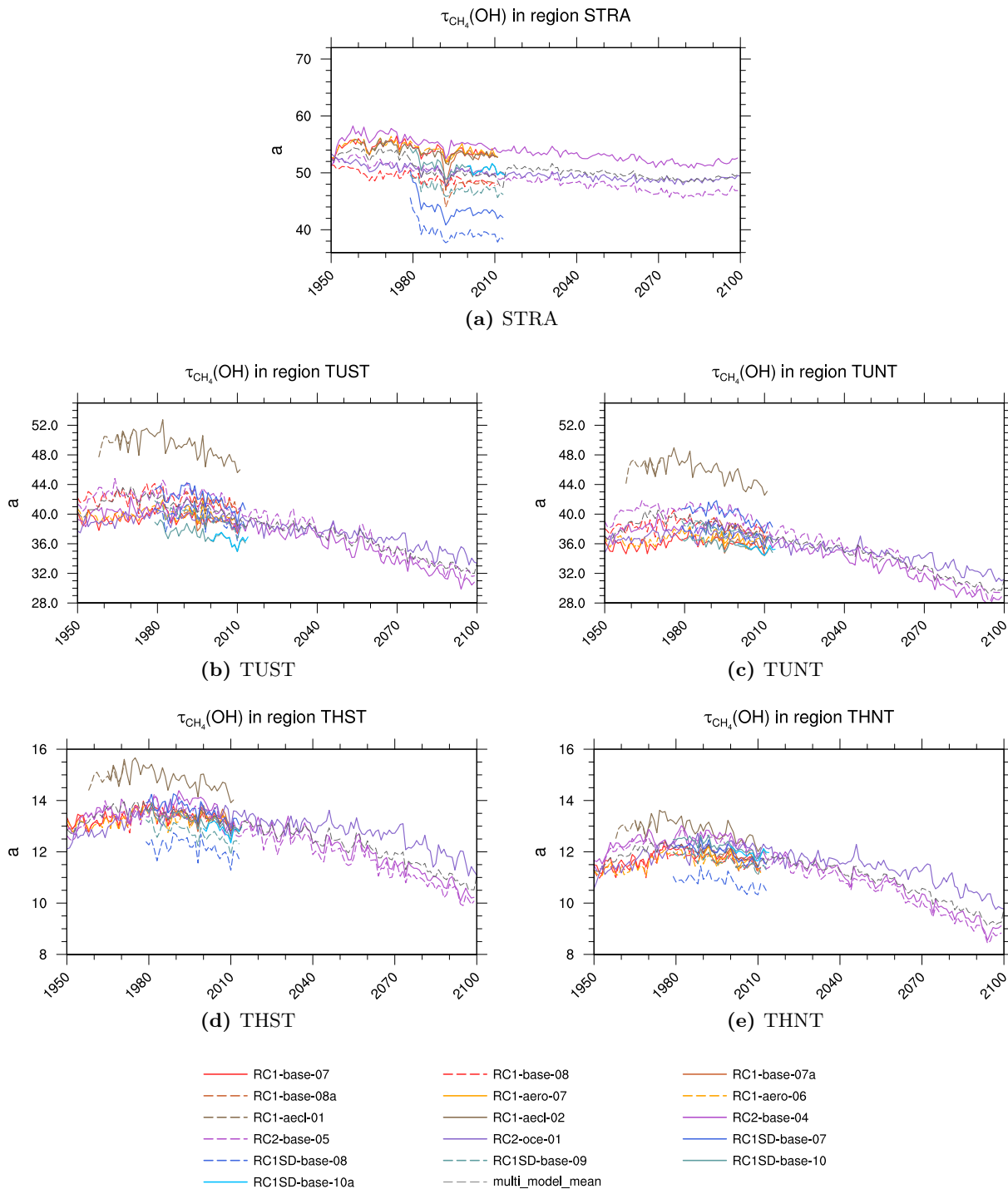
(a) STRA

(b) TUST

(c) TUNT

(d) THST

(e) THNT

Figure 4.13: $\tau_{CH_4}(\text{OH})$ of the various ESCiMo simulations calculated following formula (4.1) using a climatological tropopause level. Input values are monthly averaged before applying the formula. The lifetime is plotted in years and is yearly averaged for reasons of clarity. The panels show the lifetime in the indicated region in the stratosphere and higher tropical troposphere. A description of the region labels can be found in Table F.1.
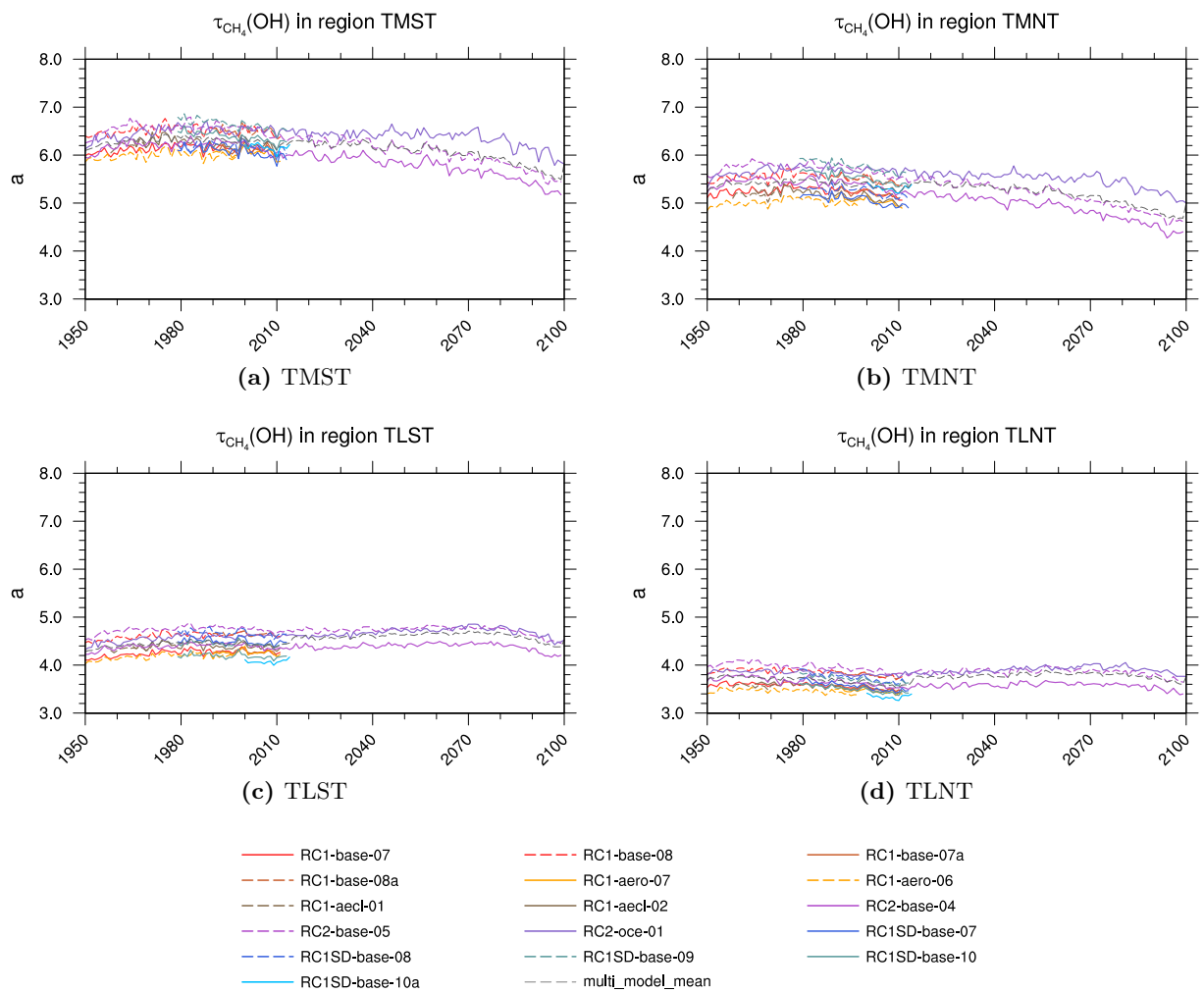
Figure 4.14: Same as Fig. 4.13 except that regions in the lower tropical troposphere are shown.
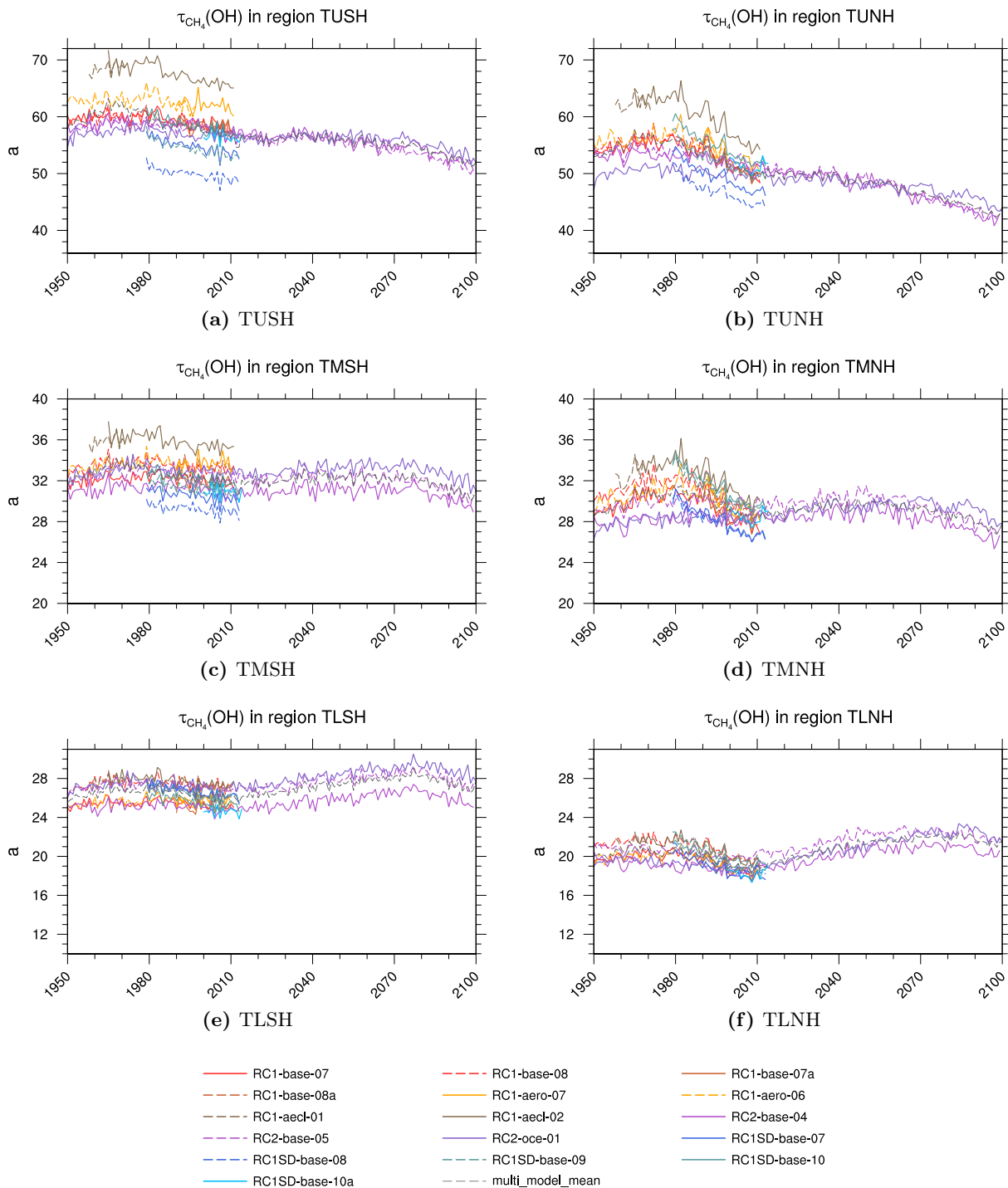
Figure 4.15: Same as Fig. 4.13 except that regions at higher latitudes are shown.
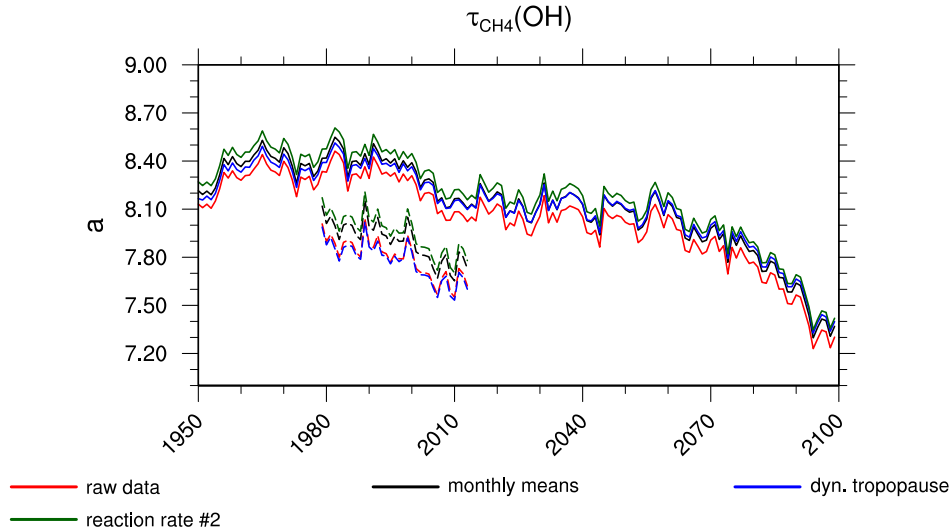
Figure 4.16: The plot shows $\tau_{CH_4}(OH)$ in [a] for the ESCiMo simulations RC2-base-04 (solid) and RC1SD-base-08 (dashed). The colors indicate the differences with respect to using raw (red) or monthly mean (black) data, applying the dynamical tropopause height (blue) and reaction rate Eq. (B.5) instead of Eq. (B.1) (green) .

using the raw data. The difference between the two methods is on average 0.08 ± 0.01 a and the annual variations are unaffected as can also be seen in Fig. 4.16, by comparing the red and black lines. Hence, it is indeed reasonable to use the post-processed data in the presented analysis.

For reasons of comparability, the calculation of the tropospheric lifetime of all simulations in this study use the same time-constant climatological tropopause (see Eq. B.8). In Fig. 4.16 the difference is depicted, if instead the on-line calculated dynamical tropopause is applied. This difference is most pronounced for the RC1SD-base-08 simulation, which is (1) with L47MA on a coarser vertical grid than the RC2-base-04 simulation and (2) is mean temperature nudged. In this study the constant climatological tropopause is used to maximize the consistency between the calculated lifetimes. However, by specifying the dynamics of the model (i.e., RC1SD simulations) and the consequent warmer troposphere, the dynamical tropopause height generally drops down. The climatological tropopause is unchanged, thus the evaluated region for the SD simulations includes boxes from above the dynamical and meteorological correct tropopause. These areas are strongly depleted in H_2O and hence in OH, which results in a likewise longer lifetime for the specified dynamics simulations, if the climatological tropopause is used rather than the dynamical one. Still, for reasons of consistency, this study follows the recommendation of Lawrence et al. [2001] and Jöckel et al. [2006] and uses the climatological tropopause throughought the analysis.

Furthermore, for the sensitivity analysis the applied reaction rate is varied using instead of Eq. (B.1) the three parameter reaction rate Eq. (B.5) from Bonard et al. [2002] recommended by Sander et al. [2011a]. Although the rates represent fairly similar expressions [Atkinson, 2003], a difference in the atmospheric lifetime is visible in Fig. 4.16. Nevertheless, this accounts for a bias between the lifetime calculated with Eq. (B.1) and Eq. (B.5) of only about 0.68% and 0.65% (< 0.7 months) for RC2-base-04 and RC1SD-base-08, respectively. However, it should be noted that the used reaction rate in Eq. (4.1) unquestionable should be the same as the reaction rate used in the chemical mechanism of the applied CCM.

4.4 Summary

This chapter comprises the results of the analysis of 16 simulations of the ESCiMo project with respect to the oxidation capacity of the atmosphere in terms of CH_4 lifetime. The most important influencing factors are identified, which potentially control the sink of CH_4 and therefore the CH_4 lifetime in the selected simulations.

It is found that the mean tropospheric CH_4 lifetime in the ESCiMo simulations is 8.11 ± 0.13 a in 2000–2010, which is lower than estimates by other studies (e.g. [Dentener et al., 2003, Fiore et al., 2006, Voulgarakis et al., 2013, Gosh et al., 2015]) and confirms earlier findings with the EMAC model (8.3 a, Righi et al. [2015]). However, the CH_4 lifetime is not constant over time, which contradicts this usual assumption in the inverse modeling of emission sources [Hein et al., 1997, Quay et al., 1999, Monteil et al., 2011, Bergamaschi et al., 2013]. Furthermore, the lifetimes of the various analyzed simulations vary by up to 0.5 a, which is caused by the specific configuration of the simulation and the, accordingly arising differences in temperature and OH abundances. The precursors of the OH radical, namely O_3 and H_2O, are strongly dependent on the given simulation set-up, which therefore determines the oxidation capacity. It is also found that OH is highly influenced by the applied cloud parameterization in the course of aerosol-cloud coupling. From this follows that the OH variation among the selected simulations is large (up to 9%), regardless that they are conducted with the same model system. Other studies claim even larger variations between different models (up to 80%, Nicely et al. [2017]), which highlights once more the uncertainty in the global OH abundance.

For the used RCP 6.0 scenario the projection simulations RC2-base-04 and RC2-oce-01 prognose a reduction of the CH_4 lifetime of -0.77 a and -0.51 a until the end of the 21st century, respectively. It is found that about one half of this reduction in RC2-base-04 is caused by a temperature rise, due to prognosticated climate warming, and the other half by OH increase, which is indirectly related to climate warming. Especially the latter is in these projections, furthermore, strongly correlated to the emissions of CH_4. Specifically, it is found that in the course of climate warming the CH_4 lifetime decreases by -0.16 a K^{-1}. For increasing OH concentrations in the atmosphere the lifetime decreases by -5.5 a $(10^6$ cm$^{-3})^{-1}$. It becomes evident that increasing emissions of CH_4 lead to a reduction of the overall OH abundance, which enlarges the CH_4 lifetime (see Fig. 4.10) and in turn increases the GWP.

Lastly, the presented analysis investigates the variations in the oxidation capacity with respect to CH_4, which is prescribed at the lower boundary using a zonal mean estimate based on observations. How estimates of sources evolve, on the contrary, with respect to a virtually prescribed OH and how the CH_4 lifetime responds to changed emission fluxes, is studied in the next chapter.

Simulating Methane with Optimized Emission Inventories

Current methane emission inventories still include large uncertainties [IPCC, 2013]. As mentioned before, these inventories are derived either by Top-Down or Bottom-Up estimates, which differ strongly due to the fundamentally different concepts. Although Top-Down estimates represent the global CH_4 budget sufficiently well (with uncertainties of 31–43 Tg CH_4 a^{-1}), they usually lack the precise regional and categorical assignments of the Bottom-Up estimates, which in turn are admittedly imprecise with an uncertainty range of 278–310 Tg CH_4 a^{-1} for the total sum of global CH_4 emissions.

To reduce this imbalance, various concepts involving inverse modeling have been proposed so far [Houweling et al., 2017] with varying resolutions of regional patterns, including additional observations of CH_3CCl_3 [Hein et al., 1997], or isotopic signatures [Fletcher et al., 2004], and partly begin to incorporate satellite retrievals (e.g. [Bergamaschi et al., 2013, Jacob et al., 2016]).

However, previous studies estimating CH_4 emissions continuously give diverse conclusions on the different source type contributions. This is, for example, evident in the debate about the varying growth rate of CH_4 in the early 2000s (see Section 2.2).

The present study aims towards an evaluation of possible reasons for these multiple solutions in the ill posed inversion problem. For the example of a specific inversion method, impact factors on the estimated emission inventory are analyzed with respect to the applied model system and the sink reactions of CH_4. Furthermore, potential feedback onto the sink of CH_4 through updated emission inventories are investigated and how these compare to preceding assumptions of the sinks.

In summary, this chapter shows and analyzes simulation results concerning optimized emission inventories of CH_4. The presented simulations are carried out with the EMAC model. These, among others, make use of the CH4 submodel, particularly including the age and emission class extension.

The chapter is structured as follows. The first section explains the applied Top-Down method to compute an optimized emission inventory, while the second section shows results of the a priori simulation including the results of the inverse optimization and a comparison of the a priori and a posteriori emission inventory. The second section also includes a discussion about the dependencies of the applied model systems. The third section presents the results of three forward simulations using the new optimized emission inventory, which also includes a simulation with the fully interactive chemistry using MECCA. Especially the latter simulation has the potential to examine feedbacks of the updated emission inventory onto the interactive chemistry. The last section contains additionally an evaluation of the a posteriori simulations with atmospheric observations.

5.1 Inverse Optimization of Emission Inventories

Top-Down estimates of emission inventories use statistical data assimilation or inversion methods to derive the strengths of the emitting sources. As stated before, for estimating CH_4 sources, several inverse modeling methods have been applied so far [Houweling et al., 2017]. These include, for example, matrix inversion approaches [Brown, 1993, 1995], synthesis inversions [Hein et al., 1997],

as well as inverse modeling using adjoint models (e.g. [Houweling et al., 1999, Meirink et al., 2008, Bergamaschi et al., 2013]). The applied statistical method in the work at hand is the fixed-lag Kalman Filter (flKF) derived by Bruhwiler et al. [2005]. Previously, estimates of CH_4 emissions based on a Kalman Filter (KF) have been calculated by Fletcher et al. [2004], Brunner et al. [2012], Bruhwiler et al. [2014] and Tsuruta et al. [2017]. In general, algorithms based on the KF method (also called Kalman Smoother, Kalman [1960]) are popular tools in scientific as well as technological applications.

In brief, for the inverse optimization of the CH_4 emission inventory using the flKF two steps are necessary. The first one is to perform a forward simulation with a first guess of the emissions – the so called "a priori inventory". The second step is to include the results of the forward (also called a priori) simulation and a collection of observations to the inversion algorithm. One noticeable advantage of the chosen method is that it can be applied in an offline mode. Hence, forward simulation and inverse optimization are separated and therefore independent concerning computational demands.

The inverse optimization technique used for the emission inventories shown in this chapter was developed at the *Eidgenössische Materialprüfungs- und Forschungsanstalt* (EMPA) in Zürich and is presented in more detail in Subsection 5.1.2. The present study benefit from the developments at the EMPA concerning the flKF and contributed to the collaboration by specifically investigating impacts on the inversion result by the applied forward model and sink variations.

In particular, the colleagues at the EMPA used the Lagrangian model FLEXPART [Stohl et al., 2005] (inclusive extensions by Henne [2018]), while the study presented in this thesis covers the results with respect to the EMAC model and includes a comparison of these two applied models.

Furthermore, similar to the FLEXPART model, the CH4 submodel has been extended accordingly to simulate age and emission classes, which are necessary for the flKF (see Section 3.3.2). Additionally, the submodel SCOUT [Jöckel et al., 2010] is used to directly sample output interpolated at the location of the chosen observation station sites.

5.1.1 Simulating Age and Emission Classes

As aforementioned, the age and emission classes in the CH4 submodel are a special feature especially implemented for the inverse optimization of methane emissions using the flKF. The motivation of this extension is to be able to distinguish specific emission types and regions during the simulation and inversion. The tracers are further defined to represent different age classes. Hence, it is possible to some extent to determine the age of the CH_4 since the emission. These additional tracers are transported in EMAC similar to any other trace gas. The partitioning in terms of regional and temporal information is necessary for the inversion algorithm to be able to estimate the contribution of the individual emission classes at the ground based sampling sites.

The emission types defined in the current inversion are: anthropogenic, wetlands, biomass burning, rice cultivation, volcanoes, wildlife, ocean, and termites. Anthropogenic sources include CH_4 from biogenic sources, such as ruminants and landfills, as well as from fossil sources, such as coal mining and oil production. Moreover, in the carried out simulation the emission types are further divided into regions based on the TransCom protocol [Gurney et al., 2000] (an overview can be found in Table 5.1 and Fig. 5.1). Regional separation depends on the emission type. Anthropogenic sources are divided into 13 regions, biomass burning and wetlands into 11, rice cultivation into 7, and the minor emission sources (volcanoes, wildlife, ocean and termites) are applied as global emission classes without further regional separation. The combination of regions and emission types results in 48 emission classes altogether.

These 48 emission classes are simulated with 5 age classes each representing one month (i.e., 1, 2, 3, 4, and ≥ 5 months since emission). Figure 5.2 shows exemplarily the evolution of one emission class

Table 5.1: Overview of the applied emission classes. Column # indicates the number of regions the respective emission category is seperated into.

emission type	#	regions
anthropogenic	11	North America, South America, ocean (mostly ship transport), Europe, Africa, Middle East, Eurasia boreal, India & Central Asia, East Asia temperate, Tropical Asia, Australia & New Zealand
biomass burning, wetlands	13	North America boreal, North America temperate, South America tropical, South America temperate, Europe, North Africa, South Africa, Middle East, Eurasia boreal, India & Central Asia, East Asia temperate, Tropical Asia, Australia & New Zealand
rice cultivation	7	North America, South America, Europe, Africa, India & Central Asia, East Asia temperate, Oceania
wildlife, volcanoes, ocean, termites	1	global

(i.e., anthropogenic emissions in Africa) from age class to age class. The upper leftmost panel shows the emissions of the year 2000 in g m^{-2} a^{-1}. The other panels show the age classes in ascending order left to right and top to down. In the first age class the emission source and corresponding source region is still easily recognizable. However, after one month the methane starts to spread over the globe. In the third month the source is only evident by a small enhancement of the methane column mixing ratio over and near Africa. In the fourth age class the methane from anthropogenic African sources is almost evenly distributed mostly in the NH. Eventually, the fifth (i.e. the last age class) shows the accumulated background of all CH$_4$ from anthropogenic African sources.

Overall, the temporal evolution of the age classes in Fig. 5.2 confirms that the 5 age classes in this set-up sufficiently track the spread of CH$_4$ towards a fairly uniform distribution, which is a prerequisite for a successful application of the inverse optimization method.

5.1.2 The fixed-lag Kalman Filter

The method of choice in the current study for the inverse optimization is the flKF based on Bruhwiler et al. [2005] and further refined for the desired application by Poberaj [2015] and Arfeuille et al. [2016] at the EMPA. The Kalman Filter optimizes the emissions in a way that the differences between simulated and observed CH$_4$ at the observation sites are minimized, taking model results and measurement uncertainties into account. The following, mostly based on Bruhwiler et al. [2005], gives a short introduction to the applied methodology.

The basis of the Kalman methodology is to connect the observation vector $y \in \mathbb{R}^N$ of N observation sites with the emission flux state vector $x \in \mathbb{R}^M$ of M sources (or in the present case emission classes including regional separation) for a specific month k:

$$y = Hx + b + \rho \qquad (5.1)$$

with $H \in \mathbb{R}^{N \times M}$ being the sensitivity matrix relating the sources with the observation sites. The elements of the sensitivity matrix H are calculated as the ratio of CH$_4$ simulated at the station and the source strength of the specific emission. $b \in \mathbb{R}^N$ is the background CH$_4$ vector and $\rho \in \mathbb{R}^N$ is the so called model-data mismatch error, which describes the data or model uncertainty. This, for example, can be sub grid scale effects of the point sampling, which cannot be represented by the
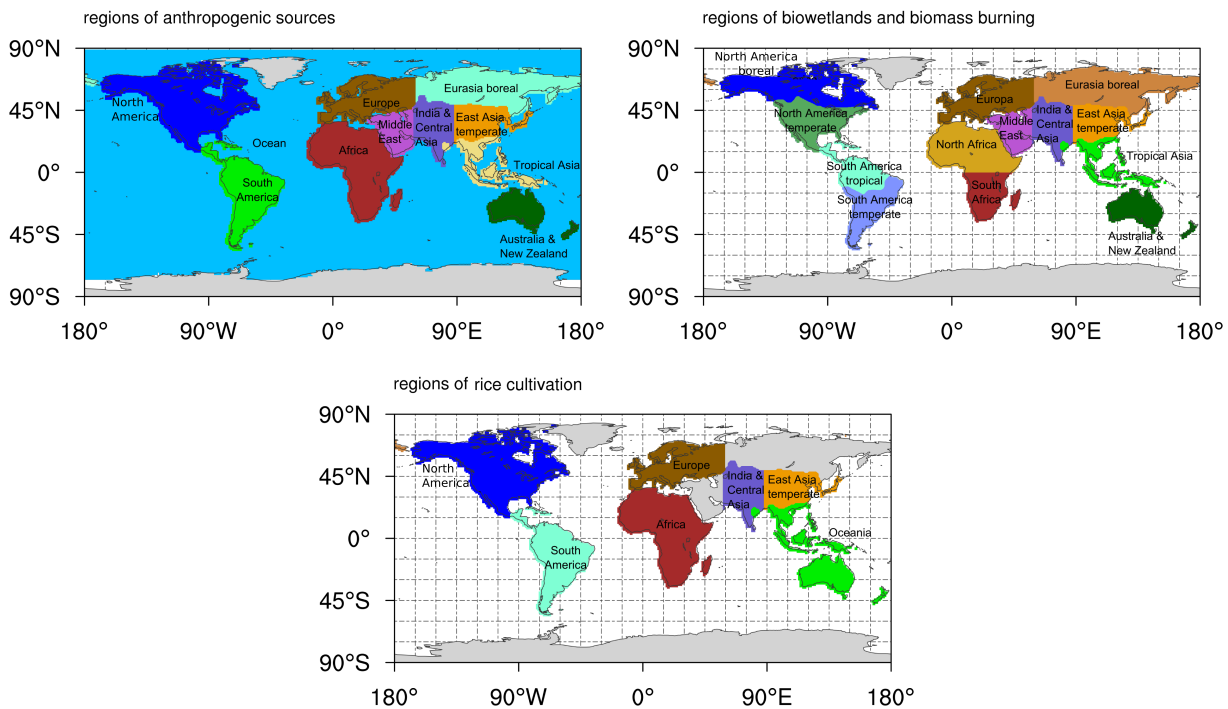
Figure 5.1: Regions used in the inverse optimization, sorted in 11 regions for anthropogenic emissions (upper, left), 13 regions for wetlands and biomass burning (upper, right) and 7 regions for rice cultivation (lower).
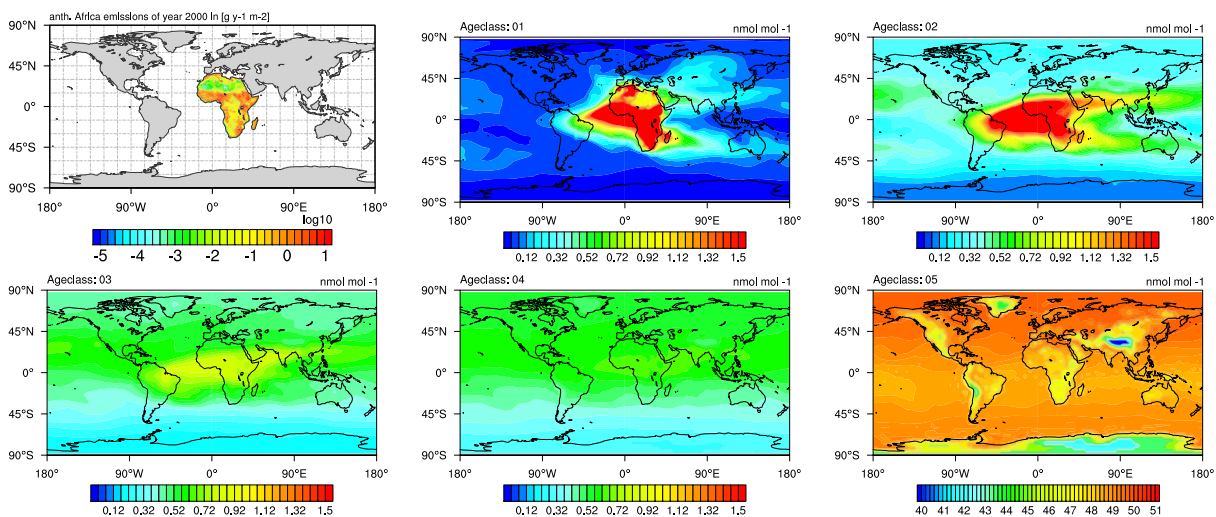

Figure 5.2: Upper leftmost panel: anthropogenic emissions in Africa. Rest: Methane as pressure weighted column up to 200 hPa of anthropogenic origin from Africa, distributed into 5 age classes, i.e. 1, 2, 3, 4, and ≥ 5 months after emission, shown exemplarily in the case of January 2000.

coarse model grid, or model related long range transport errors. It is assumed that this model-data mismatch error is normally (or Gaussian, $\mathcal{N}$) distributed with mean 0 and covariance matrix R, hence $\rho \sim \mathcal{N}(0, R)$.

For simplification of the derivation, a net observation vector y adjusted by the background b is defined:

$$\hat{y} := y - b = Hx + \rho \ . \tag{5.2}$$

Furthermore, it is assumed that an estimate x^e deviates from the true emission state vector x by ε, which is again normally distributed around 0 with covariance matrix Q. I.e.

$$x^e = x + \varepsilon \quad \text{with } \varepsilon \sim \mathcal{N}(0, Q) \ . \tag{5.3}$$

Known is the a priori state vector x^g, the observations y and the simulated CH_4 at the observation sites from the a priori simulation, which defines H. The covariance of the model-data mismatch error R is also assumed to be known for the given application. The probability of the net observation $\hat{y}$ given the source x is then, by applying the assumed normal distribution of ρ:

$$p(\hat{y}|x) = \frac{1}{\sqrt{2\pi|R|}} \exp^{-\frac{1}{2}(\hat{y}-Hx)^T R^{-1}(\hat{y}-Hx)} \ , \tag{5.4}$$

with the superscript T denoting the transpose of the given matrix.

Equally is the probability of x about the a priori (or first guess) value x^g defined to be,

$$p(x) = \frac{1}{\sqrt{2\pi|Q|}} \exp^{-\frac{1}{2}(x-x^g)^T Q^{-1}(x-x^g)} \ . \tag{5.5}$$

For the optimization of the emission sources, an estimate x^e for x should be found, which maximizes the probability of the emission sources given the observations, i.e. $p(x|\hat{y})$.

Using the Baye's Theorem the following relation applies:

$$p(x|y) = \frac{p(y|x)p(x)}{\int p(y|x)p(x)dx} . \tag{5.6}$$

Inserting the above introduced probability density functions (PDFs) (5.4) and (5.5), applying the logarithm, simplifying with respect to the adjustable variables and translating to a minimization problem, results in the following objective function:

$$\mathcal{J}(x) = (\hat{y} - Hx)^T R^{-1}(\hat{y} - Hx) + (x - x^g)^T Q^{-1}(x - x^g) \tag{5.7}$$

and eventually leads to the minimization problem

$$\min_{x \in \mathbb{R}^M} \mathcal{J}(x). \tag{5.8}$$

The estimate x^e is the state vector x, where $\frac{\partial \mathcal{J}(x)}{\partial x} = 0$ holds true, i.e.,

$$\frac{\partial \mathcal{J}}{\partial x}|_{x^e} = -(\hat{y} - Hx^e)^T R^{-1}H + (x^e - x^g)^T Q^{-1} = 0 \ . \tag{5.9}$$

The estimate for the covariance Q is found by the inverse of the second derivative of the cost function $\mathcal{J}$:

$$Q^g = (\frac{\partial^2 \mathcal{J}}{\partial x^2})^{-1} = (H^T R^{-1}H + Q^{-1})^{-1} \ . \tag{5.10}$$

Rearranging 5.9 and 5.10 results in the following discrete Kalman filter update equations:

$$
\begin{aligned}
x^e &= x^g + Q^g H^T (R + H Q^g H^T)^{-1} (\hat{y} - H x^g) &\quad (5.11) \\
Q^e &= Q^g - Q^g H^T (R + H Q^g H^T)^{-1} H Q^g . &\quad (5.12)
\end{aligned}
$$

Note that $H x^g$ is equal to the results of the forward simulation at the stations given the a priori emissions.

The Kalman gain matrix is further defined as

$$
K = Q^g H^T (R + H Q^g H^T)^{-1}. \tag{5.13}
$$

In order to avoid negative CH_4 emissions, the natural logarithm is applied to the state vector x [Brunner et al., 2012]:

$$
s = \ln(x) . \tag{5.14}
$$

This changes Eq. (5.1) to

$$
y = Ls + b + \rho , \tag{5.15}
$$

with L being the linear mapping operator of H.

The application of the linear mapping operator is straightforward, changing the Kalman Filter update equations to,

$$
\begin{aligned}
s^e &= s^g + Q^g L^T (R + L Q^g L^T)^{-1} (y - L s^g) &\quad (5.16) \\
Q^e &= Q^g - Q^g L^T (R + L Q^g L^T)^{-1} L Q^g . &\quad (5.17)
\end{aligned}
$$

The Kalman filter update Equations (5.16) and (5.17) represent the computation for one month. The time stepping of the Kalman Filter begins with the first month and an assumed background. In the second and subsequent months the emissions of the current month combine with the emissions of the previous months. For J months Eq. (5.1) becomes

$$
\begin{bmatrix} y_J \\ y_{J-1} \\ \vdots \\ y_1 \end{bmatrix} = \begin{bmatrix} L_{J,J} & L_{J,J-1} & \cdots & L_{J,1} \\ & L_{J-1,J-1} & \cdots & L_{J-1,1} \\ & & \ddots & \vdots \\ & & & J_{1,1} \end{bmatrix} \begin{bmatrix} s_J \\ s_{J-1} \\ \vdots \\ s_1 \end{bmatrix} + \begin{bmatrix} b_J \\ b_{J-1} \\ \vdots \\ b_1 \end{bmatrix} + \begin{bmatrix} \rho_J \\ \rho_{J-1} \\ \vdots \\ \rho_1 \end{bmatrix} . \tag{5.18}
$$

However, instead to include all months into the time stepping algorithm, it is sufficient to optimize with respect to a couple of directly preceding months, since the emitted CH_4 from one source and specific month eventually reaches an almost evenly distributed state after a couple of months. The inclusion of months beyond that does not contribute significant additional information to the inversion. Hence, during the time stepping, the estimates of those months are included to the background vector b_k and are not part of the optimization in subsequent steps.

As a result, Eq. (5.18) for time step k reduces to

$$
y_k = \sum_{i=k-p}^{k} L_{k,i} s_i + b_k + \rho_k , \tag{5.19}
$$

which is the basis for the deviation (similar to the one above) of the fixed-lag Kalman Filter (flKF).

In the current application time-dependent information of up to four months into the past is used to constrain the emissions, which gives the opportunity for locally emitted CH_4 to reach remote observation sites, while still being computationally efficient.
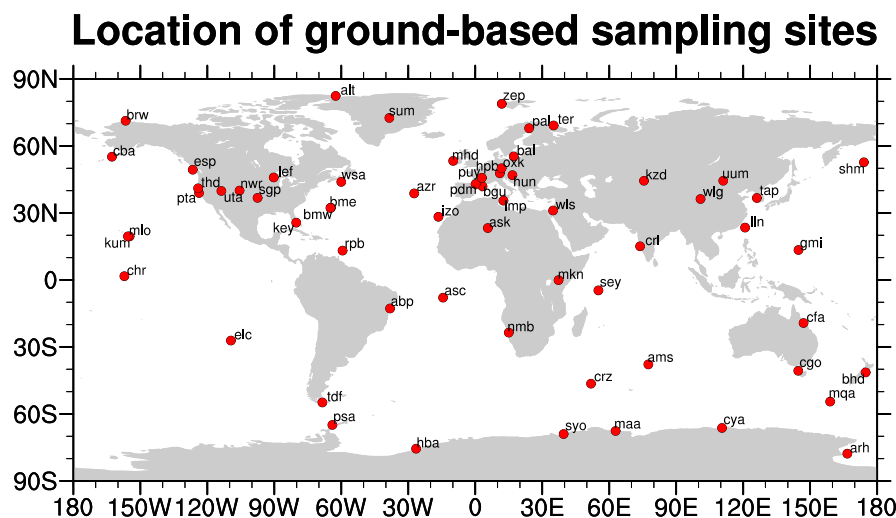
Figure 5.3: Locations of the ground-based sampling sites used for the presented analysis. The used data at the locations are provided by NOAA/ESRL, EC, LSCE, NIWA, CSIRO, ENEA, MGO and CMA. For further details see Table F.2–F.3

5.1.3   Observation Stations

The inversion method is applied using data from to 62 sites of the sampling networks of the Advanced Global Atmospheric Gases Experiment (AGAGE) (`http://agage.eas.gatech.edu`) [Prinn et al., 2016] and the Cooperative Air Sampling Network (`http://www.esrl.noaa.gov/gmd/`) [Dlugokencky et al., 1994, NOAA/ESRL]. The data is provided by the contributing institutions: NOAA/ESRL, EC, LSCE, NIWA, CSIRO, ENEA, MGO and CMA. The observations comprise flask samples and continuous measurements, with the latter performed with automatic systems using a gas chromatograph and a detector unit [Dlugokencky et al., 2017] or in-situ spectroscopy devices.

Results of the inversion with respect to data from 62 sampling sites (flask samples) are shown in Section 5.2.2. The a posteriori inventory, which is used for the presented a posteriori simulation and analysis (shown in Section 5.2.3) is, however, based on a slightly different inversion including some additional sites (Brunner, pers. comm., 2018).

5.2   Results of the a Priori Simulation

Three simulations were carried out with the a priori emissions. Two with EMAC, i.e. EMAC-apri-01 and EMAC-apri-02, and one with FLEXPART. All simulations were conducted with the same emission inventory, however, they differ in terms of the applied CH_4 reactant fields and model system. The inter-comparison of the three simulations enables to evaluate the inversion method with respect to the applied CH_4 sink. The detailed set-ups of the EMAC simulations are presented in the following subsections. The results of the inverse optimization are presented together with the later applied a posteriori emission inventory. This section also includes the discussion of potential model induced sensitivities on the optimization.

5.2.1   A Priori Simulation Set-up

For the a priori simulations EMAC-apri-01 and EMAC-apri-02, the EMAC model is applied without interactive chemistry. Instead, the chemistry of methane is calculated by the submodel CH4, applying

Table 5.2: Overview of carried out and presented simulations in this analysis. The FLEXPART simulations were conducted by colleagues at the EMPA in Zürich. $[OH]_{MMM}$: multi model mean OH field provided by EMPA; $[OH]_{RC1SD-base-10}$: monthly averaged OH field from RC1SD-base-10; $[OH]_{EMAC-apos-03}$: OH field interactively computed by MECCA in EMAC-apos-03. *CH4 ext.* refers to the isotopological extension of the CH4 submodel as described in Section 3.3.1.

Name	inventory	OH field	chemistry	isotopologues	time-period
FLEXPART	a priori	$[OH]_{MMM}$	–	–	1989–2014
EMAC-apri-01	a priori	$[OH]_{MMM}$	CH4	–	1989–2014
EMAC-apri-02	a priori	$[OH]_{RC1SD-base-10}$	CH4	CH4 ext.	1989–2014
EMAC-apos-01	a posteriori	$[OH]_{MMM}$	CH4	–	1990–2012
EMAC-apos-02	a posteriori	$[OH]_{RC1SD-base-10}$	CH4	CH4 ext.	1990–2012
EMAC-apos-03	a posteriori	$[OH]_{EMAC-apos-03}$	MECCA	MECCA-TAG	1990–2012

predefined monthly mean reactants. Both simulations are carried out at a T42L90MA resolution. The simulated time period spans from 1989 to 2014 and the simulations are conducted with specified dynamics (i.e. nudged meteorology).

As explained in Chapter 2, CH_4 is removed from the atmosphere by reaction with its three reactant species, photolysis and via soil-loss. The simulation carried out by the EMPA applying FLEXPART uses an annually repeated, monthly resolved OH field, which is a multi model mean (MMM) from 19 CCM simulations representing the annual cycle of the year 2000 and is indicated by $[OH]_{MMM}$ [Fiore et al., 2009]. This OH field is also used for the EMAC-apri-01 simulation (see Table 5.2), while EMAC-apri-02 uses a transient monthly averaged OH field $[OH]_{RC1SD-base-10}$ from the ESCiMo simulation RC1SD-base-10 (simulation with specified dynamics but not mean temperature nudged, for further information on RC1SD-base-10 see Section 4.1). Contrary to $[OH]_{MMM}$, $[OH]_{RC1SD-base-10}$ varies in time beyond the seasonal cycle, as can be observed from the corresponding $[OH]_{AW}$ time series shown in Fig. 4.7 in the previous chapter.

In EMAC-apri-01 the stratospheric sink above 60 hPa as well as the soil-loss at the surface is parameterized by a pseudo oxidation rate. In EMAC-apri-02, monthly averaged fields for $O(^1D)$ and Cl of RC1SD-base-10 are used, together with JVAL for the on-line calculation of the photolysis rate. Moreover, in EMAC-apos-02 the soil-loss is realized by the dry deposition submodel DDEP, which uses a pseudo oxidation rate in CH_4 molec. m^{-2} s^{-1} [Spahni et al., 2011, Curry, 2007]. The rate was initially constrained by a constant CH_4 concentration of 1800 ppbv and is therefore on-line scaled to the current CH_4 concentration at the corresponding surface grid-cell.

The applied a priori emission inventory was compiled by the colleagues at the EMPA. Wetland and rice emissions were derived from the LPJ model [Spahni et al., 2011]. The EDGARv4.2 2010 (Emissions Database for Global Atmospheric Research v4.2FT) fast track database [EC-JRC/PBL, 2011] provided the anthropogenic emissions, while the RETRO inventory [Schultz et al., 2008] and GFEDv3 (Global Fire Emissions Database) [van der Werf et al., 2010] were used for biomass burning emissions. Furthermore, as a first guess, climatologies for the emissions from termites [Sanderson, 1996], wild animals [Houweling et al., 1999], and ocean hydrates [Etiope et al., 2008] without annual variability were applied.
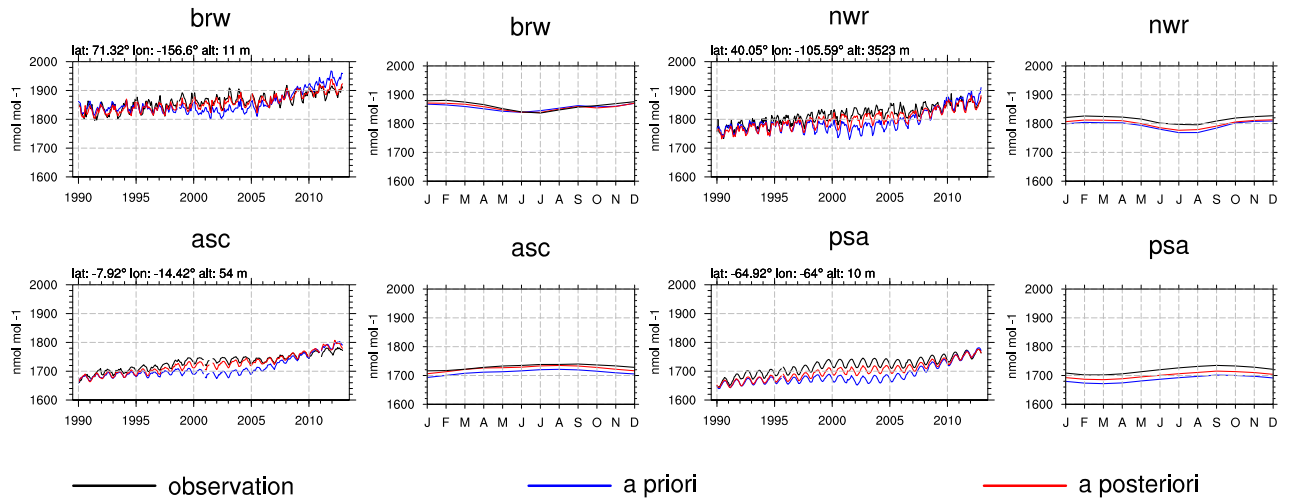
Figure 5.4: Results of the inverse optimization in terms of agreement at the observation stations (i.e. Burrows (brw), Niwot Ridge (nwr), Ascension Island (asc), Palmer Station (psa)). The black solid lines indicate the observations. The blue lines are the a priori estimates scaled to match the initial year. The red lines are the a posteriori estimates. The time series between 1989 and 2013 is shown on the left hand side and the annual cycle on the right.

5.2.2   Results of the Inverse Optimization

The inverse optimization using the flKF was performed at the EMPA. Evaluating the state vector representing the mixing ratios at the stations, which results from the flKF, gives a first indication of the quality of the inverse optimization. The state vector shows the expected agreement between observation and simulation, if the derived a posteriori inventory is applied. This evaluation further shows limitations of the inversion, i.e. where the optimization algorithm exhausts the given uncertainty ranges. Note that these time series do not represent actual simulations. They are rather a byproduct of the inversion algorithm.

The stations shown in Fig. 5.4 are chosen to represent gradually the meridional gradient, with the northern polar region (Burrows, brw), northern temperate (Niwot Ridge, nwr), tropical (Ascension Island, asc) and the southern polar region (Palmer Station, psa). Evaluations at additional stations are shown in the Appendix Figs. F.8-F.9. It becomes evident that the observed mixing ratios are underestimated mostly between 2000 and 2006. In the NH they are overestimated after 2007, while they agree quite well in the SH.

For a general overview, the Taylor diagrams [Taylor, 2001] in Fig. 5.5 comprise the results of all 62 sampling sites. The concept of these diagrams is to display the (normalized) standard deviation and correlation coefficient of the simulated time series compared to the observations in one plot as the radius and angle of a cubic coordinate system. The presented diagrams further show the root mean square error as dashed lines and include an indication of the positive or negative bias.

For the metric, monthly mean data of the time series of the years 1989–2013 and of the climatological annual cycles are used to evaluate the inverse optimization results towards the observations with respect to inter-annual variability and the annual cycle, respectively. Overall, the bias between observation and estimation with respect to the annual cycle (Fig. 5.5a) is already small in the a priori simulation. The a posteriori estimate improves the agreement just slightly. Nevertheless, the inter-annual variation (5.5b) is notably improved, with a reduced bias and correlation.
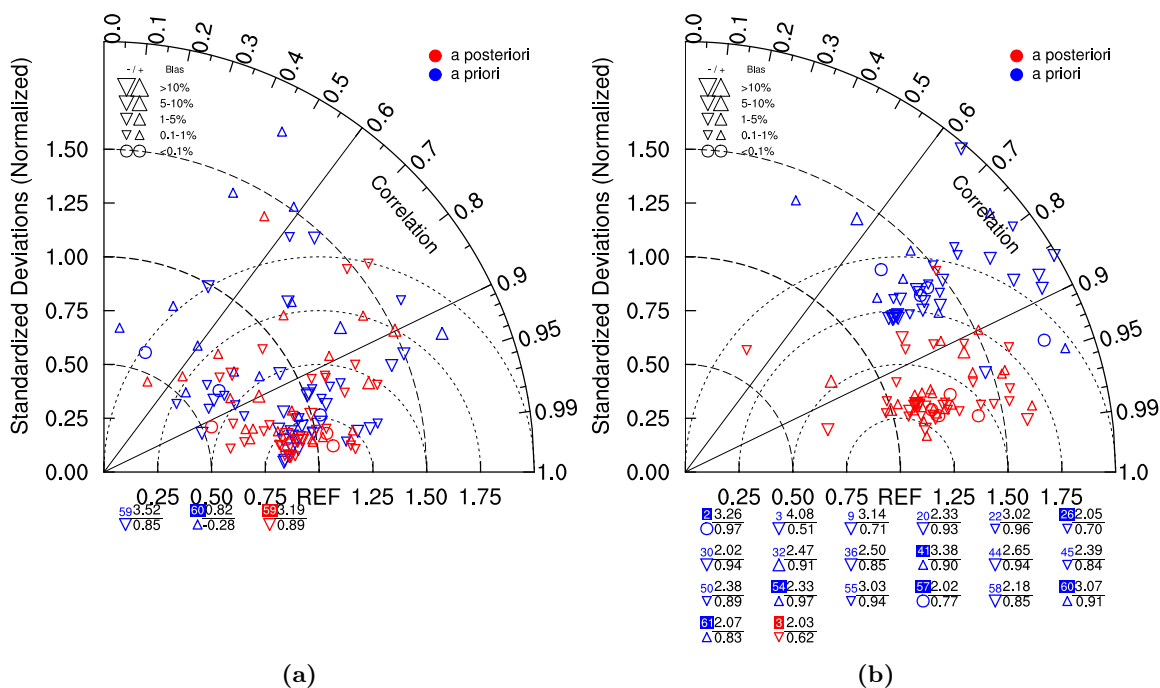
Figure 5.5: Taylor diagrams of the comparison of the state vector of the a priori simulation (blue) and the a posteriori result of the flKF (red) at various surface sampling sites. The Taylor diagram is shown with respect to the annual cycle (a) and with respect to the trend of the considered time period 1989–2013 (b). The size of the triangles indicate the bias in percent with upward oriented triangles indicating a positive and downward oriented triangles a negative bias, respectively. Circles indicate a bias of less than 0.1%. The symbols below the diagram are stations outside the displayed range of the Taylor diagram and are indicated by the colored number. The normalized standard deviation is displayed by the upper black number and the correlation coefficient by the lower black number on the right hand side of the symbol.

5.2.3   A Priori and A Posterior Emission Inventory

The flKF is conducted with the results of the EMAC-apri-01 simulation and yields factors to adjust the a priori emissions for every emission class and month from 1990 to 2012. The resulting a posteriori emission inventory is shown in Fig. 5.6b. The grey shaded area in the background (vertical axis on the left hand side) shows the total CH_4 emission in Tg CH_4 a^{-1}. The colored lines, with vertical axis on the right hand side, are the individual emission types. The type *minor* denotes the sum of volcanoes, termites, wildlife and ocean hydrates.

It is mentioned in Chapter 4 that the ESCiMo simulations used a fixed LBC for CH_4 mixing ratios instead of flux emissions. The TNUDGE submodel, which is responsible for the tracer nudging to the LBC, diagnoses a pseudo flux for the tracer representing a necessary fictive flux to attain the prescribed mixing ratio. Note that the nudging potentially introduces a positive or a negative pseudo flux depending on the current mixing ratio in the nudged grid cell of the simulation. This pseudo flux of simulation RC1SD-base-10 is shown in Fig. 5.6 as the black line (vertical axis on the left side). The total flux of the a posteriori emissions is overall comparable to this pseudo flux, which gives evidence that the nudging of the LBC as applied in the ESCiMo simulations introduces reasonable total amounts of CH_4 into the atmosphere.

Compared to the a priori inventory (Fig. 5.6a) the newly estimated emissions of the a posteriori

(a) A priori emission fluxes.

(b) A posteriori emission fluxes.

(c) Differences a posteriori minus a priori fluxes.

biomass burning   rice   anthropogenic

wetlands   minors   flux in RC1SD-base-10
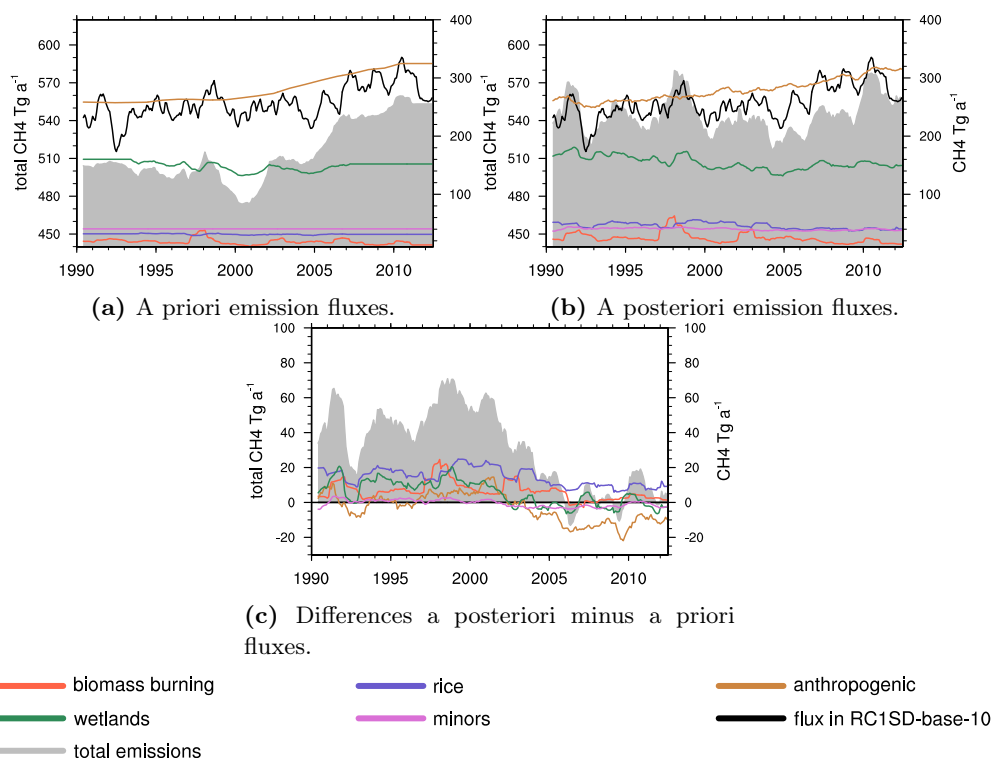
total emissions

Figure 5.6: A priori (a) and a posteriori (b) emission fluxes for the years 1990–2012 smoothed by a 12 months running average. (c) Difference of a posteriori and a priori emission fluxes. The colored lines indicate the individual emission types with *minor* being the sum of volcanoes, termites, wildlife and ocean. The corresponding axis of those is on the right side. The grey shaded areas show the total emissions as a running annual mean. The black line shows the corresponding fictive pseudo flux from the tracer nudging of the RC1SD-base-10 simulation.

inventory are larger, especially in the 1990s and early 2000s. The difference of the a posteriori and a priori inventories (shown in Fig. 5.6c) is mostly caused by enhanced rice, wetlands and biomass burning emissions in the a posteriori inventory. The a posteriori anthropogenic emissions (brown line) after 2007 are, however, considerably lower than the a priori. As mentioned in the introduction of this thesis, particularly the time periods 2000–2006 and 2007 onward are of interest, as they have shown growth rate variations of the global surface CH_4, which are still poorly understood. It is interesting that also the differences of a priori and a posteriori inventory vary strongly between these time periods. In 2000–2006, the mean a posteriori fluxes are about 28.04 Tg CH_4 a^{-1} larger than the a priori, while in 2007–2012 the difference shrinks to 5.53 Tg CH_4 a^{-1}.

Overall, the difference of the a posteriori and a priori (see Fig. 5.7) shows that anthropogenic emissions in Europe are overestimated and that rice emissions in India are underestimated by the a priori. Furthermore, wetlands in higher latitudes (mostly Europe, North America, South America temperate and Australia) are underestimated by the a priori, while wetlands in the tropics (South America boreal, Africa and South East Asia) are overestimated.

Comparing the global pattern of the differences of the fluxes averaged in the considered time periods (cf. Fig. 5.7a and 5.7d) indicates that the downward adjusted anthropogenic emissions compared to the a priori in the later time period are mostly located in China. Rice emissions in India and biomass burning all over the world are underestimated by the a priori inventory, however, the recent time period compares better (see Fig. 5.7c and 5.7f, rice not shown).

Table 5.3: A posteriori emission fluxes as mean values in [Tg CH$_4$ a^{-1}] of the indicated time periods.

	A posteriori						
	1990–1999		**2000–2006**		**2007–2012**		**2012**
Natural	**206.9**	**[133.8-280.0]**	**181.6**	**[116.9-246.3]**	**190.4**	**[128.7-252.2]**	**187.8**	**[120.8-254.8]**
wetlands	165.5	[92.4-238.5]	142.7	[78.4-207.0]	151.6	[89.9-213.3]	149.5	[82.1-217.0]
other	41.5	[37.1-45.8]	38.9	[34.6-43.2]	38.8	[35.4-42.3]	38.3	[35.0-41.5]
wildanimals	5.4	[5.2-5.6]	5.3	[5.1-5.4]	5.2	[5.1-5.3]	5.1	[5.0-5.2]
termites	26.1	[23.7-28.5]	24.3	[21.6-27.0]	23.6	[21.7-25.5]	22.9	[21.4-24.4]
volcanoes	2.6	[0-5.5]	2.7	[0-5.8]	3.2	[0.2-6.3]	3.7	[0.7-6.7]
ocean	7.4	[6.4-8.3]	6.7	[5.7-7.6]	6.8	[6.1-7.6]	6.6	[6.0-7.2]
Anthropogenic	**340.6**	**[285.0-396.2]**	**351.1**	**[293.0-409.1]**	**364.3**	**[314.6-414.1]**	**369.8**	**[320.5-419.1]**
other	261.9	[247.5-276.4]	281.1	[267.2-295.1]	306.9	[290.4-323.5]	315.1	[300.2-330.0]
rice	49.2	[10.1-88.3]	45.7	[7.6-83.8]	40.3	[10.6-70.0]	40.3	[6.9-73.8]
biomass burning	29.5	[3.1-55.8]	24.2	[1.5-47.0]	17.1	[3.4-30.8]	14.3	[4.7-23.8]
Sum sources	**547.4**	**[533.0-561.9]**	**533.2**	**[525.5-540.8]**	**554.1**	**[542.4-565.9]**	**557.1**	**[555.2-559.1]**

This provides an assessment of the used a priori emission inventory and previous assumptions of the emission distributions and strengths. Particularly, the results give evidence that total emissions have been underestimated using the a priori inventory in the time period 2000–2006 and that anthropogenic emissions from China in 2007–2012 have been overestimated.

For the following analysis, solely the new estimated emissions of the a posteriori inventory are of concern. Note, the a posteriori inventory can only resolve hot spots, which are already present in the a priori inventory, since the emissions in the a posteriori are scaled region wide.

The mean annual emission of the new a posteriori estimate of the years 2000–2006 is by 21.95 Tg CH$_4$ a^{-1} lower than those of the years 2007–2012 (see Fig. 5.8 and Table 5.3). This is comparable to previous estimates by Tsuruta et al. [2017] (18 Tg CH$_4$ a^{-1}) and Saunois et al. [2016a] ($\sim$ 16 Tg CH$_4$ a^{-1}), although lower than the combination of the EDGAR v4.2 database and results from Bousquet et al. [2011] shown in Dalsøren et al. [2016] ($>$ 50 Tg CH$_4$ a^{-1}). The latter, however, also conclude from their results that the CH$_4$ burden is likely overestimated in recent years, which is also in line with the findings given above.

The overall increase of CH$_4$ emissions is mostly caused by anthropogenic sources (+25.82 Tg CH$_4$ a^{-1}, Fig. 5.8e) and to a smaller extent by wetlands (+8.83 Tg CH$_4$ a^{-1}, Fig. 5.8f). The strong increase in anthropogenic emissions is, for example, attributable to prominent hot spots in the Eurasian region (at approx. 60° N 90° E), the Middle East and the western part of North America. Increase in wetland emissions are particularly evident in the same Eurasian region, as well as in the regions of tropical rain forests. Rice and biomass burning emissions, however, slightly decrease in the later time period (by −5.48 Tg CH$_4$ a^{-1} and −7.16 Tg CH$_4$ a^{-1}, respectively), which is mostly driven by reduced rice emissions in India and biomass burning on the South East Asian islands, in Africa and South America. The minor emissions stay almost constant (i.e. −0.06 Tg CH$_4$ a^{-1}, not shown). Although CH$_4$ emissions are reduced in recent years in Europe, India and South East Asia, these regions are still top emitters of CH$_4$.

5.2.4 Dependencies on the Applied Forward Model

The a priori simulations of EMAC and FLEXPART are carried out with the identical emission inventory and sink fields. Nevertheless, FLEXPART shows a larger CH$_4$ mixing ratio throughout the atmosphere (see Fig. 5.9a). Although sink reactants are identical in both models, the sink itself is
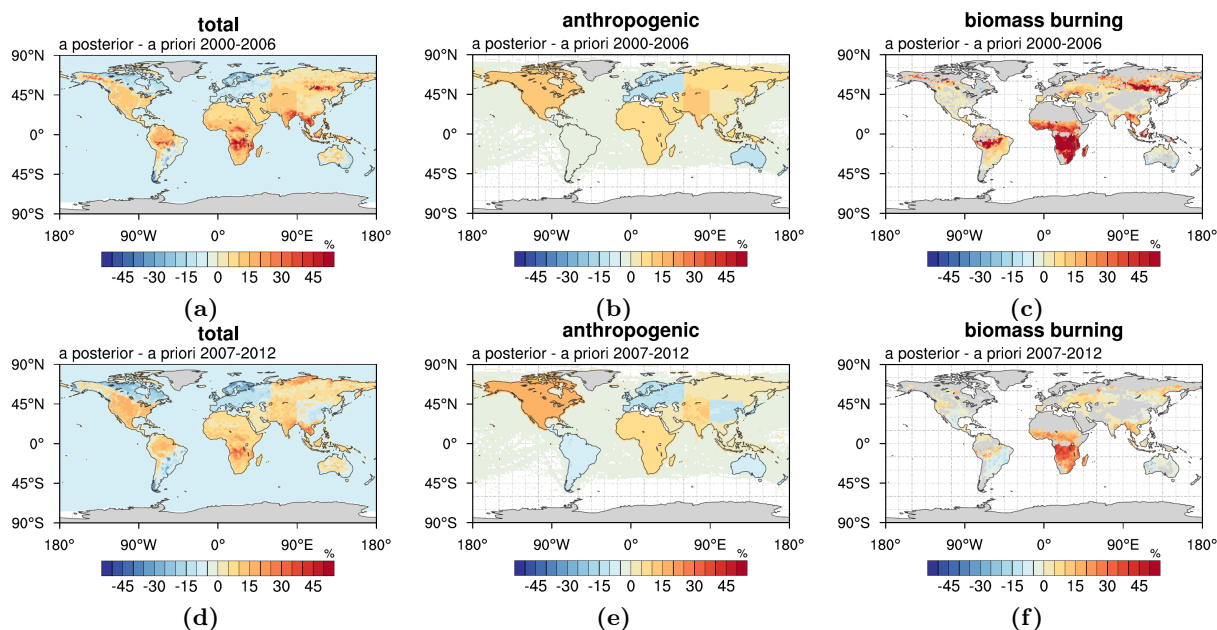
Figure 5.7: Relative difference of a posteriori and a priori emission inventory in the time periods 2000–2006 (upper) and 20007-2012 (lower) in total (left), anthropogenic (middle) and biomass burning (right). Areas where the a priori inventory overestimates the fluxes compared to the a posteriori are shaded bluish (negative) and where it underestimates the fluxes are shaded reddish (positive).
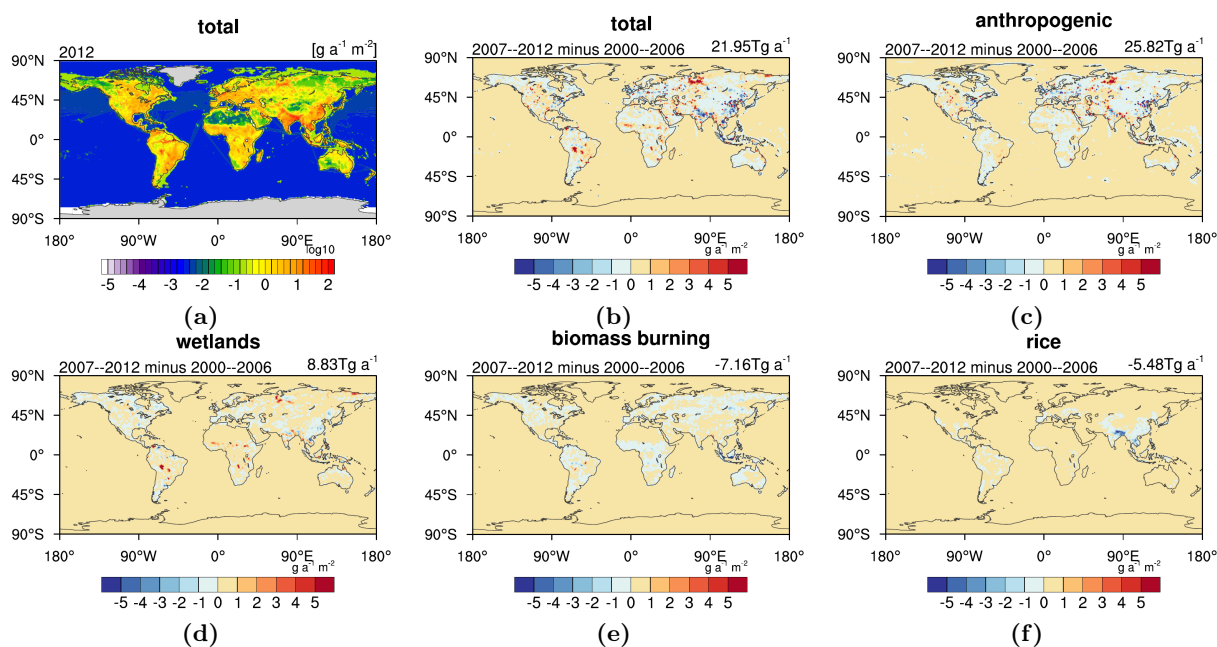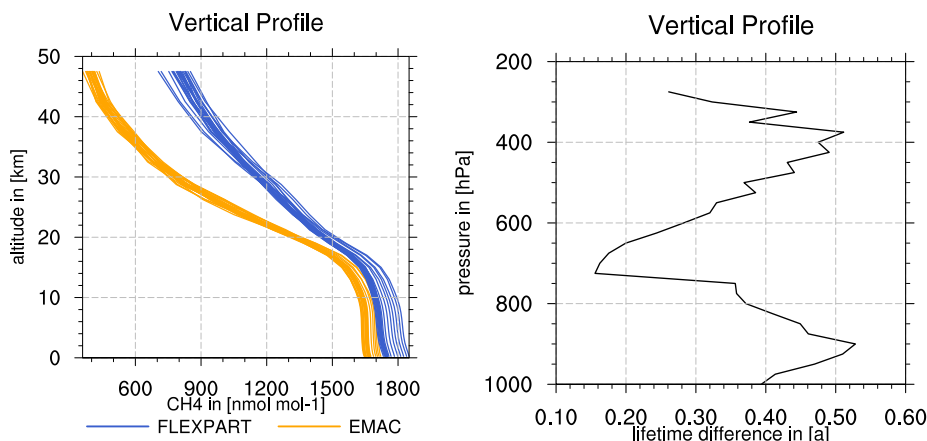

Figure 5.8: (a) Annual mean total a posteriori emission inventory of the year 2012. (b) Difference of the time periods 2007–2012 and 2000–2006 in total and of the emission classes anthropogenic (c), wetlands (d), biomass burning (e), and rice cultivation (f).

(a) Vertical profile of CH_4 mixing ratio of EMAC (yellow) and FLEXPART (blue). The individual profiles indicate the annual mean of the years 1989–2014.

(b) Absolute difference of the lifetime in FLEXPART and EMAC in years.

Figure 5.9: Comparison of the a priori simulations of EMAC and FLEXPART with respect to vertical profile and lifetime.

not, since the CH_4 lifetime is also dependent on the reaction rate and the underlying temperature field (cf. Chapter 4).

FLEXPART uses a predefined temperature field from ERA-Interim, while EMAC is only nudged to the ERA-Interim reanalysis, hence, has a certain degree of freedom to readjust its temperature. This results in a temperature bias of down to -1.9 K in the boundary layer and about $1-2$ K in the free troposphere and increasing upward. The temperature in EMAC is mostly lower than in ERA-Interim, except in the BL (see Fig. 5.10a). Applied to the same reaction rate function (see Fig. 5.10c), this decreases the reaction rate by about $0--2\%$ in the BL and increases the reaction rate by $2-4\%$ in the free troposphere and up to 12% in the upper troposphere. Additional to that, FLEXPART is equipped with a slightly different reaction rate function. EMAC uses k_{CH_4+OH} defined by Eq. (B.1) and recommended by Atkinson [2003], while FLEXPART uses $\tilde{k}_{CH_4+OH}$ defined by Eq. (B.7) from Dunlop and Tully [1993]. Note that the reaction rate function refers to the function derived from laboratory measurements to parameterize the dependency of the reaction rate to the temperature (and/or pressure, etc.), while the reaction rate indicates in this case the rate function applied to a certain temperature. After Atkinson [2003], both reaction rate functions are comparable. Nevertheless, in Fig. 5.10b it becomes evident that k_{CH_4+OH} is smaller than $\tilde{k}_{CH_4+OH}$ by $-3.3--7.9\%$ applying tropospheric temperatures and under the assumption that an identical temperature field is applied. Taking both results together, hence, comparing k_{CH_4+OH} with the temperature field of EMAC and $\tilde{k}_{CH_4+OH}$ with the ERA-Interim temperature field yields Fig. 5.10d. The plot shows that although the mainly higher temperatures of ERA-Interim would result in a faster reaction rate than the temperature field in EMAC, the influence of the two different reaction rate functions is sufficient to over-compensate this performance. Altogether, the reaction rate in FLEXPART is hardly faster (up to 2%) in some regions of the free troposphere, but slightly slower (approx. $< -2\%$) in other. In the BL, where the temperature difference between ERA-Interim and EMAC is small or negative, the difference in the applied reaction rate functions significantly affects the resulting reaction rate. In the BL the reaction rate is therefore in EMAC about 6% faster than in FLEXPART.
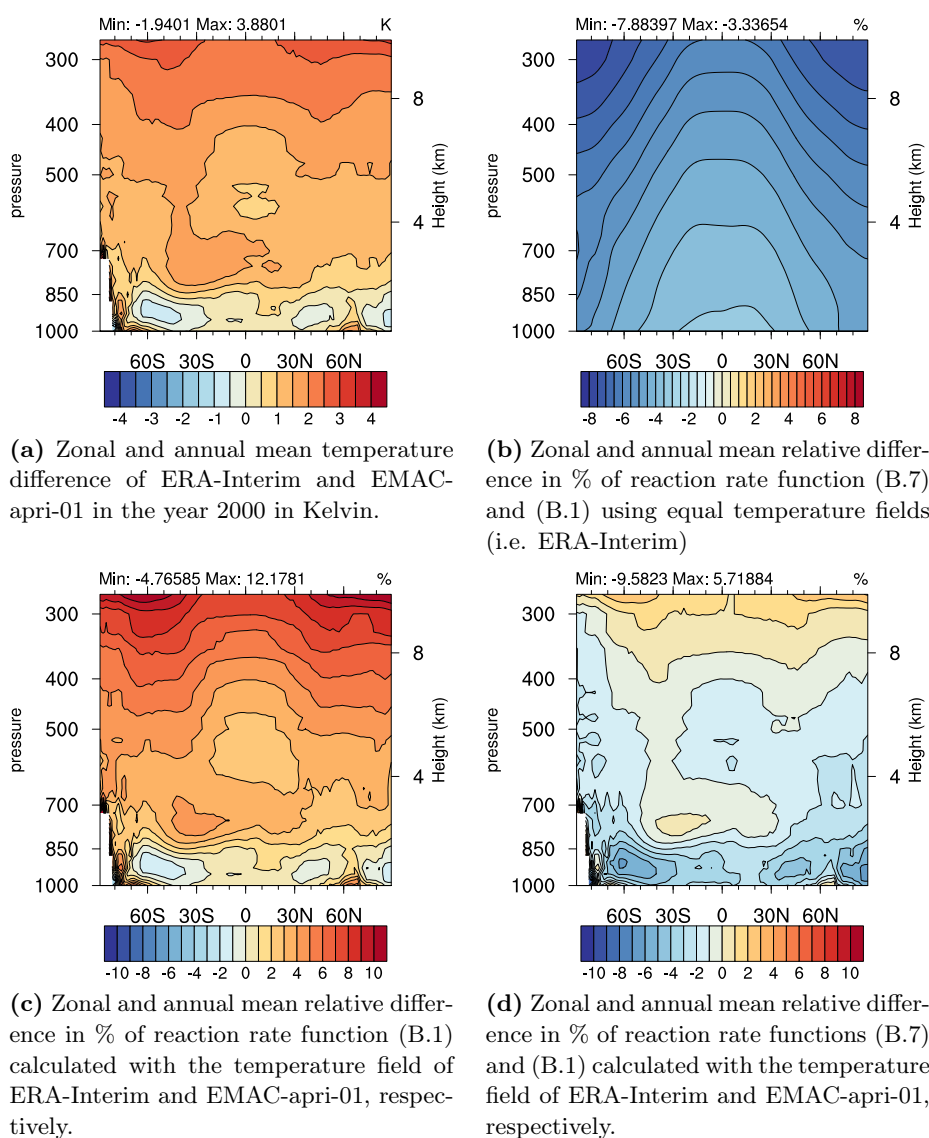
(a) Zonal and annual mean temperature difference of ERA-Interim and EMAC-apri-01 in the year 2000 in Kelvin.

(b) Zonal and annual mean relative difference in % of reaction rate function (B.7) and (B.1) using equal temperature fields (i.e. ERA-Interim)

(c) Zonal and annual mean relative difference in % of reaction rate function (B.1) calculated with the temperature field of ERA-Interim and EMAC-apri-01, respectively.

(d) Zonal and annual mean relative difference in % of reaction rate functions (B.7) and (B.1) calculated with the temperature field of ERA-Interim and EMAC-apri-01, respectively.

Figure 5.10: Influence of temperature and reaction rate function of EMAC and FLEXPART.

Consequently, the lifetime in EMAC is likewise slightly lower than in FLEXPART (see Fig. 5.9b). The difference in lifetime itself seems marginal, with a smaller CH_4 lifetime of about 0.5 a in EMAC than in FLEXPART in the BL and less above, which is equal to 6%. However, these rather small differences, affect the overall CH_4 abundance quite substantially, as is also shown by McNorton et al. [2016]. The vertical profile of CH_4 in EMAC in the troposphere (up to approx. 15 km) is, as well, about 6% lower than in FLEXPART, and can therefore almost fully be attributed to the differences in temperature and applied reaction rate functions of the two models. Note that this difference in CH_4 between the two models is larger than the inter-annual variation of the years 1989–2014, and therefore considered as significant.

The differences at higher altitudes than 15 km are not discussed in this study, since the Lagrangian model FLEXPART in the applied set-up does not provide meaningful results for the stratosphere.
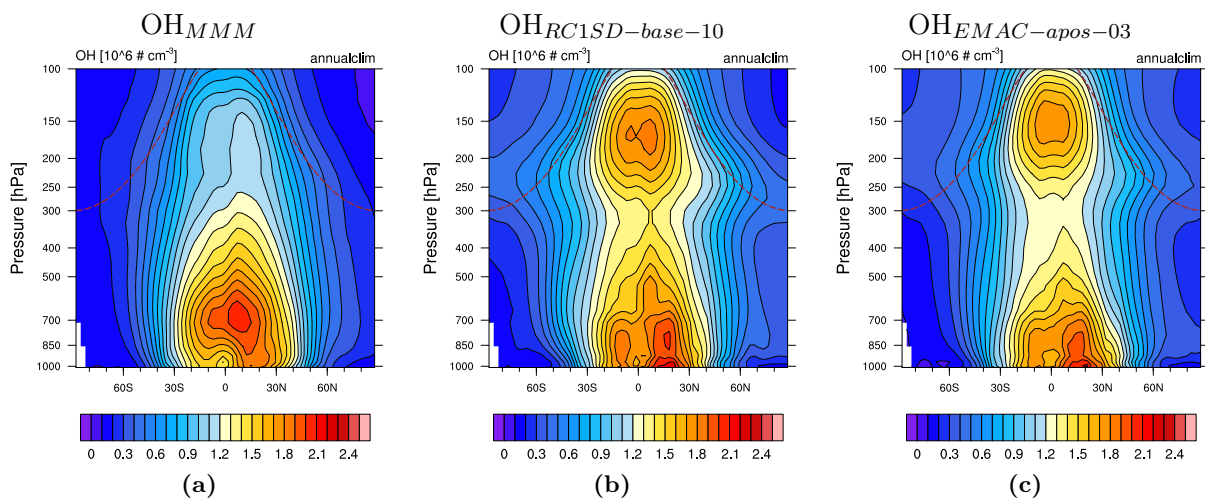
Figure 5.11: The zonal mean OH concentration in $[10^6 \times$ molec. cm$^{-3}]$. The dashed brown line indicates the height of the climatological tropopause.

5.3   Results of the a Posteriori Simulation

The a posteriori emission inventory is used in another set of simulations to further assess its quality. The simulations include, in addition to the set-ups identical to the a priori simulations, one simulation with full interactive chemistry using MECCA. The detailed configuration of all three simulations is presented in the following.

5.3.1   Configuration of Forward a Posteriori Simulation

The simulation EMAC-apos-01 (see Table 5.2) is carried out with a similar set-up as EMAC-apri-01, except that the a priori emission inventory is exchanged with the a posteriori emission inventory. EMAC-apos-02 uses the same a posteriori emission inventory and the remaining set-up is identical to EMAC-apri-02, particularly the OH data set $[OH]_{RC1SD-base-10}$ (see Fig. 5.11b) is applied. Note that the used a posteriori inventory is derived by a flKF application, which uses the results of the EMAC-apri-01 simulation. Thus the derived a posteriori inventory is primarily related to $[OH]_{MMM}$.

Instead of the simplified CH_4 chemistry provided by the CH4 submodel, the third a posteriori simulation EMAC-apos-03 uses a full interactive chemistry by applying MECCA. In this case the sink reaction partners of CH_4 adapt to the new conditions. This results in a new distinct OH distribution indicated by $[OH]_{EMAC-apos-03}$ (see Fig. 5.11c).

A decisive factor for the agreement between observations and simulation results is not only the emission inventory itself or the applied OH field, but the initial condition of CH_4. If the initial field of CH_4 is too high or too low the resulting CH_4 signal is overlaid with a potential unrealistic trend. Therefore, attention must be paid to the initial conditions to improve agreement of simulation and observations.

However, the global atmospheric CH_4 (3-dimensional) distribution, is mainly unknown. Yet, CH_4 observations agree that around 1990 the CH_4 burden shows a positive trend ([Dlugokencky et al., 2003]). This suggests that the background concentration of atmospheric CH_4 is not in an equilibrium in 1990. Hence, the straightforward approach, using a spin-up with emissions from the start year 1990 until a steady state is reached, is not advisable, as the emissions likely induce a positive trend, resulting in an equilibrium of CH_4, which is higher than the actual atmospheric concentration. More-
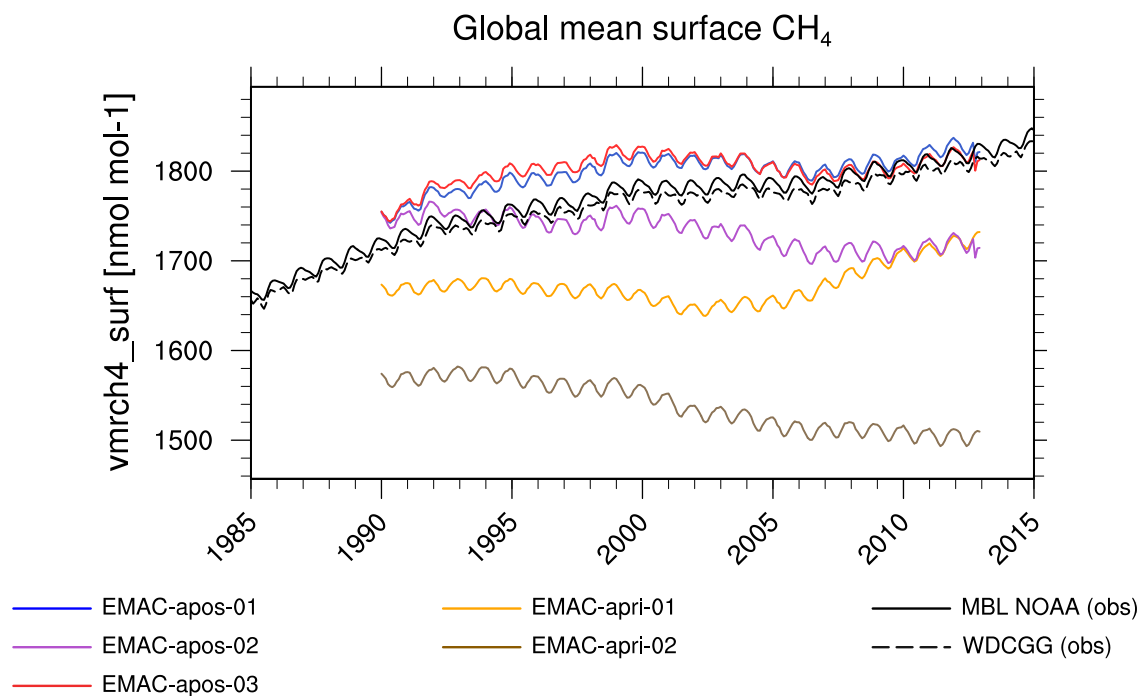
Global mean surface CH$_4$

Figure 5.12: Monthly averaged global mean surface CH$_4$ of all simulations. The black dotted line indicate the global mean marine boundary layer (MBL) reference CH$_4$ mixing ratio from NOAA/ESRL ([Dlugokencky et al., 2015a], `https://www.esrl.noaa.gov/gmd/ccgg/mbl/data.php`) and the black solid line indicates the global mean surface CH$_4$ mixing ratio from WDCGG ([WMO, 2017], `http://ds.data.jma.go.jp/gmd/wdcgg/pub/global/globalmean.html`) based on surface observations.

over, this steady state of the spin-up is dependent on the atmospheric oxidation capacity and would therefore differ between simulations with distinct OH fields, as they are applied in the carried out simulations EMAC-apos-01, EMAC-apos-02, and certainly EMAC-apos-03. Therefore, for a replicable and comparable experimental set-up, it is necessary to start with consistent initial conditions.

This motivates the development of a best guess for the global atmospheric CH$_4$ distribution and to apply this three dimensional initial field to all simulation experiments in the sensitivity study. In the present study, a global three dimensional field of CH$_4$ of an earlier simulation with EMAC is applied, which shows reasonable agreement with ground-based stationary observations in the start year 1990, although overestimates the surface mixing ratio by about 30 nmol mol^{-1}.

Again, in order to compare the simulation results at the sampling stations used for the inversion, the stationary column output provided by SCOUT sub-sampled at the sampling sites is used.

5.3.2 Comparison of a Priori and a Posteriori Simulation

In order to discuss the uncertainties of the a posteriori inventory the various a posteriori simulations are in the following compared with respect to the applied sink and model set-up.

For a first overview, the monthly averaged global mean surface CH$_4$ mixing ratio of all carried out simulations are shown in Fig. 5.12. It is apparent that the a priori simulations (i.e. EMAC-apri-01/02 in yellow and brown), as expected due to the comparably low CH$_4$ emissions in the a priori emission inventory and too low initial CH$_4$ mixing ratios, are much too low compared to the reference surface mixing ratio of CH$_4$ based on observations (black, solid and dashed). These reference surface mixing
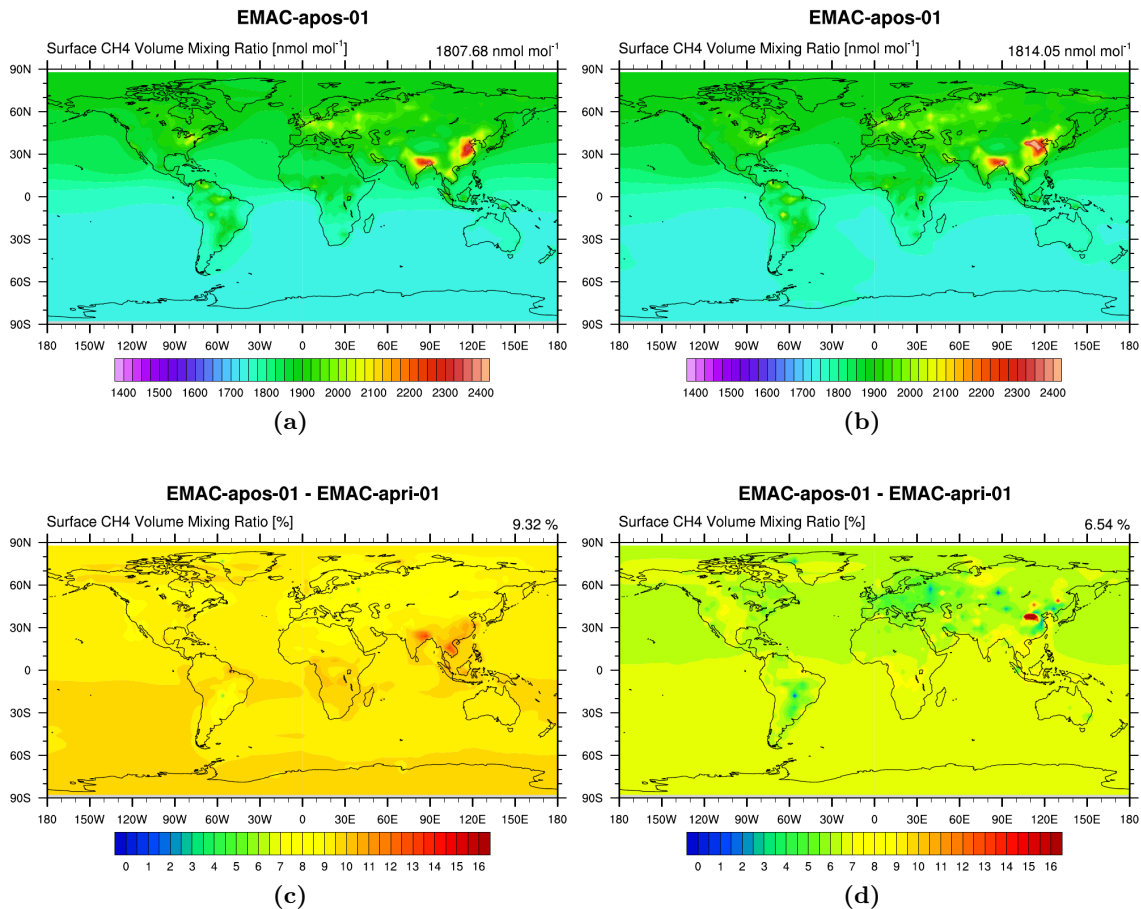
Figure 5.13: Difference of surface CH$_4$ mixing ratio of the simulations EMAC-apos-01 and EMAC-apri-01 as climatological means of the years 2000–2006 (a) and 2007–2012 (b).

ratios are the MBL reference of CH$_4$ provided by NOAA/ESRL and the global mean surface CH$_4$ mixing ratio provided by WDCGG. Both references are based on global ground-based observations. However, NOAA/ESRL included solely sampling sites representative for the MBL [Dlugokencky et al., 2015a], while the WDCGG also included continental sampling sites, potentially influenced by local CH$_4$ emissions and sinks [Tsutsumi et al., 2009], resulting in an about 0.5% smaller average than the estimate of NOAA/ESRL.

Additionally, comparing the surface CH$_4$ mixing ratio of EMAC-apos-01 with the mixing ratio of EMAC-apri-01 shows the influence of the amplified or weakened emission fluxes. In the time period of 2000–2006 (see Fig. 5.13c) the surface mixing ratio differs by 9.3%, which is more than the 6.5% in 2007–2012. From the comparison of the emission inventories it is clear that the differences in the fluxes of the a priori and a posteriori inventory are larger in the early time period than in the later one. It also shows that the areas, where prominent differences are detected between the emission inventories, are also observable in the differences in Fig. 5.13c, as for example over India, South Africa and the tropical part of South America. In the later time period, those differences are reduced (see 5.13d). However, prominent is the elevated mixing ratios in the a posterior simulation in eastern China, which are not evident in the comparison of the emission inventories. It happens that in 2008 the anthropogenic emissions in China are strongly enhanced which is not evident in the comparison of a priori and a posteriori inventories of the time period 2007–2012 due to averaging. This additionally
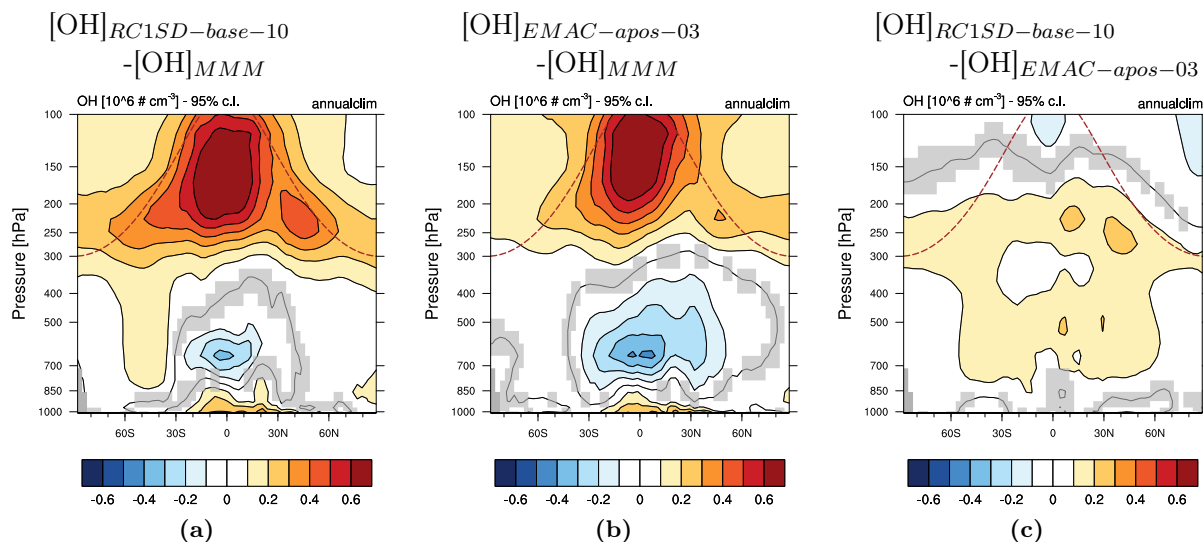
Figure 5.14: The absolute difference of the zonal mean OH concentration in $[10^6 \times$ molec. cm$^{-3}]$ of the years 2000–2009. The unshaded areas are significant on a 95% confidence level according to a two-sided Welch's test. The dashed brown line indicates the height of the climatological tropopause.

emitted CH_4 is still abundant in the following years as the depletion is relatively slow due to the already very large CH_4 mixing ratios in this region (see Fig. 5.13a and 5.13b).

As intended, all a posteriori simulations start at the same initial condition (see Fig. 5.12). Very roughly, they agree better with the reference than the a priori simulations, which, overall, indicates that the a posteriori inventory improves the simulation of CH_4 in EMAC compared to the too low a priori emission inventory. However, the carried out simulations with the a posteriori inventory also show certain differences between each other, which are discussed in the next section.

5.3.3 Influence of the Applied OH Field

Considering Fig. 5.12, EMAC-apos-02 shows a negative trend in contrast to the positive trend of the observation references. It should be noted again that the used a posteriori inventory is not optimized using data of the forward simulation EMAC-apri-02, which uses the same OH data set as EMAC-apos-02. Instead, the a posteriori inventory relates to the $[OH]_{MMM}$ used in EMAC-apri-01. EMAC-apos-01 and EMAC-apos-03, on the other hand, follow the trend of the reference, although they overestimate the surface mixing ratio until about 2007. Interestingly, the interactive chemistry simulation EMAC-apos-03 agrees well with the EMAC-apos-01, which is not necessarily expected in the first place.

At first, the predefined distinct OH fields of the simulations using the CH4 submodel are in focus. Since both simulations, EMAC-apos-01, and EMAC-apos-02, experience the same CH_4 fluxes, the difference in their CH_4 growths originates solely from the different sinks. Comparing $[OH]_{MMM}$ and $[OH]_{RC1SD-base-10}$ (see Fig. 5.14a) shows that the OH mixing ratio in the RC1SD-base-10 is considerably ($>0.6 \times 10^6$ molec. cm^{-1}) larger than $[OH]_{MMM}$, except in the lower tropical troposphere, where it is up to -0.4×10^6 molec. cm^{-1} smaller. From Fig. 5.11 it becomes apparent that the largest OH concentrations of both simulations are located in this region as well. Nevertheless, the average lifetime of EMAC-apos-02 is with 8.15 a in 2000–2009 substantially lower than the lifetime in EMAC-apos-01, which is 8.41 a.

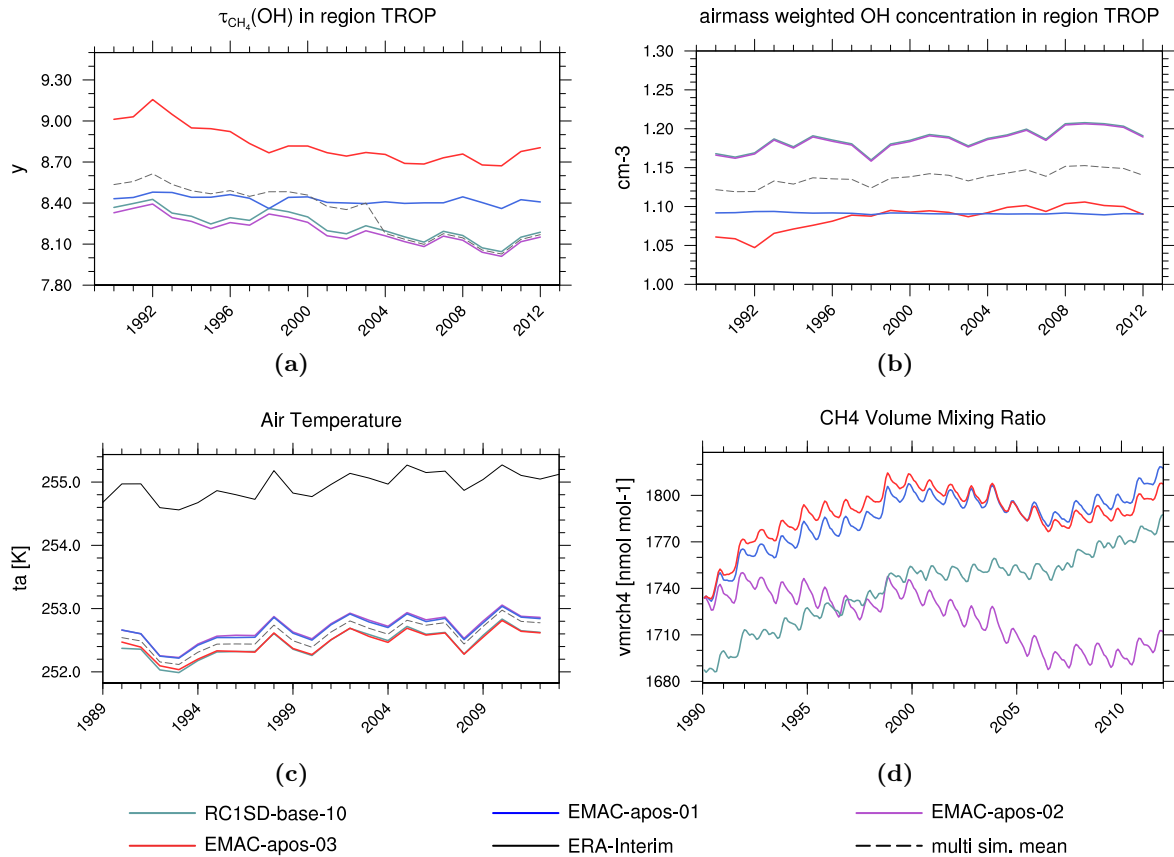In contrast to EMAC-apos-01, the simulation EMAC-apos-02 uses a predefined transient OH field,

Figure 5.15: (a) Tropospheric CH_4 lifetime with respect to OH and (b) airmass weighted tropospheric OH concentration of the a posteriori simulations EMAC-apos-01/02/03 and RC1SD-base-10. (c) Tropospheric mean temperature of the indicated simulations and ERA-Interim and (d) tropospheric mean CH_4 mixing ratios of the indicated simulations.

thus, which is not annually repeated. Particularly, the OH concentration is increasing over the considered years in this simulation (see Fig. 5.15b), which results in a decreasing CH_4 lifetime (see Fig 5.15a). The $[OH]_{AW}$ in EMAC-apos-01 is annually repeated and considerably lower than in EMAC-apos-02. The respective $\tau_{CH_4}(OH)$ of EMAC-apos-01 is therefore a bit longer and likewise nearly constant. Taken together, this leads to the observed negative trend in the surface CH_4 mixing ratio of EMAC-apos-02 and suggests that emissions are likely too low, if the OH field $[OH]_{RC1SD-base-10}$ is applied. By this, it is concluded that the chosen OH sink in the a priori simulation is a decisive factor for the a posteriori inventory and that the estimation must be set in context to this assumed OH distribution.

Furthermore, although the differences in the OH concentration show a spatial pattern and increase strongly towards the upper troposphere (Fig. 5.14a), the relative difference in the CH_4 mixing ratio does not show this, and is fairly evenly distributed in the whole troposphere with only a small North-South gradient (see Fig. 5.16a) and with on average -3.1% CH_4 at the surface (see Fig. 5.16c). These results suggest that the vertical pattern of the OH concentration has only a minor influence on the CH_4 vertical profile. Turbulent and convective mixing in the troposphere quickly results in a nearly uniform CH_4 reduction. Different interhemispheric OH imbalances yield small variations in the North-South gradient in the simulated CH_4. Further studies are needed to assess the influence of

the vertical profile of OH onto the CH_4 mixing ratios. If this independence is confirmed it supports the importance of $[OH]_{AW}$ as a tropospheric mean indicator for the CH_4 sink. In that case, future simulations of CH_4 ought to meet a realistic total tropospheric $[OH]_{AW}$ abundance, but a precise estimation of the OH vertical profile is not necessary. This would reduce the effort on the correct estimation of the OH distribution, which is, as stated before, still poorly constrained.

5.3.4 Feedback onto the OH Field in the Interactive Chemistry

The previous section analyzed the influence of predefined OH fields. The hydroxyl radical in the atmosphere is determined by its major precursors but also by its sink partners. Therefore, if emissions of CH_4 are modified, it changes the OH abundance through feedbacks in the interactive chemistry. Since strong impacts of the chosen OH data set onto the simulated CH_4 have been revealed in the section before, the effect of the a posteriori inventory onto the tropospheric OH abundance in an interactive chemistry is investigated next.

Firstly, recall the following:

- The global fluxes of the a posteriori inventory, as presented in Fig. 5.6b, compare relatively well to the pseudo-fluxes of the RC1SD-base-10 simulation, which also serves as the reference of the applied OH data set in the simulations EMAC-apos/apri-02. In the years 2000–2009 the pseudo flux is a bit higher than the flux in the a posteriori inventory.

- All other emissions of chemical species in EMAC-apos-03 are identical to the set-up of RC1SD-base-10.

- The total CH_4 mixing ratio in the troposphere in the considered – rather short – time period is strongly dependent on the initial condition, which is about 50 nmol mol^{-1} lower in the RC1SD-base-10 simulation than in the a posteriori simulations (see Fig. 5.15d).

- The vertical profiles of $[OH]_{RC1SD-base-10}$ and $[OH]_{EMAC-apos-03}$ show a second local maximum in the upper troposphere, while $[OH]_{MMM}$ is substantially lower in this region as indicated in Fig. 5.11 and Fig. 5.14.

- The global surface CH_4 mixing ratio of EMAC-apos-01 and EMAC-apos-03 agree well, as shown in Fig. 5.12.

The general pattern of the vertical profile of OH in EMAC-apos-03 with the second local maximum in the upper troposphere is induced by the temperature nudging, which is similar to the RC1SD-base-10 simulation. Humid and ozone rich air of the tropics in these simulations is carried upward by convective transport. These OH precursors increase the production of OH in the upper troposphere and shape the second maximum. Additionally, the difference of the newly derived OH field $[OH]_{EMAC-apos-03}$ and $[OH]_{MMM}$ in Fig. 5.14b is basically a reminiscent of the difference between $[OH]_{RC1SD-base-10}$ and $[OH]_{MMM}$ in 5.14a. The new OH field $[OH]_{EMAC-apos-03}$ is thereby in general lower than $[OH]_{RC1SD-base-10}$ (see Fig. 5.14c), especially in the tropics.

In Fig. 5.15b it is also apparent that the total OH is actually also lower than the $[OH]_{MMM}$ in the first simulated years and is after 1997 comparable to $[OH]_{MMM}$. Yet, $\tau_{CH_4}(OH)$ of EMAC-apos-03 is larger than those of EMAC-apos-01/02 although the tropospheric mean temperatures of all a posteriori simulations are virtually similar (see Fig. 5.15c). This difference in $\tau_{CH_4}(OH)$ is based on the fairly different vertical profiles of OH, as a considerable amount of OH is shifted from the lower tropical troposphere to the upper troposphere.
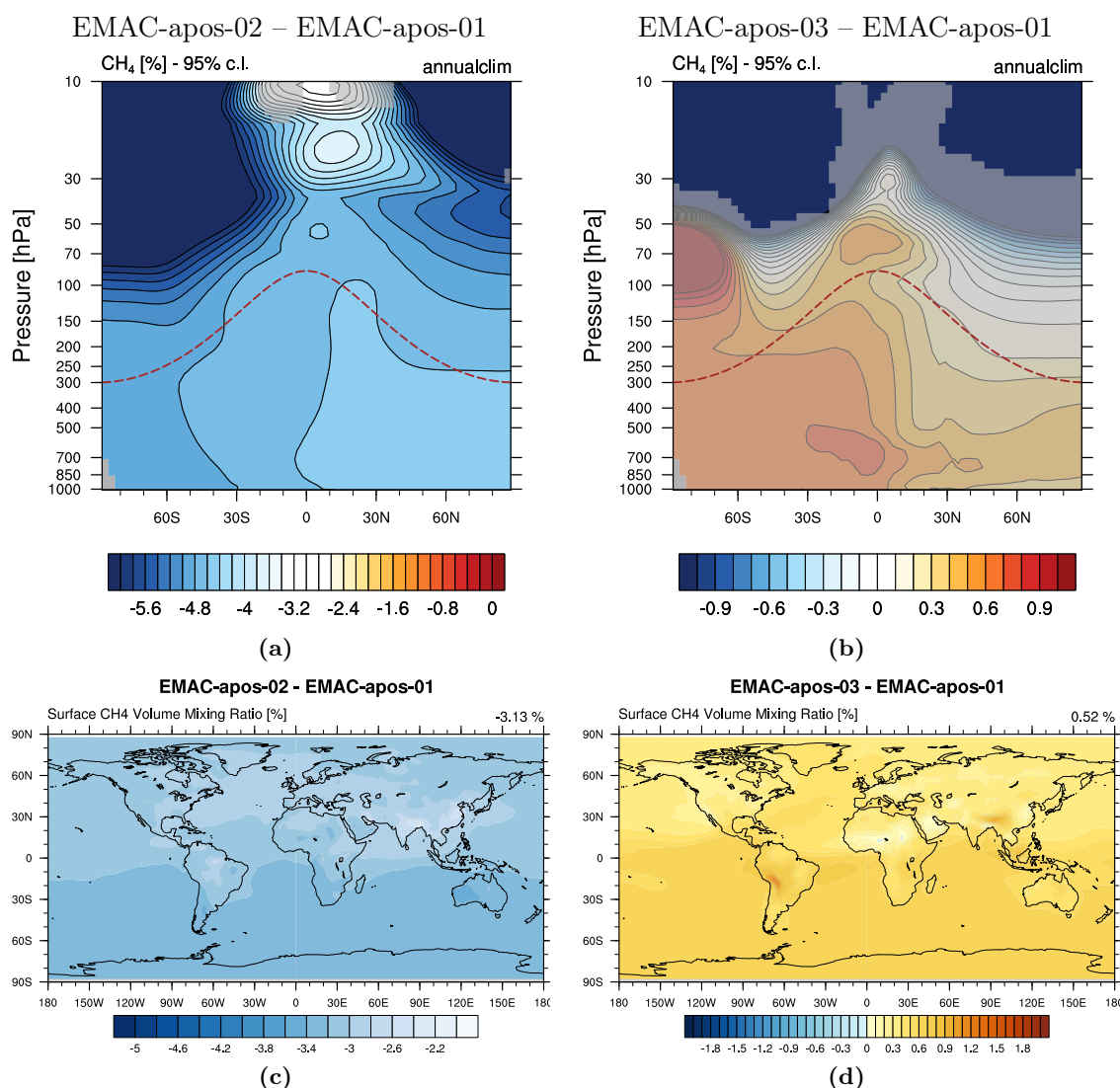
Figure 5.16: Upper panels: Relative zonal mean differences of CH_4 of the years 2000–2009. The unshaded areas in the difference plots are significant on a 95% confidence level according to a two-sided Welch's test. The dashed brown lines indicate the height of the climatological tropopause. Lower panels: Relative differences of surface CH_4 of the years 2000–2009. Note the different color scales.

It becomes clear, that the increased total CH_4 in EMAC-apos-03 compared to RC1SD-base-10, mostly determined by the initialization, strongly reduces the OH abundance. Note that due to the very fast reactions of OH, it is almost immediately in a steady state. The most intense reduction of OH is thereby located in the tropical free troposphere. Despite the differences between the OH field of the simulations EMAC-apos-01 and EMAC-apos-03, the CH_4 in those simulations differ at the surface only by about 0.5% and there are no significant differences identifiable in the vertical profile (cf. Fig. 5.16b and 5.16d). Note again that this good agreement between the simplified chemistry and interactive chemistry is initially not expected.

Obviously, the OH field in EMAC-apos-03 is adjusting towards the initial condition and the applied emission fluxes. Its OH field is especially lower than $[OH]_{MMM}$ in the, for the CH_4 lifetime most important, lower and middle tropical troposphere. Nevertheless, the total tropospheric airmass

weighted OH concentration of EMAC-apos-03 is most of the time nearly identical to the $[OH]_{MMM}$ (see Fig. 5.15b).

It seems that the OH distribution (i.e. the pattern and not in absolute terms) does not vary much with respect to variations in the emissions of chemical species and is rather dynamically driven, which results in the following rather provocative proposition: Assume the $[OH]_{MMM}$ resembles the reality and inverse optimized emissions are correct. Applied to the interactive chemistry, the OH adjusts to the used initial condition and emission fluxes. The actual vertical pattern of the OH in the troposphere is albeit of minor importance as long as the airmass weighted OH is correct. The absolute abundance of CH_4 is almost unaffected despite the large increase in the CH_4 lifetime. It seems that turbulent and convective mixing takes care that the vertical distribution of CH_4 is not very sensitive to the details of OH distribution. Therefore, the total OH concentration is a more important identifier on the tropospheric CH_4 sink.

Conclusively, this issue needs further investigation, which certainly requires additional sensitivity simulations, focusing on the adjustment of the OH field within the interactive chemistry. This, however, is beyond the scope of the present study. Nevertheless, it is found that the initial condition of CH_4 has a major influence and that the interactive chemistry includes feedbacks between CH_4 and OH, which are not yet fully understood.

5.4   Evaluation with Observations

In addition to inter-model and inter-simulation comparisons, the results of the a posteriori simulations are further evaluated with atmospheric observations of CH_4. Consequently, this assesses the quality of the a posteriori emission inventory.

5.4.1   Ground based Stationary Data

The a posteriori simulations are evaluated at the ground-based sampling sites, which also have been used for the inversion algorithm. While the results shown in Section 5.2.2 are derived by assuming a linearity between the changed emissions by optimization and the simulated CH_4 at the sampling sites, the results shown in the present section are taken from the actual forward simulations, which in case of EMAC-apos-03 include potential non-linearities.

Recall that the globally-averaged surface mixing ratio shown in Fig. 5.12 differs from the observation based value in the initial phase. Nevertheless, the initial values are well represented at the individual stations, especially in the SH (see Fig. 5.17), although simulations slightly overestimate the mixing ratio. It, however, justifies the used initial CH_4 distribution at least at the sampling sites. The differences in the globally-averaged surface mixing ratio are probably caused by the applied calculation method of the observation based reference, which includes a curve fit to the latitudinal distribution between the individual sampling sites [Dlugokencky et al., 1994, Tsutsumi et al., 2009]. However, to assess this, it needs further analyses of the global surface CH_4 distribution derived by observations and by simulations alike.

Nevertheless, over the course of time, the simulations EMAC-apos-01 and EMAC-apos-03 overestimate the observations at the evaluated sampling sites until about 2006 (10 additional sampling sites are shown in the Appendix Figs. F.10–F.11). Afterwards the observations are well represented, again, especially in the SH. Additionally, it should be noted that at certain northern sampling sites the agreement of the annual cycle in EMAC-apos-01/03 is poorer compared to EMAC-apos-02. The overestimation of the mixing ratios is potentially caused by the slightly overestimated initialization or by overestimated emission fluxes in the first half of the considered time period. Note that a posteriori
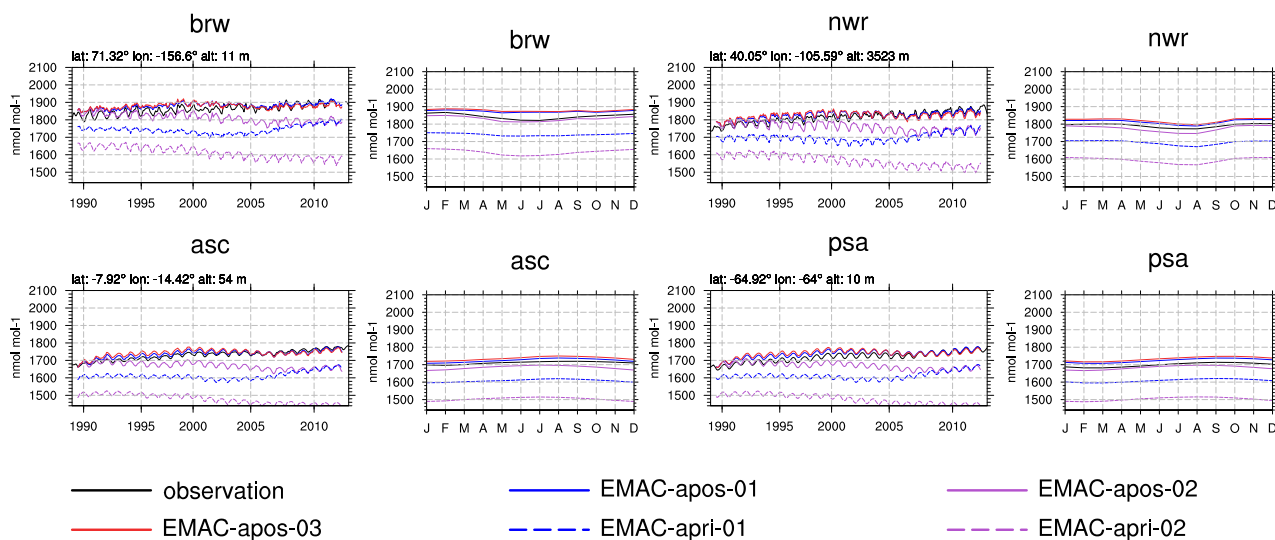
Figure 5.17: Results of the forward simulations in terms of agreement at the observation stations (i.e. Burrows, Niwot Ridge, Ascension Island, Palmer Station). The black solid line indicates the observation. Dashed are the a priori results. Solid are the a posteriori results. Blue indicates the simulations with $[OH]_{MMM}$ and purple the simulations with $[OH]_{RC1SD-base-10}$. The time series between 1990 and 2012 is shown on the left hand side and the annual cycle on the right. Note that the red line mostly overlays the blue solid line.

emission fluxes increased strongly compared to a priori fluxes. However, the results of the inverse optimization method at the stations (cf. Fig. 5.4) rather indicated an underestimation of the emission fluxes in the first two thirds of the time period. It seems that non-linear processes influence the CH_4 abundance at the sampling sites, which are not considered in the linearity assumption in the shown results of the inverse optimization.

Again, Taylor diagrams are used to jointly assess the set of 62 previously presented sampling sites. As stated in Section 5.2.2 the annual cycle at the sampling sites is already well represented in the a priori simulation and is still in the a posteriori (see Fig. 5.18a). The trend is decently improved in the a posteriori simulations EMAC-apos-01 and EMAC-apos-03, while EMAC-apos-02 has substantial deficiencies concerning the trend, as discussed before, and therefore does not appear on the Taylor diagram in Fig. 5.18b.

5.4.2 Airborne Observations

Since the inversion result is by design expected to agree well with the ground-based observations, the results are furthermore evaluated with independent airborne observations. The presented vertical profiles in Fig. 5.19 evaluate the vertical gradients of the simulated CH_4.

The presented flights are taken from the following campaigns: CONCERT2 (2011), T-NAWDEX (2012), GWLCycle (2013), ACCESS-II (2014), ECLIF (2015), GWLCycle-II (2016). The measurements were taken with a Picarro instrument, which is a Wavelength-Scanned Cavity Ring Down Spectroscopy (WS-CRDS) system and was during the campaigns mounted on the research aircraft Falcon 20-E5 operated by the German Aerospace Center [Schlager and Scheibe, 2011].

The observations during the campaign flights are compared to the simulation results sampled at the flight path in a representative annual average of the years 2000–2012. In addition to the simulations EMAC-apos-01/02/03 the figures also include results of the simulation SC1SD-base-02, which is based on the previously presented ESCiMo simulation RC1SD-base-10, but with corrected road traffic
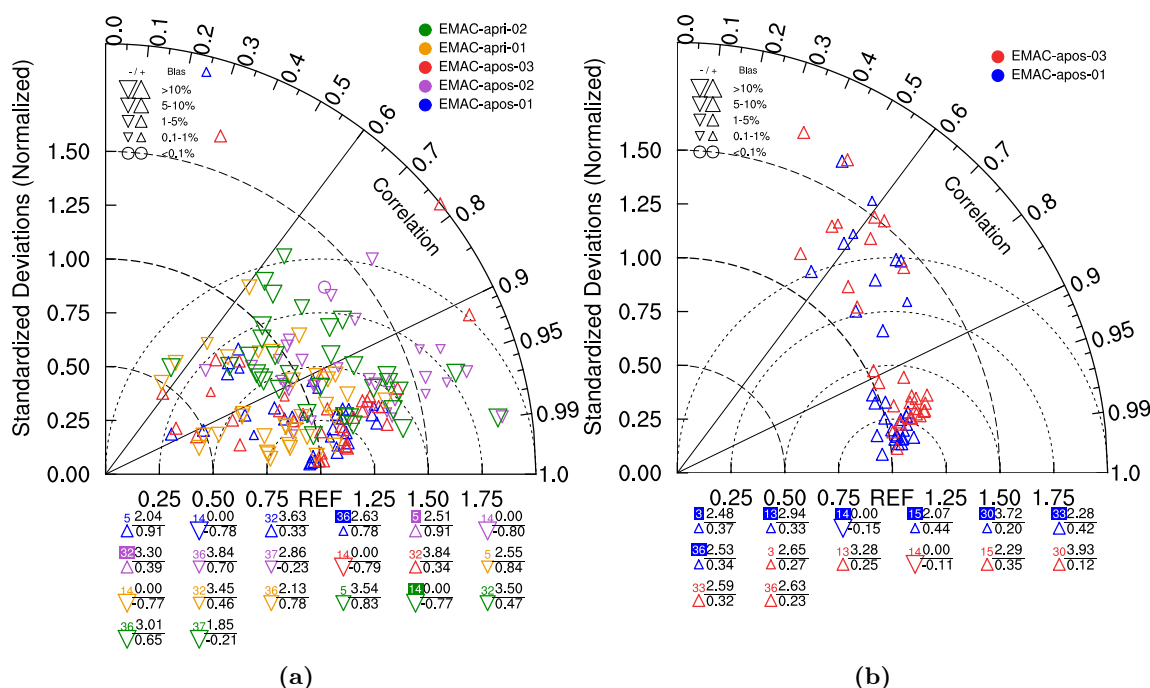
Figure 5.18: Taylor diagram of a priori and a posteriori simulations at various surface sampling sites. The Taylor diagram is shown with respect to the annual cycle (a) and with respect to the trend between 1990 and 2012 (b). The size of the triangles indicates the bias in percent with upward oriented triangles indicating a positive and downward oriented triangles a negative bias. Circles indicate a bias of less then 0.1%. The symbols below the diagram are stations outside the displayed range of the Taylor diagram and are indicated by the colored number. The normalized standard deviation is displayed by the upper black number and the correlation coefficient by the lower black number on the right hand side of the symbol.

emissions.

Again, the two simulations EMAC-apos-01 and EMAC-apos-03 perform best. Both, the simulation EMAC-apos-02, and SC1SD-base-02, underestimate the CH_4 mixing ratio. However, the vertical gradient in all simulations sufficiently represents the observed gradient.

The absolute CH_4 values of the simulations are a bit lower compared to the profiles of the two campaigns in the more recent years (ECLIF and GWLCycle-II). Since the global mixing ratio of CH_4 increased strongly since 2007 and the simulation time period ends in 2012, the used climatology of the simulations does not represent the CH_4 growth in the following years until 2016. Furthermore, the campaign ECLIF was performed to study aviation exhaust plumes with respect to alternative fuels and CH_4 observations are likely influenced by the campaigns flight set-up, which included the direct pursuit of a second aircraft.

5.5   Summary

Concludingly, this chapter presents the estimate of a new emission inventory by inverse optimization using a fixed-lag Kalman Filter. Influencing factors onto this optimization method and the resulting simulations are discussed.

Main results are that the new emission inventory improves the simulation of CH_4 in EMAC compared to the a priori inventory, which represents a combination of current recommendations of various Bottom-Up inventories (e.g. EDGAR v4.2 database and Bousquet et al. [2011]). Furthermore, by
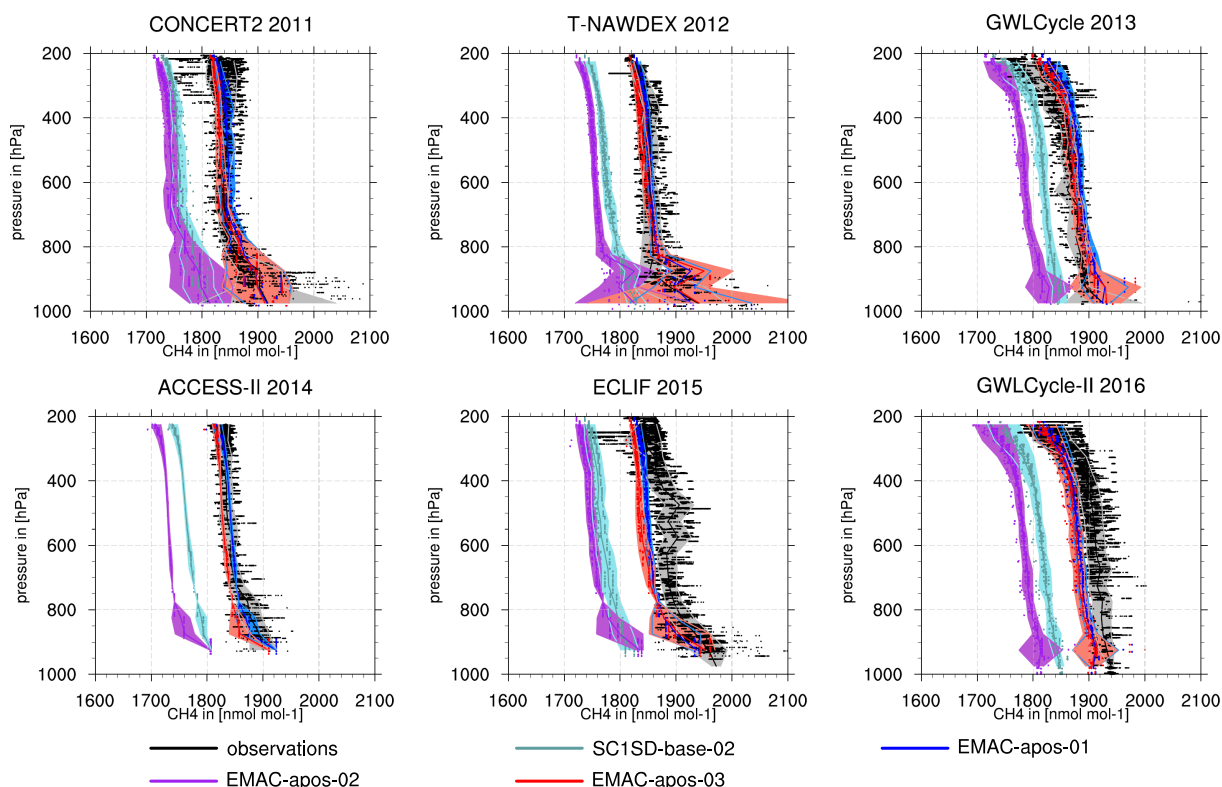
Figure 5.19: Observation based vertical profiles of CH_4 from several aircraft campaigns (black). The colored lines indicate corresponding vertical profiles of the simulations, with respect to the three dimensional position of the aircraft and the season of the observation. The used simulation data is a multi year monthly mean of the years 2000–2012. The shaded areas indicate the single standard deviation of the data points at a specific pressure level.

comparing two forward simulations with distinct OH fields and model systems, it is found that the applied forward model and assumptions on the OH sink massively influence the results of the a priori forward simulations, and therefore determine the inverse optimized emission inventory.

In the results of an interactive chemistry simulation, the feedback onto the OH sink by increased CH_4 mixing ratios becomes evident. The altered vertical pattern of OH has only a minor influence on the CH_4 abundance, which results in a virtually similar CH_4 abundance and distribution compared to the simplified set-up. Nevertheless, the changes in the OH distribution result in an increased CH_4 lifetime (from 8.4 a in EMAC-apos-01 to 8.7 a in EMAC-apos-03 in 2000–2009), although the airmass weighted OH concentration is almost identical.

Overall, it is apparent that assumptions on OH and the CH_4 sink in general are decisive factors in the estimation of CH_4 fluxes. The hydroxyl radical in turn depends on the CH_4 abundance and its fluxes. Correspondingly, feedbacks between OH and CH_4 are still not fully understood, which requires additional studies to analyze this further. Besides, for a comprehensive investigation of the OH feedbacks further knowledge (e.g. by means of observations) of the OH mixing ratio in the atmosphere are needed.

A promising additional information to constrain the sources and the sink processes of CH_4 alike, is the study of the isotopologues of CH_4. Depletion processes of CH_4 by OH and its other sink reactants introduce fractionation effects, which leave a distinct isotopic signature in the atmosphere. Potential simulation methods and their evaluation concerning CH_4 isotopologues, which are developed in the course of this thesis, are presented in the next chapter.

Modelling Methane Isotopologues

The results of the previous chapters reveal that uncertainties in the estimation of CH_4 sources are connected to uncertainties in the tropospheric sink of CH_4. In order to reduce these it is necessary to find a method to jointly analyze both, sink, and source processes of CH_4. One possible method is to exploit the information about the isotopic composition of CH_4 for the estimation of the emission sources, as has been done, among others, by Hein et al. [1997], Monteil et al. [2011] and Rigby et al. [2012]. This approach is based on the fact that each source of CH_4 has a specific isotopic signature, which can be considered as a distinct fingerprint of the emission. Moreover, fractionation processes of the CH_4 sinks influence the isotopic pattern in the atmosphere, which provides additional information on the sink processes determining the CH_4 composition.

In the context of the current work CH_4 isotopologues (specifically $^{12}CH_4$ and $^{13}CH_4$, and CH_4 and CH_3D) are used to improve the knowledge about the composition of CH_4 in the atmosphere with respect to its sources and its sink processes.

In order to achieve this, submodels and tools in EMAC are combined and extended, as well as newly introduced to provide a comprehensive framework for the simulation of CH_4 isotopologues. This enables the investigation of the pathways of CH_4 from the source to the end-products H_2O and CO. The latter is particularly investigated in detail by Gromov [2014], while the work at hand focuses on H_2O and thus on the pathways of deuterium.

The additional information of CH_4 isotopologues is analyzed in the following sections, first with respect to two different simulations, one with a simplified CH_4 chemistry and the other one with a comprehensive interactive chemistry, and later in comparison with atmospheric observations.

6.1 Modeling Isotopologues in EMAC

One aim of the present thesis is to enable the integration of CH_4 isotopologues as an additional information for the simulation of CH_4. Again, two basically different frameworks for the simulation of the chemical species and their isotopologues are applied. One is the isotopical extension of the simplified CH_4 chemistry in the CH4 submodel, and the other one is the kinetic chemistry tagging technique incorporated into the comprehensive chemical mechanism of MECCA.

Briefly recapitulated, in the course of this work, the CH4 submodel is extended to allow for the simulation of the abundant and first rare CH_4 isotopologues with respect to carbon and hydrogen isotopes, as in detail explained in Section 3.3.1. Furthermore, in case of simulating the interactive chemistry, MECCA-TAG is, in the course of the presented research, for the first time configured to take into account hydrogen/deuterium isotopologues of all included hydrogen-carrying chemical species in the mechanism. This is a novel set-up, since previous studies with MECCA-TAG focused on carbon and oxygen isotopes [Gromov et al., 2010, 2017]. Depending on the desired approach, either MECCA-TAG, the isotopological extension of CH4, or both, can be applied in the EMAC simulations.

Moreover, in the course of a previous modeling study with EMAC, the H2OISO submodel was developed, which simulates the physical isotope fractionation effects of the hydrological cycle and

creates H_2O isotopologues with respect to hydrogen and oxygen in all three phases (gas, liquid, ice) [Eichinger et al., 2015a]. This submodel also included a simplified chemical production of HDO via CH_3D oxidation. In order to combine the physical fractionation in H2OISO with the newly implemented and configured chemical fractionation processes in CH4 and MECCA-TAG, respectively, the auxiliary submodel TRSYNC is implemented.

In the next subsection the set-up of the simulations including (among others) CH_4 isotopologues are presented, whose results are used in the following evaluation of the model developments.

6.1.1 Simulation Set-up

The simulations presented in the previous chapter (see Table 5.2) partly included the additional simulation of CH_4, H_2O and other isotopologues. The results of these simulations are used to assess the capabilities of the current model system in simulating isotopologues. Particularly, the a posteriori simulations EMAC-apos-02 and EMAC-apos-03 are used for this evaluation. Details on the general set-up of these simulations are shown in Section 5.2.1 and 5.3.1, respectively.

In the simulation EMAC-apos-02, the CH4 submodel together with the isotopologue extension is applied. This includes isotopologues concerning both, carbon, and hydrogen isotopes. The submodel is set up with the KIEs as introduced in Table 2.4.

The comprehensive interactive chemistry simulation EMAC-apos-03 is conducted with MECCA-TAG concerning hydrogen isotopologues, only. This configuration is chosen to investigate the pathways of deuterium from the source towards the end-product of CH_3D, i.e. HDO. This requires to include KIEs for the intermediates, too, as well as to apply adequate branching ratios and isotope transfer probabilities.

The inclusion of carbon isotopologues with MECCA-TAG is omitted due to the fact that MECCA-TAG introduces additionally nearly twice as many chemical reactions and species as already included in the basic chemical mechanism. To maintain a computational efficient simulation, the CH4 submodel is additionally applied to simulate the carbon related CH_4 isotopologues. In this case, the `CH4_fx` tracer, acting as the master tracer for the CH_4 isotopologues in the CH4 submodel, is directly set to the CH_4 tracer in EMAC to ensure an identical overall CH_4 budget. The CH4 submodel also uses directly the on-line calculated OH, $O(^1D)$ and Cl distribution from MECCA.

The interactive chemistry includes an extensive set of chemical reactions and species. MECCA-TAG basically doubles the chemical mechanism of MECCA. However, most of the corresponding KIEs and isotope branching ratios are still unknown. In that case, solely stochastic branching is assumed. Additional to that, it is assumed that in reactions with the deuterated hydroxyl radical (OD), the deuterium stays connected to the oxygen and either forms HDO or deuterated hydroperoxyl (DO_2). The few KIEs based on laboratory measurements used in the simulations are listed in Table 2.5. Specifically for the reaction of $CH_3O + O_2 \longrightarrow HO_2 + HCHO$ the following temperature dependent branching from Hu et al. [2012] is applied:

$$CH_2DO + O_2 \xrightarrow{k_a} HCDO + HO_2 \tag{R 6.13}$$

$$\xrightarrow{k_b} HCHO + DO_2 \tag{R 6.14}$$
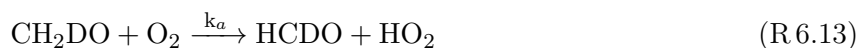
with

$$\frac{k_a}{k_b} = \exp(\frac{416.0}{T} + 0.52) \ . \tag{6.1}$$

with T being the temperature in [K].

Table 6.1: The isotopic signature of the emission sources as used in the model simulations with EMAC. All δ-values and ranges are given in [‰].

	$\delta^{13}C(CH_4)$			$\delta D(CH_4)$		
Natural sources	δ-value	$\pm$	references	δ-value	$\pm$	references
wetlands	-59.4	1.5	1,2,3,4,6	-336.2	23.8	3,4,6
other						
wildanimals	-61.5	0.5	1	-319.0	/	5
termites	-63.3	6.5	1,2,3	-390.0	35.5	3
volcanoes	-40.9	0.9	1,2	-253.4	53.4	3,7
ocean (hydrates)	-59.0	1.0	1,2,3	-220.0	/	3
Anthropogenic sources						
anthropogenic (collective)	-46.8	10.3	3,4,6,8	-223.5	23.5	3,4,6
rice	-63.0	1.0	1,2,3,4,6	-324.3	5.5	3,4,6
biomass burning	-23.9	1.6	1,2,3,4,6	-213.0	7.5	3,4,6

references: [1] [Monteil et al., 2011] [2] [Fletcher et al., 2004] [3] [Whiticar and Schaefer, 2007] [4] [Snover and Quay, 2000] [5] [Rigby et al., 2012] [6] [Quay et al., 1999] [7] [Kiyosu, 1983] [8] [Zazzeri et al., 2015]

Additionally, for completeness, some CH_4 branching ratios have been estimated by Pieterse et al. [2009], who uses a method based on an independent bond approximation. These results are, however, not included in the simulations at the moment, as they represent model results and have not yet been verified by laboratory measurements. In future, sensitivity simulations could be performed to investigate the robustness of these estimates.

6.1.2 Signatures of Emission Sources

As introduced in Chapter 2, sources emit CH_4 isotopologues in a specific ratio, the so called isotopic signature of the emission source. The signature depends thereby on the involved processes producing CH_4 and especially differ between biogenic and fossil sources, as wetlands or coal mines, respectively (see Fig. 2.3).

The applied emission inventory in the presented simulations in this chapter is the a posteriori inventory derived in the chapter before. The specific isotopic signatures of the emission sources used in the model are listed in Table 6.1. They are mostly identical to the isotopic signatures introduced in Section 2.3.2. However, due to the merging of the anthropogenic emission types ruminants, landfills, coal and natural gas to one auxiliary anthropogenic class, the corresponding isotopic signature is a combination of those types as well. Unfortunately, these emission types are in different process categories. Ruminants and landfills are biogenic, and coal and natural gas are fossil sources. These categories exhibit quite distinct isotopic signatures, thus are mixed in the current simulation set-up. This, of course, causes additional uncertainties in the ranges of the isotopic signatures, which are especially high for fossil fuels as stated by Zazzeri et al. [2015].

Nevertheless, the presented set-up is expected to suffice for a first evaluation of the novel model developments. In future simulations an appropriate emission inventory is desirable, which distinguishes between biogenic and fossil sources.
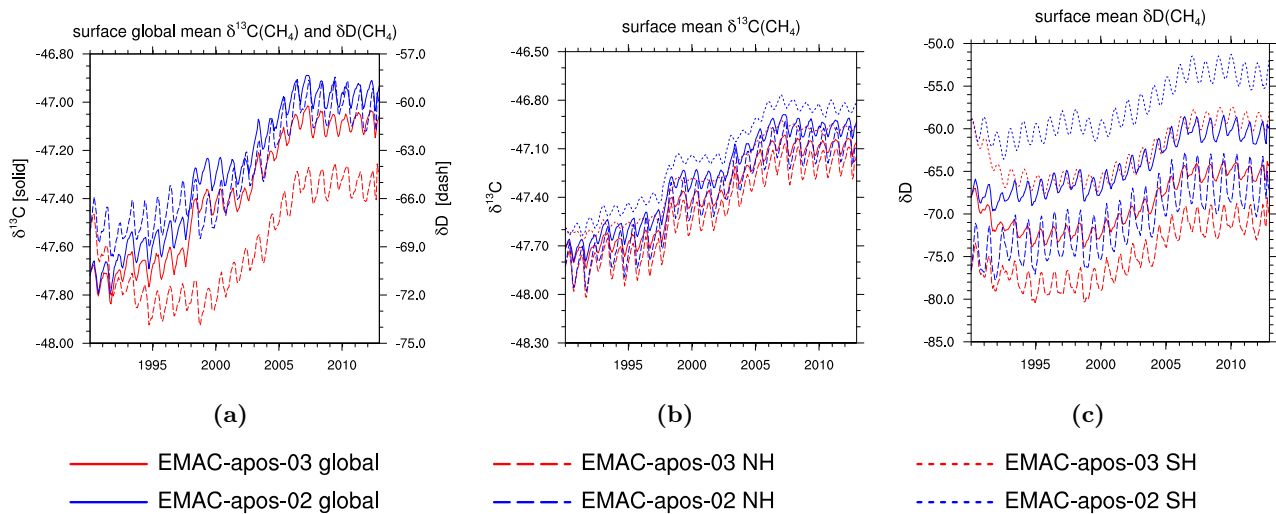
Figure 6.1: (a) Surface global mean δ^{13}C(CH$_4$) (solid) and δD(CH$_4$) (dashed) of the simulations EMAC-apos-02 (blue) and EMAC-apos-03 (red). (b) Surface mean δ^{13}C(CH$_4$) of the simulations EMAC-apos-02 (blue) and EMAC-apos-03 (red) separated into global (solid), NH (dashed) and SH (dotted). (c) The same as (b) just for δD(CH$_4$). All presented δ-values are in [‰].

6.2   CH$_3$D and ^{13}CH$_4$ in the Atmosphere

To start with the evaluation of the simulation with respect to the representation of the isotopic content, the overall distribution of CH$_3$D and ^{13}CH$_4$ is presented. The study includes additionally the comparison of the simulations EMAC-apos-02 and EMAC-apos-03 with respect to their simulation of CH$_4$ isotopologues. This comprises the analysis with respect to the different methods to simulate D-carrying isotopologues using the CH4 submodel and MECCA-TAG, respectively.

6.2.1   Surface Mean Isotopic Composition

The simulated global mean isotopic composition shown in Fig. 6.1a shows two main aspects:

- Between 1990 and 2012 both δ-values increase, hence CH$_4$ gets isotopically enriched. This can partly be attributed to increasing OH concentrations and to an increase in the isotopically relatively heavy anthropogenic emission in this time period. Moreover, δD(CH$_4$) exhibits an overall larger variation in both, annual variation, and trend compared to δ^{13}C(CH$_4$). This is self-consistent considering the larger range of δ-values in CH$_4$ emissions concerning δD(CH$_4$) (approx. -420 to -100‰) compared to δ^{13}C(CH$_4$) (approx. -70 to -22‰).

- By design, both simulations start with identical initial isotopic conditions. However, EMAC-apos-03 shows a decrease in the first years, especially for δD(CH$_4$). This is potentially caused by a too high initial condition.

Overall, the isotopic composition in EMAC-apos-02 is isotopically enriched compared to EMAC-apos-03 (see Fig. 6.1a). This agrees well with the reduced sink in EMAC-apos-03, as revealed in the chapter before, which reduces the CH$_4$ mixing ratio and consequently isotopically enriches CH$_4$ due to fractionation processes in the sink reactions. Furthermore, while the trend in δ^{13}C(CH$_4$) from 1990–2012 adds up to 0.79‰ in EMAC-apos-02 and 0.66‰ in EMAC-apos-03, respectively, δD(CH$_4$)

increases by as much as 8.31‰ in EMAC-apos-02 and 3.95‰ in EMAC-apos-03, respectively. The difference between EMAC-apos-02 and EMAC-apos-03 is also larger for δD(CH$_4$) than for δ^{13}C(CH$_4$). Particularly, the averaged difference of EMAC-apos-02 and EMAC-apos-03 (1998–2012) concerning δ^{13}C(CH$_4$) is only 0.12‰, which is almost within the seasonal variation. Nevertheless, the corresponding difference in δD(CH$_4$) is with up to 5.15‰ significant. The stronger isotopic depletion concerning δD(CH$_4$) compared to δ^{13}C(CH$_4$) in EMAC-apos-03 again results from the reduced sink in this simulation. From Table 2.4 it is known that the KIE of the reaction CH$_3$D + OH is to a considerable degree larger than the KIE of ^{13}CH$_4$ + OH (for relevant temperature ranges it is ~ 1.3 for CH$_3$D and 1.0039 for ^{13}CH$_4$). This strong KIE results in an isotopically enriched CH$_4$ with respect to D in EMAC-apos-02 compared to EMAC-apos-03, which is not as evident concerning ^{13}C.

Additionally, it should be noted that the seasonal variations in the isotopic compositions occurs due to varying relative contributions of distinct sources and due to the variable sink. The isotopic signature of the different emission types in the model by design do not vary with time.

Recall that there is an apparent asymmetry between NH and SH concerning OH and regarding CH$_4$ emissions. Therefore, the isotopic composition of the simulation is also compared with respect to the hemispheres (see Fig. 6.1b and 6.1c). Again, δ^{13}C(CH$_4$) values show relatively small variations. Additionally, the NH is in both signatures isotopically depleted. This seems to contradict the larger OH concentration in the NH. However, most and largest, isotopically light emissions as wetlands and rice are located in the NH, while isotopical heavy sources like biomass burning are mostly located in the SH.

Overall, the surface δ^{13}C(CH$_4$) values compare well with the global estimate of Quay et al. [1999] being -47.3 ± 0.04‰, also concerning the range between NH and SH. The δD(CH$_4$) values in the presented simulations, however, are isotopically too heavy compared to the estimate from Quay et al. [1999] being -86 ± 3‰. EMAC-apos-03 compares better than EMAC-apos-02, nevertheless, both exhibit a too large north-south gradient. This gives a first indication that δ^{13}C(CH$_4$) seems to be well represented in the simulations, while the δD signatures of the CH$_4$ sources need further adjustments.

6.2.2 Vertical Profile of δ-Composition

Besides the surface isotopic distribution, which is mostly influenced by the nearby emission signatures, the vertical profile gives further information about the fractionation processes through the elevation of CH$_4$ and the thereby continuously occurring sink processes.

In Fig. 6.2 again EMAC-apos-02 and EMAC-apos-03 are compared, this time, with respect to their zonal mean profile. It is already shown in the chapter before that the master CH$_4$ tracer in EMAC-apos-02 is by about 50 nmol mol^{-1} lower than in EMAC-apos-03 in the troposphere. In the upper stratosphere above 30 hPa, however, it is the other way round. The δ^{13}C(CH$_4$) value shows overall very small variations in the troposphere and CH$_4$ gets isotopically enriched with altitude. Moreover, the differences between the two simulations are small (less than 0.1‰) and are even smaller concerning the north-south gradient, which is also shown in the section before with the results on surface level. Towards higher altitudes in the stratosphere the difference between these two simulations increases. Nevertheless, in the stratosphere, where the simulated CH$_4$ in EMAC-apos-02 is larger than in EMAC-apos-03, the difference is considerably smaller than in other regions of the stratosphere. Still, the apparent large differences in the stratosphere indicate that there are additional chemical feedbacks of the interactive chemistry regarding the CH$_4$ fluxes on the stratospheric sink species, such as O(^{1}D) and Cl.
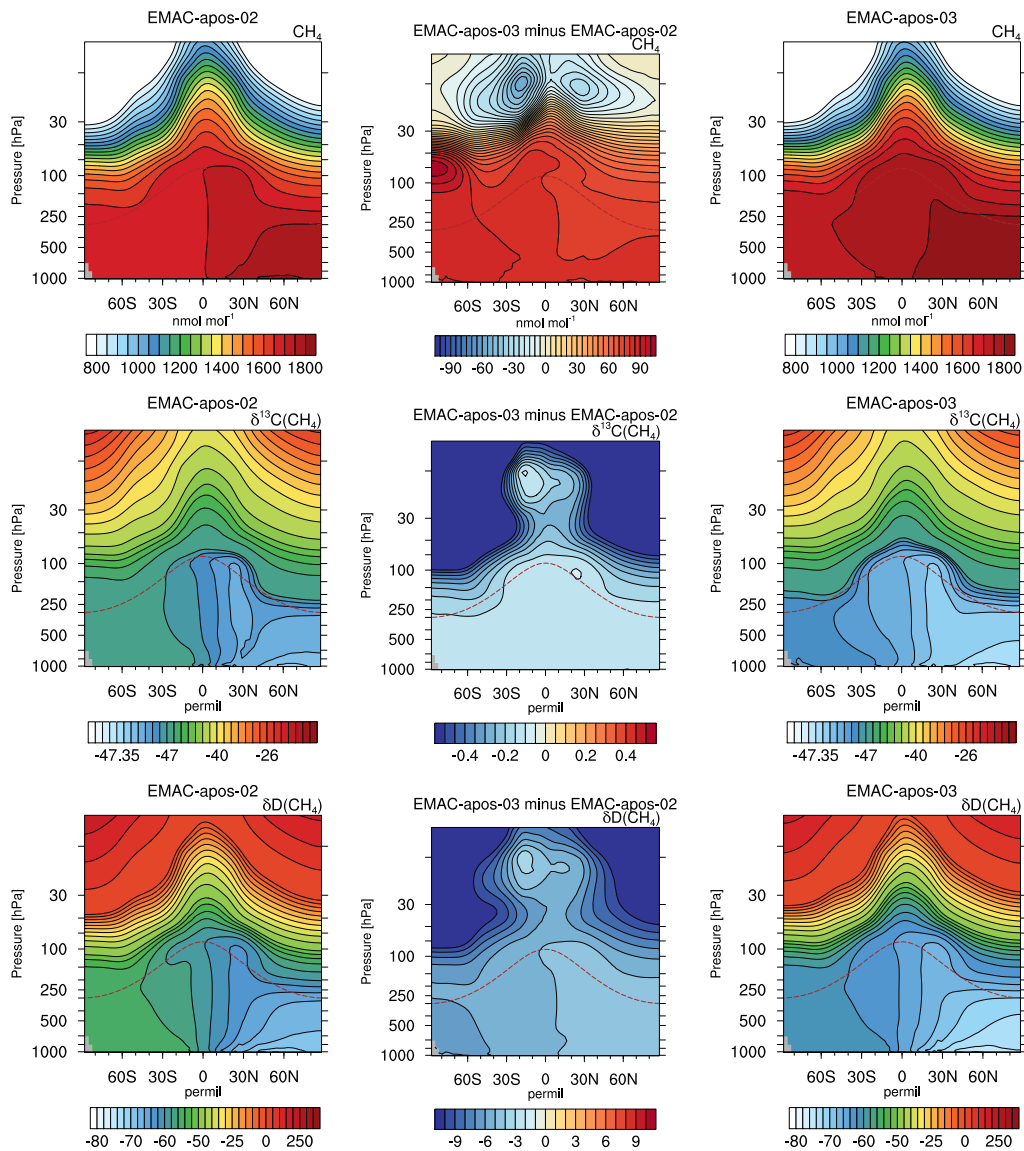
Figure 6.2: Zonal mean climatologies of 2000–2009 for CH_4 in [nmol mol^{-1}] (upper), $\delta^{13}C(CH_4)$ in [‰] (middle) and $\delta D(CH_4)$ in [‰] (lower) of the simulations EMAC-apos-02 (left) and EMAC-apos-03 (right). The middle column shows the differences between EMAC-apos-03 and EMAC-apos-02. The dashed brown lines indicate the height of the climatological tropopause.

The overall zonal mean profile of $\delta D(CH_4)$ is basically similar to $\delta^{13}C(CH_4)$, i.e., lower δ-values in the NH and an isotopical enrichment towards the stratosphere. Considering the difference of the two simulations it becomes apparent that the north-south gradient is again stronger in EMAC-apos-02. Furthermore, $\delta D(CH_4)$ also exhibits relatively low values in the tropical upper stratosphere, as is also detected in $\delta^{13}C(CH_4)$.

During the summer months in the NH the δ-values reveal a depletion in the northern tropics, while the winter months do not show such a particular depletion or enrichment (see Fig. 6.3). The reason for this is strong convective transport over the continents and enhanced emissions from light biogenic emission sources in the hot season over India and south-east Asia. The OH concentration maximum is shifted towards the summer hemisphere (see Fig. F.1 in the Appendix F), yet, fractionation effects
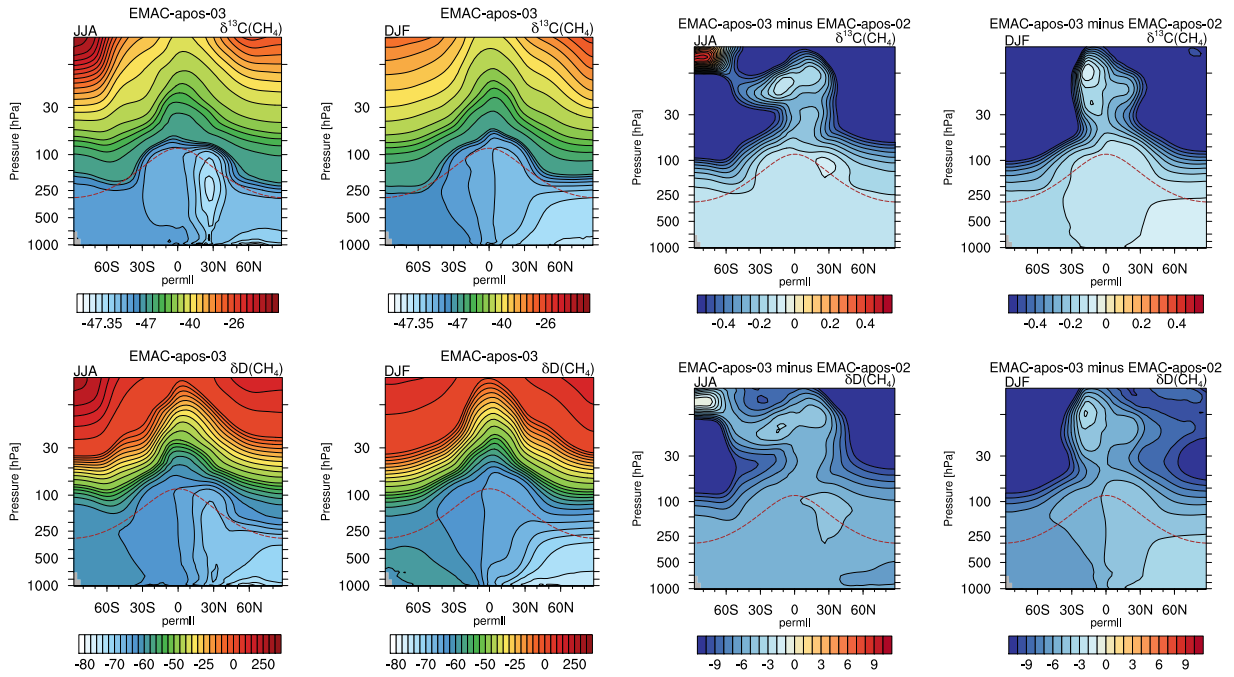
Figure 6.3: Columns 1 and 2 show the seasonal zonal mean climatology of 2000–2009 for $\delta^{13}C(CH_4)$ in [‰] (upper) and $\delta D(CH_4)$ in [‰] (lower) of EMAC-apos-03. Columns 3 and 4 show the seasonal zonal mean climatology difference for $\delta^{13}C(CH_4)$ in [‰] (upper) and $\delta D(CH_4)$ in [‰] (lower) of EMAC-apos-03 minus EMAC-apos-02. The dashed brown lines indicate the height of the climatological tropopause.

do not completely counteract the depleted areas in the zonal mean profile. From Fig. 6.3 it is also concluded that the difference in the north-south gradient of EMAC-apos-02 and EMAC-apos-03 varies with season. While basically no enhanced gradient is visible for $\delta^{13}C(CH_4)$ in June, July, and August (JJA), such a gradient becomes apparent in the NH winter months (DJF). In $\delta D(CH_4)$ the gradient of the difference even reverses. Since emissions and meteorology are identical in both simulations, these variations can solely be attributed to the variations in the OH distribution.

6.3 Evaluation of Methane Isotopologues with Observations

This section addresses the evaluation of the model simulation with atmospheric observations. Available data is provided by airborne and ground based, as well as balloon-borne observations. Especially the latter have the advantage that the observed gradients can be used to evaluate the simulation results at stratospheric altitudes as well.

6.3.1 Surface Sampling Sites

To start with the evaluation of the simulation results, isotopic observations from NOAA/ESRL sampling sites [White et al., 2016, 2017] are compared to the surface mixing ratios and δ-values of the simulations. For the comparison a climatological mean of 2000–2009 is used since this time period is represented by most of the stations and the adjustment of the simulated isotopic composition from the initial condition (as visible especially in EMAC-apos-03) has passed.

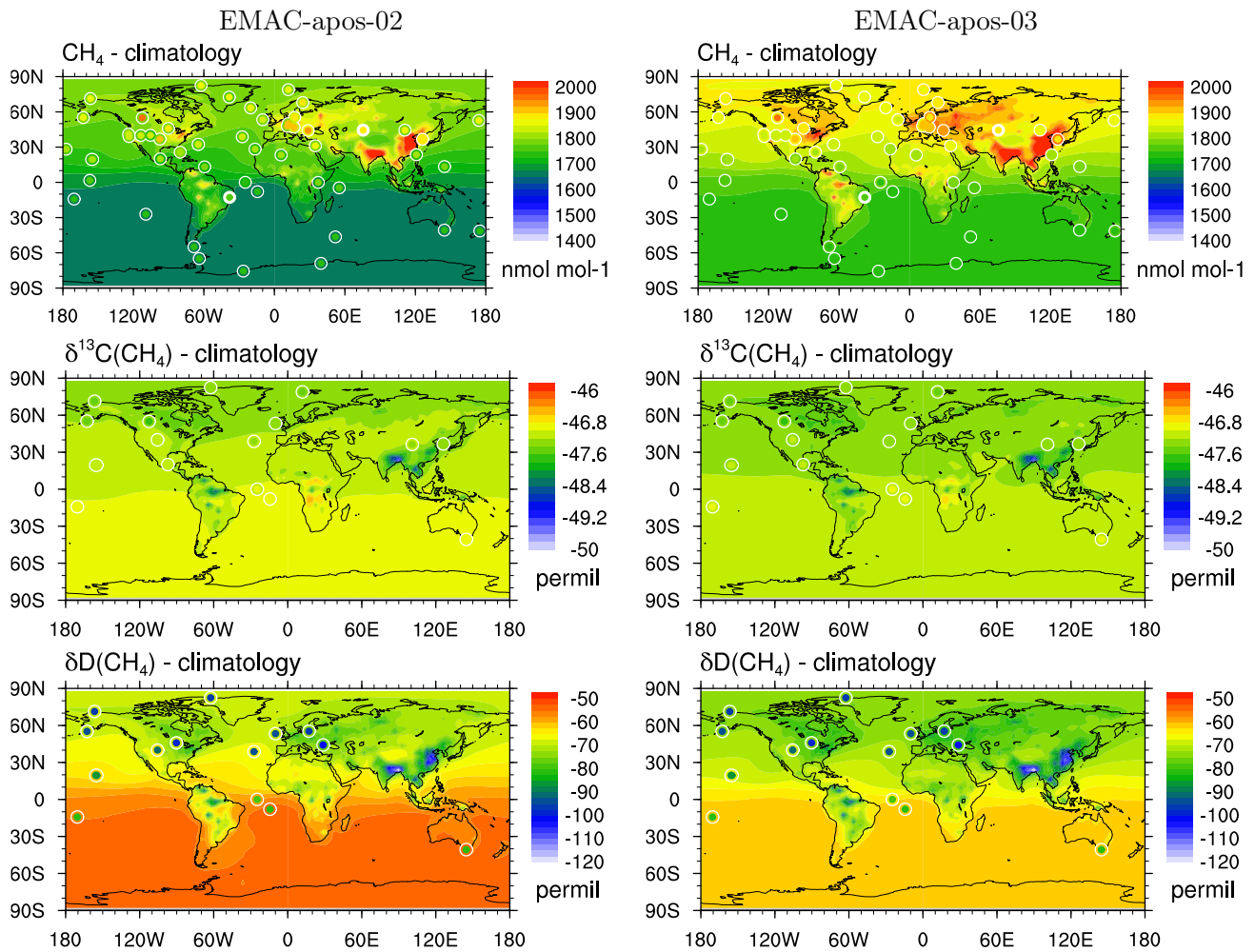The surface mixing ratio of CH_4 and the corresponding δ-values are depicted in Fig. 6.4. First

Figure 6.4: Surface climatology of 2000–2009 of CH_4 mixing ratio in [nmol mol^{-1}] (upper), $\delta^{13}C(CH_4)$ in [‰] (middle) and $\delta D(CH_4)$ in [‰] (lower). The left column shows results of EMAC-apos-02 and the right column those from EMAC-apos-03. The colored dots indicate the surface observations from NOAA/ESRL. The circles around the dots are the value of the simulation at the specific sampling height of the observation (in order to account for sub-grid orographic differences between simulation and observation).
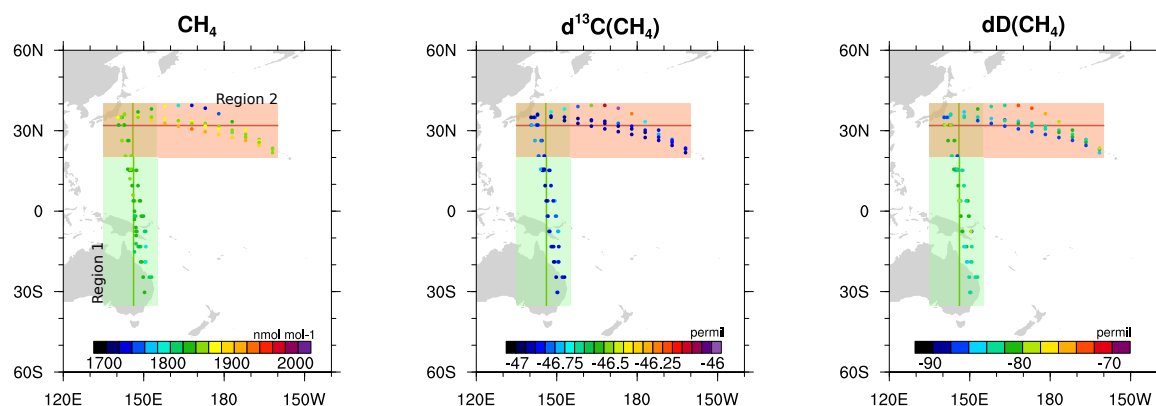
Figure 6.5: Observations provided by the CONTRAIL project [Umezawa et al., 2012]. The green shaded area indicates region 1, and the red shaded area indicates region 2.

of all, the overall surface pattern shows that areas with prominently high CH_4 mixing ratios have a quite low isotopic signature, as being evident in India and south-east Asia. However, these regions are also mostly influenced by light biogenic emissions from rice cultivation. The same accounts for regions influenced by wetland emissions as in South America, Canada and Russia. Notably enriched signatures are for example evident in Central Africa, which are caused by isotopically heavy CH_4 emissions from pyrogenic sources (biomass burning).

From the previous evaluation of the emission inventory it is no surprise that EMAC-apos-03 agrees well with the stations regarding the CH_4 mixing ratio. Interesting is that the $\delta^{13}C(CH_4)$ values are slightly better represented in EMAC-apos-02 compared to EMAC-apos-03, whereas the agreement is overall quite well in both simulations. This suggests that the emission signatures are a bit too low for $^{13}CH_4$ in connection with the OH concentration in EMAC-apos-03. On the other hand, in case of $\delta D(CH_4)$, EMAC-apos-03 agrees better, however, is still isotopically enriched compared to the station samples. This indicates that the chosen emission signatures for CH_3D are too heavy.

Unfortunately, observations of the isotopic signal at surface level are still very sparse, especially for deuterium. Areas where a lot of spatial variations are visible in the simulations, as in Asia and South America, currently lack CH_3D observations completely. Emerging satellite measurements of CH_4 isotopologues, as presented by Buzan et al. [2016], are promising to fill these gaps in the global coverage in future.

6.3.2 Airborne Observations

During the Comprehensive Observation Network for TRace gases by AIrLiner (CONTRAIL) project, atmospheric air samples were taken with an Automatic air Sampling Equipment (ASE) mounted on a commercial aircraft [Umezawa et al., 2012]. These air samples were later measured concerning the isotopic composition of CH_4 using a gas chromatography system and a flame ionization detector. The here presented sampling data comprise several flights between 2006 and 2010, with each flight providing up to 12 air samples.

The presented flights are seperated into two regions, as depicted in Fig. 6.5. The first region (green) indicates the flights on a north-south route, bound from Narita airport (Japan) to Sydney, Brisbane (Australia) or Guam, and the second region (red) represents those flights on an east-west route, bound from Narita to Honolulu (Hawaii).

Especially the first region provides the opportunity to investigate the representation of the merid-
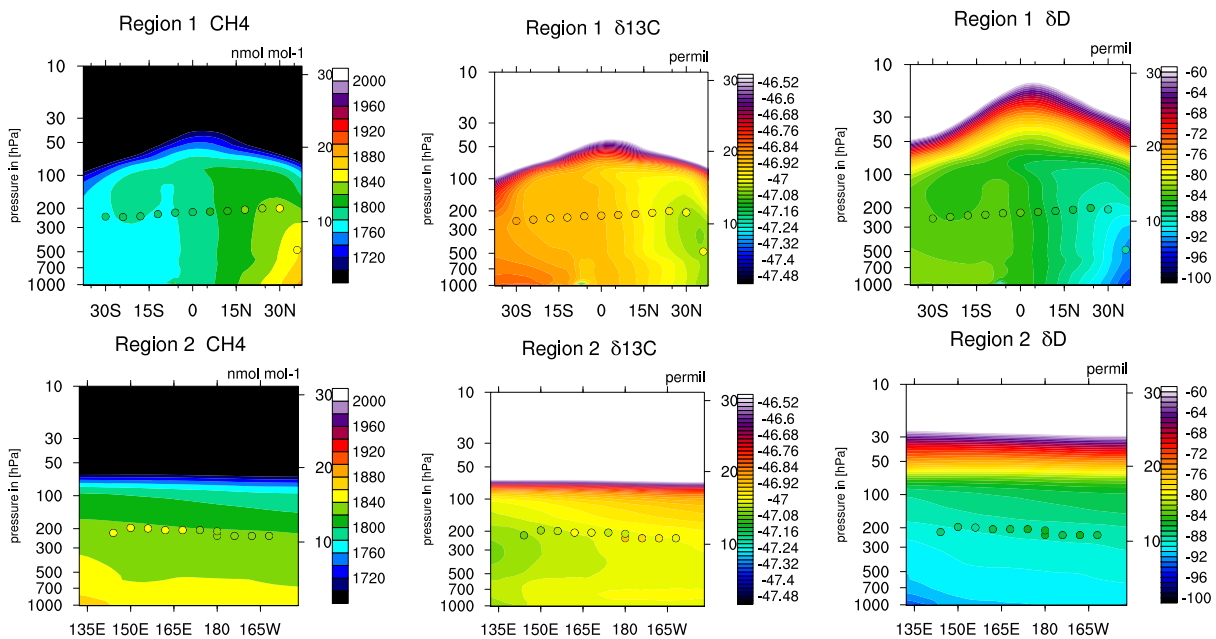
Figure 6.6: The background shows the mean vertical profile of simulation EMAC-apos-03 of the regions as presented in Fig. 6.5 derived from a climatology of 2006–2010. The simulation results of CH_4, $\delta^{13}C(CH_4)$ and $\delta D(CH_4)$ are adjusted by 25.0 nmol mol^{-1}, 0.11‰ and -24.0‰, respectively. The colored markers indicate the mean airborne observations of the CONTRAIL project.

ional gradient and the north-south imbalance in the δ-values in the model as it nicely spans over the tropics (40° S−40° N). Simulation results and the airborne observations in this region are depicted in the upper panels of Fig. 6.6. The background vertical profile of the simulation EMAC-apos-03 is a climatological mean of the years 2006–2010 and is averaged over the longitudinal range of the observations. The values CH_4, $\delta^{13}C(CH_4)$ and $\delta D(CH_4)$ of the simulation are adjusted by 25.0 nmol mol^{-1}, 0.11‰ and -24.0‰, respectively, for better comparison of the meridional gradient. The observations of the multiple flights are averaged and are indicated by the colored markers in the foreground. The lower panels display the longitudinal profiles (i.e., region 2), which show a nearly uniform vertical gradient, except for the eastern end of the displayed region, where CH_4 mixing ratios increase (indicated by observation and simulation). In this area the observed values for $\delta^{13}C(CH_4)$ are lower, which is captured quite well by the simulation.

Additional to the vertical profiles, the agreement between observation and simulation is quantifiable in Fig. 6.7, where green dots indicate the observations. The dark green line indicates the mean of the observations and the shaded green area is the corresponding standard deviation. Simulated values are included as the red and blue dots respectively. Overall, the CH_4 mixing ratio is underestimated by the simulations EMAC-apos-02 and EMAC-apos-03 by about 110 nmol mol^{-1} and 25 nmol mol^{-1}, respectively (see Fig. 6.7a). Indeed the values of EMAC-apos-03 are within the observed standard deviation of the observations, which again confirms the good representation of CH_4 in this simulation. As mentioned before, $\delta^{13}C(CH_4)$ in simulation EMAC-apos-02 is in better agreement with the observations than EMAC-apos-03 (bias of 0.11‰, see Fig. 6.7b). Nevertheless, the values from EMAC-apos-03 are still within the single standard deviation. For $\delta D(CH_4)$ both simulations show too high values, i.e. a bias of -29.0‰ and -24.0‰ for EMAC-apos-02 and EMAC-apos-03, respectively.

It is apparent from the shown results that the meridional gradient in the simulations concerning CH_4 and both isotopic signatures are well represented, although the absolute values differ. This indicates
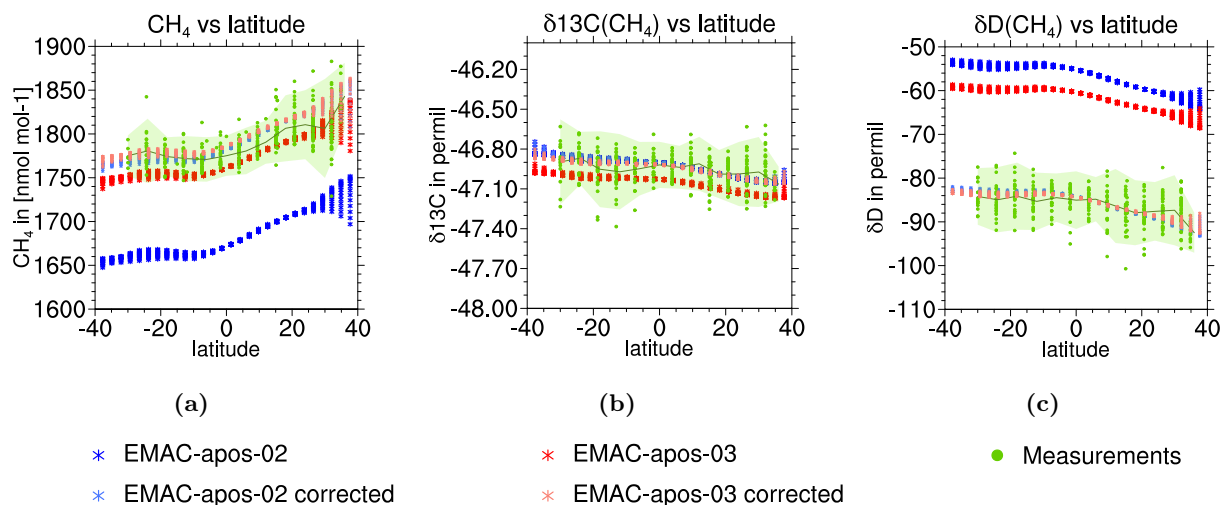
Figure 6.7: Comparison of airborne observations (green) in the meridionally aligned region 1 with simulation data from EMAC-apos-02 (blue) and EMAC-apos-03 (red). The lighter red and blue colored markers indicate the de-biased simulation data for the direct comparison to the meridional gradient of the observations. The dark green line indicates the mean of the observations with the greenish shaded area being the corresponding single standard deviation.

that the implemented KIE in the model is reasonable and that adjustments to the signatures of the emission inventory are required.

6.3.3 Balloon Borne Observations

The presented airborne observations are solely able to infer tropospheric chemical compositions. The high-altitude range of balloon borne observations enables to investigate the stratospheric isotopic signatures, as well.

The observational data is provided by Röckmann et al. [2011] and was obtained by altogether 13 balloon flights between 1987 and 2003 at four launch stations: Hyderabab in India (HYD), Aire sur l'Adour in France (ASA), Gap in France (GAP) and Kiruna in Sweden (KIR) (see Fig. 6.8). The balloon-borne high-altitude air samples are obtained up to 10 hPa (35 km) and were later examined with respect to CH_4 mixing ratios as well as its isotopic composition concerning $^{13}CH_4$ and CH_3D using a high precision continuous flow isotope ratio mass spectrometer [Brass and Röckmann, 2010].

The observations shown in Fig. 6.9 indicate two features:

- First, while CH_4 gets reduced towards higher altitudes, the isotopic content gets enriched (both, in $\delta^{13}C(CH_4)$ and $\delta D(CH_4)$). This occurs due to fractionation processes, which prefer lighter isotopologues in the sink reactions over heavier isotopologues.

- Secondly, again, a meridional gradient is visible. Polar regions tend to have less CH_4 than tropical regions, indicating to some extent the older age of the polar air masses. Consequently, polar regions are isotopically enriched compared to regions at mid and low latitudes.

The balloon-borne observations are compared to the simulations in Fig. 6.10 at pressure levels from 200 hPa to 10 hPa and separated into polar, mid-latitude and tropical regions. For the comparison, the monthly averaged data of the simulation is sampled at the specific year, month and location of the
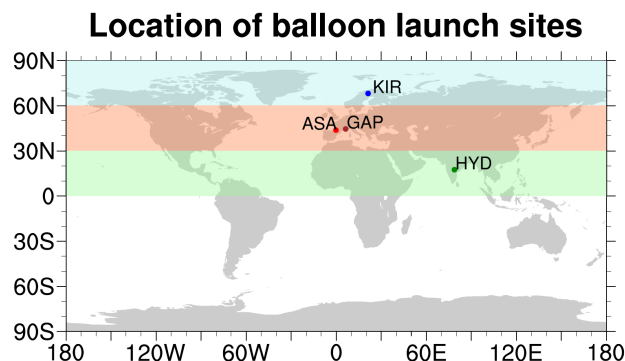
Figure 6.8: Balloon launch sites: Hyderabad, India (HYD, 17.5° N, 78.60° E), Kiruna, Sweden (KIR, 67.9° N, 21.10° E), Aire sur l'Adour, France (ASA, 43.70° N, −0.30° E) and Gap, France (GAP, 44.44° N, 56.14 E). The colored shaded regions indicate the polar region (blue), the mid-latitudes (red) and tropics (green).

observation and interpolated from model levels to pressure levels. The plots in Fig. 6.10 further show the single standard deviation of the observations by the grey shaded areas and the standard deviation of all vertical profiles in the corresponding latitudinal region of the simulations as the shaded area in the color of the respective simulation.

In the mid-latitudes and the tropics the vertical gradient of all three variables is well represented. However, the simulations in the polar region show a considerably weaker vertical gradient. Most of the observations in Kiruna are performed during arctic winter with an apparent arctic vortex or during the final warming [Röckmann et al., 2011]. The age of air in the polar region in EMAC simulations is about two years shorter than observation based estimates by the Michelson Interferometer for Passive Atmospheric Sounding (MIPAS) suggest [Dietmüller et al., 2017]. This shorter residence time in stratospheric and mesospheric regions, where CH_4 lifetime is very short, yields simulated air parcels, which are not as reduced in CH_4 as the observations indicate. This further results in isotopic signatures, which are not as enriched as in the observed air samples. This potentially explains the evident deviation of the simulation results from the observations. However, a confirmation is still needed, which potentially requires to integrate the CH_4 loss along the stratospheric trajectory of an air parcel reaching the polar region. This is beyond the scope of the current study. Nevertheless, in further studies, the influence of the BDC onto CH_4 and its isotopic composition in the polar region should be investigated in detail.

Additional to the underestimated stratospheric residence time, the single standard deviation of the simulated profiles (blue and red shaded areas in the figures) within the sampling site region (i.e., polar, mid-latitudes, tropics) and the sampling time period 1990–2003 is partly overlapping the single standard deviation of the observations, which indicates that the profiles are not all statistically distinguishable. It is apparent from the minimum and maximum values of the simulation in the specific region and time period (see Appendix Fig. F.12) that large local and temporal variations are expected in the polar region. Furthermore, the simulation shows in other parts of the polar region as low mixing ratios and as enriched isotopic signatures as the observations indicate. Hence the model is able to represent the overall CH_4 depletion in the polar vortex but it is possible that the local conditions at Kiruna, which is located at the edge of the polar vortex, are not sufficiently captured by the simulation.

At mid-latitudes, the mixing ratio of CH_4 is overestimated by EMAC-apos-03. EMAC-apos-02, however, despite its deficiencies observed in the troposphere, agrees better with the observation.
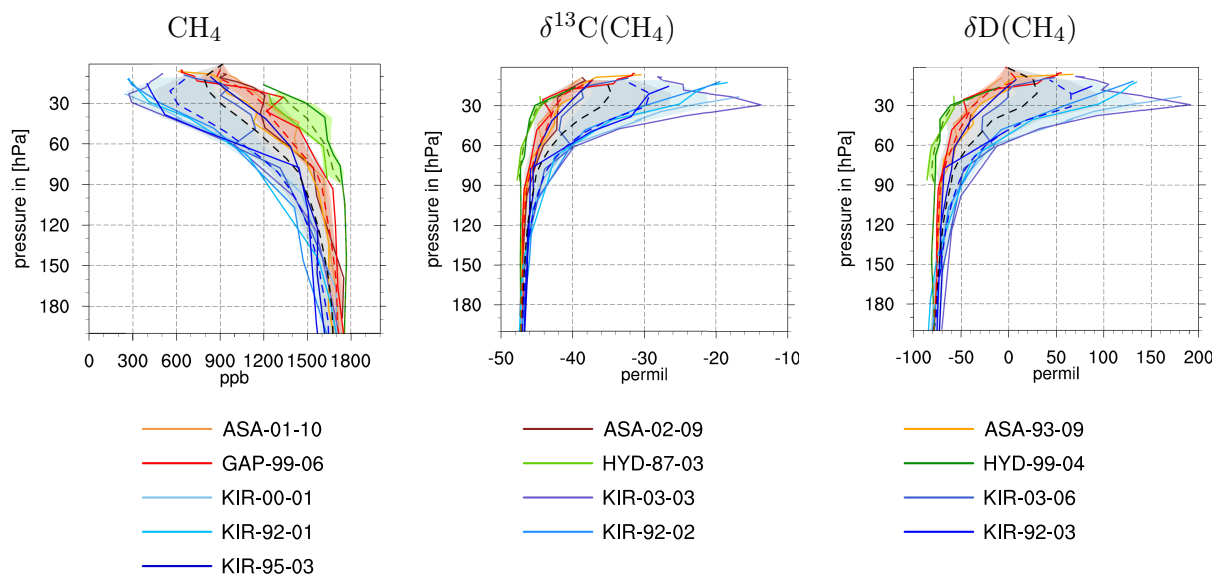
Figure 6.9: Balloon borne observations from Röckmann et al. [2011]. Bluish colors indicate the station at Kiruna (polar region), reddish colors Aire sur l'Adour and Gap (mid-latitudes) and greenish colors Hyderabad (tropical region).

In the mid-latitudes simulated $\delta D(CH_4)$ and $\delta^{13}C(CH_4)$ also agree very well with the observations, although $\delta D(CH_4)$ is slightly overestimated in the lower stratosphere. In the tropics the vertical gradients are also represented by the simulations. However, in this region only two balloon flights are available, which makes the data basis rather sparse.

Comparing the different regions it is apparent that the simulations, next to the vertical gradient, also represent the meridional shift of the profiles (lower CH_4 values, but isotopically enriched towards the polar region). This is evident although the vertical gradient at the polar region is generally underestimated in the simulations.

6.4 HDO in the Stratosphere

The current study aims at a full comprehension of the life-cycle of CH_4. This also includes its radiative active and climate impacting oxidation products, which is in particular stratospheric water vapor (SWV). Similar to the analysis of CH_4 isotopologues it is proposed that the isotopic composition of H_2O is able to provide additional insight into the processes forming the H_2O distribution including physical processes and transport, as well as its chemical source [Eichinger et al., 2015a].

The abundance of HDO in the stratosphere is partly dependent on the transport through the tropopause and hence on the present abundance in the troposphere. The latter is in turn dependent on the physical fractionation processes in the troposphere. Furthermore, stratospheric HDO is influenced by the kinetic (i.e. chemical) isotope fractionation in the stratosphere during the oxidation of CH_3D and subsequent onward reactions of D carrying species. Note that kinetic isotopic fractionation in the troposphere is in comparison to the present physical isotopic fractionation negligible, since tendencies of the latter one exceed the kinetic rates by orders of magnitude.

In the present section an overview of the current representation of HDO in EMAC is given and it is evaluated how the developments of the work at hand are contributing to this. Particularly, results of the simulation using the simplified CH_4 chemistry using the empirical formula proposed by Eichinger
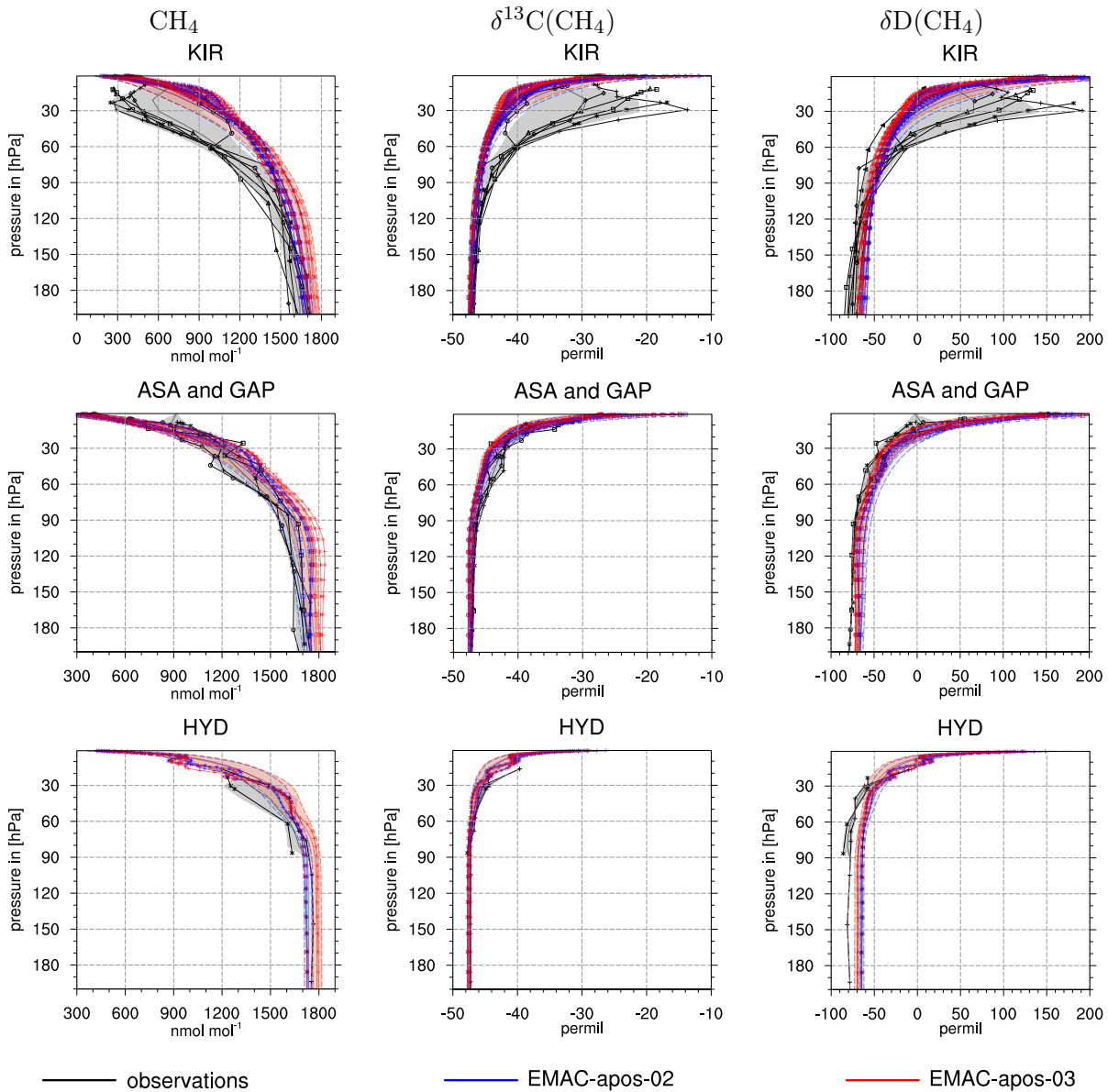
Figure 6.10: Balloon borne observations from Röckmann et al. [2011] (black) together with simu-
lation results from EMAC-apos-02 (blue) and EMAC-apos-03 (red). The rows of panels from top to
bottom present balloon launches in the polar region in Kiruna in Sweden (KIR), in the mid-latitude
region in Aire sur l'Adour in France (ASA) and Gap in France (GAP), and in the tropical region in
Hyderabab in India (HYD). The profiles of the simulations are taken from monthly averaged data in
the specific year, month and at the location of the observation. For observations before the simulation
start, the simulated year 1990 is used. Shaded areas indicate the single standard deviation of the
observations (grey) and the simulations (blue, and red, respectively) concerning the variations within
the specific latitudinal region and the years 1990–2003.

et al. [2015a] are compared to results of the the interactive chemistry with MECCA-TAG.

6.4.1 The Role of Background $\delta D(H_2)$ for $\delta D(H_2O)$

Oxidation of CH_3D produces a certain amount of HDO. However, some of the D in CH_3D becomes part of HD and therefore isotopically enriches the H_2 composition [Rahn et al., 2003, Röckmann et al., 2003]. In this context, in the simplified chemistry as applied in EMAC-apos-02, it is assumed that the production of HDO from CH_3D oxidation follows the function 3.3 introduced in Chapter 3. This function accounts for the D which is transferred to HD instead of HDO. However, it does not include additional fractionation effects during the formation of HDO by HD, which is also partly produced at the surface and transported into the stratosphere [Eichinger et al., 2015a].

In the interactive chemistry set-up with MECCA-TAG the intermediates between CH_3D, HD and HDO are explicitly simulated. This naturally accounts for the D passing from CH_3D into HD instead to HDO. However, in contrast to the simplified simulations the delta value concerning D of H_2O ($\delta D(H_2O)$) in the comprehensive chemistry set-up additionally relies on the background delta value concerning D of H_2 ($\delta D(H_2)$), since HD produced in the troposphere potentially enters the stratosphere and oxidizes there. It is therefore in addition to CH_3D essential to accurately simulate HD, which is produced by surface emissions, but is also reduced by soil-loss. This soil-loss of H_2 plays a decisive role for the atmospheric content of H_2 and also shows a strong isotopic fractionation [Rhee et al., 2006, Chen et al., 2015]. This fractionation in the soil-loss explains the deuterium enriched atmospheric H_2 with $\delta D(H_2)$ of about 130‰ [Gerst and Quay, 2001, Rahn et al., 2003, Rice et al., 2010], despite the highly depleted emission sources of H_2 (e.g. fossil fuel combustion -270‰ [Rahn et al., 2002b], biogenic N_2 fixation -700‰ [Rahn et al., 2002a], biomass burning -290‰ [Gerst and Quay, 2001]).

To take the soil sink processes into account, the simulations with EMAC use a predefined LBC for H_2 (similar to the LBC of CH_4 in the ESCiMo simulations). The tracer of H_2 is nudged to the predefined values with a relaxation time of 3 hours. The fractionation of the soil sink is not explicitly parameterized in the model, hence the H_2 isotopologues, HH and HD, are as well nudged to a lower boundary condition, which is derived from the mixing ratio for the master tracer H_2 to resemble a tropospheric value of 120‰ in the NH and 141‰ in the SH (values are taken from ship cruise observations from Gerst and Quay [2000]).

6.4.2 The $\delta D(H_2O)$ Tape Recorder

By means of observations, Mote et al. [1996] described a so called "tape recorder" signal in the observed tropical SWV. This signal is based on seasonal variations in the mixing ratio of H_2O entering the stratosphere. These parcels of H_2O enriched and depleted air, respectively, are moving upward as the air masses are elevated by the BDC and form a characteristic pattern of alternating H_2O enriched and H_2O depleted air. This tape recorder signal is not only evident in H_2O, but also in HDO as shown by Steinwagner et al. [2010] and Lossow et al. [2011] based on satellite observations. Furthermore, a previous study from Eichinger et al. [2015b] found that the fractionation effects of CH_4 oxidation have a dampening effect on the stratospheric tape recorder signal in $\delta D(H_2O)$ in the upper layers of the stratosphere.

For an evaluation of the HDO representation in EMAC, the two simulations EMAC-apos-02 (simplified CH_4 chemistry) and EMAC-apos-03 (comprehensive interactive chemistry) are analyzed concerning this tape recorder in H_2O as well as its isotopic content. This analysis is similar to investigations of Eichinger et al. [2015b]. However, while Eichinger et al. [2015b] performed model simulations with a simplified CH_4 chemistry only, the present investigations include a simulation with interactive

chemistry simulations as well, which is therefore a particular novelty. In this context, recall that the simplified chemistry is producing H_2O with respect to the assumption that two molecules of H_2O are directly produced by one oxidized CH_4 molecule, while the interactive chemistry also resolves every intermediate and feedback interaction in the CH_4 oxidation chain and potentially differs from the simplified assumption.

Figure 6.11 shows the temporal evolution of the tape recorder signal in the monthly averaged simulation results. The data is further averaged zonally and over the tropics (23° S–23° N). In this figure, in both, EMAC-apos-02, and EMAC-apos-03, the tape recorder signal in H_2O (upper panels) is clearly evident. However, the interactive chemistry is generally dryer than the simulation with the simplified CH_4 chemistry. Viewing the difference of EMAC-apos-02 and EMAC-apos-03 (Fig. 6.11b), it becomes evident that SWV in the humid periods (during boreal summer) is strongly reduced, while the dry periods (in boreal winter) show a smaller discrepancy. Partly, this is explainable by the fact that the temperature in EMAC-apos-02 is about 1–2 K higher in the Upper Troposphere and Lower Stratosphere (UTLS) than in EMAC-apos-03 (see Fig. 6.12). This reduces the H_2O intrusion into the stratosphere in EMAC-apos-03 compared to EMAC-apos-02 since this intrusion is strongly dependent on the cold point temperature [Fueglistaler and Haynes, 2005].

The first two years of simulation are influenced by the initialization. However, the strongly enhanced H_2O mixing ratios in the second half of 1991 are a consequence of the volcanic eruption of the Mt. Pinatubo [Löffler et al., 2016]. The impact of this eruption is included in the interactive chemistry simulation EMAC-apos-03 but not in the simplified set-up in EMAC-apos-02. The volcanic aerosols in EMAC-apos-03 induce a rise of the cold point temperature, which leads to enhanced transport of H_2O into the stratosphere.

Overall, H_2O is reduced in EMAC-apos-03 compared to EMAC-apos-02 and the mixing ratio of HDO is larger in EMAC-apos-03 than in EMAC-apos-02 (see Fig, 6.11e). This consequently leads to a larger $\delta D(H_2O)$ in EMAC-apos-03.

However, interesting again is the volcanic eruption. After the volcanic eruption, the stratosphere of EMAC-apos-03 is both, enriched in H_2O and in HDO, and therefore no particular feature is evident in $\delta D(H_2O)$. More HDO enters together with H_2O the stratosphere due to increased temperatures at the tropopause. Since the $\delta D(H_2O)$ is not affected by the volcanic eruption it seems that this intrusion is not accompanied by prominent isotopic fractionation effects.

From these results it becomes apparent that the interactive chemistry resolves processes controlling the H_2O and HDO mixing ratio, which are not represented by the simplified chemistry. The differences of the chemical set-ups involve two major points, (1) the production of H_2O via CH_4 oxidation and (2) the isotope fractionation effects in the production of HDO. Since the interactive chemistry indicates a dryer stratosphere, it is also possible that the production of H_2O from CH_4 oxidation in the simplified chemistry is overestimated by the assumption of two produced H_2O molecules per oxidized CH_4 molecule, which is investigated further in Chapter 7.

Concerning the second point, recall that the HDO production in the simplified chemistry in EMAC-apos-02 is parameterized by the function 3.3 from Eichinger et al. [2015a], which is empirically derived based on observations from [McCarthy et al., 2004]. Eichinger et al. [2015a] argued that some effects on the formation of HDO are not taken into account by this equation. This includes multiply substituted (clumped) isotopologues and the reaction with OD. Clumped isotopologues are neglected in both presented simulation set-ups. However, OD is indeed included in the interactive chemistry using MECCA-TAG and is a potential candidate to explain the differences between simplified and interactive chemistry. Moreover, also likely is that the resolved HD in the interactive chemistry simulation introduces additional D and consequently enriches the stratosphere. H_2 is not in the focus of the current study, but this suggests that the accurate simulation of HD in the troposphere is an important
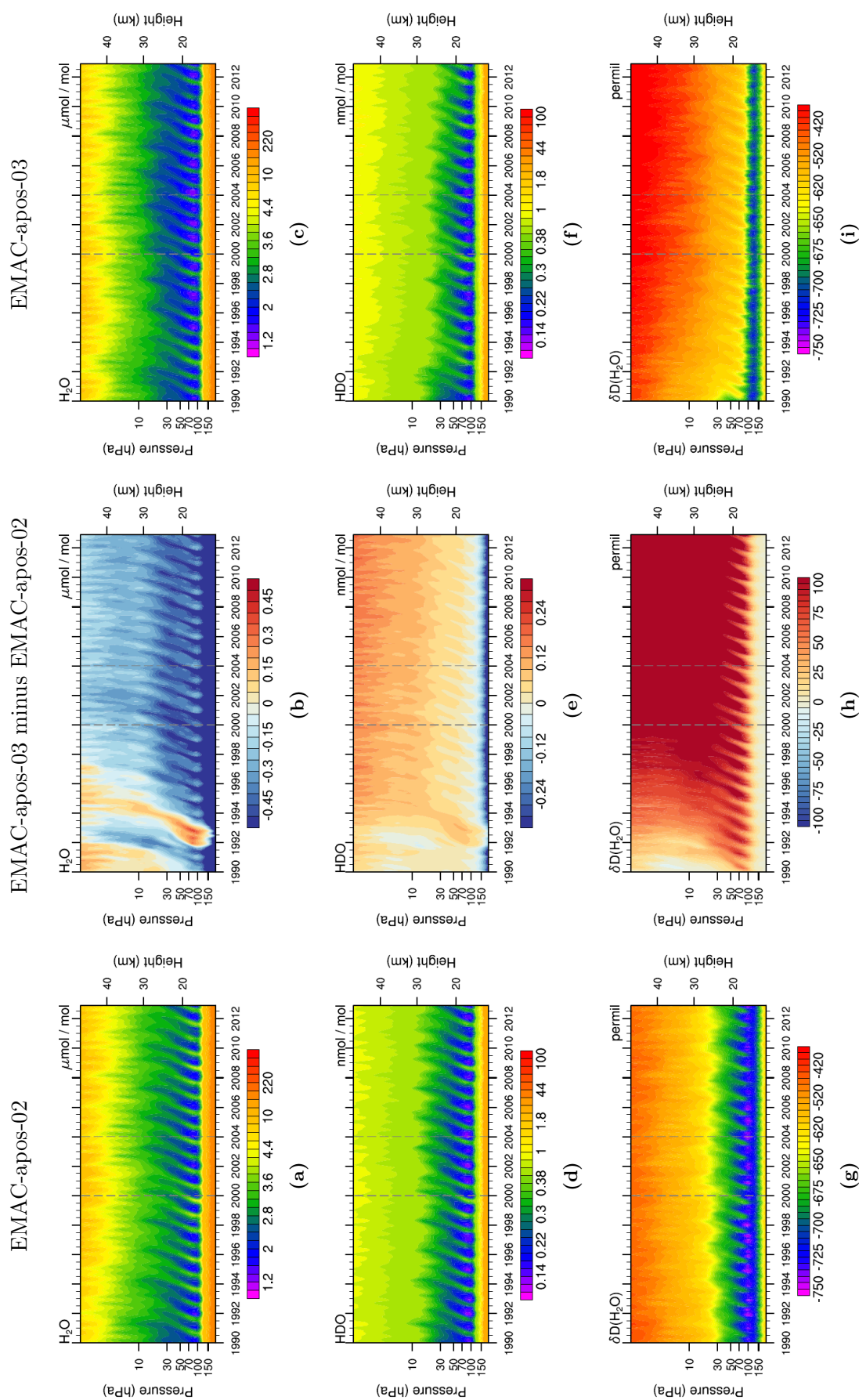
Figure 6.11: Tropical stratospheric tape recorder signal of H$_2$O (upper), HDO (middle) and in δD(H$_2$O) (lower) in the simulations EMAC-apos-02 (left column) and EMAC-apos-03 (right column). Simulation data is averaged monthly, zonally and over the tropics between 23° S–23° N. The corresponding difference of both simulations is shown in the middle column. The grey dashed lines are included for eye guidance in the comparison of the tape recorder signal.
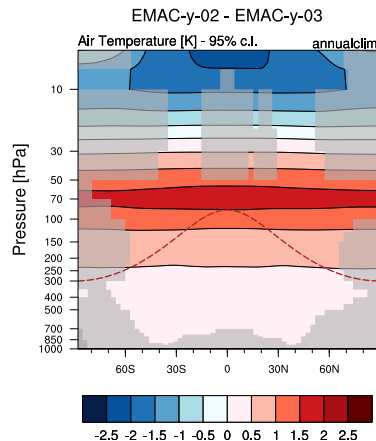
Figure 6.12: Dry air temperature differences of the simulations EMAC-apos-02 and EMAC-apos-03. The unshaded areas in the difference plots are significant on a 95% confidence level according to a two-sided Welch's test. The dashed brown line indicates the height of the climatological tropopause.

factor and needs to be assessed. Additional to that, for a detailed investigation of the various different processes between the simplified and interactive chemistry additional sensitivity studies are necessary, which are beyond the scope of the current study. Nevertheless, in the outlook at the end of this thesis potential simulation set-ups for these studies are proposed.

6.4.3   Evaluation with Satellite Observations

In addition to the simulation intercomparison in the section before, the simulations are compared to observational data. This comparison makes use of vertical profiles of H_2O and HDO provided by the MIPAS instrument mounted on the ENVISAT satellite [Steinwagner et al., 2007, Lossow et al., 2011]. The ENVISAT satellite is on a sun-synchronous orbit around the Earth, completing the circuit 14 times a day. These observational data comprise the time period July 2002 to March 2004 and represent high-resolution FTS measurements, observing the thermal mid-infrared emissions of HDO measured in the Earth limb (backward-looking) towards the sun. The vertical range of the observations extends from 6 to 68 km (i.e. approx. the range 100–1 hPa) with a vertical resolution of 3–8 km.

   Again the simulation data is monthly and zonally averaged over the tropics. Similar to the conclusions of Eichinger et al. [2015a] it is observed that the EMAC model underestimates the H_2O mixing ratio in Figs. 6.13a–6.13c. This is associated with a too cold tropopause in EMAC, as shown in Section 4.1.1, where a temperature bias of -2 to -6 K is detected in the upper troposphere. This reduces the H_2O transported into the stratosphere since more gas phase H_2O freezes and becomes sedimented.

   Additional to that, the HDO mixing ratios are likewise underestimated by the simulations as depicted in Figs. 6.13d–6.13f. Particularly the strong enriched areas in October, which are visible at 100–70 hPa, are not represented in the simulations. Furthermore, in both simulations it is evident that the tape recorder signal is a bit shifted in comparison to the profiles of MIPAS. This phase shift of 2 to 3 months was also observed by Eichinger et al. [2015a], but is still poorly explained. Eichinger et al. [2015a] argued that it is not expected that EMAC has a phase shift in the seasonality of convection and that a shift in MIPAS data is likely, although this would account for only 1 month.

   In the section above it is found that the $\delta D(H_2O)$ in EMAC-apos-03 is considerably larger than in EMAC-apos-02. Comparing Fig. 6.13h with 6.13i indicates a better agreement concerning the $\delta D(CH_4)$ in EMAC-apos-03 with the MIPAS observations, which suggests that although the absolute
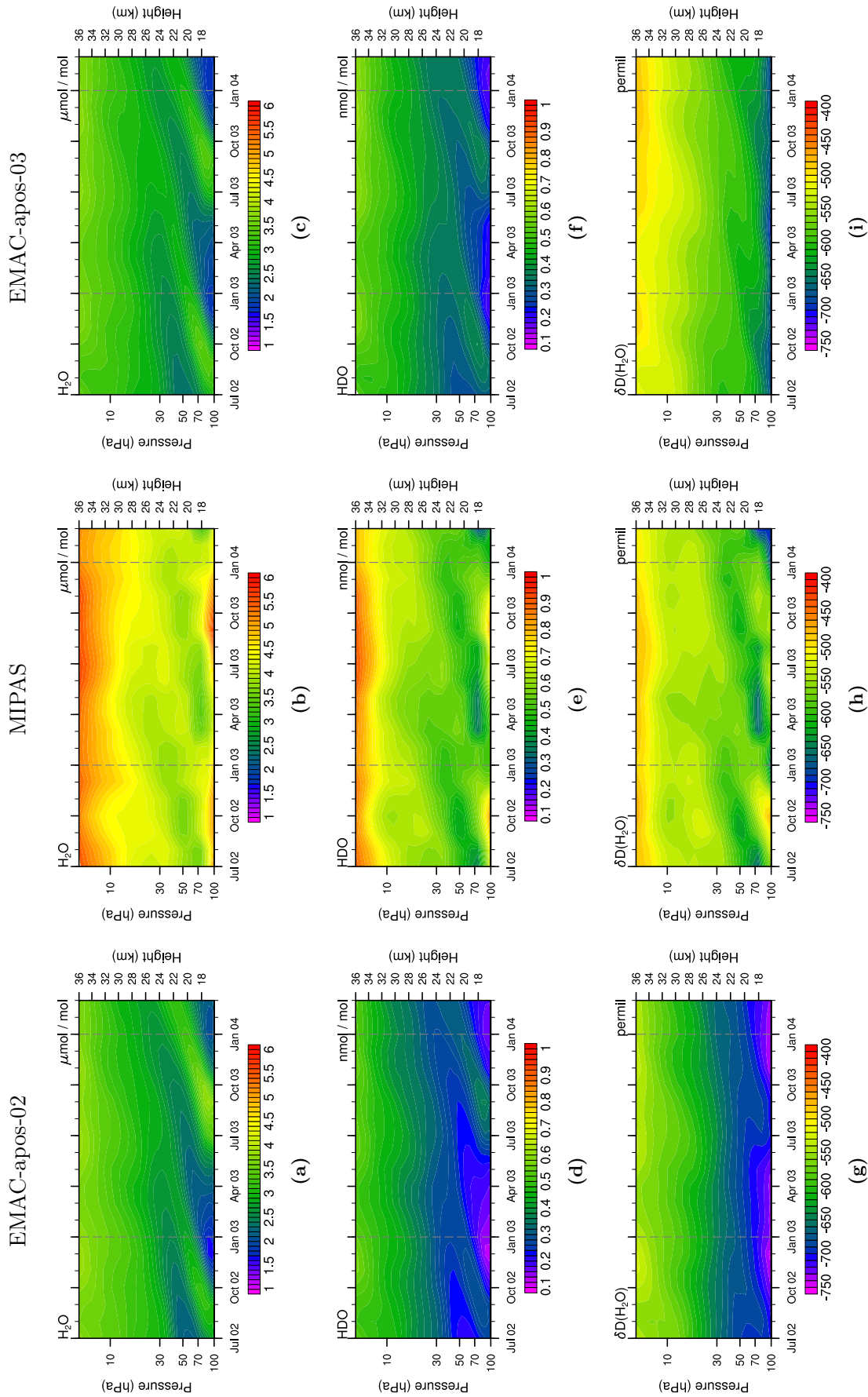
Figure 6.13: Tropical stratospheric tape recorder signal of H_2O (upper), HDO (middle) and in $\delta D(H_2O)$ (lower) in MIPAS data (middle column) and the simulations EMAC-apos-02 (right column) and EMAC-apos-03 (left column) in the time period July 2002 to March 2004. Simulation data is averaged monthly, zonally and over the tropics between 23° S–23° N and are displayed between 100 and 1 hPa. The grey dashed lines are included for eye guidance in the comparison of the tape recorder signal.

H_2O and HDO mixing ratios are not met, the relative composition is well represented.

The differences in HDO in EMAC-apos-02 compared to EMAC-apos-03 and MIPAS are potentially caused by (1) the function 3.3 from Eichinger et al. [2015a] used in EMAC-apos-02, which possibly does not capture important fractionation processes in the oxidation chain of CH_3D, and (2) the HD, produced at the surface and propagating into the stratosphere, which is not included in the simplified chemistry, but represents an additional source of HDO. For an accurate simulation of stratospheric HDO this source needs to be considered as well in future simulations.

Concluding, the deficiencies of the simulations compared to the observations in terms of absolute mixing ratios of both, H_2O, and HDO must be improved first. For that matter, however, the already well represented variations in the isotopic composition, as shown in this section, will in future enable the investigation of specific processes in more detail. Especially, the implemented coupling of MECCA-TAG and H2OISO enables an interactive chemistry simulation including isotopologues of H_2O and CH_4.

The presented evaluation of the SWV focuses on the tropical region, by considering the there apparent dynamically driven tape recorder signal. However, at higher latitudes physical processes relating to the PSCs and heterogeneous chemistry become important as well. In EMAC corresponding parameterizations are adopted by the Multi-phase Stratospheric Box Model (MSBM). Extensions in this submodel have been made in the course of the present work. First simulations including MSBM (not shown) have proven that certain processes in the heterogeneous chemistry are subject to fractionation effects, which are, however, still poorly quantified [Stowasser et al., 1999]. Therefore, the presented simulations in this thesis do not include stratospheric heterogeneous chemistry and the special consideration of PSCs using MSBM since this would additionally demand an accurate parameterization of the implied fractionation effects, which is beyond the scope of this study.

6.5 Summary

Concluding, knowledge about the isotopic composition is a valuable information in the investigation of CH_4 sources and sinks. In order to enable this in EMAC, the CH4 submodel is extended to allow for the simulation of the abundant and first rare isotopologue. Furthermore, MECCA-TAG together with an interactive chemistry simulation is for the first time configured to simulate isotopologues with respect to D of all hydrogen carrying species, which are included in the applied mechanism.

In this chapter these developments in EMAC concerning the isotopologues of CH_4 are evaluated. Particularly, the representation of CH_4 isotopologues in simulations with a simplified chemistry (i.e. the CH4 submodel extended for isotopologues) and the interactive chemistry using MECCA-TAG are presented and compared.

It is found that vertical and meridional gradients are well represented in both, the simulation with simplified chemistry and with interactive chemistry. Uncertainties in the isotopic composition are to some degree caused by uncertainties in the background CH_4, and by uncertainties of the signatures of the emission sources. Discrepancies in the polar region seem to be associated with deficiencies in the stratospheric transport of the EMAC model (faster BDC). However, the data basis of the current evaluation is rather sparse and additional observations (e.g. airborne measurements) could provide the necessary information to analyze this further. Additional observations, especially concerning $\delta D(CH_4)$, in south-east Asia and South America would also improve the data basis and consequently the understanding of the seasonally highly variable sources in these regions.

Furthermore, the work at hand implemented additional developments in EMAC, which close the

gap between chemical and physical isotopic fractionation processes. The framework makes use of the previously developed submodel H2OISO and combines this with the newly implemented isotopologue extension of the CH4 submodel and with MECCA-TAG. By this, it is possible to track the D content from its origin in the CH_4 emissions towards the end-product HDO. It is further shown that former results of Eichinger et al. [2015a] are reproducible. Again, the comparison of interactive and simplified chemistry gives evidence that the production of HDO from CH_3D and HD is underestimated in the simplified chemistry, especially since the latter is not resolved by the simplified chemistry.

Particularly, the reduced H_2O mixing ratio in the comprehensive interactive chemistry compared to the simplified chemistry gives evidence that the simplified chemistry does not achieve a consistent reproduction of the stratospheric water vapor (SWV) compared to the interactive chemistry, yet, which mostly relates to the apparent temperature bias. However, some uncertainties in the chemical impact onto the SWV are expected as well. In the CH4 submodel it is assumed that two H_2O molecules are produced by one oxidized CH_4 molecule. However, this must not hold at all times [le Texier et al., 1988] and is in detail investigated in the next chapter.

Feedback of Methane Oxidation onto H_2O

The results of this chapter have been published as part of Frank et al. [2018].

It is beyond question, that H_2O is an important GHG. The strong linkage of CH_4 and SWV represents a decisive factor of the net climate effect of CH_4. Enhanced CH_4 concentrations are likely expected in the future Earth's atmosphere and can impact the otherwise rather dry stratosphere substantially [Rohs et al., 2006].

Nevertheless, to account for the contribution of CH_4 to SWV, in current climate modeling it is common either to use a CCM with a complex chemistry set up, which puts high demands on computational resources, or a GCM or Chemical Transport model (CTM) with – if at all – a parameterization of the chemical sources of SWV. A parameterization of the chemical feedback onto SWV requires to estimate the yield of H_2O from CH_4 oxidation, which is defined as the production of H_2O per oxidized CH_4 molecule. A common simple assumption of the yield of H_2O from CH_4 oxidation is that one oxidized CH_4 molecule produces two H_2O molecules in the stratosphere. This simple parameterization is based on a first estimation of the H_2O yield from CH_4 oxidation, using a simplified methane chemistry without chlorine in a two dimensional photochemistry model [le Texier et al., 1988].

This is a widely accepted approximation [Myhre et al., 2007, Stowasser et al., 1999] and is also affirmed by aircraft observations, which state that $2 \cdot [CH_4] + [H_2O]$ (also named as the total stratospheric hydrogen budget) is fairly constant in the stratosphere being 6.8-7.6 ppmv [Hurst et al., 1999, Rahn et al., 2003, Dessler et al., 1994, Stowasser et al., 1999]. Although this suggests that all H from CH_4 oxidation reaches H_2O, it must be noted that the referenced observation studies do not distinguish, whether the H in H_2O comes from CH_4 or from H_2, which also originates from the troposphere. Thus, calculations based on observed mixing ratios show a net production of H_2O only, but not the yield of H_2O specifically from CH_4 oxidation [Hurst et al., 1999]. Furthermore, H_2 mixing ratios, when measured as well, show an almost absent vertical gradient, which can be explained by the supposition that the H_2 sink is in photochemical equilibrium with its production from CH_4 oxidation. Hence, all additional H_2 by CH_4 is leveled by the oxidation of H_2 and balances the $2 \cdot [CH_4] + [H_2O]$ and H_2 content in the stratosphere [Rahn et al., 2003]. Nevertheless, Hurst et al. [1999] took the weak anti-correlation of H_2 and CH_4 into account and calculated a net production of H_2O over loss of CH_4 of 1.973 ±0.003, differing from the assumed value of 2, which would only be the case if all H goes into H_2O.

Still, for reasons of simplification, several GCMs use the approximation that the yield of H_2O from CH_4 oxidation is exactly two [Monge-Sanz et al., 2013, ECMWF, 2007, Austin et al., 2007, Boville et al., 2001, Mote, 1995, Eichinger et al., 2015a]. In the EMAC model, for example, explicitly configured in a pseudo-CCM mode without interactive chemistry, the CH4 submodel is used to parameterize the yield of H_2O from CH_4 oxidation. This yield is calculated in a simplified way according to:

$$\frac{d}{dt}[H_2O] = -\gamma_{H_2O} \cdot \frac{d}{dt}[CH_4] \tag{7.1}$$

with $\gamma_{H_2O} = 2$ as the yield of H_2O.

However, this approximation first and foremost neglects the chemical loss of H$_2$O (mostly by re-action with O(^{1}D) and by photolysis). Using this parameterization, SWV is solely added and not removed by chemistry. Moreover, the results of le Texier et al. [1988] also suggest that the yield of H$_2$O from CH$_4$ oxidation is not exactly two, accounting for the part of H diverted into H$_2$ production and that the share of H$_2$ increases at higher altitudes. Therefore, following the results of le Texier et al. [1988] precisely, it would generate a certain bias by using a yield of 2 in Eq. (7.1), especially at higher altitudes, where 2·[CH$_4$]+[H$_2$O] approx. const. does not hold anymore. In the mesosphere, for example, the loss of H$_2$O becomes increasingly relevant, shifting the balance between H$_2$O and H$_2$ towards the latter. Furthermore, the net production calculated by Hurst et al. [1999] and the yield of le Texier et al. [1988] also do not agree well in the lower stratosphere, which can indeed be explained by the indistinguishable inputs from H$_2$ and CH$_4$ oxidation in observations as stated before. Yet, this does also indicate that the yield from CH$_4$ oxidation itself must be even lower than suggested by the net production, which is calculated based on observations. It is, therefore, questionable, if the assumption of $\gamma_{H_2O} = 2$ for the CH$_4$ oxidation is indeed applicable.

In this study the findings of le Texier et al. [1988] are re-evaluated with multiple approaches using a modern CCM, namely EMAC, with a complex state-of-the-art chemistry mechanism. The main goal is to assess the currently used assumption of the constant yield as in Eq. 7.1 with $\gamma_{H_2O} = 2$ and investigate, whether a parameterization solely based on CH$_4$ is sufficient to reproduce the chemical yield of H$_2$O from CH$_4$ oxidation. As an additional remark, it should be noted that difficulties with yield estimates can be expected especially in the stratosphere, as it is not as well mixed as the turbulent troposphere.

This chapter shows three approaches to determine the yield of H$_2$O from CH$_4$ oxidation. The first two approaches use the MECCA-TAG, either (1) in a box model set-up with the CAABA [Sander et al., 2011a] and (2) in a global simulation, with the EMAC model. For the third approach (3) again in a global simulation the assumption is used that the hydrogen budget in the stratosphere is conserved, mostly consisting of fractions of H, H$_2$, H$_2$O and CH$_4$.

MECCA-TAG is applied in all approaches to run a comprehensive chemistry setup, while being able to track the production of H$_2$O originating explicitly from CH$_4$ oxidation. A conceptionally different approach would be the extended Crutzen's sequential method used by Johnston and Kinnison [1998] to estimate the gross ozone loss by CH$_4$. Despite that the this study focuses on the tropospheric and lower stratospheric O$_3$, it is a practical example on the derivation of atmospheric trace gas yields. By applying MECCA-TAG, however, it is not necessary to explicitly write down the chemical net reactions as this is done in the extended Crutzen's sequential method.

7.1   Model Set-Up and Methods

For this analysis EMAC is applied in a slightly varied set-up compared to the sections before. Firstly, additionally CAABA is used to study the chemical mechanism in a box model, and secondly, MECCA-TAG is applied for fractional tagging rather than with respect to isotopologues. These specific model set-ups are presented in the following. Furthermore, in this section the definition of the so called chemical yield of H$_2$O from CH$_4$ oxidation as will be used throughout this chapter is given.

7.1.1   Model Set-up

This subsection provides an overview of the model configuration with respect to MECCA-TAG, the box model CAABA and the global model.

First of all, the conducted simulations presented in this chapter use the kinetic chemistry tagging

technique (MECCA-TAG) as presented in Section 3.5. This time, it is configured in the so called fractional mode, thus, is tracking the pathways of hydrogen from CH_4 towards H_2O. The study in this chapter, further, makes use of the MECCA-TAG internal counters, which indicate the production and recycling of H_2O and H_2, respectively.

For the photochemical box model studies the Chemistry As A Boxmodel Application (CAABA) in model version 3.0 [Sander et al., 2011a] is applied. CAABA equipped with MECCA (CAABA/MECCA) provides an atmospheric chemistry box model, simulating single air parcels with the chemical mechanism identical to that used in EMAC. CAABA/MECCA is, moreover, using the MESSy interface to attach certain submodels to the box model system. The used submodels in the box model study, in addition to MECCA, are SEMIDEP (applies deposition fluxes) and JVAL (calculates photolysis rates) [Sander et al., 2014].

CAABA simulates one box at one pressure and temperature specific for a given latitude and altitude in the atmosphere. To derive a pseudo vertical profile of the yield, 35 independent boxes superimposed upon each other at the equator are simulated with prescribed conditions following a standard atmosphere profile ([NOAA/NASA, 1976] accessed via `https://www.digitaldutch.com/atmoscalc/` [digital dutch, 1999]). The equator is chosen for its negligible seasonal cycle. Since the boxes represent different temperature and pressure levels and therefore distinct chemical regimes throughout the middle atmosphere, it is possible to illustrate the vertical dependence of the yield.

Note that the purpose of the box model simulation is to demonstrate the steady state conditions expected at different altitudes. In order to do so, the effect of vertical transport between the boxes is mimicked by prescribing the vertical distribution of the relevant species concentrations for:

1. CH_4 and all species acting as in-situ sources of H (primarily NMHCs and HCFCs), which are not produced in the chemical mechanism,

2. long-lived substances, such as NH_3 and N_2O,

3. N_2 and O_2, whose mixing ratios are virtually constant throughout the considered altitude range,

4. NO and $O(^1D)$, to constrain the HOx-NOx-cycle to the given initial state

5. SO_2, Cl and Br, for the same reason as in 4. with respect to ClOx, BrOx and sulfate compounds,

6. H_2O and H_2 mixing ratios and therefore serving as a H sink for the limitless influx of H via the fixed source species (indicated in 1.).

Other species, particularly the OH and HO_2 radicals, are unconstrained in the simulations unless otherwise noted. All initial mixing ratios of the chemical species are taken from a climatology over the years 2000–2010 of the RC1SD-base-10 EMAC simulation of the ESCiMo project [Jöckel et al., 2016].

Because a priori fractions of H from CH_4 (or tagged H) in the species of the chemical mechanism is not known, all tagged species are initialized with zero. The simulation of every box is run for 200 years to make sure that all tagged species have filled up to a steady state.

For the global simulations in the present study EMAC is applied in the T42L90MA-resolution. The applied model setup comprises particularly the submodels MECCA (Module Efficiently Calculating the Chemistry of the Atmosphere) [Sander et al., 2005] and MECCA-TAG (kinetic chemistry tagging technique) [Gromov et al., 2010].

The chemical mechanism is basically identical to the one used for the simulations in the chapters before, however, due to the application of MECCA-TAG in the fractional mode, the doubled chemical reactions for the isotopologues are replaced by the fractional counterparts indicating the H atoms in

the mechanism stemming from CH_4. These additional tracers in the model defined by MECCA-TAG are marked (tagged) to be distinguishable from each other. In the following, these tracers are indicated by the label *tagged* for reasons of comprehensibility. The full chemistry of MECCA plus MECCA-TAG, which more than triples the amount of simulated tracers, increases the computational demands substantially. A spin-up simulation of 6 years with a reduced vertical resolution is carried out in a global set-up to pre-adjust tagged tracers. The results of the global simulation shown in this chapter originate from a subsequent simulation on L90MA resolution, which is executed for another two years model time.

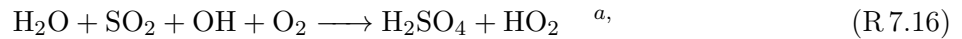### 7.1.2   Calculation of the Chemical H_2O Yield from CH_4 Oxidation

A straight forward definition of the direct yield is the ratio of the production of H_2O molecules by the loss of CH_4, as depicted in Eq. (7.2).

$$\gamma_{H_2O}^{direct}(CH_4) = \frac{\mathbf{P}_{H_2O}^{I}}{\mathbf{L}_{CH_4}} \tag{7.2}$$

with variables listed in Table 7.1.

The yield of H_2O from the oxidation of CH_4 (γ_{H_2O}) represents the units of molecule H_2O per molecule CH_4 (i.e. [molecule/molecule]) and is displayed dimensionless throughout this chapter.

Recall that the loss of CH_4 ($\mathbf{L}_{CH_4}$) in MECCA consists of the reactions with OH, $O(^1D)$ and Cl, as well as photolysis (see Reactions (R 2.1) - (R 2.6)). Following these reactions, H atoms from CH_4 are distributed among intermediates (not shown) and eventually reach H_2O. Produced H_2O reacts further and gets removed by the reactions (R 7.15), (R 7.16) and (R 7.17).

$$H_2O + O(^1D) \longrightarrow 2\,OH \qquad ^{a,} \tag{R 7.15}$$

$$H_2O + SO_2 + OH + O_2 \longrightarrow H_2SO_4 + HO_2 \qquad ^{a,} \tag{R 7.16}$$

$$H_2O + h\nu \longrightarrow H + OH \qquad ^{b,} \tag{R 7.17}$$

with reaction rates of a, from Sander et al. [2011b] and photolysis rate of b, calculated by JVAL [Sander et al., 2014].

In consecutive reactions H is again recycled into H_2O. The direct yield calculated by Eq. (7.2) represents the H_2O, which is produced in the chemical mechanism and directly emerges from CH_4 oxidation. However, this is not the additional H_2O of the whole chemical process. It also cannot be used in a simplified set-up for the methane chemistry and the production of SWV parameterized as by Eq. (7.1), because no chemical depletion of water is considered. Hence, an effective yield of H_2O is defined, which takes into account that water is recycled in consecutive reactions and that recycled water is again destroyed. During this recycling process (as sketched in Fig. 7.1), some H is converted to species other than H_2O, filling up to a steady state or leaving the HOx-cycle once and for all. The effective yield is therefore always equal to or smaller than the direct yield in a closed system.

The effective yield of H_2O in this study is defined in Eq. (7.3), with μ accounting for the lost H_2O, due to subsequent loss and recycling of H_2O molecules:

$$\gamma_{H_2O}^{eff}(CH_4) = \frac{\mathbf{P}_{H_2O}^{I} - \mu_{H_2O}}{\mathbf{L}_{CH_4}} \quad \text{with} \quad \mu_{H_2O} = \mathbf{L}_{H_2O}^{I} + \mathbf{L}_{H_2O}^{II} - \mathbf{P}_{H_2O}^{II} \tag{7.3}$$

Variables are listed in Table 7.1.

Similar to that for H_2O, recycling of H_2 is calculated in the chemical mechanism, that is, the recycled H is counted as soon as it is leaving H_2. The corresponding formula for H_2 is derived similarly to Eq.
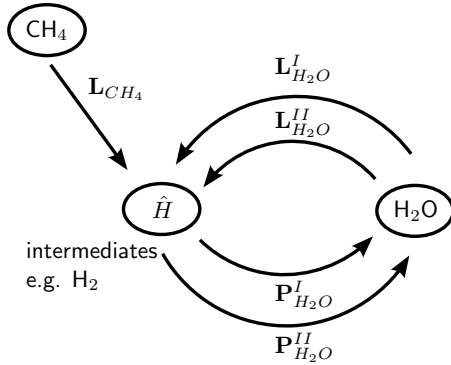
Figure 7.1: Sketch on the production and recycling of H_2O.

Table 7.1: Variable names as used in Equations 7.2, 7.3 and 7.4.

name	description
$\mathbf{L}_{CH_4}$	loss of CH_4 molecules
$\mathbf{P}^I_{H_2O/H_2}$	direct production of H_2O/H_2 by H from CH_4
$\mathbf{L}^I_{H_2O/H_2}$	loss of directly produced H_2O/H_2
$\mathbf{P}^{II}_{H_2O/H_2}$	production of recycled H_2O/H_2, hence the H already has been part of a H_2O/H_2 produced by CH_4
$\mathbf{L}^{II}_{H_2O/H_2}$	loss of recycled H_2O/H_2
μ_{H_2O/H_2}	lost H_2O/H_2 during the recycling

(7.3) and reads as follows:

$$\gamma^{eff}_{H_2}(CH_4) = \frac{\mathbf{P}^I_{H_2} - \mu_{H_2}}{\mathbf{L}_{CH_4}} \quad \text{with} \quad \mu_{H_2} = \mathbf{L}^I_{H_2} + \mathbf{L}^{II}_{H_2} - \mathbf{P}^{II}_{H_2} \tag{7.4}$$

Due to the implementation of the tagging technique, counting of recycled H can only be applied with respect to one species at once. Hence, the effective yield can only be calculated either for H_2O or H_2 in the same simulation.

The chemical conversion from CH_4 to H_2O follows some intermediate reactions. Hence, the loss of CH_4 and the eventual production of H_2O do not occur simultaneously. Furthermore, in reality, chemistry undergoes diurnal variations. The major changes occur during daylight. At night, virtually no photo-sensitive chemistry takes place, which results in very low OH concentrations. This reduces CH_4 loss and H_2O production to a nighttime-low. A diurnal average smoothes the difference between day and night to a representative value. This is based on the assumption that the system is in a quasi-steady-state. A quasi-steady-state implies that equal integral production and loss are simulated throughout a given time interval, e.g. a day, a month or a year. This study presents monthly averaged γ_{H_2O} values. These average over the simulated diurnal cycle and are sufficient for the application of a simplified CH_4 loss/H_2O production rates calculation with prescribed monthly varying OH distributions as applied in the CH4 submodel in most of the presented simulations in this thesis.

For these reasons, in this analysis Eq. (7.3) is applied to annual averages of the production and sink terms simulated in the boxes representing conditions typical for the tropics, where in addition seasonal variations are negligible. In the presented global simulations with EMAC an average over zonally averaged tropical bands is calculated.

In the following a comparison of the direct and effective yields of H_2O and H_2 from the CH_4 oxidation in the stratosphere, obtained in simulations with the box model CAABA and with EMAC are shown and discussed.

7.2 Results of the Different Approaches

The results of this study are presented next separately for the three different approaches, with (1) the box model, (2) the global model and (3) with respect to the ratio of H, H_2 and H_2O.
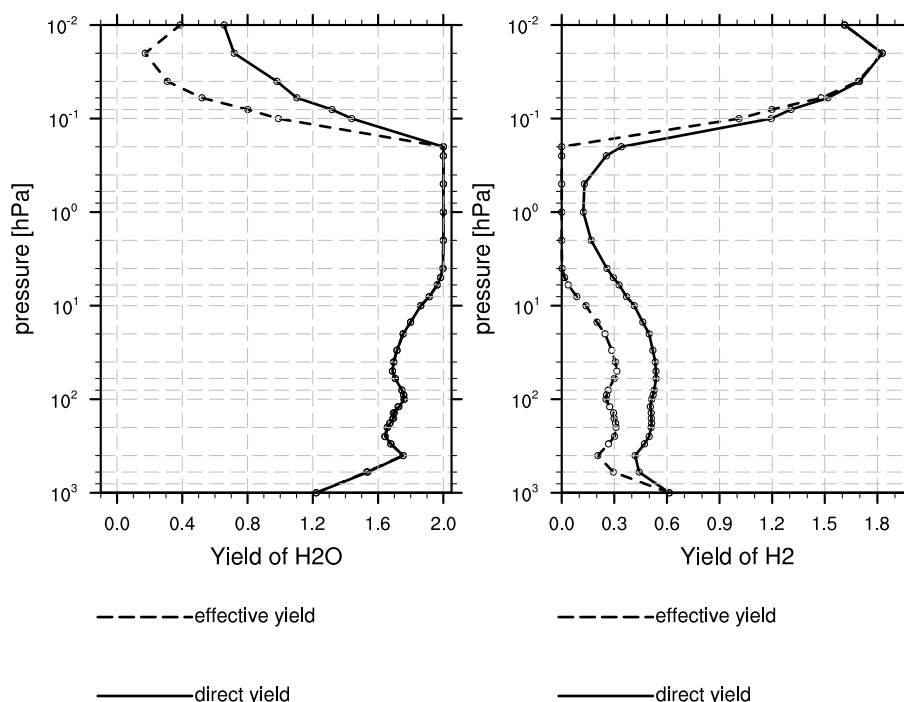
Figure 7.2: The pseudo vertical profile shows the H_2O yield (left) and H_2 yield (right), calculated by the box model approach. The solid line represents the direct yield, the dashed line represents the effective yield and circles indicate the pressure levels of the model boxes.

7.2.1   Box Model Approach

The box model approach is presented at first since it is intended to be a first example of the yield estimation and gives an overview of the sensitivities of the chemical mechanism with respect to CH_4 oxidation.

7.2.1.1   Simulation with Unrestrained Oxidation Capacity

The direct and the effective yield of H_2O from CH_4 oxidation of the box model approach (i.e. simulation Exp1, see Table 7.2), calculated as indicated in Eq. (7.2) and Eq. (7.3) respectively, are shown as a pseudo vertical profile in Fig. 7.2 by 35 vertically stacked boxes following the standard atmosphere at the equator. The presented results comprise also boxes on tropospheric levels. However, since the physical water cycle (e.g. evaporation, clouds) exceeds the influence of the CH_4 oxidation onto H_2O, the kinetic production of H_2O is irrelevant in the troposphere. All values below the tropopause level (approximately 100 hPa in the tropics) are therefore not part of the analysis presented in this chapter.

   The direct yield in Fig. 7.2 (left) is 1.7 around the tropopause and increases monotonically up to 2 at 4 hPa. It remains constant until 0.2 hPa, where it starts to decrease monotonically down to about 0.65 at the uppermost layer.

   The direct and the effective yields do not differ significantly for water vapor throughout the stratosphere and most of the mesosphere. This suggests that the H_2O recycling at these pressure levels and chemical regimes is predominant and all broken down water is regenerated. Nevertheless, in the mesosphere at approx. 0.1 hPa, the effective yield decreases more strongly than the direct yield, reaching the minimum of 0.17 at 0.02 hPa, with a slight increase to 0.39 at the topmost layer at 0.01 hPa.

Table 7.2: Overview of simulations carried out in this study, including box model simulations and the sensitivity study concerning the H_2O yield dependence on OH. The table also includes the global simulation Exp2 simulated with EMAC.

Name	description
Exp1	Experiment with unconstrained OH
Ref	Reference with standard fixed OH concentration from yearly climatology of RC1SD-base-10
SS1	Sensitivity simulation with 0.5×OH from Ref
SS2	Sensitivity simulation with 0.1×OH from Ref
SS3	Sensitivity simulation with 0.05×OH from Ref
SS4	Sensitivity simulation with 0.01×OH from Ref
SS5	Sensitivity simulation with 2.0×OH from Ref
Exp2	Global simulation with EMAC, MECCA and MECCA-TAG

The value of 2 between 4 and 0.2 hPa reflects that all H from CH_4 reaches H_2O eventually at these altitudes, supporting the assumption as accepted in the literature. In the lower stratosphere and upper mesosphere, however, the box model results show that assuming a yield of 2 will lead to an overestimated H_2O production.

The yield of H_2 (see Fig. 7.2 (right)) shows a mostly anti-correlated behavior with respect to the yield of H_2O. Throughout most of the stratosphere the effective and direct yields of H_2 differ by about 0.2, while the effective yield drops down to 0 between 4 and 0.2 hPa, i.e. exactly in the region where the yield of H_2O attains its maximum. In accordance with the decreasing yield of H_2O, the direct and effective yields of H_2 increase substantially at higher altitudes, giving evidence that more and more H becomes diverted to and stays in H_2 instead of continuing towards H_2O.

A good indicator for the rate of general chemical reactivity in the atmosphere is the CH_4 lifetime, which is mostly influenced by both, temperature, and the concentration of the reaction partners. The τ_{CH_4} with respect to its sinks OH, Cl, $O(^1D)$ and photolysis is defined as:

$$\tau_{CH_4} = \frac{1}{(k_{OH} * [OH] + k_{Cl} * [Cl] + k_{O1D} * [O1D]) * c_{air} + j_{CH_4}} \tag{7.5}$$

with k_X being the reaction rate coefficients of CH_4+X in [cm^3 s^{-1}], [X] being the mixing ratio of species X, c_{air} the concentration of dry air in [molec. cm^{-3}] and j_{CH_4} the photolysis rate of CH_4 in [molec. s^{-1}].

The area, where the H_2O yield attains its maximum, i.e. where it is 2, corresponds to the area, where the lifetime of CH_4 attains its stratospheric minimum (see Fig. 7.3). However, the CH_4 lifetime does not fully explain the behavior of the chemical yield since in the upper mesosphere both, yield and lifetime, drop to a minimum, which can be explained by the emerging role of photolysis in this area. This further suggests that OH is an important factor in the H_2O yield in the stratosphere, but does not influence it alone. It becomes replaced by photolysis in the mesosphere, which influences the CH_4 lifetime and, more importantly, destroys H_2O and initiates its recycling.

A sensitivity study concerning the impact of OH onto γ_{H_2O} is presented in the next section.
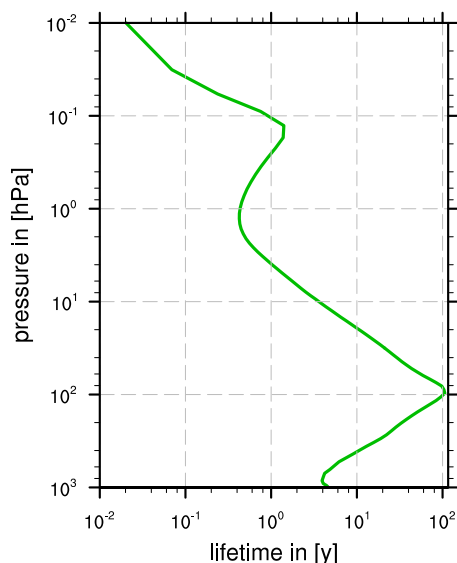
Figure 7.3: Vertical profile of CH$_4$ lifetime in the tropics with respect to removal by OH, O(^{1}D), Cl and photolysis in years.
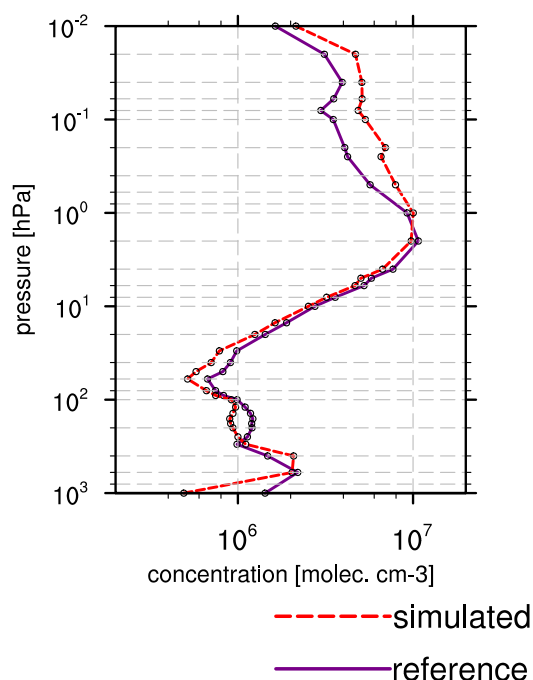
Figure 7.4: Reference OH concentration in the tropics from ESCiMo experiment RC1SD-base-10a (purple) and OH concentration as simulated in respective boxes (red).

7.2.1.2   Sensitivity with respect to OH

The results of the previous section revealed that the effective yield of water vapor from CH$_4$ oxidation depends on the box location, hence the chemical regime at a certain pressure level. Particularly, OH is one of the major oxidants that largely controls the conversion of CH$_4$ to H$_2$ and H$_2$O respectively.

In the simulations shown above (Exp1) the OH is unconstrained, however, its final (equilibrated) OH concentration does not deviate much from the initial values (see Fig. 7.4).

In further sensitivity simulations with CAABA, OH is initialized with the reference value from a EMAC simulation multiplied with constants and kept constant throughout the simulation. This introduces an additional prescribed hydrogen carrying species, which introduces or withdraws hydrogen to or from the system. However, contribution of OH to the total H abundance in the system was found negligible. The first four simulations reduce the OH concentration by the factors of 0.5 (SS1), 0.1 (SS2), 0.05 (SS3) and 0.01 (SS4) respectively, while the fifth one is performed with a doubled OH concentration (SS5). One additional simulation represents the reference simulation (Ref), which started with an OH concentration identical to the analysis above, except that OH is kept constant. The simulations are listed in Table 7.2. The sensitivity simulations use extreme perturbations of the OH concentration to provide a qualitative estimate of the impact of OH onto the H$_2$O yield from CH$_4$ oxidation.

The results of the sensitivity simulations are shown in Fig. 7.5. First of all, the initial experiment Exp1 (see Fig. 7.2) and the reference experiment of the sensitivity study Ref (see Fig. 7.5 red line) show mostly consistent results compared to each other concerning the effective and direct yield, which confirms that prescribing OH is adequate. However, in the upper mesosphere, where the OH concentration has the largest difference (cf. Fig. 7.4), the effective yield in the experiment Ref drops
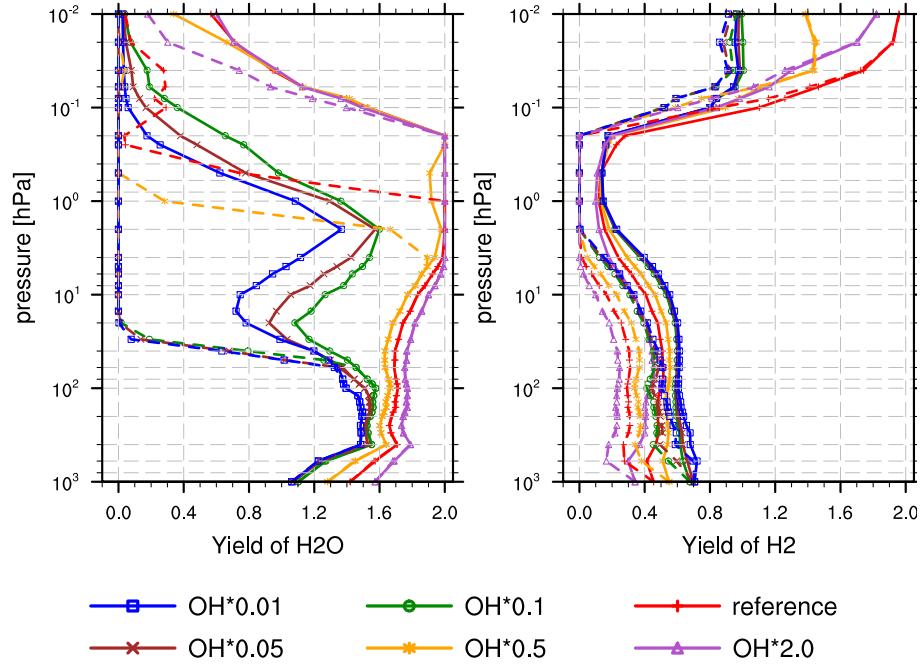
Figure 7.5: Pseudo vertical profiles of the H_2O yield (left) and H_2 yield (right), calculated by the box model approach. Solid lines represent the direct yield, the dashed lines the effective yield and circles indicate the pressure levels of the model boxes. OH concentrations are prescribed in all simulations to the initial values of the respective vertical box. The plot shows simulations with the reference OH concentration (Ref, red, plus signs) as well as the OH concentration times 2 (SS5, purple, triangles), times 0.5 (SS1, orange, asterisks), times 0.1 (SS2, green, circles), times 0.05 (SS3, brown, crosses) and times 0.01 (SS4, blue, squares).

already at 1 hPa significantly. Additionally, the effective yield in the experiment Ref reaches a value lower than the effective yield in the experiment Exp1 in this area. Nevertheless, the direct yield is not considerably different between these two experiments. This once more supports the assumption of a strong OH dependence of γ_{H_2O}.

Comparing experiment Ref with SS1 shows that reducing the OH concentrations by half reduces the direct and effective yields by about 0.05 in the lower stratosphere. Altogether, the direct yield profiles are rather similar in experiment Ref and SS1, with an exception of lower values in SS1 within the 10–1 hPa range and above 0.2 hPa. Prominent, however, is the difference in the effective yield. In the experiment SS1 the effective yield drops to zero already at 0.04 hPa and does not have the local enhancement seen in experiment Ref around 0.2–0.02 hPa.

Considering the sensitivity simulations SS2–SS4, the effect of OH reduction on γ_{H_2O} becomes more apparent. The effective yield drops to zero already above 60 hPa. The direct yield shows strongly reduced values in the stratosphere, with a local minimum at 20 hPa for SS2 and SS3 and a bit above for SS4, being 1.08, 0.92 and 0.78 respectively. Above 20 hPa the direct yield increases towards a local maximum at 2 hPa, following the profile of the CH_4 lifetime. Above 2 hPa the direct yield decreases nearly monotonically.

In the experiment SS5, with doubled OH, γ_{H_2O} is about 0.07 higher compared to experiment Ref and nearly replicates the results of experiment Exp1 in the mesosphere, where the OH equilibrated at a value of about twice that of the reference OH concentration from EMAC.
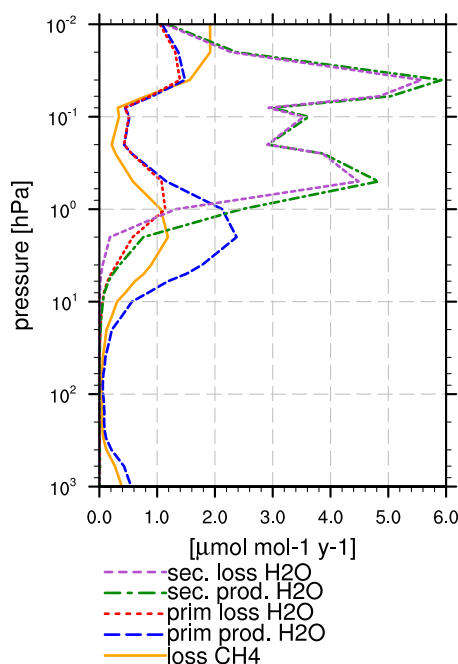
Figure 7.6: Separate loss of CH_4 and primary and secondary loss and production of H_2O from box model simulation Ref.

Compared to the yields of H_2O, the effective and direct yields of H_2 show moderate dependence on OH concentration. The yield of H_2 is rather constant at lower levels, reaches its minimum around the stratopause and increases again above that to its maximum. Around the stratopause and in the lower mesosphere all experiments show similar results. In lower boxes the simulations with lower OH show higher yields and vice versa. In contrast to this, the boxes in the middle mesosphere and above show an inverted behavior. Except, however, for experiment SS5, which results in a lower yield than in the reference simulation.

Moreover, profiles of yield of H_2 from the oxidation of CH_4 (γ_{H_2}) of experiments SS2, SS3 and SS4 overall do not vary much compared to each other.

To investigate the vertical profile of the effective yield of H_2O in more detail, all terms of Eq. (7.3) are plotted separately in Fig. 7.6 for the experiment Ref. In line with the CH_4 lifetime, it is apparent that loss of CH_4 and production of H_2O minimize around the tropopause and maximize close to the stratopause. The maximum of the primary loss of H_2O in the stratosphere is slightly shifted vertically. Above the stratopause, the recycling of H_2O becomes more important. This is indicated by increased secondary loss and production of H_2O and is further reflected by the reduced effective yield in the mesosphere.

Summarizing, reduction of the OH concentrations leads to a proportionally larger decrease in the H_2O yield at higher altitudes owing to the differences in the chemical regimes. On the other hand, increasing the OH concentration also increases the direct and foremost the effective yield of H_2O.

The results of the sensitivity study suggest that the effective yield of H_2O is highly dependent on the OH concentration and they give evidence that a minimum OH concentration is required for an effective H_2O recycling.

The γ_{H_2} shows an anti-correlated behavior to that of the H_2O yield, however, as an exception, doubling of OH shows a lower yield than the reference in the mesosphere.
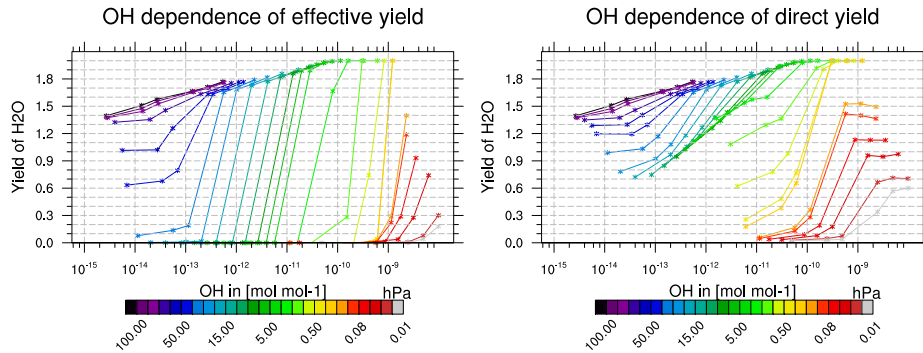
Figure 7.7: Effective yield (left) and direct yield (right) versus OH; colors indicate pressure levels from low to high pressure.
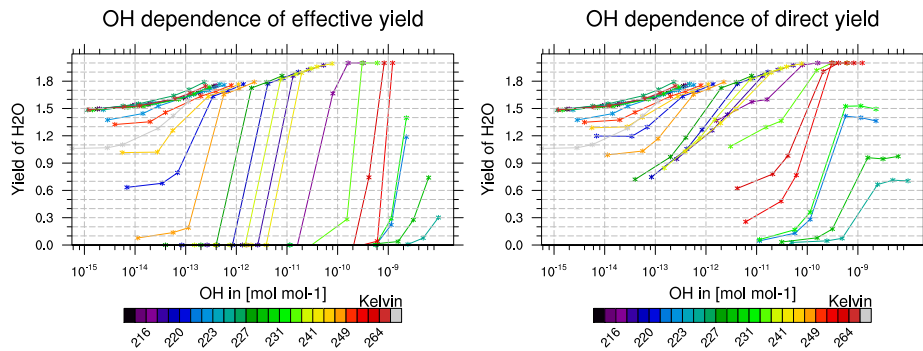

Figure 7.8: Effective yield (left) and direct yield (right) versus OH; colors indicate temperatures from low to high temperatures.

7.2.1.3 Dependencies on Pressure and Temperature

The results shown in the previous subsection indicate that there is an OH dependence in both the effective and direct yield. To investigate whether this dependency is systematic, simulated H_2O yields are plotted as γ_{H_2O} versus OH mixing ratio in Fig. 7.7. Generally, there is no linear correlation between these two parameters. However, a systematic dependence is evident for each box, i.e. at each pressure level. The slope of the correlation is thereby dependent on the pressure level. For higher pressure the gradient is low and becomes steeper for lower pressure levels.

The slope of the correlation of OH and the direct yield (see Fig. 7.7 (right)) is smaller for pressure levels at 2–80 hPa than the slope of the effective yield (see Fig. 7.7 (left)) at corresponding pressure levels. Moreover, the effective yield has a sharp transition from low to high OH values, while the direct yield increases more gradually.

The scatter plots give evidence that in a certain range of pressure levels the yields exhibit a saturation-like behavior with respect to OH concentrations. Furthermore, there is no indication of a connection between the yield-OH-dependence and the temperature (see Fig. 7.8 and the non-ordered colors indicating the temperature), despite the fact that reaction rates in the $CH_4 \longrightarrow H_2 \, / \, H_2O$-cycle are usually stronger impacted by temperature than by pressure.

Additional sensitivity studies are carried out in order to investigate the temperature dependence of the yield on a given pressure level. Results are displayed in Fig. 7.9. The simulation set-ups are identical to that of experiment Ref, except that temperature in every box was varied within -15 K to +15 K with 5 K steps. This temperature range is chosen as it represents a range exceeding day-night
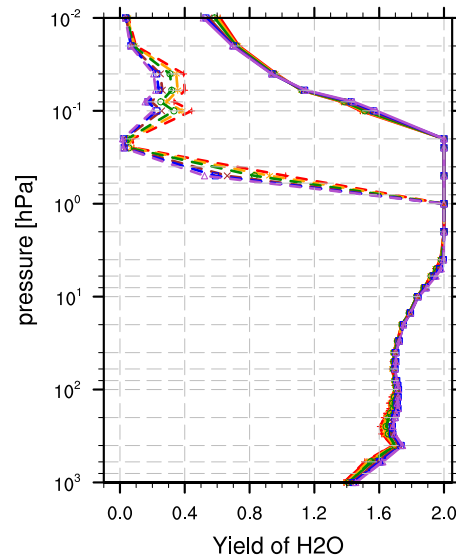
Figure 7.9: The pseudo vertical profile of the H_2O yield calculated by the box model approach. Solid lines represent the direct yield, the dashed lines the effective yield and circles indicate the pressure levels of the model boxes. OH is kept constant to the initial values of the respective vertical box. The plot shows sensitivities concerning temperature. Temperature is varied from the standard atmosphere value by -15 K (red), -10 K (orange), -5 K (green), +5 K (brown), +10 K (blue) and +15 K (purple).

differences (less than ± 5 K) and the annual cycle (less than ± 10 K) in the tropics. In the lower stratosphere there is no indication of a significant temperature sensitivity of the effective and direct yields. The latter also does not show any significant sensitivity at higher altitudes. The effective yield in the upper stratosphere and mesosphere shows a small dependence in a way that lower temperatures increase the yield and vice versa.

Consideration of the obvious vertical dependence and the very low temperature dependence gives evidence that not the physical parameters (temperature and pressure) itself are crucial for the H_2O yield, but rather the chemical composition of the box. This chemical composition, however, changes with altitude (hence with pressure) and depends additionally on transport.

7.2.2   Global Model Approach

As stated before, the box model approach does not take into account vertical transport and requires certain assumptions. Consequently, the boxes do not fully represent atmospheric conditions. To investigate the production of SWV in a comprehensive set-up, MECCA-TAG is applied in a global simulation with EMAC as described in Section 7.1.1.

Although the global simulation provides a three dimensional field, the focus of the current study is on the vertical zonal mean profile of the yield of H_2O from CH_4 oxidation (γ_{H_2O}) averaged over the tropics. An analysis of the zonal mean without the meridional averaging is presented at the end of this section and shows that the conclusions presented also apply to a certain degree at mid latitudes.

Figure 7.10 shows the vertical profile of the direct and effective yield of H_2O in the tropics (23° S–23° N). Both match the vertical profile of the results of the box model simulation Exp1 superficially. However, there are certain differences.

First, the yield of H_2O from CH_4 oxidation increases in the upper stratosphere and lower mesosphere to a value above 2, because the global model, unlike the box model, includes transport. The tagged
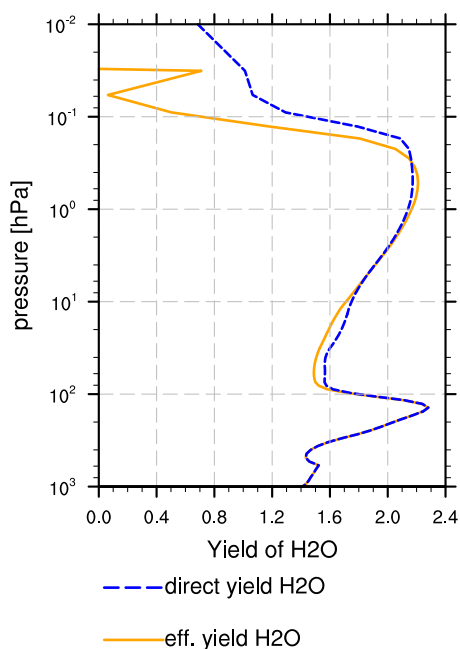
Figure 7.10: Effective and direct yield calculated from results of the global simulation in the tropics (23° S–23° N)
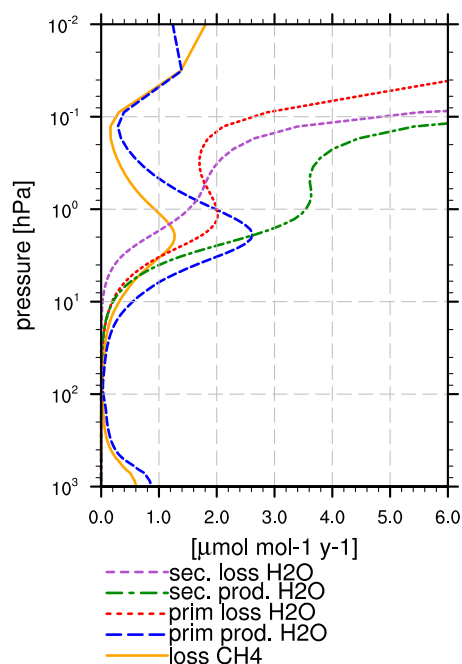
Figure 7.11: Separate loss of CH_4 and primary and secondary loss and production of H_2O from the global simulation (23° S–23° N).

rather long-lived intermediates (e.g. tagged methyl (CH_3), HCHO etc.) which are produced at lower levels are transported upward and are finally converted to H_2O. This results in a production of more than two H_2O molecules per oxidized CH_4 in one specific layer, because the additional production via transported intermediates is counted as well. In layers, where this increased production takes place, high OH concentration supports the conversion of the intermediates towards H_2O, since OH is the main driver of the chemistry.

The three topmost model layers in the upper mesosphere (0.06–0.01 hPa) are possibly subject to artifacts due to the nearby top of the global model and are therefore not considered in this analysis. It is assumed that the trend, which is evident below 0.1 hPa, showing decreasing γ_{H_2O} values also applies to the upper mesosphere, which would be similar to the box model results in the section above.

In Fig. 7.11 it also becomes obvious that the loss of H_2O increases at higher altitudes. Additionally, the recycling of H_2O contributes considerably to the effective yield. The photooxidation of H_2O drives the continuously recycling of H_2O to H_2 and back, shifting the equilibrium between these two gases towards H_2.

Altogether, the separated H_2O and H_2 loss/production terms of the global model are consistent with the box model findings. They also show a local maximum in loss of CH_4 and primary production of H_2O below the stratopause and the strongly pronounced secondary loss and production of H_2O in the middle and towards the upper mesosphere.

The panels of Fig. 7.12 show the zonal mean of the effective and direct yield as an annual and seasonal climatology. Overall, the vertical profile in the tropics generally applies to the mid latitudes as well. The area below the tropopause, where the yield peaks in values above 2, is also represented at higher latitudes, where the tropopause is lower than in the tropics. A notable exception is that in the summer hemisphere the yield below the tropopause is smaller and in the upper stratosphere
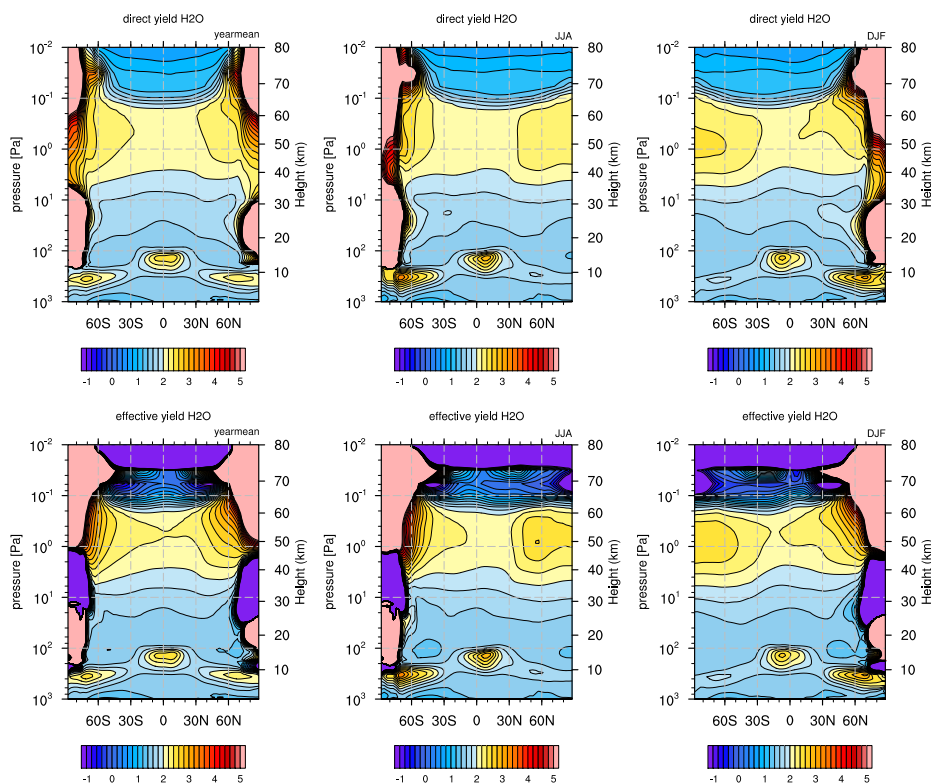
Figure 7.12: Zonal mean of effective (upper panels) and direct yield (lower panels) from global model as an annual climatology (left column), seasonal climatology of the months June, July and August (middle column) and of the months December, January and February (right column) respectively.

larger than in the tropics. It is, however, not possible to apply the presented method to calculate γ_{H_2O} in the winter polar region, since through the absence of sunlight the concentrations of OH are very low and therefore the loss of CH_4 so small that numerical errors influence the calculation of γ_{H_2O} too much for a reliable estimate.

7.2.3   Ratio of $H{:}H_2{:}H_2O$

A different approach than the first two presented ones to determine γ_{H_2O} in the stratosphere is to use the fact that the vertical profile of the H content in terms of atoms is fairly constant above the tropopause (see Fig. 7.13) compared to tropospheric variations. The H content in the stratosphere consists mostly of CH_4, H_2O, H_2, and, in the topmost layers, H. Other H carrying substances, such as OH, nitric acid (HNO_3), can be neglected for the H budget. The chemical regime determines the proportion between H, H_2 and H_2O, but the total H content is preserved.

The effective yield of H_2O from CH_4 oxidation, as explained in previous sections, describes the net production of H_2O. Precisely it is an indicator for the interaction of loss and production of H_2O, further influencing the production of H_2 and H as well. As a first assumption, additional H from CH_4 oxidation should be partitioned to the reservoirs of H, H_2 and H_2O in the same proportion as is present in the steady state. This is based on the supposition that it does not matter, whether the H, which is injected to the hydrogen cycling and reaches the indicated H reservoirs, comes from CH_4 or any other hydrogen supply. If it is assumed further that the simulated proportion of H, H_2 and H_2O at a certain level is approximately constant in time and that CH_4 is at higher layers the only

additional hydrogen supply, it is possible to determine the effective yield of H_2O by CH_4 oxidation through the proportion of H atoms in H_2O to the total hydrogen content of H, H_2 and H_2O. This proportion of the total hydrological content is subsequently called the H portion of H_2O.

In Fig. 7.14 the H portion of tagged and total H_2O is plotted with respect to the sum of tagged and total H in the CH_4 oxidation products H, H_2 and H_2O, from the global experiment Exp2.

The H portion of H_2O in the hydrogen budget is 2 in the troposphere and decreases to a minimum right above the tropopause. The hydrological cycle is producing a generally humid troposphere. Therefore, H_2O in the lower layers of the atmosphere is prevailing versus H_2 and H, which are quickly oxidized as soon as they are produced. The minimum of the H portion of H_2O above the troposphere can be explained by the freeze drying at the cold point. This reduces the H portion of H_2O versus the one of H and H_2.

This minimum is not equally plain in the tagged H_2O. Note that tagged H_2O in the troposphere is already lower than the total H_2O, since it is solely produced by CH_4 oxidation. When CH_4 ascends from the troposphere through the cold point into the stratosphere it continuously produces H_2O, although at low rates (due to low temperatures). Therefore, tagged H_2O is still produced by CH_4 and even though it partly freezes out, the proportion to H and H_2 is not much impacted. However, in the lower stratosphere the mixing ratio of tagged H_2 increases, while H_2O is still restrained by the cold point. This behavior becomes more apparent in case of the tagged species, since their absolute amounts are fairly low compared to the total ones.

Nevertheless, the H portion of tagged H_2O and total H_2O behave similar above the minimum at the tropopause, as seen in the maximum around the stratopause and in the lower mesosphere and the strong decrease in the middle mesosphere and above. The general behavior of the vertical profile also agrees well with the above findings of the yield calculations using box model and global model results.

Considering the zonal mean of the H portions (see Fig. 7.15), it becomes again apparent that the tropical profile of the H portion is a good estimate for its annual climatology. The local minimum at the tropopause is, for example, evident throughout the year. In the summer hemispheres the hydrogen content in H_2O increases in the upper stratosphere and mesosphere, while it decreases substantially at the same altitudes in the winter hemisphere. Where the share of H portion of H_2O is low, the share of H_2 increases. For polar stratospheric clouds variations in the ratio of H_2O to H_2 are decisive. An investigation of this influence is, however, beyond the scope of this study.

7.3   Comparison of the Presented Approaches

The presented results show three different approaches to estimate γ_{H_2O}. Taking the results of the separate approaches together gives the opportunity to discuss certain processes, which are differently parameterized and decisive for the yield estimation. Firstly, the general benefits and limitations of the approaches are discussed.

In the box model the opportunity is given to study a chemical regime without transport. It enables to solely assess the involved chemical kinetics. Clearly, the box model chemistry does not fully represent the intended atmospheric conditions. Setting certain species to a constant value does change the chemical regime. However, without constraints on the chemical species the model would run into a new equilibrium, which changes the regime as well. It therefore needs careful weighing to specify, which species should be kept constant and which species should be allowed to re-adjust, to be able to simulate a representative chemical regime.

The global model is not restricted to one vertical profile and provides the possibility to evaluate
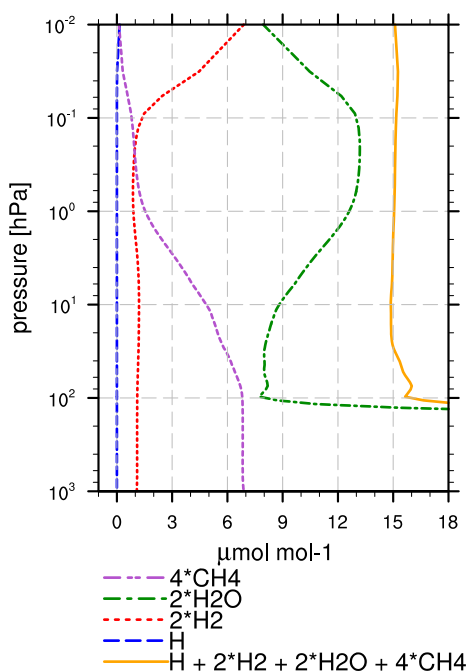
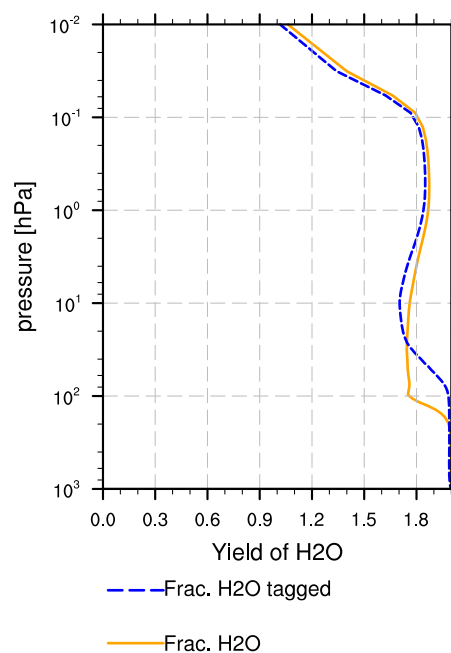**Figure 7.13:** Annual zonal average of H content by species (in ppmv) over the tropics (23° S–23° N).

Figure 7.14: H portion of tagged and total H$_2$O with respect to the tagged and total hydrogen content (H+2×H$_2$+2×H$_2$O), respectively.

the yield in three dimensions. Nevertheless, the effects of transport and chemical regime onto the yield cannot be separated, since transport influences the chemical regime. The vertical profile of γ_{H_2O} is for this reason susceptible to changes in dynamical processes as for example the Brewer-Dobson circulation.

The third approach, which used the total H budgets and portions, helps to quantitatively evaluate the methods, which are calculating the effective yield. It shows the actual portion of hydrogen from CH$_4$ in the total hydrogen without a production and loss term, which is sensitive to variations in the chemical regime. Yet, this approach is not directly linked to the loss of CH$_4$ and it is not possible to explicitly resolve the influence of chemistry, since, for example, it is not clear if the decreasing values of γ_{H_2O} in the mesosphere are due to the increasing loss of H$_2$O or due to the reduced oxidation of CH$_4$.

Figure 7.16 shows the vertical profiles of the H$_2$O yields and H portions calculated by the approaches described in the previous sections combined in one plot.

Comparing the results of the box model and the global model in the lower stratosphere, γ_{H_2O} in the global model is lower than in the box model. This suggests that CH$_4$-produced H$_2$O is transported into the stratosphere, where it is destroyed, adding to the loss of H$_2$O. This reduces γ_{H_2O} while the oxidation of CH$_4$ is low, due to the exceptionally long lifetime of CH$_4$ due to low temperatures and low OH concentrations. In the upper stratosphere, global model γ_{H_2O} is larger than box model γ_{H_2O} and, more importantly, larger than 2, which is attributed to transport. This time, CH$_4$-derived intermediates are elevated and produce H$_2$O independent of the CH$_4$ oxidized in this region. This contradicts the assumption that two H$_2$O molecules are immediately produced from CH$_4$ oxidation, since intermediates do play an important role.

In the middle mesosphere, box model and global model γ_{H_2O} decrease substantially. Although,
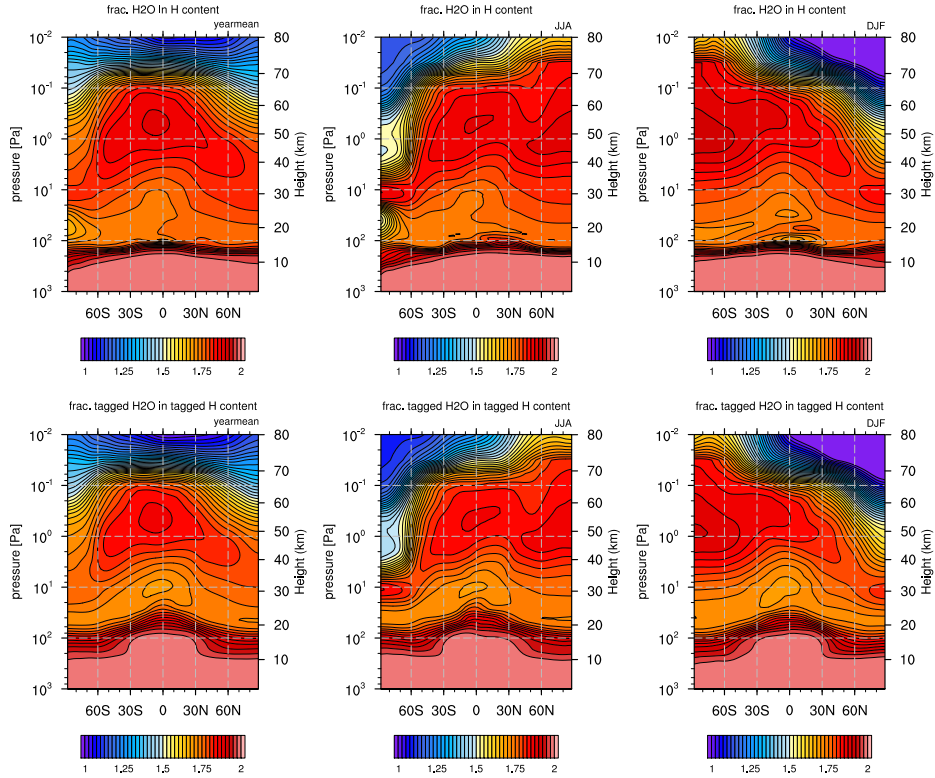
Figure 7.15: Zonal mean of un-tagged (upper panels) and tagged (lower panels) H portion in H_2O with respect to the un-tagged and tagged hydrogen content ($H+2\times H_2+2\times H_2O$) as annual climatology (left column), seasonal climatology of the months June, July and August (middle column) and of the months December, January and February (right column) respectively.

the topmost layers must be considered with caution due to potential artifacts, it is possible that the yield of the global model reaches values below zero. In the global model tagged H_2O is transported into the mesosphere, where it is destroyed, due to the enhanced sink of H_2O through photooxidation. The effective yield decreases below zero, since the loss of H_2O becomes larger than the production of H_2O ($\mathbf{P}_{H_2O}^I + \mathbf{P}_{H_2O}^{II} < \mathbf{L}_{H_2O}^I + \mathbf{L}_{H_2O}^{II}$). This emphasizes the importance of H_2O destruction at higher altitudes, which particularly is not included, when parameterizing the chemical γ_{H_2O} of H_2O with two H_2O molecules per CH_4 molecule oxidized.

Moreover, the effective yield in the box model setup with fixed OH profile drops down at 1 hPa, while the yield of the box model with variable OH (Exp1) and the global model (Exp2) do not drop until 0.2 hPa. Additionally, Exp1 and Exp2 agree well concerning the altitude of the drop (the small peak in Exp2 (red line) is most likely an artifact as discussed in Section 7.2.2). This suggests further that the chemical regime of the box model presented by the annual mean of the reference simulation (Ref) is not consistent with the chemical regime at the corresponding altitude concerning OH. The initialized and fixed value of OH at these levels is too low to realistically capture the chemical situation. This also shows that unconstrained OH is crucial and that the vertical profile of OH of simulation Exp1 in this region better agrees with the OH in the global simulation Exp2.

The H portion of H_2O in the hydrogen content matches qualitatively the results of the yield calculations in the box and global model approach. MECCA-TAG again enables to focus on H in H_2O particularly from CH_4 oxidation and to ignore the H from other sources. The minimum of the H portion of H_2O in the lower stratosphere and its maximum close to the stratopause and in the lower
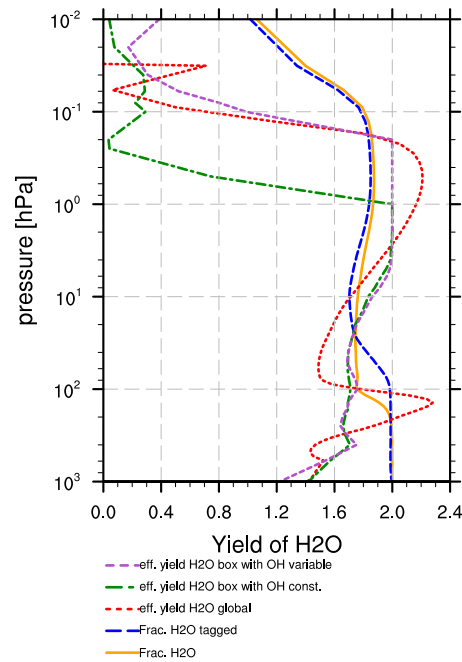
Figure 7.16: Comparison of all approaches determining the H_2O yield: Effective yield by box model simulations with variable OH (purple, dashed) and fixed OH (green, dash-dotted), effective yield by global model simulations (red, dotted), H portion of total (yellow, solid) and tagged (blue, long dashed) H_2O with respect to the hydrogen content.

mesosphere therefore shows that the production of H_2O from CH_4 oxidation relative to the production of H_2 from CH_4 oxidation is smaller in the lower stratosphere and becomes larger towards the upper stratosphere. Accordingly, it is concluded that the estimation that γ_{H_2O} differs significantly from 2 in the lower stratosphere is reliable.

Altogether, the different approaches yield consistent results. All suggest a yield of less than 2 in the lower stratosphere, varying between 1.5 and 1.7. The smallest value is estimated in the global simulation Exp2, where the yield is larger than the one of le Texier et al. [1988], which is $\gamma_{H_2O}=1.3$ at corresponding altitudes. The results of le Texier et al. [1988] also showed a maximum around 1 hPa, which is consistent with the presented results in the current study, albeit being a bit above 1.8 and with that lower than the here presented estimate of 2 (or more in case of the global simulation) in that region.

Overall, the estimated yield of H_2 from le Texier et al. [1988] and the yield of H_2 estimated by the box model approach are consistent as well. While the presented resulting γ_{H_2O} is larger than in le Texier et al. [1988], the γ_{H_2} is lower. Still, the vertical profiles of γ_{H_2} in both studies are comparable.

The fundamental study of le Texier et al. [1988] does not capture the influence of the increasing loss of H_2O at higher altitudes. They only considered the direct yield of H_2O and do not include H_2O loss in their calculation. Nevertheless, the findings in this thesis show, that the difference between effective and direct yield becomes only apparent above 0.1 hPa and le Texier et al. [1988] do not discuss results above this pressure level. Yet, it seems critical to use the results of le Texier et al. [1988] to justify the approximation of $\gamma_{H_2O}=2$ at lower altitudes.

Hurst et al. [1999] calculated a net production of H_2O of 1.973 ± 0.003, which includes a loss of H via H_2 of 0.027 ± 0.003. These values differ from the findings in the box model approach. The

estimated γ_{H_2O} is smaller and the corresponding γ_{H_2} is larger than estimated by Hurst et al. [1999]. As noted before, by using observational data it is not possible to distinguish between H_2 from the troposphere and H_2 produced by H from CH_4, which results in this rather low net production of H_2. Assume, for example, that H_2 is not produced in the stratosphere. The mixing ratio of H_2 will then decrease with respect to altitude. However, the contribution from CH_4 oxidation onto H_2 fills up the oxidized molecules, and only if $\gamma_{H_2} \cdot [CH_4]$ is larger than the total loss of H_2, observed H_2 and CH_4 are anti-correlated. Using the kinetic tagging provides the opportunity to distinguish between the total loss of H_2 and the loss of those H_2 molecules carrying H from CH_4. The findings in this chapter offer therefore an additional insight into processes, which determine the observed vertical profiles and provide estimates for the contribution of CH_4 separated from the background H_2 and H_2O.

It must be noted, however, that a small fraction of H_2O potentially is produced from H_2 ascending from the troposphere. This likely reduces the SWV bias in GCMs simulations using the approximation of $\gamma_{H_2O}=2$, since those models do not include a separate H_2O production from H_2 oxidation. Nevertheless, to be punctilious, the yield of H_2O from CH_4 oxidation should be distinguished from the net chemical production of H_2O. In subsequent studies, it is intended to apply the tagging method for estimating a γ_{H_2O} from H_2 oxidation ($\gamma_{H_2O}(H_2)$). H_2 and CH_4 may oxidize at a similar rate, but the resulting products are different, which likely results in a varied γ_{H_2O} with respect to the source gas (i.e. $\gamma_{H_2O}(CH_4) \neq \gamma_{H_2O}(H_2)$).

Another important disadvantage of the parameterization as in Eq. (7.1) with $\gamma_{H_2O}=2$ is that it does not account for the loss of H_2O in the mesosphere. Even though CH_4 oxidation becomes negligible at these altitudes, this simple parameterization does not consider that H_2O gets chemically destroyed. Strictly speaking, the loss of H_2O is independent of CH_4 and should potentially be included separately. MacKenzie and Harwood [2004] and McCormack et al. [2008] presented, for example, sophisticated parameterizations, which target this issue in their 2D atmospheric models. Based on the results in this chapter, it is recommended to apply a parameterization, which is not solely based on the loss of CH_4, but accounts for the reduced yield in the lower stratosphere and also includes the loss of H_2O.

Besides this, transport of intermediates is an important factor for the vertical profile of the γ_{H_2O}. It must be noted that atmospheric transport is not constant in time. The Brewer-Dobson circulation for example is predicted to change in future climate projections [Butchart et al., 2010]. For a comprehensive parameterization of γ_{H_2O} these changes in transport must be taken into account. However, changes in transport depend on various factors and are therefore difficult to be included into γ_{H_2O} parameterizations. This raises the question, whether a simplified parameterization of γ_{H_2O} is indeed applicable for future climate projections or if it is necessary to simulate the full-chemistry, if an accurate SWV is desired.

7.4   Summary

Summarizing, the analysis in this chapter re-evaluates the assumption that two molecules of H_2O are produced by one oxidized CH_4 molecule. In order to do so, a comprehensive systematic analysis using a state-of-the art CCM, namely the EMAC model, is performed and three approaches to investigate the yield of H_2O and H_2 from CH_4 oxidation are presented. This includes the application of the interactive chemistry module MECCA in a box model and global model configuration. Furthermore, MECCA-TAG is used to investigate the chemical pathways between CH_4, H_2O and H_2, by being able to distinguish between hydrogen atoms stemming from CH_4 and other sources. For reasons of simplification, the study focuses on the tropical zone between 23° S-23° N, where seasonal variations are negligible. Nevertheless, results of the global approach confirm that presented results are mostly

valid for mid latitudes as well.

The three presented approaches agree that applying a constant $\gamma_{H_2O}=2$ as the contribution to H_2O by the oxidation of CH_4 in climate models likely overestimates the production of H_2O in the lower stratosphere (calculated as $1.5 - 1.7$). Additionally, transport and subsequent photochemical processing of longer-lived intermediates raise the local yield values in the upper stratosphere and lower mesosphere above 2 (maximum > 2.2). In the middle and upper mesosphere, the influence of loss and recycling of H_2O increases, making it a crucial factor in the parameterization of the yield of H_2O from CH_4 oxidation. An additional sensitivity study with the CAABA box model shows a dependence of the yield on the OH abundance. Besides, no significant temperature dependence is found.

These conclusions question the use of a constant yield of H_2O from CH_4 oxidation in climate modeling and encourage to apply comprehensive parameterizations, which follow the vertical profiles of the H_2O yield derived here and take the chemical H_2O loss into account.

Conclusion and Outlook

Recapitulating, methane is one of the major players in the anthropogenically caused climate change. Anthropogenic CH_4 emissions already started to rise with the increasing number of livestock and agriculture and they will remain even if combustion engines and exhaust from industries are abandoned [Wuebbels and Hayhoe, 2002]. Furthermore, CH_4 has a comparably short lifetime, hence an attractive mitigation potential [Dlugokencky et al., 2011]. However, reasons for the variable growth rates of CH_4 in the 1990s to 2010s are still highly uncertain and give rise to a lot of debates [Gosh et al., 2015, Schaefer et al., 2016, Nisbet et al., 2016, Rigby et al., 2017]. It is beyond question that it is a prerequisite to understand the atmospheric budget and growth of CH_4 to establish reasonable mitigation concepts. This, among others, requires and benefits from a comprehensive representation of CH_4 in Chemistry-Climate models.

The aim of the presented modeling study is to introduce, evaluate and understand such a representation of atmospheric CH_4 in the model system EMAC. This model is used to provide answers to the scientific questions proposed in the introduction (Chapter 1). The following paragraphs recapitulate the results shown in detail in the Chapters 4–7 in view of these scientific questions, and conclude with a summarized gain in knowledge from the present study. At the end a short outlook is given concerning the questions, which are raised by this thesis, and aims for future studies are proposed.

8.1 Summary and Conclusions

What are influencing factors onto the lifetime of atmospheric CH_4 and how does the lifetime change in a changing climate?

This question is addressed in the first part of the present thesis, which analyses the CH_4 lifetime in the simulations conducted during the ESCiMo project. In order to investigate the influencing factors onto the CH_4 lifetime in detail, in total 16 simulations carried out with the EMAC model are analyzed and compared concerning their oxidation capacity. This particularly includes the quantification of the influences of temperature and OH abundance.

Overall, the tropospheric lifetime of CH_4 in EMAC is calculated to be 8.11±0.13 a, which is at the lower end of similar estimates in literature, both, derived from observations, and model simulations [Dentener et al., 2003, Fiore et al., 2006, Prather et al., 2012, Voulgarakis et al., 2013, Nicely et al., 2017]. A major result is thereby that the CH_4 lifetime exhibits significant temporal variations, thus is not constant. Additionally, deviations of 0.5 a between the simulations are evident, caused by various model configurations.

It is found that the most important parameters for the CH_4 lifetime are temperature and the OH concentration. Both parameters depend on the applied model configuration. For instance, the chosen relaxation method (i.e., including the mean temperature or not) distinctly shapes the temperature distribution. Furthermore, the OH concentration is determined by its precursors, namely specific humidity, the photolysis rate of O_3 (forming $O(^1D)$) and the O_3 abundance itself. These precursors are in turn influenced by the model configuration. For example, the lightning flash frequency and

resulting NO_x emissions vary strongly with respect to the convection in the model and thus differ from simulation to simulation, depending on the specific configuration (e.g. by temperature nudging, ocean coupling etc.) [Jöckel et al., 2016].

Additionally, the evolution of the CH_4 lifetime with respect to the prescribed RCP 6.0 scenario is analyzed. The CH_4 lifetime is predicted to decrease until the end of the 21st century by 0.51 a or 0.77 a, depending whether an interactively coupled ocean model for the projection simulation is applied or not. This lifetime reduction is partly induced by increasing tropospheric temperatures (climate warming) and partly by increasing OH concentrations. From the analyzed vertical profiles no evidence is found for a direct relation of the temperature distribution and the OH distribution. Nevertheless, climate warming is expected to influence the OH abundance, since increasing temperatures lead to enhanced specific humidity and consequently to an increased production of OH. However, increasing OH concentrations are not observed in the simulations results until 2070 because OH is depleted by increasing emissions in the prescribed RCP scenario.

With climate warming the atmospheric lifetime of CH_4 in the model is decreasing, which further increases its mitigation potential. Conversely, additional emissions of methane negatively influence its atmospheric abundance by enlarging its atmospheric lifetime.

It is concluded that the assumption of a constant or well buffered OH content does not hold with respect to decadal time periods and between different simulations, even though these are conducted with the same model system. Boundary conditions, particularly those affecting temperature and the OH precursors, impact the atmospheric oxidation capacity.

What kind of challenges can be expected in the CH_4 emission estimation?

The so called Top-Down CH_4 emission estimation is commonly based on inverse modeling concepts. Nevertheless, different estimates deviate largely from each other [IPCC, 2013, Saunois et al., 2016a]. This is particularly the case concerning the attribution of emission categories and the corresponding region, if such a separation of the emissions is included anyway. The first part of this thesis shows that the oxidation capacity of CH_4 varies depending on the overall climatic conditions and the model configuration, which is potentially a reason for the discrepancies in the estimated emission inventories. This is supported by other studies, which concluded a decisive influence of the OH abundance on the atmospheric CH_4 mixing ratio and growth rates [Fiore et al., 2006, McNorton et al., 2016, Rigby et al., 2017].

The study in Chapter 5 particularly investigates the impacts of different OH distributions and model systems onto the estimated emission inventories. The study further evaluates the feedback of such an inverse optimized emission inventory onto the interactive chemistry and the oxidation capacity of the atmosphere. It is found that the assumed CH_4 sink is a decisive factor for the emission estimation. This includes the OH distribution, as well as the applied reaction rate coefficient of the $CH_4 + OH$ reaction, and the simulated temperature, all three being determining factors of the CH_4 lifetime.

Next, a newly-estimated, inverse optimized, a posteriori emission inventory is presented. This is derived using a fixed-lag Kalman Filter applied to simulation results from a forward simulation conducted with a simplified CH_4 chemistry in EMAC based on an annually repeated monthly resolved OH distribution. The derived fluxes of the a posteriori emission inventory are within earlier Top-Down estimates but disagree with Bottom-Up estimates, which are used as the a priori information in terms that e.g. anthropogenic emissions in China are not as large as previously assumed.

Forward simulations with EMAC (again applying a simplified CH_4 chemistry) reveal that the emission inventory is only valid with respect to the prescribed OH distribution of the a priori simulation. If a different OH distribution is applied, instead of the one used for the a priori forward simulation,

the deviation between simulation and observations increases drastically.

Additionally an interactive chemistry simulation is conducted. This simulation indicates an increased CH_4 lifetime, while the CH_4 mixing ratio and airmass weighted OH concentration compares to the prescribed OH distribution in the simulation with simplified CH_4 chemistry. The interactive chemistry includes the chemical feedback onto the OH sink of CH_4. Thus, the increased CH_4 mixing ratio and emission inventory lead to a modified OH distribution. The OH adjusts according to the applied CH_4 emissions. This suggests that the emissions determine the CH_4 mixing ratio, which is fairly independent of the feedbacks of the interactive chemistry onto the OH field.

This raises the question whether the differences in the vertical distribution of OH between the carried out simulations is influential onto the CH_4 distribution, if the average tropospheric concentration of OH is the same. The discrepancy between the derived CH_4 lifetime and the airmass weighted OH concentration questions the suitability of the CH_4 lifetime as a direct measure of the oxidation capacity. The airmass weighted OH concentration represents the impact onto the CH_4 abundance, while the CH_4 lifetime depends greatly on the actual distribution of OH.

Nevertheless, the oxidation capacity in terms of the magnitude of the OH concentration is an important factor for the CH_4 mixing ratio. Thus, an accurate estimation of CH_4 emissions requires knowledge about the OH abundance. Current estimates of OH depend largely on the model system and the used proxy (^{14}CO, CH_3CCl_3, etc.). Model estimates of OH are uncertain of up to 80% [Nicely et al., 2017], and OH is also poorly constrained by direct observations. For this reason, it is recommended that future CH_4 emission estimates are set into context with the corresponding assumed CH_4 sink, and that, preferably, the sources and sinks of CH_4 are jointly estimated.

How does knowledge about the isotopological signature of atmospheric CH_4 benefit the estimation of the global CH_4 budget?

The isotopic signature of various compounds is already widely used in many scientific areas to determine their origin, age and composition. If sources and sinks of CH_4 alike are in the focus for the estimation of the CH_4 budget as proposed above, the investigation of CH_4 isotopologues is a powerful method to jointly constrain these.

In order to provide this opportunity to include isotopologues of CH_4 into the analysis of the CH_4 budget, the EMAC model is extended to allow for tracing this additional information. This is done in EMAC on the one hand by implementing the CH_4 isotopologue chemistry to the simplified CH_4 chemistry with prescribed sinks and on the other hand by a new configuration of the kinetic chemistry tagging technique [Gromov et al., 2010] in the interactive chemistry. Especially the comparison of these two concepts of simulating CH_4 isotopologues provides additional insights into the influence of sink feedbacks onto the CH_4 budget and its isotopic composition, since the interactive chemistry changes the CH_4 sinks due to chemical feedbacks.

The corresponding model developments are assessed by two simulations, one with the simplified and one with the interactive chemistry. Both simulations are performed with the a posteriori emission inventory from the inversion, as mentioned above.

The evaluation of the developments using observational data indicates that the vertical and meridional gradients of $\delta^{13}C(CH_4)$ and $\delta D(CH_4)$ are well represented in both simulations. The results show further that the simulated $\delta^{13}C(CH_4)$ agrees well with the observations. Moreover, the simulation with interactive chemistry overall agrees better with the observed CH_4 mixing ratios and it is assumed that therefore the sink reactions better represent the actual sink in the atmosphere. Based on this, the slightly worse agreement with observations in terms of $\delta^{13}C(CH_4)$ compared to the simplified chemistry indicates that the chosen emission signatures for $^{13}CH_4$ are marginally isotopically too

light. The mismatch of the $\delta D(CH_4)$ signatures is even more pronounced, which indicates the chosen emission signatures as being isotopically too heavy concerning D.

The comparison of the vertical profile with high-altitude balloon observations from Röckmann et al. [2011] indicates some deficiencies in the representation of the polar stratospheric air, which is depleted in CH_4 and simultaneously isotopically enriched. The discrepancy between simulation and observation is associated with the underestimated residence time of air masses in the middle atmosphere in EMAC [Dietmüller et al., 2017] and a mismatch of the extent and temporal variation of the polar vortex in the simulations. This incidentally suggests that CH_4 and its isotopological content are potential tracers to constrain the representation of processes forming the composition of arctic air. However, the observational data basis to date is very sparse. Also, since the high-altitude evaluation focuses on observations in the northern hemisphere, the provided results need to be verified by observations in the southern hemisphere as well.

Additional to the model developments for the CH_4 isotopologues, one oxidation product of CH_4, namely H_2O, is considered as well concerning its isotopic content. Previous model developments on H_2O isotopologues [Eichinger et al., 2015a] are successfully coupled to both, the simplified, and the interactive isotopic CH_4 chemistry as part of this thesis. The expanded model now provides the opportunity to trace the isotopic content of CH_4 from the source to its oxidation products. The comparison between simulations with a simplified and an interactive chemistry reveals that important fractionation processes in the production of HDO in the stratosphere are not captured by the simplified CH_4 chemistry. A comparison to satellite observations [Steinwagner et al., 2007, Lossow et al., 2011] shows that in the interactive chemistry, although the absolute abundances of H_2O and HDO are not reproduced by the simulation, the $\delta D(H_2O)$ signature, thus, the relative content of H_2O and its isotopologues, indeed is.

Summarizing, the present work enables and evaluates the simulation of the isotopological content of CH_4 and H_2O in EMAC concerning ^{13}C and D. This is a first step towards a modeling framework to constrain the sources and sink processes of CH_4 by using observable isotopic information.

How much water vapor is introduced into the stratosphere by CH_4 oxidation?

The evaluation of the isotopological composition of H_2O in the stratosphere shown above reveals that the stratosphere simulated with an interactive chemistry is overall dryer compared to a stratosphere simulated with a simplified chemistry. This is partly associated with a lower cold point temperature in the interactive chemistry simulation. However, it is also investigated whether the common assumption holds that two H_2O molecules are produced per oxidized CH_4 molecule.

A comprehensive analysis of the chemical yield of H_2O from CH_4 oxidation in the middle atmosphere is presented. Results of three different approaches to estimate this yield (γ_{H_2O}) are shown and advantages and challenges are discussed.

It is concluded that the widely used assumption that one CH_4 molecule produces two water molecules overestimates the kinetic H_2O production in the stratosphere up to 4 hPa and in the mesosphere above 0.2 hPa. The results also show that a local yield larger than 2 in certain areas is possible through ascended comparably long-lived intermediate oxidation products. Transport is generally an issue when dealing with kinetic yields since it influences the chemical regimes at all altitudes. It also renders the interpretation of the presented approaches challenging, when these are investigated separately.

Nevertheless, γ_{H_2O} is shown to be substantially lower than 2 in the lower stratosphere, has a local maximum between 0.2 and 0.4 hPa and is exceedingly low in the upper mesosphere. Furthermore, a low γ_{H_2O} in the middle and upper mesosphere is found since the loss of H_2O at higher altitudes

increases, shifting the equilibrium between H_2O and H_2 towards H_2. The chemical loss is therefore a crucial factor for the correct parameterization of SWV production from CH_4 oxidation. At some point, the loss of H_2O is so strong that H_2O is effectively destroyed per oxidized CH_4.

Moreover, the chemical yield of H_2O depends on the OH concentration and, more general, on the chemical regime (e.g. lower vs. upper stratosphere). A strong temperature dependence, however, could not be detected.

Furthermore, the presented results agree with earlier kinetic estimates of γ_{H_2O} from le Texier et al. [1988], who state that not exactly two molecules are produced from CH_4 oxidation. The results further elucidate observations (e.g. Hurst et al. [1999], Rahn et al. [2003]), which are limited in detecting the chemical origin of H_2O.

In consequence, calculating the yield of H_2O from CH_4 oxidation requires that the loss of H_2O is taken into account and renders the task of creating a simple parameterization challenging. In order to represent the chemical interrelations it is necessary to create a subset of the chemical mechanism. The extent of such a subset is determinative for the correct representation of the H_2O content in the middle atmosphere. However, it must be noted that a set of reactions required for the comprehensive simulation of H_2O kinetics is not substantially different from the one incorporated in the comprehensive chemistry set-up and is therefore less beneficial in terms of computational resources than a parameterized model. Nevertheless, as stated before, an oversimplified parameterization introduces large uncertainties, rendering it challenging to preserve the required accuracy for applications in the simulation of climate projections, where atmospheric dynamics (e.g. the Brewer-Dobson circulation) and chemistry potentially differ from the present-day atmosphere.

8.2 Outlook

The presented results highlight the fact that uncertainties are associated with both, sources, and sinks of CH_4 and that both are equally important. Furthermore, the given conclusions stress that further studies are needed to improve the knowledge especially concerning the sink of CH_4 via OH.

Nevertheless, the employed framework of CH_4 isotopologues in this thesis provides the highly valuable opportunity to investigate sources and sinks simultaneously. Additionally, the coupling to the isotopical hydrological cycle extends this framework even to the oxidation product H_2O. This enables further studies concerning the sources, global budget and sinks of CH_4.

Starting with the overall representation of the total CH_4 mixing ratio in EMAC, it must be noted that although the a posteriori emission inventory does improve the agreement with observations, the absolute values are not fully reproduced, yet, due to the initial condition. To refine the simulated CH_4 and therefore the agreement with observations, an accurate initial condition is required. In order to achieve this, either the investigation period needs to be enlarged or an initial condition based on a nudged simulation needs to be used. It yet has to be assessed whether the latter appropriately represent the CH_4 budget, not only at the surface but also concerning the vertical profile.

Additionally, in future simulations including CH_4 isotopologues, the inverse optimized emission inventory needs to be further refined. In particular a separation of biogenic and fossil sources is desirable. In a next step, the signatures associated with the emission categories need to be further investigated. A sensitivity study with various combinations of emission signatures can potentially constrain the present emission signatures in order to better represent atmospheric observations. By doing so, it is further possible to identify whether the inverse optimized inventory is able to reproduce the atmospheric isotopic composition of CH_4 within reasonable uncertainties of the source signatures and would constitute the first step towards the inclusion of isotopic signatures into the CH_4 emission

estimation.

It is shown that the stratospheric vertical profile of the H_2O production from CH_4 oxidation is vertically not constant. It is expected that this holds for the HDO production from CH_3D as well. Since the current parameterization in the CH4 submodel based on Eichinger et al. [2015a] does not fully capture the fractionation effects and impact factors onto HDO in the stratosphere, a similar study concerning the production of HDO from CH_3D oxidation is recommended. This should further include the investigation of the impact of H_2 and HD, which are produced in the troposphere and transported into the stratosphere, onto the stratospheric H_2O and HDO content.

As a closing remark, this thesis provides a comprehensive overview of the state-of-the-art CH_4 modeling. It points towards important aspects and challenges in the simulation of CH_4, which in turn motivates and demands future studies. Altogether, an improved simulation of CH_4 and its isotopologues requires additional observational data. Particularly the polar region and the, regarding CH_4, prominent regions in Asia and South America need to be further constrained.

Acronyms, Symbols and Chemical Tracer

Acronyms

AGAGE	Advanced Global Atmospheric Gases Experiment.
AIRS	Atmospheric Infrared Sounder.
AO-CCM	Atmosphere-Ocean Chemistry-Climate model.
ASA	Aire sur l'Adour in France.
ASE	Automatic air Sampling Equipment.
BDC	Brewer-Dobson circulation.
BL	boundary layer.
BMIL	Base Model Interface Layer.
BML	Base Model Layer.
CAABA	Chemistry As A Boxmodel Application.
CCM	Chemistry-Climate model.
CCMI	Chemistry-Climate Model Initiative.
CERA	Climate and Environmental Retrieval and Archive.
CESM	Community Earth System Model.
CH4	simplified CH_4 chemistry.
CONTRAIL	Comprehensive Observation Network for TRace gases by AIrLiner.
COSMO	Consortium for Small-Scale Model.
CRDS	Cavity Ring Down Spectroscopy.
CTM	Chemical Transport model.
DJF	December, January, and February.
DKRZ	*Deutsches Klimarechenzentrum*.
ECHAM5	5th generation European Centre Hamburg general circulation model.
EIE	Equilibrium Isotope Effect.
EMAC	ECHAM/MESSy Atmospheric Chemistry.
EMPA	*Eidgenössische Materialprüfungs- und Forschungsanstalt*.
ENVISAT	ENVIronmental SATellite.
ESCiMo	Earth System Chemistry integrated Modelling.
flKF	fixed-lag Kalman Filter.
FTIR	Fourier transform infrared.
FTS	Fourier Transform Spectrometer.
GAP	Gap in France.

GAW	Global Atmosphere Watch.
GCM	General Circulation model.
GHG	greenhouse gas.
GOSAT	Greenhouse gases Observing SATellite.
GWP	global warming potential.
H2OISO	H_2O ISOtopologues.
HPC	high performance computer.
HYD	Hyderabab in India.
IASI	Infrared Atmospheric Sounding Interferometer.
IPCC	Intergovernmental Panel on Climate Change.
IRMS	isotope ratio mass spectrometry.
JJA	June, July, and August.
JMA	Japan Meteorological Agency.
KF	Kalman Filter.
KIE	Kinetic Isotope Effect.
KIR	Kiruna in Sweden.
KPP	kinetic preprocessor.
LBC	lower boundary condition.
LIDAR	LIght Detection And Ranging.
MAM	March, April, and May.
MBL	Marine Boundary Layer.
MECCA	Module Efficiently Calculating the Chemistry of the Atmosphere.
MECCA-TAG	kinetic chemistry tagging technique.
MERLIN	MEthane Remote LIdar missioN.
MESSy	Modular Earth Submodel System.
MIPAS	Michelson Interferometer for Passive Atmospheric Sounding.
MMM	multi model mean.
MOM	Mainz Organic Mechanism.
MSBM	Multi-phase Stratospheric Box Model.
MSM	multi simulation mean.
NH	northern hemisphere.
NOAA/ESRL	National Oceanic and Atmospheric Administration/Earth System Research Laboratory.
OFFEMIS	OFFline EMISsions.
PDB	PeeDee Belemnite.
PDF	probability density function.
PSC	polar stratospheric cloud.

QBO	quasi-biennial oscillation.
QCLAS	quantum cascade laser absorption spectroscopy.
RCP	Representative Concentration Pathways.
RF	radiative forcing.
SCIAMACHY	Scanning Imaging Absorption Spectrometer for Atmospheric Cartography.
SH	southern hemisphere.
SIC	sea ice concentration.
SMCL	Submodel Core Layer.
SMIL	Submodel Interface Layer.
SON	September, October, and November.
SST	sea surface temperature.
STE	stratosphere-troposphere exchange.
SWIR	shortwave infrared.
SWV	stratospheric water vapor.
TANSO-FTS	Thermal And Near-infrared Sensor for carbon Observation - Fourier transform spectrometer.
TCCON	Total Carbon Column Observing Network.
TIR	thermal infrared.
TROPOMI	TROPOspheric Monitoring Instrument.
TRSYNC	TRacer SYNChronization.
UTLS	Upper Troposphere and Lower Stratosphere.
VSMOW	Vienna Standard Mean Ocean Water.
WDCGG	World Data Center for Greenhouse Gases.
WMO	World Meteorological Organization.

Symbols

$\delta D(CH_4)$	delta value concerning D of CH_4.
$\delta D(H_2O)$	delta value concerning D of H_2O.
$\delta D(H_2)$	delta value concerning D of H_2.
$\delta^{13}C(CH_4)$	delta value concerning ^{13}C of CH_4.
γ_{H_2O}	yield of H_2O from the oxidation of CH_4.
γ_{H_2}	yield of H_2 from the oxidation of CH_4.
$\mathbf{L}_{CH_4}$	loss of CH_4.
‰	per thousand.
τ_{CH_4}	lifetime of CH_4.
$\tau_{CH_4}(OH)$	lifetime of CH_4 with respect to OH.
$j_{O_3 \rightarrow O(^1D)}$	phololysis rate of $O_3 \rightarrow O(^1D)$.
$[OH]_{AW}$	airmass weighted OH concentration.

$[OH]_{EMAC-apos-03}$	OH provided by the EMAC-apos-03 simulation.
$[OH]_{MMM}$	OH derived by a multi-model-mean.
$[OH]_{RC1SD-base-10}$	OH provided by the RC1SD-base-10 simulation.
`CH4_fx`	CH_4 tracer of the CH4 submodel.

a	year.
a^{-1}	per year.

$kg\ kg^{-1}_{moist\ air}$	one kg of the tracer per one kg of moist air.

molec.	molecules.
$mol\ mol^{-1}$	one mole of the chemical tracer per one mole of dry air.

ppbv	parts per billion volume.
ppmv	parts per million volume.

q	specific humidity.

$Tg\ CH_4\ a^{-1}$	10^{12} g CH_4 per year.

Chemical Tracer

^{12}C	carbon-12.
$^{12}CH_4$	methane containing ^{12}C.
^{13}C	carbon-13.
$^{13}CH_4$	methane containing ^{13}C.
^{14}CO	carbon monoxide containing radio carbon.

Br	bromine.

C	carbon.
CFC	chlorofluorocarbon.
CH_2DO	deuterated CH_3O.
CH_3	methyl.
CH_3CCl_3	methylchloroform.
CH_3O	methoxy radical.
CH_2D	deuterated methyl.
CH_3D	deuterated methane.
CH_4	methane.
Cl	chlorine.
CO	carbon monoxide.
CO_2	carbon dioxide.

D	deuterium.
DO_2	deuterated hydroperoxyl.

H	atomic hydrogen.

H_2	hydrogen gas.
H_2O	water vapor.
HCFC	hydrochlorofluorocarbon.
HCHO	formaldehyde.
HD	deuterated hydrogen gas.
HDO	deuterated water vapor.
HNO_3	nitric acid.
HO_2	hydroperoxyl.
HO_x	odd hydrogen.
I	jodine.
LNO_x	NO_x produced from lightning activity.
N_2O	nitrous oxide.
NMHC	non-methane hydrocarbon.
NO_2	nitrogen dioxide.
NO_x	nitrous oxides.
O	atomic oxygen.
O_2	molecular oxygen.
O_3	ozone.
$O(^1D)$	excited oxygen.
OD	the deuterated hydroxyl radical.
OH	the hydroxyl radical.

Definitions and Propositions

B.1 Reaction Rates of CH$_4$ Depletion

The reaction rates for the reaction (R1 - R3) applied in this study are:

$$k_{OH} = 1.85 \times 10^{-20} \cdot \exp(2.82 \cdot \log(T) - \frac{987}{T}) \tag{B.1}$$

$$= 1.85 \times 10^{-20} \cdot T^{2.82} \cdot \exp\left(-\frac{987}{T}\right) \tag{B.2}$$

$$k_{Cl} = 6.6 \times 10^{-12} \cdot \exp(\frac{-1240}{T}) \tag{B.3}$$

$$k_{O1D} = 1.75 \times 10^{-10} \tag{B.4}$$

Eq. (B.3) and (B.4) are from Sander et al. [2011a] and Eq. (B.1) from Atkinson [2003]

For certain sensitivity studies a varied reaction rate for (R1) from Sander et al. [2011a], Bonard et al. [2002] is used:

$$k_{OH} = 2.8 \times 10^{-14} \cdot \exp(0.667 \cdot \log(T) - \tfrac{1575}{T}) \tag{B.5}$$

A two parameter reaction rate for (R1) is recommended by Sander et al. [2011a] with:

$$k_{OH} = 2.45 \times 10^{-12} \cdot \exp(-\tfrac{1775}{T}) \tag{B.6}$$

Another three parameter reaction rate from Dunlop and Tully [1993] for (R1) is used for the presented FLEXPART simulations:

$$k_{OH} = 9.65 \times 10^{-20} \cdot \exp(2.58 \cdot \log(T) - \tfrac{1082}{T}) \tag{B.7}$$

B.2 Fundamental Physical Equations

A climatological tropopause height

Tropopause height in terms of pressure p (in hPa):

$$p = 300 - 215 \cdot (cos(\Phi))^2 \tag{B.8}$$

with Φ being the latitude in degrees north Jöckel et al. [2000]. This paramterization was derived by fitting a cosinus function to a climatological mean of tropopause heights.

The ideal gas equation

Especially for the unit conversion from kg kg$^{-1}_{\text{moist air}}$ to mol mol$^{-1}_{\text{dry air}}$ and from mixing ratio to concentration, the concentration of air is used, which is derived via the ideal gas equation.

$$p = \frac{n_0}{N_A} \cdot R_{gas} \cdot T \,, \tag{B.9}$$

with n_0 being molecules per unit volume (here $[\frac{molec.}{m^3}]$), p is pressure (of moist air) and T is temperature in K. R_{gas} is the gas constant in $[\frac{J}{K\,mol}] = [\frac{kg\,m^2}{\frac{s^2}{K\,mol}}]$ and N_A is the Avogadro constant (both, see Section B.3),

Concentration of air

Using the ideal gas equation one can derive a formula for the concentration of air:

$$p = \frac{n_0}{N_A} \cdot R_{gas} \cdot T$$

$$\Rightarrow n_0 = N_A \cdot \frac{p}{R_{gas} \cdot T}$$

For c_{air} in molecules per cm^3 dry air, multiply with: $10^{-6}\frac{m^3}{cm^3} \cdot \frac{M_{\text{moist air}}}{M_{air}} = 10^{-6}\frac{m^3}{cm^3} \cdot (1 + (\frac{M_{air}}{M_{H2O}} - 1) \cdot q)^{-1}$. Note M_{air} denotes the molar mass of dry air and $M_{\text{moist air}} = \frac{g_{air} + g_{H_2O}}{mol_{air} + mol_{H_2O}}$.

It follows:

$$n_0 = N_A \cdot \frac{p}{R_{gas} \cdot T}$$

$$n_0 \cdot 10^{-6}\frac{m^3}{cm^3} \cdot \frac{M_{\text{moist air}}}{M_{air}} = \frac{N_A}{10^6} \cdot \frac{p}{R_{gas} \cdot T \cdot \frac{M_{air}}{M_{\text{moist air}}}} \,,$$

which results in concentration of air c_{air} as a function of pressure p in Pa, temperature T in K and specific humidity q in kg kg$^{-1}_{\text{moist air}}$:

$$c_{air}(p, T, q) = \frac{N_A}{10^6} \cdot \frac{p}{R_{gas} \cdot T \cdot (1 + (\frac{M_{air}}{M_{H2O}} - 1) \cdot q)} \cdot \tag{B.10}$$

Unit conversion:

The unit conversion of specific humidity q in kg kg$^{-1}_{\text{moist air}}$ to mixing ratio μ_{H_2O} in mol mol$^{-1}_{\text{dry air}}$ and back:

$$\mu_{H_2O} = \frac{M_{air}}{M_{H_2O}} \frac{q}{1 - q} \tag{B.11}$$

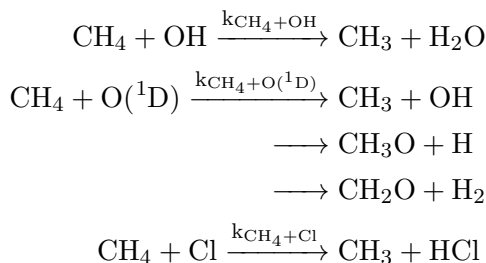$$q = \left(1 + \frac{M_{air}}{M_{H_2O}} \frac{1}{\mu_{H_2O}}\right)^{-1} \tag{B.12}$$

B.3   Constants

- Avogadro constant: $N_A = 6.02214129(27) \times 10^{23}\frac{1}{mol}$

- Gas constant: $R_{gas} = 8.3145[\frac{J}{K\,mol}] = 8.3145 \left[\frac{kg\,m^2}{\frac{s^2}{K\,mol}}\right]$

- Molar mass of dry air: $M_{air} = 28.970\frac{g_{air}}{mol_{air}}$

- Molar mass of H$_2$O: $M_{H_2O} = 18.02\frac{g_{H_2O}}{mol_{H_2O}}$, HDO: $M_{HDO} = 19.02\frac{g_{HDO}}{mol_{HDO}}$

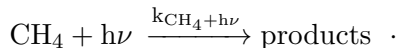- Molar mass of CH$_4$: $M_{CH_4} = 16.04\frac{g_{CH_4}}{mol_{CH_4}}$

Documentation of the CH4 submodel

C.1 Introduction

The CH4 submodel represents a simplified CH_4 chemistry. The simplification is achieved by reducing the chemical mechanism to the four sink reactions of CH_4, namely the reaction with OH, $O(^1D)$, and Cl:

$$CH_4 + OH \xrightarrow{k_{CH_4+OH}} CH_3 + H_2O$$

$$CH_4 + O(^1D) \xrightarrow{k_{CH_4+O(^1D)}} CH_3 + OH$$

$$\longrightarrow CH_3O + H$$

$$\longrightarrow CH_2O + H_2$$

$$CH_4 + Cl \xrightarrow{k_{CH_4+Cl}} CH_3 + HCl$$

and the depletion by photolysis:

$$CH_4 + h\nu \xrightarrow{k_{CH_4+h\nu}} products \ .$$

The reaction partners are thereby imported from external data. All changes of the reaction partners are neglected.

The CH4 submodel defines the tracer, i.e. `CH4_fx`. This tracer is initialised from external data via TRACER [Jöckel et al., 2008] and modified by either emissions, which need to be introduced via the submodel OFFline EMISsions (OFFEMIS) [Kerkweg et al., 2006b] or by Newtonian relaxation towards a lower boundary condition with the submodel TNUDGE [Kerkweg et al., 2006b]. It further gets reduced via the above reactions. Optionally, a feedback onto the specific humidity can be applied.

Additional to that, the CH4 submodel is extended with two features. One is the simulation of the CH_4 isotopologues and the other one is the representation of age- and emission classes of CH_4, which, to some extent, are able to resolve an additional spatial and temporal information of the CH_4 emissions.

The extension concerning the CH_4 isotopologues can optionally be applied with respect to ^{13}C isotopologues, D isotopologues, or both. The submodel defines the following tracers for the given isotopologues: `CH4_12C` ($^{12}CH_4$), `CH4_13C` ($^{13}CH_4$), `CH4_D0` (CH_4), and `CH4_D1` (CH_3D). The reaction rates k_H (H for heavy) of the individual sink reactions of the rare isotopologues ($^{13}CH_4$ and CH_3D) are equal to the reaction rates of the abundant isotopologue k_L (L for light), but are scaled by the applied KIEs, which are user defined via the submodel CTRL namelist, i. e.

$$k_H = \frac{1}{KIE} \cdot k_L \ .$$

The extension concerning the age- and emission classes introduces additional tracers depending on the chosen number of age and emission classes. For every combination of age- and emission class one

tracer is created, thus, if N is the number of age classes and M is the number of emission classes, in total $N \times M$ additional tracers are created. The tracers are denoted by the names `CH4_fx_e[mm]_a[nn]`, with `[mm]` being the identifying number of the emission class and `[nn]` the number of the age class.

The following documents the subroutines, which are part of the CH4 submodel and in the section "User interface" the entries in the corresponding namelists are explained.

C.2   MODULE messy_ch4_si: Subroutines in SMIL

These subroutines follow the general structure mandatory for MESSy submodels.

- SUBROUTINE `ch4_initialize`: Initializes the submodel, reads the control and coupling namelists and broadcasts the information to all parallel tasks.

- SUBROUTINE `ch4_new_tracer`: Creates the new tracers, which also includes the additional tracers regarding the submodel extensions (if applied).

- SUBROUTINE `ch4_init_memory`: Defines the channel objects.

- SUBROUTINE `ch4_init_coupling`: Sets pointers for coupling to the basemodel and other submodels.

- SUBROUTINE `ch4_global_start`: Sets start variables, depending on the chosen namelist parameters.

- SUBROUTINE `ch4_vdiff`: Currently not used.

- SUBROUTINE `ch4_physc`: Entry point in time loop. This subroutine calls the integration step of the submodel, i.e. `ch4_integrate`. It further adds the H_2O feedback, if it is switched on. The tendencies for the age- and emission class tracers and the isotopologue tracers are calculated in separate integration routines, namely `class_integrate_gp/lg` and `iso_integrate_gp/lg`.

- SUBROUTINE `ch4_global_end`: Dedicated as entry point in time loop for LG calculations, but currently not used.

- SUBROUTINE `ch4_free_memory`: Deallocation of allocated memory.

C.3 MODULE messy_ch4: Subroutines in SMCL

The following subroutines represent the core layer of the submodel.

SUBROUTINE ch4_integrate		(CH4_te, CH4, OH, O1D, Cl, j_CH4, temp, press, spechum, iso_id)	
name	type	intent	description
mandatory arguments:			
CH4_te	REAL	OUT	CH_4 tendency
CH4	REAL	IN	CH_4 mixing ratio
OH	REAL	IN	OH mixing ratio
O1D	REAL	IN	$O(^1D)$ mixing ratio
Cl	REAL	IN	Cl mixing ratio
j_CH4	REAL	IN	photolysis rate of CH_4
temp	REAL	IN	temperature
press	REAL	IN	pressure
spechum	REAL	IN	specific humidity
iso_id	INTEGER	IN	ID of isotopologue

description:
This subroutine executes the integration step of the submodel. It applies the implemented reaction rate functions of the sink reactions of CH_4 and accounts for the KIE in the case of rare isotopologues.

SUBROUTINE sca_tend		(m, mte, s, ste, dt, a)	
name	type	intent	description
mandatory arguments:			
m	REAL	IN	master tracer
mte	REAL	IN	tendency of master tracer
s	REAL	IN	sum of fractional tracers
ste	REAL	IN	sum of fractional tracer tendencies
dt	REAL	IN	time step length
a	REAL	OUT	resulting correction factor

description:
Calculates the necessary correction factor so that the fractional tracers including their tendencies add up to the master tracer (incl. its current tendency).

SUBROUTINE adj_tend		(f, t, a, dt, tadj)	
name	type	intent	description
mandatory arguments:			
f	REAL	IN	fractional tracer
t	REAL	IN	tendency of fractional tracer
a	REAL	IN	correction factor
dt	REAL	IN	time step length
tadj	REAL	OUT	resulting additional tendency for adjustment

description:
Calculates the necessary additional tendency to adjust for the given correction factor.

SUBROUTINE ch4_read_nml_ctrl		(status, iou)	
name	type	intent	description
mandatory arguments:			
status	INTEGER	OUT	error status info
iou	INTEGER	IN	I/O unit

description:
This subroutine is used to read the CTRL-namelist of the submodel.

C.4   User interface

CH4 CTRL namelist

The control (CTRL) namelist of the CH4 submodel includes the entries concerning the KIE values applied in the isotopologue extension of the submodel. This includes the KIEs for all four sink reactions and both isotopologues. The entries are: KIE_CH4_13C_OH, KIE_CH4_13C_O1D, KIE_CH4_13C_CL, KIE_CH4_13C_jval, KIE_CH4_D1_OH, KIE_CH4_D1_O1D, KIE_CH4_D1_CL and KIE_CH4_D1_jval.

The KIE is represented in the form $KIE = A \cdot \exp(B/T)$, with A and B being the individual parameters and T the temperature in [K]. The namelist entries are given therefore as:
KIE_CH4_XX_YY = A, B.
For those KIE, which are temperature independent, B is set to 0.0.

CH4 CPL namelist

The coupling (CPL) namelist of the CH4 submodel sets the parameters for the applied extensions and feedback on the specific humidity. It further controls the used channel objects used as the reaction partners in the CH$_4$ oxidation.

- i_H2O_feedback takes an integer, which controls the feedback of CH$_4$ oxidation on the specific humidity. Allowed values are: 0: no feedback, 1: feedback from GP and 2: feedback from LG. GP and LG denote Gaussian representation and Lagrangian representation, respectively.

- `l_ef_re` is a logical switch indicating whether the empirical formula introduced by Eichinger et al. [2015a] is used (`T`) or not (`F`).

- `L_GP` and `L_LG` are both logical switches implying whether the Gaussian representation (GP) or Lagrangian representation (LG), or both are applied. The following namelist entries are shown for GP, however, there a identical entries for LG as well (indicated by gp and lg, respectively).

- `c_gp_OH`, `c_gp_O1D`, `c_gp_Cl` and `c_gp_jCH4` define the chosen channel objects for the reaction partners of CH_4. They take two strings, the first indicates the channel, the second the object name.

- `i_gp_nclass_emis_age` denotes the number of emission- and age classes. It takes two integers, the first is the number of emission classes, the second is the number of age classes.

- `r_gp_age_cll` is an optional entry, which adjusts the time period (in days) of one age class. If this entry is not set, the default of 30.44 days is applied.

- `l_gp_adj_tend` is a logical optional swich, which indicates whether the tendencies are adjusted so that the additional age- and emission class tracers sum up to the master tracer `CH4_fx`. The default is `T` (true).

- `i_gp_ageing` is an integer switch indicating the ageing method, which means the advancing of CH_4 from one age class to the next older one. It can be chosen between:

  - 0: monthly in one step
  - 1: continuously (default)
  - 2: monthly

  Note, in first one the Leapfrog time stepping with the Asselin-filter might cause numerical oszillations with negative values etc.. Furthermore, the last one is not conform with the sub-model TENDENCY, hence the corresponding diagnostic output created by TENDENCY is not meaningful.

- `l_gp_iso_C` and `l_gp_iso_H` are logical switches (`.TRUE.`/`.FALSE.`) indicating wheter the iso-topologues of CH_4 concerning ^{13}C, D, or both are simulated.

C.5 Private subroutines

Private subroutines in `messy_ch4_si`

SUBROUTINE ch4_re ad_nml_cpl		(status, iou)	
name	type	intent	description
mandatory arguments:			
status	INTEGER	OUT	error status info
iou	INTEGER	IN	I/O unit
description:			
This subroutine is used to read the CPL-namelist of the submodel.			

SUBROUTINE `class_integrate_gp`		(temp, press, spechum)	
name	type	intent	description
mandatory arguments:			
temp	REAL, DIMENSION(:,:)	IN	temperature
press	REAL, DIMENSION(:,:)	IN	pressure
spechum	REAL, DIMENSION(:,:)	IN	specific humidity

description:
This subroutine calls `ch4_integrate` for every age- and emission class tracer separately.

SUBROUTINE `class_age_move_gp`		(CH4c, CH4c_te)	
name	type	intent	description
mandatory arguments:			
CH4c	REAL, DIMENSION(:,:)	IN	current CH_4 tracer mixing ratio
CH4c_te	REAL, DIMENSION(:,:)	IN	current CH_4 tracer tendency

description:
Accounts for the shifting from one age class to the next.

SUBROUTINE `class_adj_tend_gp`		(CH4c, CH4c_te)	
name	type	intent	description
mandatory arguments:			
CH4c	REAL, DIMENSION(:,:)	IN	current CH_4 tracer mixing ratio
CH4c_te	REAL, DIMENSION(:,:)	IN	current CH_4 tracer tendency

description:
Adjusts the tendencies of the age- and emission class tracers so that the tracers sum up to the master tracer `CH4_fx`, which is required to correct for potential numerical inaccuracies.

SUBROUTINE iso_integrate_gp		(temp, press, spechum, CH4_te)	
name	type	intent	description
mandatory arguments:			
temp	REAL, DIMENSION(:,:)	IN	temperature
press	REAL, DIMENSION(:,:)	IN	pressure
spechum	REAL, DIMENSION(:,:)	IN	specific humidity
CH4_te	REAL, DIMENSION(:,:)	IN	current CH_4 tracer tendency

description:
Calls `ch4_integrate` for every isotopologue tracer separately. It further
calculates the tendency added to the HDO, either by the simple assumption
that one HDO molecule is produced by one oxidized CH_3D molecule, or by the
function:

$$\frac{\partial(HDO)}{\partial t} = \frac{-\frac{\partial(CH_3D)}{\partial t} + 6.32 \times 10^{-5} \cdot \frac{\partial(CH_4)}{\partial t}}{\frac{M_{air}}{M_{HDO}} \left(\frac{1}{1-HDO}\right)^2} \ . \tag{C.1}$$

proposed by Eichinger et al. [2015a].

SUBROUTINE class_adj_tend_gp		(CH4c, CH4c_te, idt_gp_iso_adj)	
name	type	intent	description
mandatory arguments:			
CH4c	REAL, DIMENSION(:)	IN	current CH_4 tracer mixing ratio
CH4c_te	REAL, DIMENSION(:)	IN	current CH_4 tracer tendency
idt_gp_iso_adj	REAL, DIMENSION(:)	IN	list of tracer IDs

description:
Adjusts the tendencies of the isotopologue tracers so that the tracers regarding
the isotopes of the same element sum up to the master tracer `CH4_fx`, which is
required to correct for potential numerical inaccuracies.

Private subroutines in `messy_ch4`

SUBROUTINE calc_KIE		(KIE_AB_val, temp_t, KIE_t)	
name	type	intent	description
mandatory arguments:			
KIE_AB_val	REAL, DIMENSION(2)	IN	KIE parameters A and B
temp_t	REAL	IN	temperature
KIE_t	REAL	OUT	KIE value

description:
Calculates the KIE with the equation: $KIE\_t = A \cdot \exp(B/temp)$.

Documentation of the TRSYNC submodel

D.1 Introduction

In brief, TRSYNC guarantees that the physical H_2O tracers (incl. their isotopologues) receive also the correct tendencies of the corresponding chemical tracers.

The submodels H2OISO, CH4 and MECCA-TAG are responsible for the simulation of isotopologues in EMAC. CH4 creates the tracer `HDO`, the submodel H2OISO creates `H2OISOHDOvap` and MECCA-TAG in MECCA creates `I2H2O` (or a different idiom, chosen by the user). To combine the physical and chemical fractionation and their impact on the hydrological cycle in EMAC, it is necessary to couple these tracers accordingly, which is done by the auxiliary submodel TRacer SYNChronization (TRSYNC).

Overall, TRSYNC preserves the modular character of MESSy, while being able to switch between feedback onto isotopologues of H_2O from submodel CH4 or from MECCA-TAG, without altering code. It is implemented to take care of the proper synchronization of the isotopological tracers of water vapor from H2OISO and from a chemical source, either MECCA-TAG or CH4.

Without any isotopological extension solely the ECHAM5 intrinsic tracer for specific humidity (q) is present. In this case, chemically produced H_2O (either from CH4 or from MECCA) directly adds to q. However, in case of an isotopological extension using H2OISO, CH4 and/or MECCA-TAG the following additional tracers are created:

- `H2OISOHHOvap` and `H2OISOHDOvap` (created by H2OISO): The former is the total water tracer and the latter is the tracer of the rare isotopologue. Note that in H2OISO the two tracers do not add up to a master tracer, actually, `H2OISOHHOvap` represents and is identical to the master tracer (i.e. q).

- `HDO` (created by CH4).

- `I1H2O` and `I2H2O`, representing H_2O and HDO, respectively (created by MECCA-TAG): Both sum up to the chemical master tracer `H2O`.

- `H2O` (created by MECCA): This tracer is originally not created in MECCA, but is necessary in combination with MECCA-TAG for the internal scaling of `I1H2O` and `I2H2O`.

Figure D.1 depicts the schematics of the coupling. At the beginning of every time step, `H2OISOHHOvap` is set to the current value of q, correcting any numerical deviations of `H2OISOHHOvap` from q caused in the previous time step. Next, basically all tracers are modified by the same physical processes: advection, vertical diffusion and convection. However, for the submodels E5VDIFF, CONVECT and CLOUD the hydrological processes are doubled in H2OISO to allow for isotope effects. The submodel MSBM calculates a tendency for q, which is added to `H2OISOHHOvap` as well. An

equivalent tendency is added to `H2OISOHDOvap`, which is derived such that no additional fractionation by the multi-phase stratospheric chemistry is implied.

After all physical processes are complete, the submodel TRSYNC is called. It takes care that all tendencies of the previous (physical) processes of `HDO` and `I2H2O` are deleted and overwritten by the corresponding tendencies of the H2OISO equivalent `H2OISOHDOvap`. `I1H2O` is exceptional, as it must be set to the difference of the total tracer `H2OISOHHOvap` and the rare isotopologue `H2OISOHDOvap`. Note that for technical reasons the tracer `H2OISOHDOvap` is defined as one half of the corresponding chemical isotopological tracers `HDO` and `I2H2O`.

Next CH4 computes the CH_4 oxidation and derives the feedback onto q and HDO. At the very beginning of MECCA, the intrinsic `H2O` tracer is synchronized with q. Before and after KPP, `I1H2O` and `I2H2O` are scaled appropriately to add up to `H2O`. After this, the feedback onto H_2O is passed to q. To be precise, the sketch in Fig. D.1 suggests that CH4 and MECCA are executed in the same simulation. This is indeed possible, but not necessary and it should be taken care of that only one of the two is providing the chemical feedback onto q, which can be arranged by corresponding switches in the namelists.

After the chemical processes, TRSYNC synchronizes the tracers `HDO` or `I2H2O` backward onto `H2OISOHDOvap`, and H2OISO also adds the chemical tendency of q to `H2OISOHHOvap`. As a last step H2OISO adjusts the tendency of `H2OISOHHOvap` so that it is conform to the tendency of q.

The following documents the subroutines, which are part of the TRSYNC submodel and in the section "User interface" the entries of the corresponding namelist are explained.

D.2   MODULE messy_trsync_si: Subroutines in SMIL

These subroutines follow the general structure mandatory for MESSy submodels.

- SUBROUTINE `trsync_initialize`: Initializes the submodel, reads the coupling namelist and broadcasts necessary information to all parallel tasks.

- SUBROUTINE `trsync_init_memory`: Registers the tracers at the TENDENCY submodel, if the latter is applied.

- SUBROUTINE `trsync_init_coupling`: Sets pointers to the used tracers and checks whether the synchronized tracers are identical in terms of their molar mass.

- SUBROUTINE `trsync_init_tracer`: Initializes the tracers, hence checks whether the tracers are already initialized and accounts for a synchronized initial state.

- SUBROUTINE `trsync_physc`: Entry point in time loop. This subroutine is called two times. The first time before the chemistry calls of CH4 and MECCA and the second time after. It provides the necessary unit conversion and numerical adjustment to synchronize the chosen tracers.

- SUBROUTINE `trsync_free_memory`: Currently not necessary.
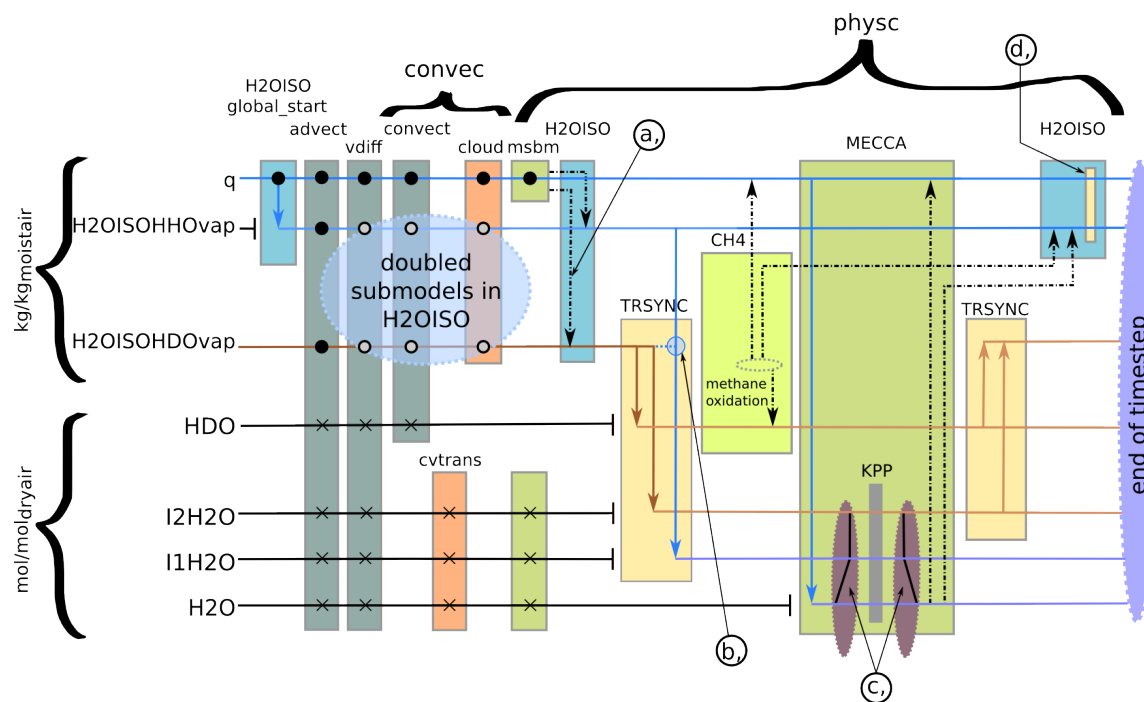
Figure D.1: Sketch depicting the coupling of the hydrological cycle tracers in EMAC. q is the intrinsic variable of ECHAM5 for water vapor. Similar, H2OISOHHOvap and H2OISOHDOvap are defined by H2OISO. q, H2OISOHHOvap and H2OISOHDOvap are in units kg $\mathrm{kg}^{-1}_{\mathrm{moist\ air}}$. HDO is created by CH4, H2O is created by MECCA, and I1H2O and I2H2O are created by MECCA-TAG in mol $\mathrm{mol}^{-1}_{\mathrm{dry\ air}}$. Arrows with dashed lines indicate that solely tendencies are added. Solid arrow lines correspond to a replacement of the contents. (a) relative tendency of MSBM of HHO tracer without fractionation, (b) sets I1H2O to the mol $\mathrm{mol}^{-1}_{\mathrm{dry\ air}}$ equivalent of H2OISOHHOvap - 2·H2OISOHDOvap, (c) adjusts I1H2O and I2H2O so that I1H2O + I2H2O = H2O, (d) numerical adjustment to ensure that the tendency of H2OISOHHOvap is equal to the tendency of q.

D.3   MODULE messy_trsync: Subroutines in SMCL

The following subroutines represent the core layer of the submodel.

SUBROUTINE convert_unit		(traten, case, type, molarmass, spechum, spechum_te, tracer)	
name	type	intent	description
mandatory arguments:			
traten	REAL	INOUT	tracer or tendency to be converted
case	INTEGER	IN	case of conversion (1: kg/kg->mol/mol or 2: mol/mol->kg/kg)
type	INTEGER	IN	type of conversion (1: tracer or 2: tendency)
molarmass	REAL	IN	molar mass of the converted tracer
spechum	REAL	IN	specific humidity
optional arguments:			
spechum_te	REAL	IN	tendency of specific humidity
tracer	REAL	IN	additional tracer mixing ratio if `traten` indicates the tendency

description:
This subroutine leads over to the private subroutines `convert_to_molmol`, `convert_to_kgkg`, `convert_to_molmol_te` and `convert_to_kgkg_te`, depending on the chosen case and type.

D.4   User interface

TRSYNC CPL namelist

The coupling (`CPL`) namelist of the TRSYNC submodel lists the tracers to be synchronized.

`TRSYNC` takes two strings and one integer switch. The first string indicates the chemical tracer in $\mathrm{mol\ mol^{-1}_{dry\ air}}$. The second string indicates the physical tracer in $\mathrm{kg\ kg^{-1}_{moist\ air}}$. The integer string denotes, whether the synchronization is done in both ways (0), the chemical tracer is synchronized by the physical tracer before chemistry only (1), or the physical tracer is synchronized by the chemical tracer after chemistry (2).

D.5 Private subroutines

Private subroutines in `messy_trsync_si`

SUBROUTINE trsync_read_nml_cpl		(status, iou)	
name	type	intent	description
mandatory arguments:			
status	INTEGER	OUT	error status info
iou	INTEGER	IN	I/O unit
description:			
This subroutine is used to read the CPL-namelist of the submodel.			

Private subroutines in `messy_trsync`

SUBROUTINE convert_to_kgkg		(tr_a, molarmass, spechum)	
name	type	intent	description
mandatory arguments:			
tr_a	REAL	INOUT	tracer in mol mol$^{-1}_{\text{dry air}}$ to be converted
molarmass	REAL	IN	molar mass of the converted tracer
spechum	REAL	IN	specific humidity
description:			
This subroutine converts the tracer `tr_a` from mol mol$^{-1}_{\text{dry air}}$ to kg kg$^{-1}_{\text{moist air}}$.			

SUBROUTINE convert_to_molmol		(tr_b, molarmass, spechum)	
name	type	intent	description
mandatory arguments:			
tr_b	REAL	INOUT	tracer in kg kg$^{-1}_{\text{moist air}}$ to be converted
molarmass	REAL	IN	molar mass of the converted tracer
spechum	REAL	IN	specific humidity
description:			
This subroutine converts the tracer `tr_b` from kg kg$^{-1}_{\text{moist air}}$ to mol mol$^{-1}_{\text{dry air}}$.			

SUBROUTINE convert_kgkg_te		(tr_a_te, tr_a, molarmass, spechum, spechum_te)	
name	type	intent	description
mandatory arguments:			
tr_a_te	REAL	INOUT	tendency in mol mol$^{-1}_{\text{dry air}}$ to be converted
tr_a	REAL	IN	corresponding tracer of tendency to be converted
molarmass	REAL	IN	molar mass of the converted tracer
spechum	REAL	IN	specific humidity
spechum_te	REAL	IN	tendency of specific humidity

description:

This subroutine converts the tendency `tr_a_te` from mol mol$^{-1}_{\text{dry air}}$ to kg kg$^{-1}_{\text{moist air}}$.

SUBROUTINE convert_molmol_te		(tr_b_te, tr_b, molarmass, spechum, spechum_te)	
name	type	intent	description
mandatory arguments:			
tr_b_te	REAL	INOUT	tendency in kg kg$^{-1}_{\text{moist air}}$ to be converted
tr_b	REAL	IN	corresponding tracer of tendency to be converted
molarmass	REAL	IN	molar mass of the converted tracer
spechum	REAL	IN	specific humidity
spechum_te	REAL	IN	tendency of specific humidity

description:

This subroutine converts the tendency `tr_b_te` from kg kg$^{-1}_{\text{moist air}}$ to mol mol$^{-1}_{\text{dry air}}$.

Chemical Mechanism

The presented chemical mechanism, as applied to MECCA and used in the simulations conducted in the course of this thesis, is presented on the next pages. The presented reactions are the reduced to those, which differ from the chemical mechanism applied in the ESCiMo simulations, which is in whole published in the supplement of Jöckel et al. [2016].

The Chemical Mechanism of MECCA

KPP version: `2.2.3_rs`

MECCA version: `3.8f`

Date: March 18, 2018.

Selected reactions:
"(((Tr && (G || Het) && !I) || St) && !Hg)"

Number of aerosol phases: 0

Number of species in selected mechanism:

Gas phase:	123
Aqueous phase:	0
All species:	123

Number of reactions in selected mechanism:

Gas phase (Gnnn):	246
Aqueous phase (Annn):	0
Henry (Hnnn):	0
Photolysis (Jnnn):	73
Aqueous phase photolysis (PHnnn):	0
Heterogeneous (HETnnn):	12
Equilibria (EQnn):	0
Isotope exchange (IEXnnn):	0
Tagging equations (TAGnnn):	0
Dummy (Dnn):	0
All equations:	331

Table 1: Gas phase reactions

#	labels	reaction	rate coefficient	reference
G1000	UpStTrG	$O_2 + O(^1D) \rightarrow O(^3P) + O_2$	3.3E-11*EXP(55./temp)	Sander et al. (2011)
G1001	UpStTrG	$O_2 + O(^3P) \rightarrow O_3$	6.E-34*((temp/300.)**(-2.4))*cair	Sander et al. (2011)
G1002a	UpStG	$O_3 + O(^1D) \rightarrow 2\ O_2$	1.2E-10	Sander et al. (2011)*
G1003	UpStG	$O_3 + O(^3P) \rightarrow 2\ O_2$	8.E-12*EXP(-2060./temp)	Sander et al. (2011)
G2100	UpStTrG	$H + O_2 \rightarrow HO_2$	k_3rd(temp,cair,4.4E-32,1.3, 7.5E-11,-0.2,0.6)	Sander et al. (2011)
G2101	UpStG	$H + O_3 \rightarrow OH + O_2$	1.4E-10*EXP(-470./temp)	Sander et al. (2011)
G2102	UpStG	$H_2 + O(^1D) \rightarrow H + OH$	1.2E-10	Sander et al. (2011)
G2103	UpStG	$OH + O(^3P) \rightarrow H + O_2$	1.8E-11*EXP(180./temp)	Sander et al. (2011)
G2104	UpStTrG	$OH + O_3 \rightarrow HO_2 + O_2$	1.7E-12*EXP(-940./temp)	Sander et al. (2011)
G2105	UpStTrG	$OH + H_2 \rightarrow H_2O + H$	2.8E-12*EXP(-1800./temp)	Sander et al. (2011)
G2106	UpStG	$HO_2 + O(^3P) \rightarrow OH + O_2$	3.E-11*EXP(200./temp)	Sander et al. (2011)
G2107	UpStTrG	$HO_2 + O_3 \rightarrow OH + 2\ O_2$	1.E-14*EXP(-490./temp)	Sander et al. (2011)
G2108a	UpStG	$HO_2 + H \rightarrow 2\ OH$	7.2E-11	Sander et al. (2011)
G2108b	UpStG	$HO_2 + H \rightarrow H_2 + O_2$	6.9E-12	Sander et al. (2011)
G2108c	UpStG	$HO_2 + H \rightarrow O(^3P) + H_2O$	1.6E-12	Sander et al. (2011)
G2109	UpStTrG	$HO_2 + OH \rightarrow H_2O + O_2$	4.8E-11*EXP(250./temp)	Sander et al. (2011)
G2110	UpStTrG	$HO_2 + HO_2 \rightarrow H_2O_2 + O_2$	k_HO2_HO2	Burkholder et al. (2015), Kircher and Sander (1984)*
G2111	UpStTrG	$H_2O + O(^1D) \rightarrow 2\ OH$	1.63E-10*EXP(60./temp)	Sander et al. (2011)
G2112	UpStTrG	$H_2O_2 + OH \rightarrow H_2O + HO_2$	1.8E-12	Sander et al. (2011)
G3100	UpStGN	$N + O_2 \rightarrow NO + O(^3P)$	1.5E-11*EXP(-3600./temp)	Sander et al. (2011)
G3101	UpStTrGN	$N_2 + O(^1D) \rightarrow O(^3P) + N_2$	2.15E-11*EXP(110./temp)	Sander et al. (2011)
G3102a	UpStGN	$N_2O + O(^1D) \rightarrow 2\ NO$	7.25E-11*EXP(20./temp)	Sander et al. (2011)
G3102b	StGN	$N_2O + O(^1D) \rightarrow N_2 + O_2$	4.63E-11*EXP(20./temp)	Sander et al. (2011)
G3103	UpStTrGN	$NO + O_3 \rightarrow NO_2 + O_2$	3.E-12*EXP(-1500./temp)	Sander et al. (2011)
G3104	UpStGN	$NO + N \rightarrow O(^3P) + N_2$	2.1E-11*EXP(100./temp)	Sander et al. (2011)
G3105	UpStGN	$NO_2 + O(^3P) \rightarrow NO + O_2$	5.1E-12*EXP(210./temp)	Sander et al. (2011)
G3106	StTrGN	$NO_2 + O_3 \rightarrow NO_3 + O_2$	1.2E-13*EXP(-2450./temp)	Sander et al. (2011)
G3107	UpStGN	$NO_2 + N \rightarrow N_2O + O(^3P)$	5.8E-12*EXP(220./temp)	Sander et al. (2011)
G3108	StTrGN	$NO_3 + NO \rightarrow 2\ NO_2$	1.5E-11*EXP(170./temp)	Sander et al. (2011)
G3109	UpStTrGN	$NO_3 + NO_2 \rightarrow N_2O_5$	k_NO3_NO2	Sander et al. (2011)*
G3110	StTrGN	$N_2O_5 \rightarrow NO_2 + NO_3$	k_NO3_NO2/(2.7E-27*EXP(11000./temp))	Sander et al. (2011)*

2

Table 1: Gas phase reactions (... continued)

#	labels	reaction	rate coefficient	reference
G3200	TrGN	NO + OH → HONO	k_3rd(temp,cair,7.0E-31,2.6, 3.6E-11,0.1,0.6)	Sander et al. (2011)
G3201	UpStTrGN	NO + HO$_2$ → NO$_2$ + OH	3.3E-12*EXP(270./temp)	Sander et al. (2011)
G3202	UpStTrGN	NO$_2$ + OH → HNO$_3$	k_3rd(temp,cair,1.8E-30,3.0, 2.8E-11,0.,0.6)	Sander et al. (2011)
G3203	StTrGN	NO$_2$ + HO$_2$ → HNO$_4$	k_NO2_HO2	Sander et al. (2011)*
G3204	TrGN	NO$_3$ + HO$_2$ → NO$_2$ + OH + O$_2$	3.5E-12	Sander et al. (2011)
G3205	TrGN	HONO + OH → NO$_2$ + H$_2$O	1.8E-11*EXP(-390./temp)	Sander et al. (2011)
G3206	StTrGN	HNO$_3$ + OH → H$_2$O + NO$_3$	k_HNO3_OH	Sander et al. (2011)*
G3207	StTrGN	HNO$_4$ → NO$_2$ + HO$_2$	k_NO2_HO2/(2.1E-27*EXP(10900./temp))	Sander et al. (2011)*
G3208	StTrGN	HNO$_4$ + OH → NO$_2$ + H$_2$O	1.3E-12*EXP(380./temp)	Sander et al. (2011)
G3209	TrGN	NH$_3$ + OH → NH$_2$ + H$_2$O	1.7E-12*EXP(-710./temp)	Kohlmann and Poppe (1999)
G3210	TrGN	NH$_2$ + O$_3$ → NH$_2$O + O$_2$	4.3E-12*EXP(-930./temp)	Kohlmann and Poppe (1999)
G3211	TrGN	NH$_2$ + HO$_2$ → NH$_2$O + OH	4.8E-07*EXP(-628./temp) *temp**(-1.32)	Kohlmann and Poppe (1999)
G3212	TrGN	NH$_2$ + HO$_2$ → HNO + H$_2$O	9.4E-09*EXP(-356./temp) *temp**(-1.12)	Kohlmann and Poppe (1999)
G3213	TrGN	NH$_2$ + NO → HO$_2$ + OH + N$_2$	1.92E-12*((temp/298.)**(-1.5))	Kohlmann and Poppe (1999)
G3214	TrGN	NH$_2$ + NO → N$_2$ + H$_2$O	1.41E-11*((temp/298.)**(-1.5))	Kohlmann and Poppe (1999)
G3215	TrGN	NH$_2$ + NO$_2$ → N$_2$O + H$_2$O	1.2E-11*((temp/298.)**(-2.0))	Kohlmann and Poppe (1999)
G3216	TrGN	NH$_2$ + NO$_2$ → NH$_2$O + NO	0.8E-11*((temp/298.)**(-2.0))	Kohlmann and Poppe (1999)
G3217	TrGN	NH$_2$O + O$_3$ → NH$_2$ + O$_2$	1.2E-14	Kohlmann and Poppe (1999)
G3218	TrGN	NH$_2$O → NHOH	1.3E3	Kohlmann and Poppe (1999)
G3219	TrGN	HNO + OH → NO + H$_2$O	8.0E-11*EXP(-500./temp)	Kohlmann and Poppe (1999)
G3220	TrGN	HNO + NHOH → NH$_2$OH + NO	1.66E-12*EXP(-1500./temp)	Kohlmann and Poppe (1999)
G3221	TrGN	HNO + NO$_2$ → HONO + NO	1.0E-12*EXP(-1000./temp)	Kohlmann and Poppe (1999)
G3222	TrGN	NHOH + OH → HNO + H$_2$O	1.66E-12	Kohlmann and Poppe (1999)
G3223	TrGN	NH$_2$OH + OH → NHOH + H$_2$O	4.13E-11*EXP(-2138./temp)	Kohlmann and Poppe (1999)
G3224	TrGN	HNO + O$_2$ → HO$_2$ + NO	3.65E-14*EXP(-4600./temp)	Kohlmann and Poppe (1999)
G4100	UpStG	CH$_4$ + O(^{1}D) → .75 CH$_3$ + .75 OH + .2 CH$_3$O + .2 H + .05 HCHO + .05 H$_2$	1.75E-10	Sander et al. (2011)
G4101	StTrG	CH$_4$ + OH → CH$_3$ + H$_2$O	1.85E-20*EXP(2.82*LOG(temp) -987./temp)	Atkinson (2003)

Additional details

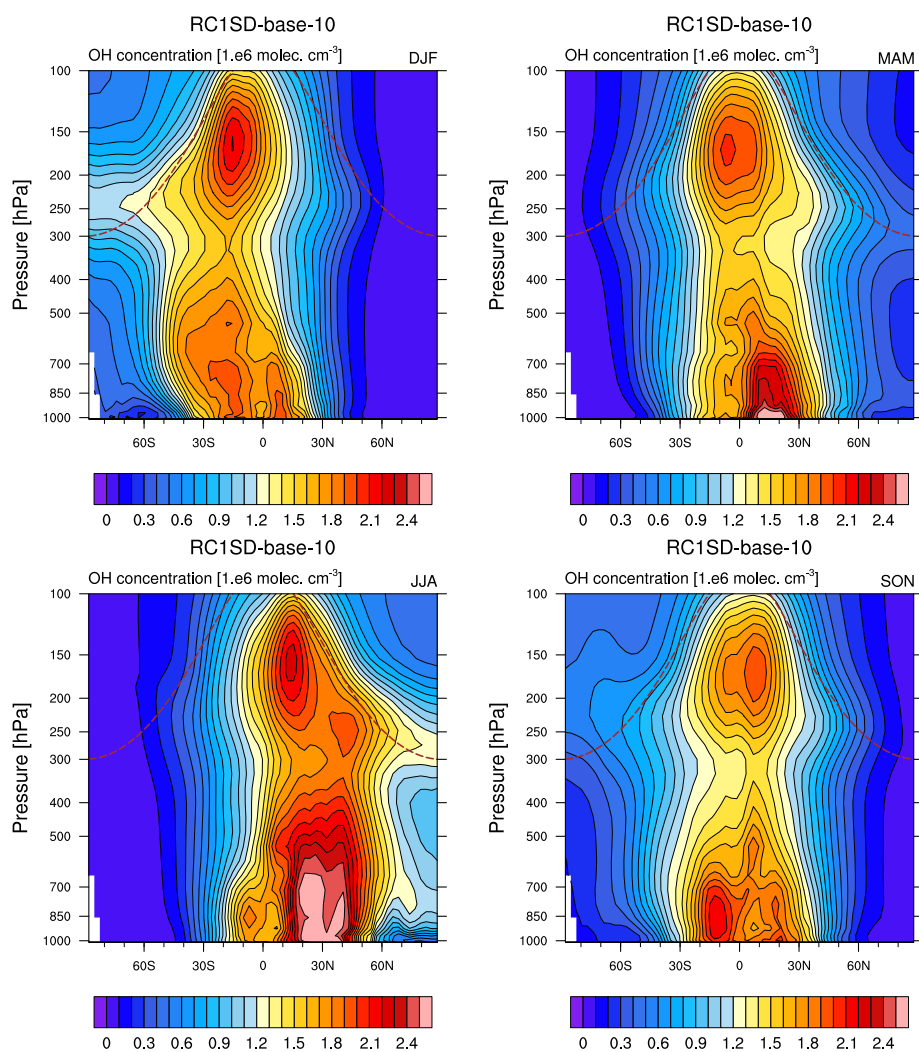## F.1 Correspoding to Chapter: Lifetime of Methane in EMAC

Figure F.1: (a) Seasonal climatology of concentration of OH of RC1SD-base-10. The data is monthly and zonally averaged for the period 2000–2010.
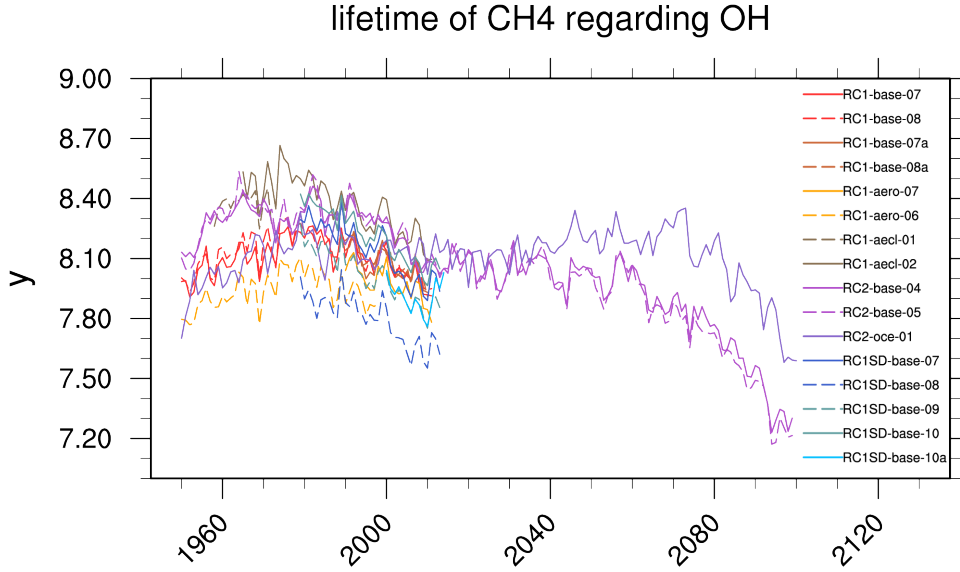
Figure F.2: τ_{CH_4}(OH) of the various ESCiMo simulations calculated following formula (4.1) using a climatological tropopause level. The lifetime is plotted in years and is yearly averaged for reasons of clarity. In contrast to Fig. 4.6 input valuse are not averaged monthly before applying the formula.

Table F.1: Definition of the labels for the regions of the zonal lifetime with respect to latitude and pressure. A schematic is depicted in Fig. 4.11. *clim. tpp* refers to the climatological tropopause level of the respective latitude calculated as described in B.2.

label	latitude degrees north	levmin hPa	levmax hPa
STRA	$-90° - 90°$	clim. tpp	1.
TROP	$-90° - 90°$	surface	clim. tpp
TUSH	$-90° - -60°$	500	clim. tpp
TUST	$-60° - 0°$	250	clim. tpp
TUNT	$0° - 60°$	250	clim. tpp
TUNH	$60° - 90°$	500	clim. tpp
THST	$-60° - 0°$	500	250
THNT	$0° - 60°$	500	250
TMSH	$-90° - -60°$	750	500
TMST	$-60° - 0°$	750	500
TMNT	$0° - 60°$	750	500
TMNH	$60° - 90°$	750	500
TLSH	$-90° - -60°$	surface	750
TLST	$-60° - 0°$	surface	750
TLNT	$0° - 60°$	surface	750
TLNH	$60° - 90°$	surface	750
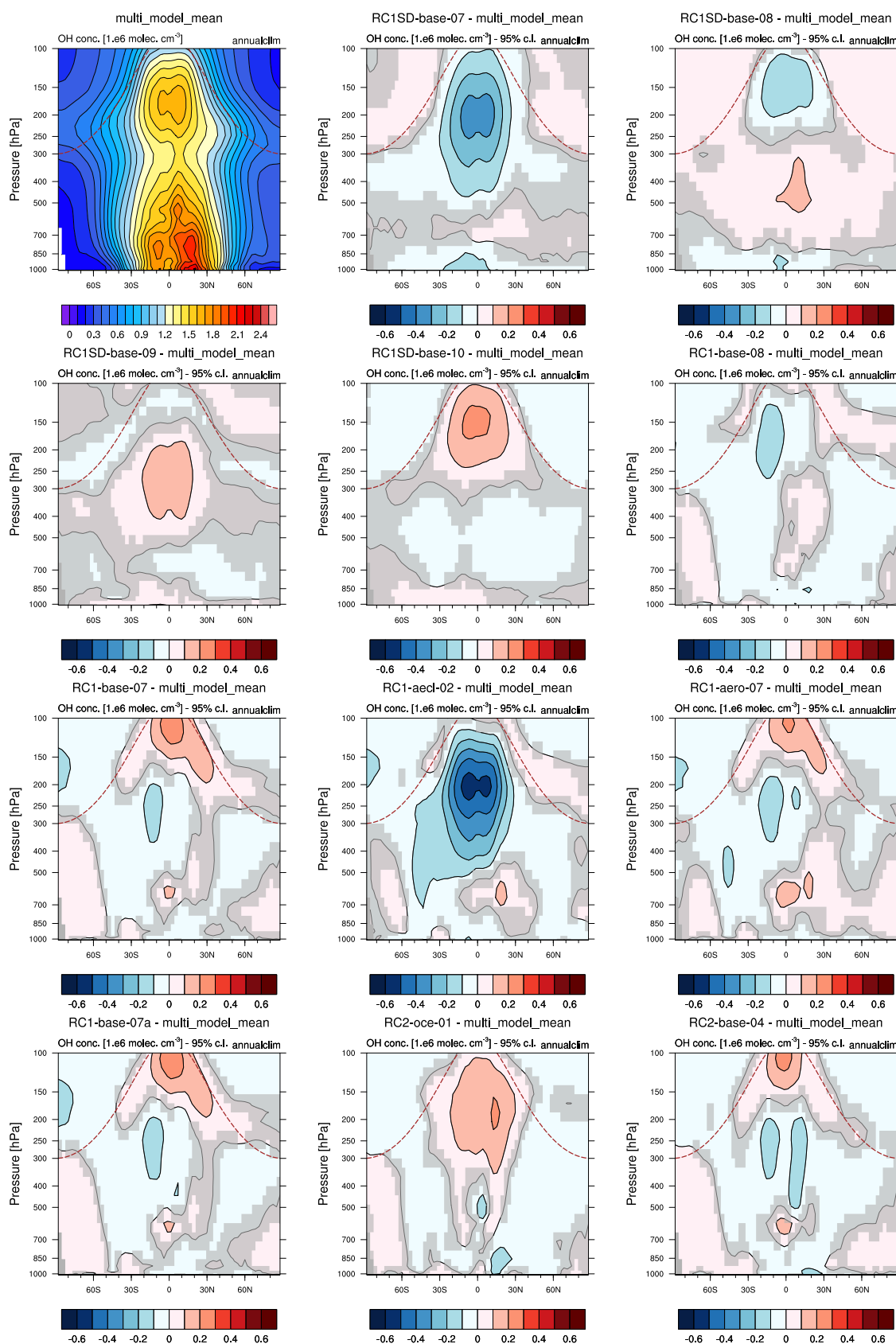
Figure F.3: (a) Climatology of concentration of OH of the MSM. The data were monthly and zonally averaged for the period 2000–2010. (b)–(h) OH concentration absolute differences of selected ESCiMo simulations compared to the MSM. The unshaded areas in the difference plots are significant on a 95% confidence level according to a two-sided Welch's test.
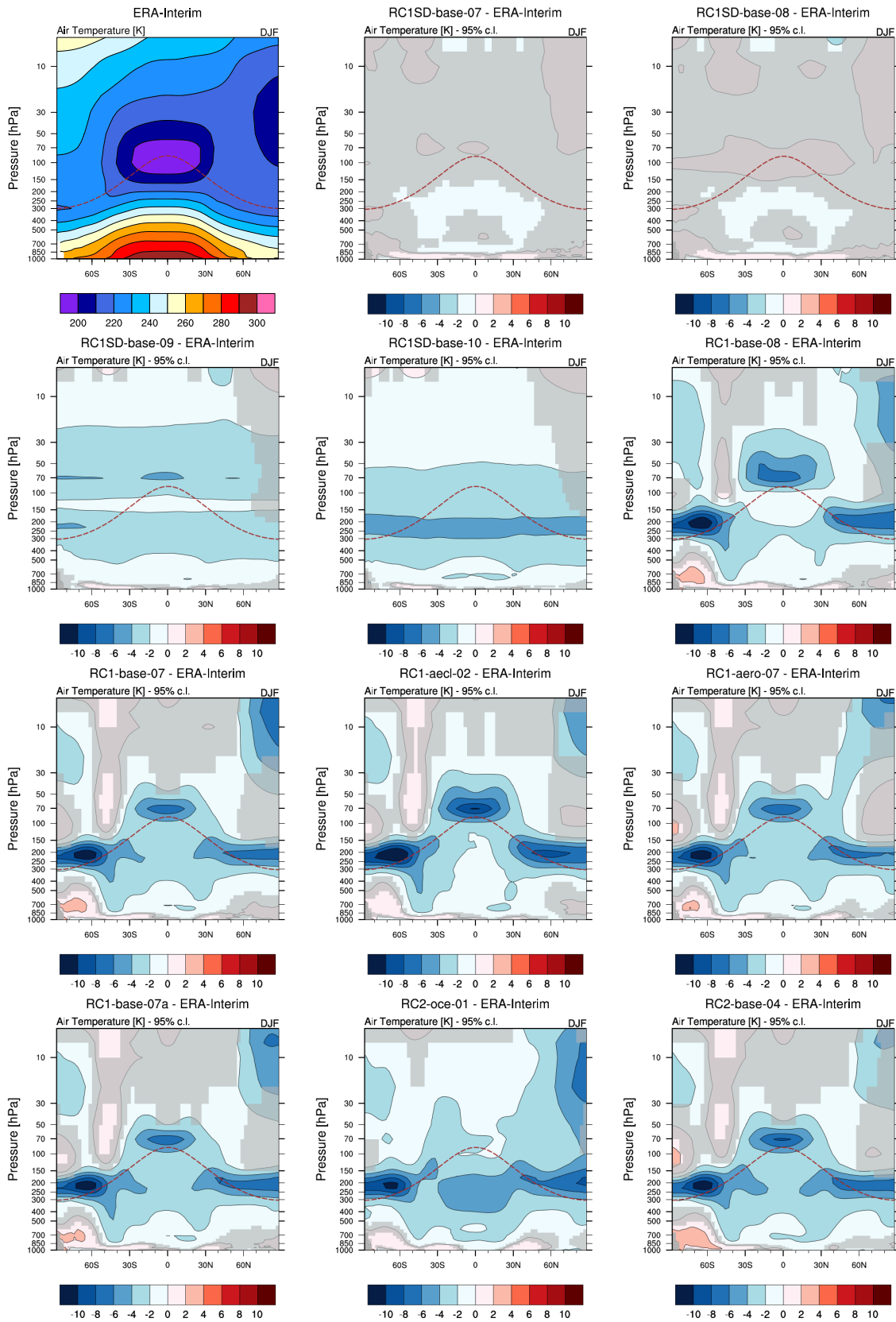
Figure F.4: (a) Seasonal climatology DJF of total dry air temperature of ERA-Interim in Kelvin. The data were monthly and zonally averaged for the period 2000 - 2010. (b)–(h) dry air temperature differences of selected ESCiMo simulations compared to ERA-Interim data in DJF. The unshaded areas in the difference plots are significant on a 95% confidence level according to a two-sided Welch's test. The dashed brown line indicates the height of the climatological tropopause.
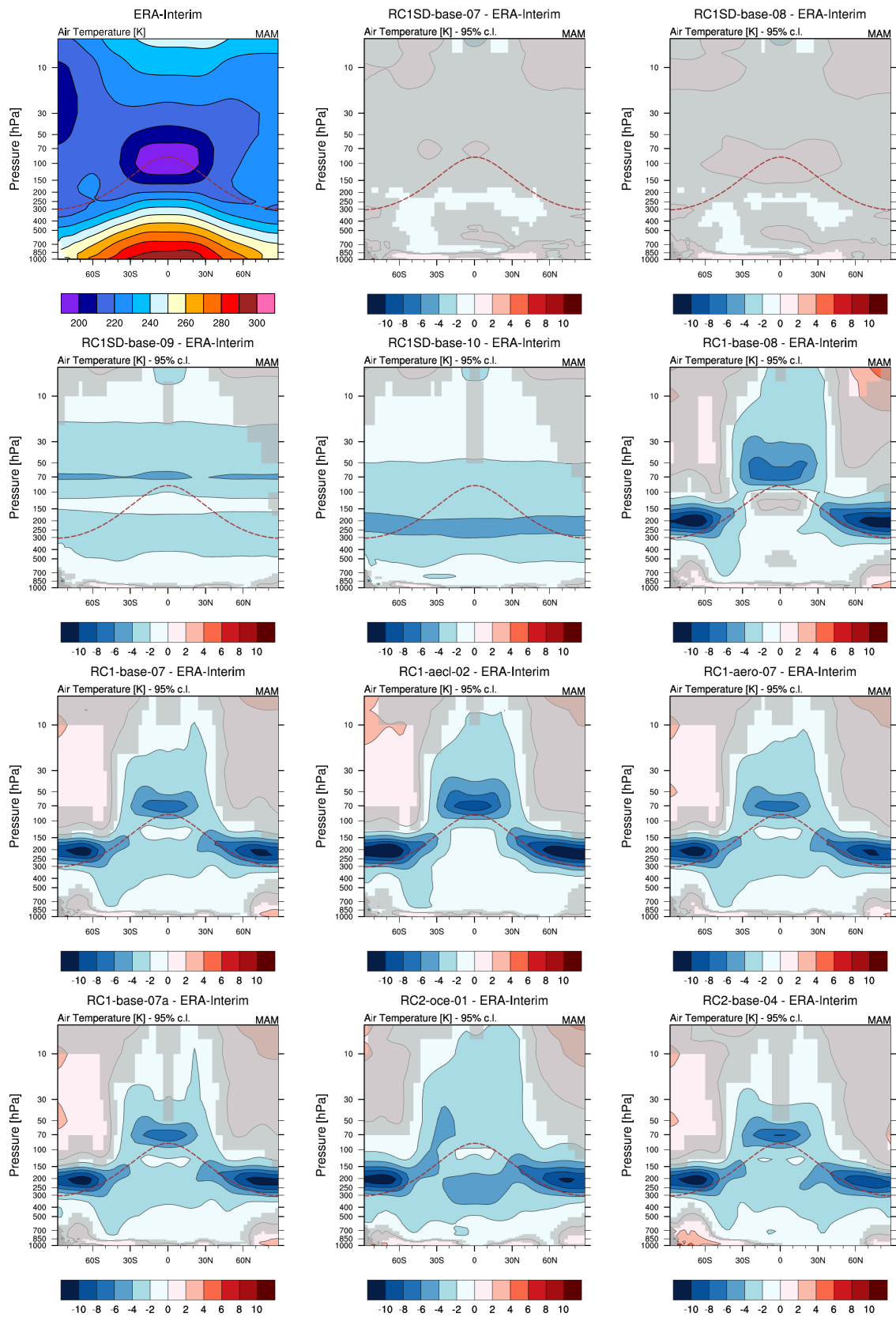
Figure F.5: (a) Seasonal climatology March, April, and May (MAM) of total dry air temperature of ERA-Interim in Kelvin. The data were monthly and zonally averaged for the period 2000 - 2010. (b)–(h) dry air temperature differences of selected ESCiMo simulations compared to ERA-Interim data in MAM. The unshaded areas in the difference plots are significant on a 95% confidence level according to a two-sided Welch's test. The dashed brown line indicates the height of the climatological tropopause.
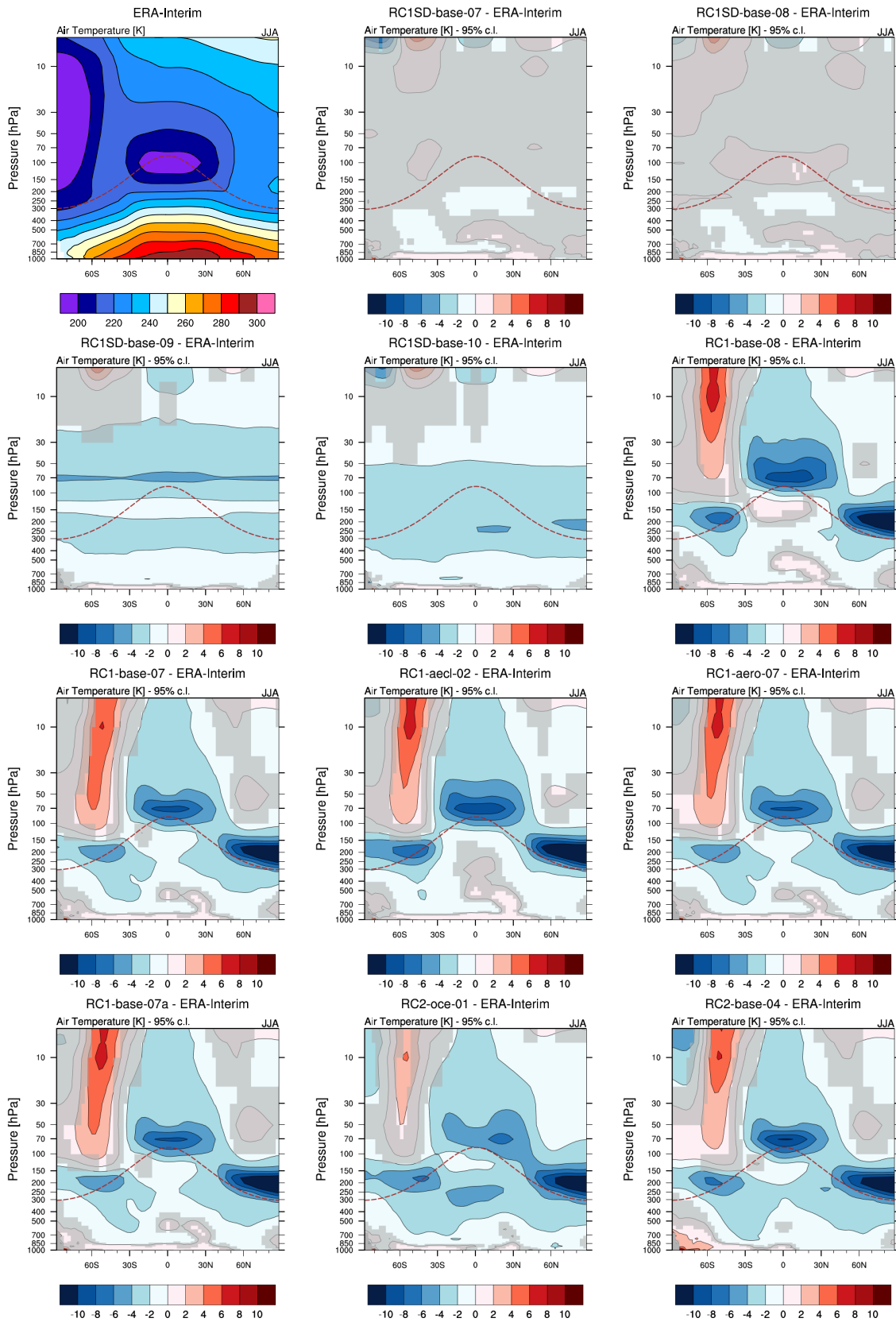
Figure F.6: (a) Seasonal climatology JJA of total dry air temperature of ERA-Interim in Kelvin. The data were monthly and zonally averaged for the period 2000 - 2010. (b)–(h) dry air temperature differences of selected ESCiMo simulations compared to ERA-Interim data in JJA. The unshaded areas in the difference plots are significant on a 95% confidence level according to a two-sided Welch's test. The dashed brown line indicates the height of the climatological tropopause.
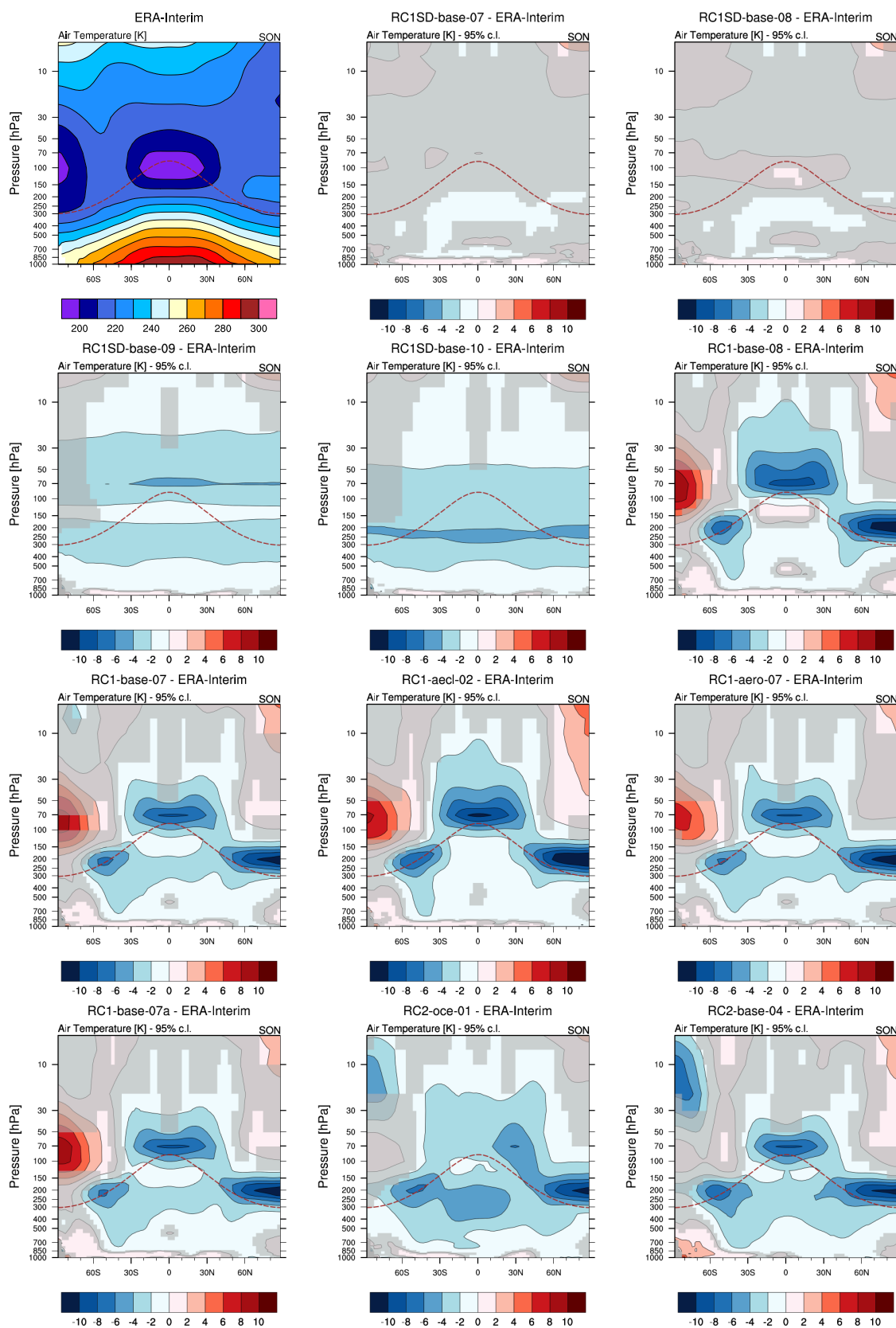
Figure F.7: (a) Seasonal climatology September, October, and November (SON) of total dry air temperature of ERA-Interim in Kelvin. The data were monthly and zonally averaged for the period 2000 - 2010. (b)–(h) dry air temperature differences of selected ESCiMo simulations compared to ERA-Interim data in SON. The unshaded areas in the difference plots are significant on a 95% confidence level according to a two-sided Welch's test. The dashed brown line indicates the height of the climatological tropopause.

F.2   Correspoding to Chapter: Optimized Emission Inventories

Table F.2: Overview of NH stations used for the inverse modeling. Latitude (lat) is given in degrees north, longitude (lon) in degrees east and altitude (alt) in m above ground.

Name	ID	lat	lon	alt	time-period	contributor
NH polar region:						
Alert	alt	82.45	-62.52	210	1990–2012[a]	NOAA/ESRL
Barrow	brw	71.32	-156.6	11	1990–2012	NOAA/ESRL
Pallas-Sammaltunturi	pal	67.97	24.12	560	2001–2012	NOAA/ESRL
Summit	sum	72.58	-38.48	3238	1997–2012	NOAA/ESRL
Teriberka	ter	69.2	35.1	40	1999–2012	MGO
Zeppelinfjellet	zep	78.9	11.88	475	1994–2012	NOAA/ESRL
NH midlatitudes:						
Terceira Island	azr	38.77	-27.37	40	1990–2012	NOAA/ESRL
Baltic Sea	bal	55.35	17.22	28	1992–2011	NOAA/ESRL
Begur	bgu	41.97	3.23	13	2000–2010	LSCE
St. Davids Head	bme	32.37	-64.65	30	1990–2007[a]	NOAA/ESRL
Tudor Hill	bmw	32.27	-64.87	30	1990–2012	NOAA/ESRL
Cold Bay	cba	55.2	-162.72	25	1990–2012	NOAA/ESRL
Estevan Point	esp	49.38	-126.55	39	2009–2012[a]	EC
Hohenpeissenberg	hpb	47.8	11.02	985	2006–2012	NOAA/ESRL
Hegyhatsal	hun	46.95	16.65	248	1993–2012	NOAA/ESRL
Sary Taukum	kzd	44.45	75.57	412	1997–2009	NOAA/ESRL
Park Falls	lef	45.92	-90.27	868	1994–2012	NOAA/ESRL
Lampedusa	lmp	35.52	12.63	45	1995–2012[a]	ENEA
Mace Head	mhd	53.33	-9.9	8	1991–2012	NOAA/ESRL
Niwot Ridge	nwr	40.05	-105.59	3523	1990–2012	NOAA/ESRL
Ochsenkopf	oxk	50.03	11.8	1185	2006–2012[a]	NOAA/ESRL
Pic du Midi	pdm	42.94	0.14	2877	2001–2010	LSCE
Point Arena	pta	38.95	-123.72	17	1999–2011	NOAA/ESRL
Puy de Dome	puy	45.77	2.97	1465	2001–2010	LSCE
Southern Great Plains	sgp	36.78	-97.5	314	2002–2012	NOAA/ESRL
Shemya Island	shm	52.72	174.08	40	1990–2012	NOAA/ESRL
Tae-ahn Peninsula	tap	36.72	126.12	20	1991–2012[a]	NOAA/ESRL
Trinidad Head	thd	41.05	-124.15	120	2002–2012	NOAA/ESRL
Wendover	uta	39.88	-113.72	1320	1993–2012	NOAA/ESRL
Ulaan Uul	uum	44.45	111.08	914	1992–2012	NOAA/ESRL
Sede Boker	wis	31.12	34.87	400	1995–2012	NOAA/ESRL
Mt. Waliguan	wlg	36.28	100.9	3810	1991–2012	NOAA/ESRL[b]
Sable Island	wsa	43.93	-60.02	5	2003–2012[a]	EC

[a] time period of event flask data used in the inversion differs: alt: 1999–2012 (EC), bme: 1990–2010, esp: 1999–2012, lmp: 1995–2010, oxk: 2003–2012, tap: 1990–2012, wsa: 1999–2012
[b] with contribution of CMA

Table F.3: Overview of tropics and SH stations used for the inverse modeling. Latitude (lat) is given in degrees north, longitude (lon) in degrees east and altitude (alt) in m above ground.

Name	ID	lat	lon	alt	time-period	contributor
tropics:						
Arembepe	abp	-12.77	-38.17	0	2006–2010	NOAA/ESRL
Ascension Island	asc	-7.92	-14.42	54	1990–2012	NOAA/ESRL
Assekrem	ask	23.27	5.63	2710	1995–2012	NOAA/ESRL
Cape Ferguson	cfa	-19.28	147.05	2	1991–2012	CSIRO
Christmas Island	chr	1.7	-157.17	3	1990–2012	NOAA/ESRL
Cape Rama	cri	15.08	73.83	60	1993–2012	CSIRO
Easter Island	eic	-27.13	-109.45	50	1994–2012	NOAA/ESRL
Guam	gmi	13.43	144.78	2	1990–2012	NOAA/ESRL
Izana	izo	28.3	-16.5	2367	1991–2012	NOAA/ESRL
Key Biscayne	key	25.67	-80.2	3	1990–2012	NOAA/ESRL
Cape Kumukahi	kum	19.52	-154.82	3	1990–2012	NOAA/ESRL
Lulin	lln	23.47	120.87	2867	2006–2012	NOAA/ESRL
Mt. Kenya	mkn	-0.06	37.3	3678	2003–2011	NOAA/ESRL
Mauna Loa	mlo	19.54	-155.58	3397	1990–2012	NOAA/ESRL
Ragged Point	rpb	13.17	-59.43	45	1990–2012	NOAA/ESRL
Mahe Island	sey	-4.67	55.17	7	1990–2012	NOAA/ESRL
SH midlatitudes:						
Amsterdam Island	ams	-37.8	77.53	55	2003–2010	LSCE
Baring Head	bhd	-41.41	174.87	85	1999–2012	NOAA/ESRL
Cape Grim	cgo	-40.68	144.68	94	1990–2012	NOAA/ESRL
Crozet	crz	-46.45	51.85	120	1995–2012[a]	NOAA/ESRL
Macquarie Island	mqa	-54.48	158.97	12	1990–2012	CSIRO
Tierra del Fuego	tdf	-54.87	-68.48	20	1994–2012	NOAA/ESRL
SH polar region:						
Arrival Heights	arh	-77.8	166.67	184	1990–2012	NIWA
Casey Station	cya	-66.28	110.53	60	1997–2012	CSIRO
Halley Bay	hba	-75.57	-26.5	33	1990–2012	NOAA/ESRL
Mawson	maa	-67.62	62.87	32	1990–2012	CSIRO
Palmer Station	psa	-64.92	-64	10	1990–2012	NOAA/ESRL
Syowa	syo	-69	39.58	16	1990–2012	NOAA/ESRL

[a] time period of event flask data used in the inversion differs: crz: 1991–2012 inversion
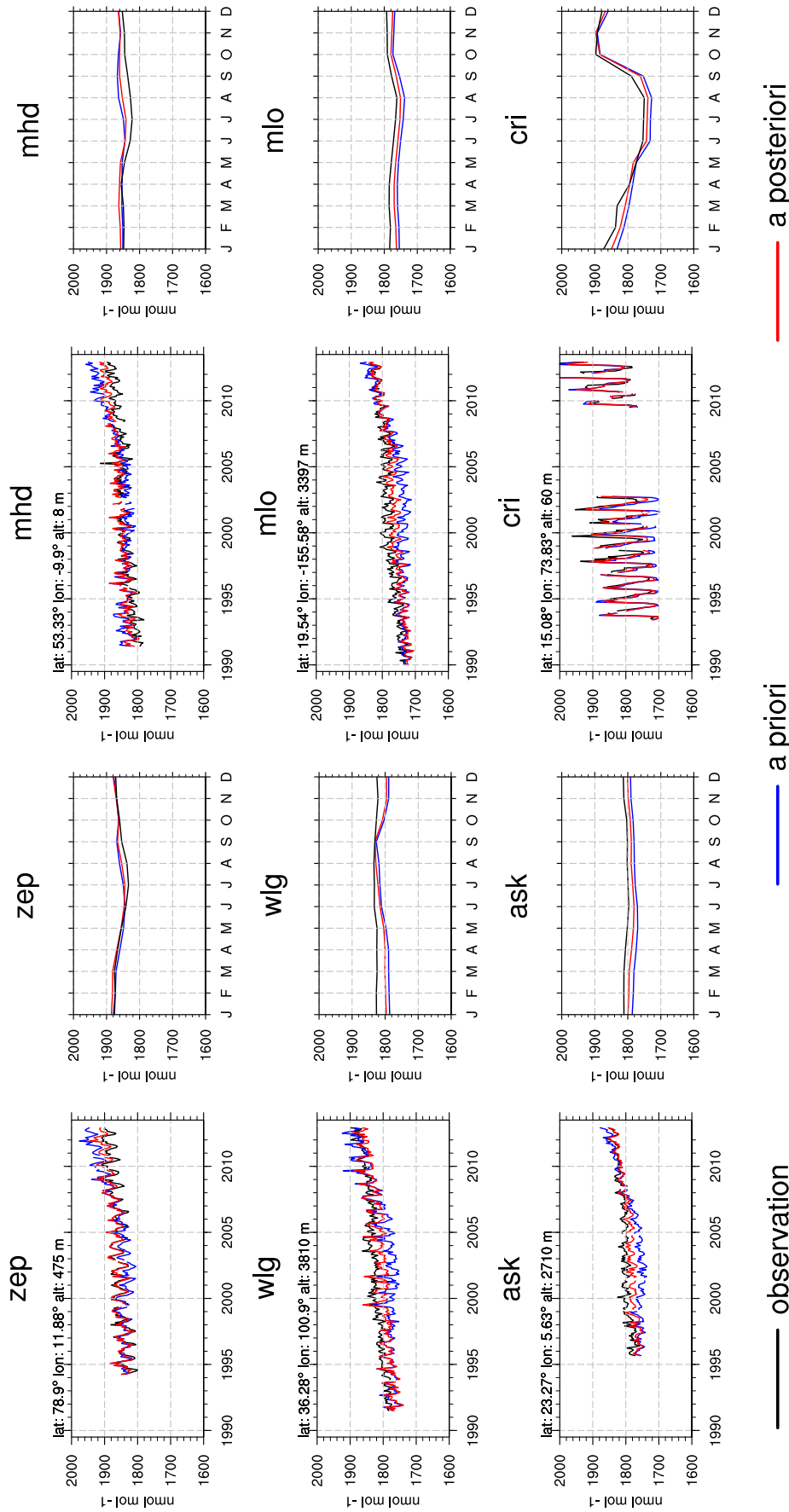
Figure F.8: Results of the inverse optimization in terms of agreement at the observation stations (i.e. Zeppelinfjellet (zep), Mace head (mhd), Mt. Waliguan (wlg), Mauna Loa (mlo), Assekrem (ask), Cape Rama (cri)). The black solid lines indicate the observations. Yellow dashed are the a priori estimates scaled to match the initial year. The green dash-dotted lines are the a posteriori estimates. The time series between 1989 and 2013 is shown on the left hand side and the annual cycle on the right.
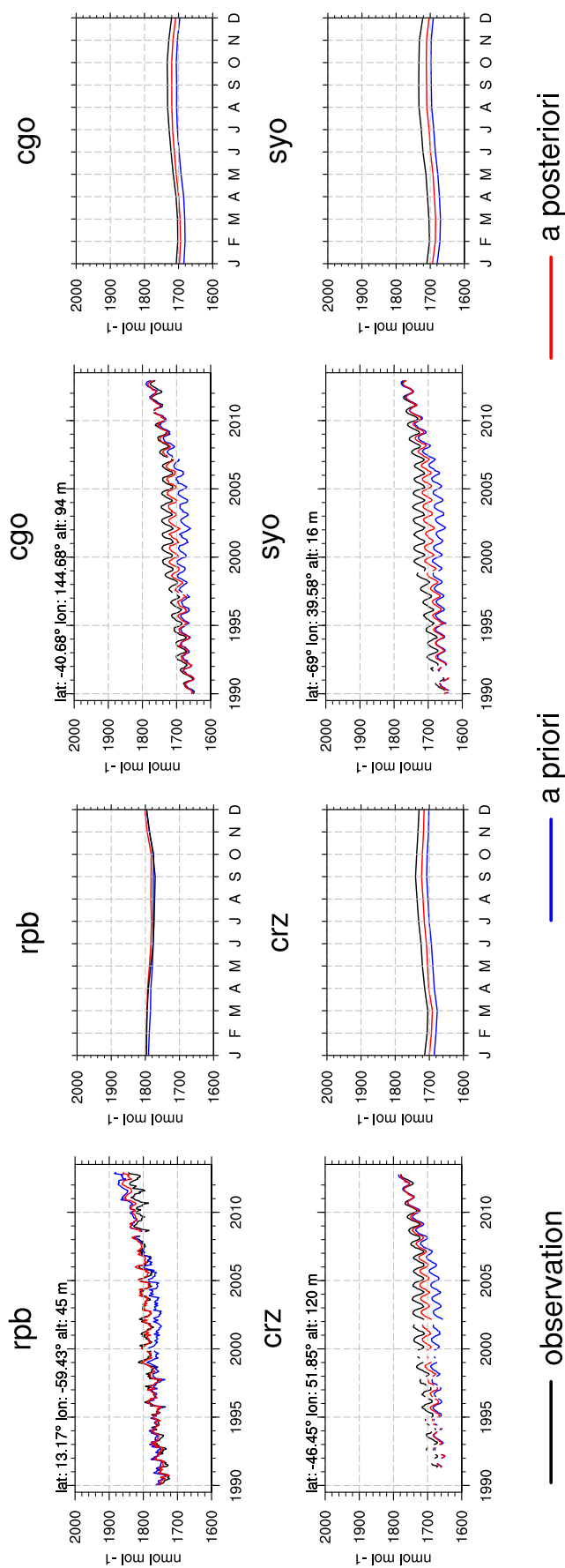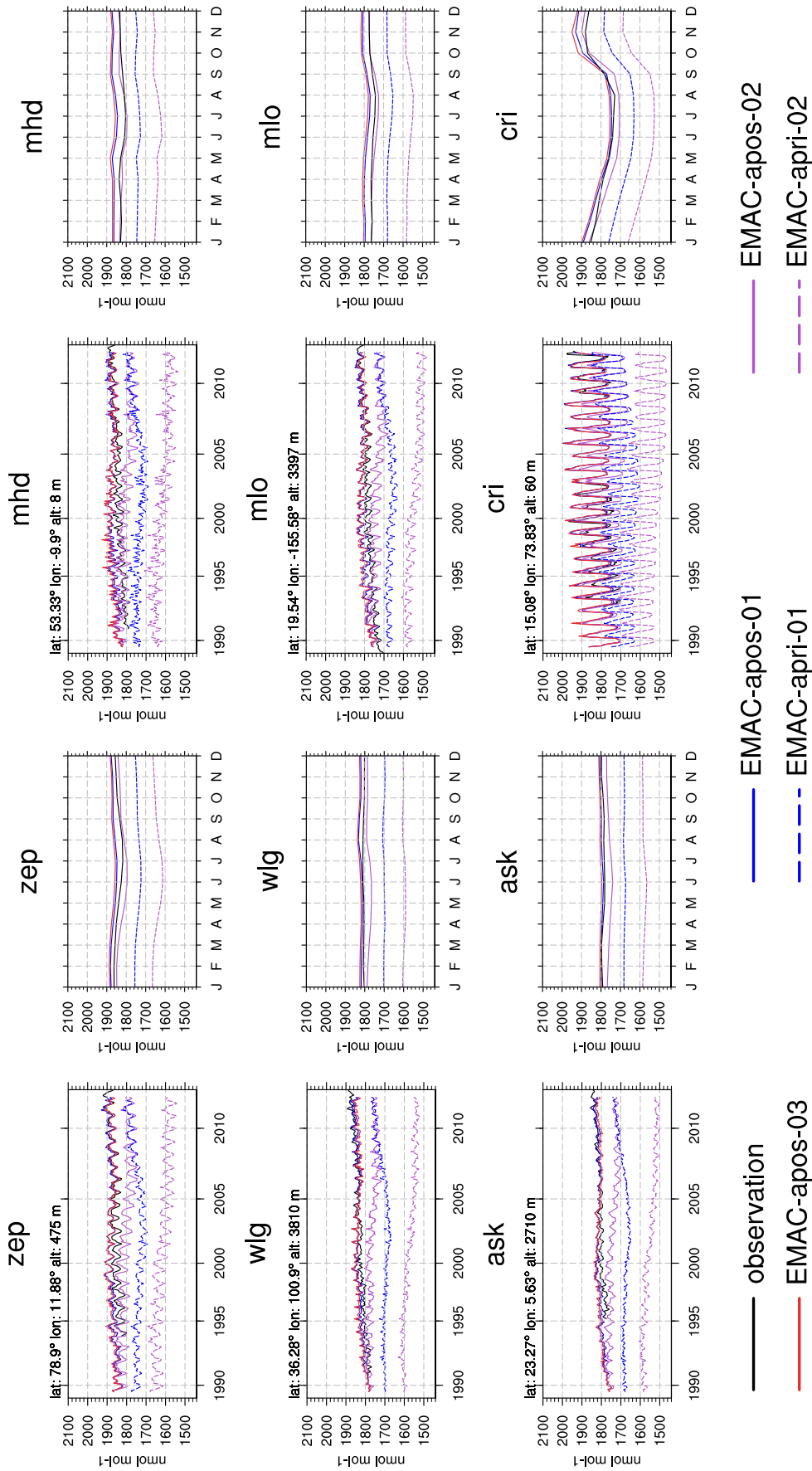
Figure F.9: Results of the inverse optimization in terms of agreement at the observation stations (i.e. Ragged Point (rpb), Cape Grim (cgo), Crozet (crz) and Syowa (syo)). The black solid lines indicate the observations. Yellow dashed are the a priori estimates scaled to match the initial year. The green dash-dotted lines are the a posteriori estimates. The time series between 1989 and 2013 is shown on the left hand side and the annual cycle on the right.

Figure F.10: Results of the forward simulations in terms of agreement at the observation stations (i.e. Zeppelinfjellet (zep), Mace head (mhd), Mt. Waliguan (wlg), Mauna Loa (mlo), Assekrem (ask), Cape Rama (cri)). The black solid line indicates the observation. Dashed are the a priori results. Solid are the a posteriori results. Blue indicates the simulations with $[OH]_{MMM}$ and purple the simulations with $[OH]_{RC1SD-base-10}$. The time series between 1990 and 2012 is shown on the left hand side and the annual cycle on the right.
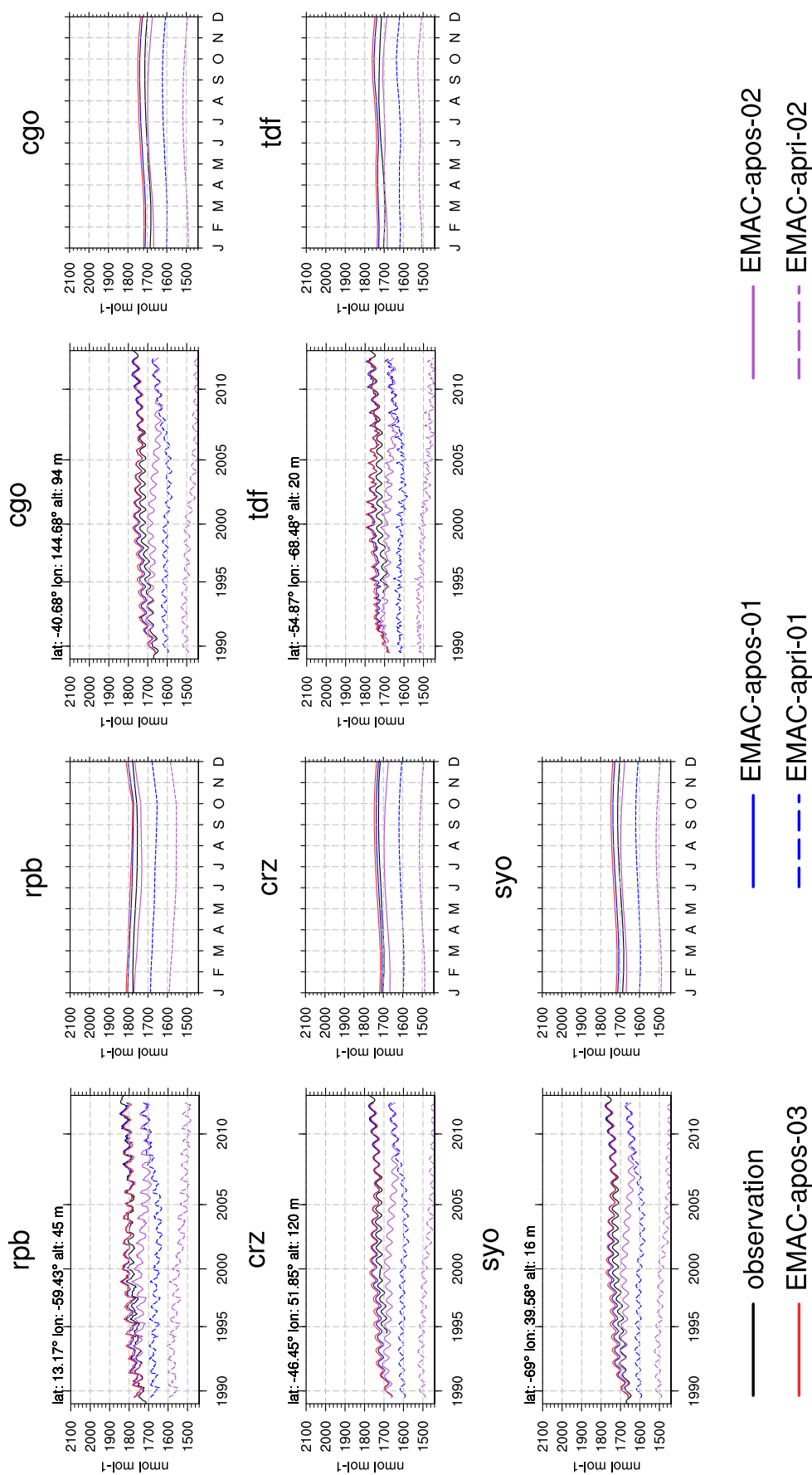
Figure F.11: Results of the forward simulations in terms of agreement at the observation stations (i.e. Ragged Point (rpb), Cape Grim (cgo), Crozet (crz), Tierra del Fuego (tdf) and Syowa (syo)). The black solid line indicates the observation. Dashed are the a priori results. Solid are the a posteriori results. Blue indicates the simulations with $[OH]_{MMM}$ and purple the simulations with $[OH]_{RC1SD-base-10}$. The time series between 1990 and 2012 is shown on the left hand side and the annual cycle on the right.

F.3   Correspoding to Chapter: Modelling Methane Isotopologues
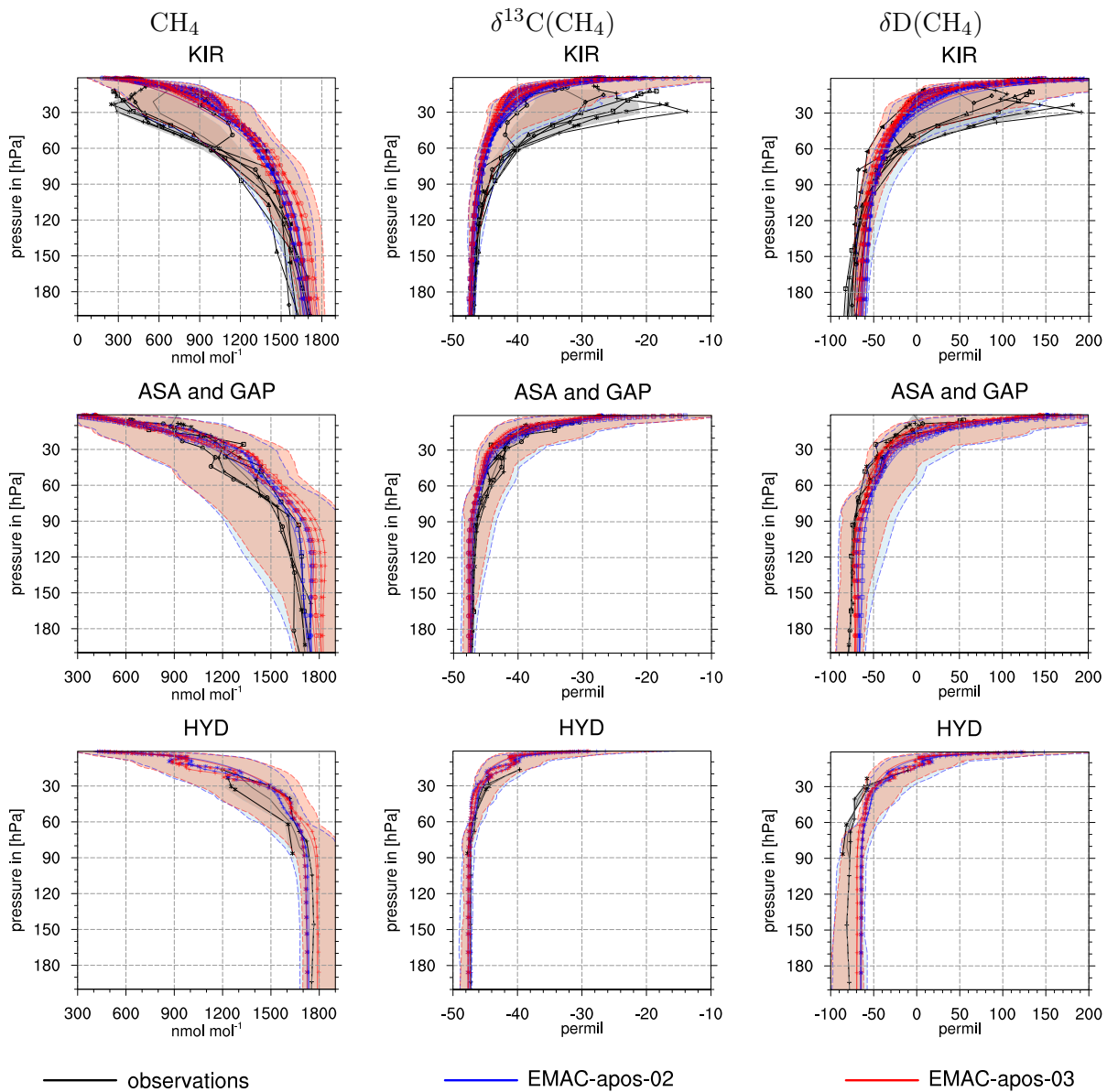
Figure F.12: Balloon borne observations from Röckmann et al. [2011] (black) together with simulation results from EMAC-apos-02 (blue) and EMAC-apos-03 (red). The rows of panels present balloone launches in the polar region in KIR, in the midlatitude region in ASA and GAP, and in the tropical region in HYD. The profiles of the simulations are taken from monthly averaged data at the specific year, month and location of the observation. For observations before the simulation start, the simulated year 1990 is used. Shaded areas indicate the minimum and maximum values of the observations (grey) and the simulations (blue, and red, respectively) concerning the variations within the specific latitudinal region and the years 1990–2003.

Bibliography

[Ackerman et al. 1988]   Ackerman, T. P., Liou, K.-N., Valero, F. P. J., and Pfister, L. Heating rates in tropical anvils. *J. Atmos. Sci.*, 45(10):1606–1623, 1988. URL `https://doi.org/10.1175/1520-0469(1988)045<1606:HRITA>2.0.CO;2`. (Cited on page 37.)

[Albaladejo et al. 2002]   Albaladejo, J., Jiménez, E., Notario, A., Cabañas, B., and Martínez, E. CH_3O yield in the $CH_3 + O_3$ reaction using the LP/LIF technique at room temperature. *J. Phys. Chem. A*, 106:2512–2519, 2002. doi: 10.1021/jp012249o. (Cited in Appendix E.)

[Arfeuille et al. 2016]   Arfeuille, F., Henne, S., Poberaj, C. S., et al. Global lagrangian transport model and inverse modelling for emissions estimates: Evolution of the global atmospheric methane (1990-2012). 2016. in prep. (Cited on page 63.)

[Atkinson 2003]   Atkinson, R. Kinetics of the gas-phase reactions of OH radicals with alkanes and cycloalkanes. *Atmos. Chem. Phys.*, 3:2233–2307, 2003. (Cited on pages 44, 59, 74 and 141.)

[Atkinson et al. 2006]   Atkinson, R., Baulch, D. L., Cox, R. A., et al. Evaluated kinetic and photochemical data for atmospheric chemistry: Volume II – gas phase reactions of organic species. *Atmos. Chem. Phys.*, 6:3625–4055, 2006. (Cited in Appendix E.)

[Austin et al. 2007]   Austin, J., Wilson, J., Li, F., and Vömel, H. Evolution of water vapor concentrations and stratospheric age of air in coupled chemistry-climate model simulations. *Am. Met. Soc.*, pages 905–921, 2007. doi: 10.1175/JAS3866.1. (Cited on pages 26 and 109.)

[Bacer et al. 2016]   Bacer, S., Christoudias, T., and Pozzer, A. Projection of north atlantic oscillation and its effect on tracer transport. *Atmos. Chem. Phys.*, 16:15581–15592, 2016. doi: 10.5194/acp-16-15581-2016. URL `www.atmos-chem-phys.net/16/15581/2016/`. (Cited on page 35.)

[Barone et al. 1995]   Barone, S. B., Turnipseed, A. A., and Ravishankara, A. R. Role of adducts in the atmospheric oxidation of dimethyl sulfide. *Faraday Discuss.*, 100:39–54, 1995. (Cited in Appendix E.)

[Baskaran 2011]   Baskaran, M., editor. *Handbook of Environmental Isotope Geochemistry*. Springer, 2011. ISBN 9788578110796. doi: 10.1007/978-3-642-10637-8. (Cited on page 17.)

[Baulch et al. 2005]   Baulch, D. L., Bowman, C. T., Cobos, C. J., et al. Evaluated kinetic data for combustion modeling: Supplement II. *J. Phys. Chem. Ref. Data*, 34:757–1397, 2005. (Cited in Appendix E.)

[Baumgaertner et al. 2013]   Baumgaertner, A. J. G., Jöckel, P., Aylward, A. D., and Harris, M. J. *Climate and Weather of the Sun-Earth System (CAWSES)*, chapter Simulation of Particle Precipitation Effects on the Atmosphere with the MESSy Model System, pages 301–316. Springer Atmospheric Sciences. Springer Netherlands, 2013. doi: 10.1007/978-94-007-4348-9_17. (Cited on page 25.)

[Bell et al. 2003]   Bell, N., Heard, D. E., Pilling, M. J., and Tomlin, A. S. Atmospheric lifetime as a probe of radical chemistry in the boundary layer. *Atmos. Environ.*, 37(16):2193–2205, 2003. ISSN 13522310. doi: 10.1016/S1352-2310(03)00157-2. (Cited on pages 20 and 34.)

[Bergamaschi et al. 1996]   Bergamaschi, P., Brühl, C., Brenninkmeijer, C. A. M., et al. Implications of the large carbon kinetic isotope effect in the reaction $CH_4 + Cl$ for the $^{13}C/^{12}C$ ratio of stratospheric CH_4. *Geophys. Res. Lett.*, 23(17):2227–2230, 1996. doi: 10.1029/96GL02139. (Cited on page 18.)

[Bergamaschi et al. 2013]   Bergamaschi, P., Houweling, S., Segers, A., et al. Atmospheric CH_4 in the first decade of the 21st century: Inverse modeling analysis using SCIAMACHY satellite retrievals and NOAA surface measurements. *J. Geophys. Res. Atmos.*, 118(13):7350–7369, 2013. ISSN 21698996. doi: 10.1002/jgrd.50480. (Cited on pages 6, 44, 60, 61 and 62.)

[Bergamaschi et al. 2017]   Bergamaschi, P., Karstens, U., Manning, A. J., et al. Inverse modelling of European CH_4 emissions during 2006–2012 using different inverse models and reassessed atmospheric observations. *Atmos. Chem. Phys. Discuss.*, 2017:1–23, 2017. doi: 10.5194/acp-2017-273. URL `https://www.atmos-chem-phys-discuss.net/acp-2017-273/`. (Cited on page 1.)

[Bigeleisen 2005]   Bigeleisen, J. *Isotope Effects in Chemistry and Biology*, chapter Chapter 01 Theoretical Basis of Isotope Effects from an Autobiographical Perspective, pages 1–40. 2005. ISBN 978-0-8247-2449-8. doi: 10.1201/9781420028027.ch1. URL `http://dx.doi.org/10.1201/9781420028027.ch1`. (Cited on page 17.)

[Bloss et al. 2007]   Bloss, W. J., Lee, J. D., Heard, D. E., et al. Observations of OH and HO_2 radicals in coastal antarctica. *Atmos. Chem. Phys.*, 16:4171–4185, 2007. doi: 10.5194/acp-7-4171-2007. URL `https://www.atmos-chem-phys.net/7/4171/2007/`. (Cited on page 33.)

[Bonard et al. 2002]   Bonard, A., Daële, V., Delfau, J.-L., and Vovelle, C. Kinetics of OH radical reactions with methane in the temperature range 295-660 K and with dimethyl ether and methyl-tert-butyl ether in the temperature range 295-618 K. *J. Phys. Chem. A*, 106:4384–4389, 2002. doi: 10.1021/jp012425t. (Cited on pages 59 and 141.)

[Bossolasco et al. 2014]   Bossolasco, A., Faragó, E. P., Schoemaecker, C., and Fittschen, C. Rate constant of the reaction between CH_3O_2 and OH radicals. *Chem. Phys. Lett.*, 593:7–13, 2014. doi: 10.1016/j.cplett.2013.12.052. (Cited in Appendix E.)

[Bousquet et al. 2006]   Bousquet, P., Ciais, P., Miller, J. B., et al. Contribution of anthropogenic and natural sources to atmospheric methane variability. *Nature*, 443:439–443, 2006. doi: 10.1038/nature05132. URL `http://dx.doi.org/10.1038/nature05132`. (Cited on page 1.)

[Bousquet et al. 2011]   Bousquet, P., Ringeval, B., Pison, I., et al. Source attribution of the changes in atmospheric methane for 2006–2008. *Atmos. Chem. Phys.*, 11(8):3689–3700, 2011. doi: 10.5194/acp-11-3689-2011. URL `https://www.atmos-chem-phys.net/11/3689/2011/`. (Cited on pages 6, 72 and 85.)

[Boville et al. 2001]   Boville, B. A., Kiehl, J. T., Rasch, P. J., and Bryan, F. O. Improvements to the NCAR CSM-1 for transient climate simulations. *J. Climate*, 14(2):164–179, 2001. doi: 10.1175/1520-0442(2001)014<0164:ITTNCF>2.0.CO;2. (Cited on pages 26 and 109.)

[Brass and Röckmann 2010]   Brass, M. and Röckmann, T. Continuous-flow isotope ratio mass spectrometry method for carbon and hydrogen isotope measurements on atmospheric methane. *Atmos. Meas. Tech.*, 3(6):1707–1721, 2010. doi: 10.5194/amt-3-1707-2010. URL `https://www.atmos-meas-tech.net/3/1707/2010/`. (Cited on page 97.)

[Brenninkmeijer 2009]   Brenninkmeijer, C. Applications of stable isotope analysis to atmospheric trace gas budgets. *The European Physical Journal Conferences*, 1:137–148, 2009. ISSN 2100-014X. doi: 10.1140/epjconf/e2009-00915-x. URL `http://www.epj-conferences.org/10.1140/epjconf/e2009-00915-x`. (Cited on page 21.)

[Brenninkmeijer et al. 1992]   Brenninkmeijer, C. A. M., Manning, M. R., Lowe, D. C., et al. Interhemispheric asymmetry in OH abundance inferred from measurements of atmopsheric ^{14}CO. *Letters to Nature*, 356:50–52, 1992. (Cited on pages 15, 33 and 55.)

[Brinkop et al. 2016]   Brinkop, S., Dameris, M., Jöckel, P., et al. The millennium water vapour drop in chemistry–climate model simulations. *Atmos. Chem. Phys.*, 16(13):8125–8140, 2016. doi: 10.5194/acp-16-8125-2016. URL `https://www.atmos-chem-phys.net/16/8125/2016/`. (Cited on pages 22 and 35.)

[Brown 1993]   Brown, M. Deduction of emissions of source gases using an objective inversion algorithm and a chemical transport model. *J. Geophys. Res. Atmos.*, 98(D7):12639–12660, 1993. doi: 10.1029/93JD01003. URL `http://dx.doi.org/10.1029/93JD01003`. (Cited on page 61.)

[Brown 1995]   Brown, M. The singular value decomposition method applied to the deduction of the emissions and the isotopic composition of atmospheric methane. *J. Geophys. Res. Atmos.*, 100 (D6):11425–11446, 1995. doi: 10.1029/95JD00367. URL `http://dx.doi.org/10.1029/95JD00367`. (Cited on page 61.)

[Bruhwiler et al. 2014]   Bruhwiler, L., Dlugokencky, E., Masarie, K., et al. CarbonTracker-CH$_4$: an assimilation system for estimating emissions of atmospheric methane. *Atmos. Chem. Phys.*, 14(16): 8269–8293, 2014. doi: 10.5194/acp-14-8269-2014. URL `https://www.atmos-chem-phys.net/14/8269/2014/`. (Cited on page 62.)

[Bruhwiler et al. 2005]   Bruhwiler, L. M. P., Michalak, A. M., Peters, W., Baker, D. F., and Tans, P. An improved Kalman Smoother for atmospheric inversions. *Atmos. Chem. Phys.*, 5:2691–2702, 2005. doi: 10.5194/acp-5-2691-2005. URL `https://www.atmos-chem-phys.net/5/2691/2005/`. (Cited on pages 62 and 63.)

[Brunner et al. 2012]   Brunner, D., Henne, S., Keller, C. A., et al. An extended Kalman-filter for regional scale inverse emission estimation. *Atmos. Chem. Phys.*, 12(7):3455–3478, 2012. doi: 10.5194/acp-12-3455-2012. URL `https://www.atmos-chem-phys.net/12/3455/2012/`. (Cited on pages 62 and 66.)

[Butchart et al. 2010]   Butchart, N., Cionni, I., Eyring, V., et al. Chemistry-climate model simulations of twenty-first century stratospheric climate and circulation changes. *J. Climate*, 23(20): 5349–5374, 2010. doi: 10.1175/2010JCLI3404.1. (Cited on page 127.)

[Butkovskaya et al. 2012]   Butkovskaya, N., Kukui, A., and Le Bras, G. Pressure and temperature dependence of methyl nitrate formation in the CH$_3$O$_2$ + NO reaction. *J. Phys. Chem. A*, 116: 5972–5980, 2012. doi: 10.1021/jp210710d. (Cited in Appendix E.)

[Butz et al. 2012]   Butz, A., Galli, A., Hasekamp, O., et al. TROPOMI aboard Sentinel-5 Precursor: Prospective performance of CH$_4$ retrievals for aerosol and cirrus loaded atmospheres. *Remote Sensing of Environment*, 120:267 – 276, 2012. ISSN 0034-4257. doi: 10.1016/j.rse.2011.05.030. URL `http://www.sciencedirect.com/science/article/pii/S003442571200082X`. The Sentinel Missions - New Opportunities for Science. (Cited on page 11.)

[Buzan et al. 2016]   Buzan, E. M., Beale, C. A., Boone, C. D., and Bernath, P. F. Global stratospheric measurements of the isotopologues of methane from the Atmospheric Chemistry Experiment Fourier transform spectrometer. *Atmos. Meas. Tech.*, 9(3):1095–1111, 2016. doi: 10.5194/amt-9-1095-2016. URL `https://www.atmos-meas-tech.net/9/1095/2016/`. (Cited on page 95.)

[Chai et al. 2014]   Chai, J., Hu, H., Dibble, T. S., Tyndall, G. S., and Orlando, J. J. Rate constants and kinetic isotope effects for methoxy radical reacting with NO_2 and O_2. *J. Phys. Chem. A*, 118: 3552–3563, 2014. doi: 10.1021/jp501205d. (Cited in Appendix E.)

[Chen et al. 2015]   Chen, Q., Popa, M. E., Batenburg, A. M., and Röckmann, T. Isotopic signatures of production and uptake of H_2 by soil. *Atmos. Chem. Phys.*, 15(22):13003–13021, 2015. doi: 10.5194/acp-15-13003-2015. URL `https://www.atmos-chem-phys.net/15/13003/2015/`. (Cited on page 101.)

[Christensen et al. 2004]   Christensen, T. R., Johansson, T., Åkerman, H. J., et al. Thawing sub-arctic permafrost: Effects on vegetation and methane emissions. *Geophys. Res. Lett.*, 31(4), 2004. doi: 10.1029/2003GL018680. L04501. (Cited on pages 1 and 8.)

[Crowley et al. 1999]   Crowley, J. N., Saueressig, G., Bergamaschi, P., Fischer, H., and Harris, G. W. Carbon kinetic isotope effect in the reaction CH_4+Cl: a relative rate study using FTIR spectroscopy. *Chem. Phys. Lett.*, 303(3–4):268–274, 1999. ISSN 00092614. doi: 10.1016/S0009-2614(99)00243-2. (Cited on page 18.)

[Curry 2007]   Curry, C. L. Modeling the soil consumption at atmospheric methane at the global scale. *Glob. Biogeochem. Cycles*, 21(4):1–15, 2007. ISSN 08866236. doi: 10.1029/2006GB002818. (Cited on page 68.)

[Dalsøren et al. 2016]   Dalsøren, S. B., Myhre, C. L., Myhre, G., et al. Atmospheric methane evolution the last 40 years. *Atmos. Chem. Phys.*, 16(5):3099–3126, 2016. ISSN 16807324. doi: 10.5194/acp-16-3099-2016. URL `https://www.atmos-chem-phys.net/16/3099/2016/`. (Cited on pages 1, 2, 34 and 72.)

[Dameris and Jöckel 2013]   Dameris, M. and Jöckel, P. Numerical modeling of climate-chemistry connections: Recent developments and future challenges. *Atmos.*, 4(2):132–156, 2013. doi: 10. 3390/atmos4020132. URL `http://www.mdpi.com/2073-4433/4/2/132`. (Cited on page 24.)

[Dee et al. 2011]   Dee, D. P., Uppala, S. M., Simmons, A. J., et al. The ERA-Interim reanalysis: configuration and performance of the data assimilation system. *Quart. J. Roy. Meteor. Soc.*, 137 (656):553–597, 2011. doi: 10.1002/qj.828. URL `http://dx.doi.org/10.1002/qj.828`. (Cited on page 35.)

[Dentener et al. 2003]   Dentener, F., Peters, W., Krol, M., et al. Interannual variability and trend of CH_4 lifetime as a measure for OH changes in the 1979–1993 time period. *J. Geophys. Res.*, 108 (D15):4442, 2003. doi: 10.1029/2002JD002916. (Cited on pages 20, 33, 34, 60 and 129.)

[Dessler et al. 1994]   Dessler, A. E., Weinstock, E. M., Hintsa, E. J., et al. An examination of the total hydrogen budget of the lower stratosphere. *Geophys. Res. Lett.*, 21(23):2563–2566, November 1994. (Cited on page 109.)

[Dessler et al. 2013]   Dessler, A. E., Schoeberl, M. R., Wang, T., Davis, S. M., and Rosenlof, K. H. Stratospheric water vapor feedback. *PNAS*, 110(45):18087–18091, 2013. doi: 10.1073/pnas. 1310344110. URL `www.pnas.org/cgi/doi/10.1073/pnas.1310344110`. (Cited on page 22.)

[Dietmüller et al. 2014]   Dietmüller, S., Ponater, M., and Sausen, R. Interactive ozone induces a negative feedback in CO_2-driven climate change simulations. *J. Geophys. Res. Atmos.*, 119(4): 1796–1805, 2014. doi: 10.1002/2013JD020575. URL `http://dx.doi.org/10.1002/2013JD020575`. (Cited on page 41.)

[Dietmüller et al. 2016]   Dietmüller, S., Jöckel, P., Tost, H., et al. A new radiation infrastructure for the modular earth submodel system (MESSy, based on version 2.51). *Geosci. Model Dev.*, 9(6): 2209–2222, 2016. doi: 10.5194/gmd-9-2209-2016. URL `https://www.geosci-model-dev.net/9/2209/2016/`. (Cited on page 25.)

[Dietmüller et al. 2017]   Dietmüller, S., Eichinger, R., Garny, H., et al. Quantifying the effect of mixing on the mean Age of Air in CCMVal-2 and CCMI-1 models. *Atmos. Chem. Phys. Discuss.*, 2017:1–34, 2017. doi: 10.5194/acp-2017-1143. URL `https://www.atmos-chem-phys-discuss.net/acp-2017-1143/`. (Cited on pages 98 and 132.)

[digital dutch 1999]   digital dutch, 1999. URL `https://www.digitaldutch.com/atmoscalc/`. (last accessed Jan 2018). (Cited on page 111.)

[Dlugokencky et al. 2015a]   Dlugokencky, E., Lang, P., Crotwell, A., Masarie, K., and Crotwell, M. Atmospheric methane dry air mole fractions from the NOAA ESRL carbon cycle cooperative global air sampling network, 2015a. URL `ftp://aftp.cmdl.noaa.gov/data/trace_gases/ch4/flask/surface/`. (Cited on pages 6, 7, 77 and 78.)

[Dlugokencky et al. 2015b]   Dlugokencky, E., Lang, P., Masarie, K., et al. An update on the atmospheric methane growth rate: Growth surges during 2014. In *NOAA ESRL GLOBAL MONITORING ANNUAL CONFERENCE*, May 2015b. (Cited on pages 2 and 6.)

[Dlugokencky et al. 2017]   Dlugokencky, E., Crotwell, A., Lang, P., and Mund, J. Atmospheric methane dry air mole fractions from quasi-continuous measurements at Barrow, Alaska and Mauna Loa, Hawaii, 1986–2016, 2017. URL `ftp://aftp.cmdl.noaa.gov/data/trace_gases/ch4/in-situ/surface/`. Version: 2017-01-20. (Cited on page 67.)

[Dlugokencky et al. 1994]   Dlugokencky, E. J., Steele, L. P., Lang, P. M., and Masarie, K. A. The growth rate and distribution of atmospheric methane. *J. Geophys. Res. Atmos.*, 99(D8):17021–17043, 1994. doi: 10.1029/94JD01245. (Cited on pages 2, 6, 40, 67 and 83.)

[Dlugokencky et al. 1995]   Dlugokencky, E. J., Steele, L. P., Lang, P. M., and Masarie, K. A. Atmospheric methane at Mauna Loa and Barrow observatories: Presentation and analysis of in situ measurements. *J. Geophys. Res. Atmos.*, 100(D11):23103–23113, 1995. doi: 10.1029/95JD02460. (Cited on page 10.)

[Dlugokencky et al. 2003]   Dlugokencky, E. J., Houweling, S., Bruhwiler, L., et al. Atmospheric methane levels off: Temporary pause or a new steady-state? *Geophys. Res. Lett.*, 30(19), 2003. doi: 10.1029/2003GL018126. URL `http://dx.doi.org/10.1029/2003GL018126`. 1992. (Cited on pages 1, 6 and 76.)

[Dlugokencky et al. 2011]   Dlugokencky, E. J., Nisbet, E. G., Fisher, R., and Lowry, D. Global atmospheric methane: Budget, changes and dangers. *Philosophical transactions. Series A, Mathematical, physical, and engineering sciences*, 369(1943):2058–2072, 2011. ISSN 1364-503X. doi: 10.1098/rsta.2010.0341. (Cited on pages 1, 2, 6, 7 and 129.)

[Dunlop and Tully 1993]   Dunlop, J. R. and Tully, F. P. A kinetic study of OH radical reactions with methane and perdeuterated methane. *J. Phys. Chem.*, 97:11148–11150, 1993. doi: 10.1021/j100145a003. (Cited on pages 74 and 141.)

[EC-JRC/PBL 2011]   EC-JRC/PBL. Emission database for global atmospheric research (EDGAR), release version 4.2., 2011. URL http://edgar.jrc.ec.europa.eu. Last Accessed: Feb 2018. (Cited on page 68.)

[ECMWF 2007]   ECMWF. *IFS DOCUMENTATION - Cy31r1, Part IV: Physical Processes*, 2007. URL https://www.ecmwf.int/sites/default/files/elibrary/2007/9221-part-iv-physical-processes.pdf. (Cited on pages 26 and 109.)

[Ehret et al. 2017]   Ehret, G., Bousquet, P., Pierangelo, C., et al. MERLIN: A French-German space lidar mission dedicated to atmospheric methane. *Remote Sensing*, 9(10), 2017. doi: 10.3390/rs9101052. URL http://www.mdpi.com/2072-4292/9/10/1052. (Cited on page 11.)

[Eichinger 2014]   Eichinger, R. *Investigation of stratospheric water vapour by means of the simulation of water isotopologues*. PhD thesis, Ludwig Maximilian Universität München, 2014. (Cited on pages 17 and 30.)

[Eichinger et al. 2015a]   Eichinger, R., Jöckel, P., Brinkop, S., Werner, M., and Lossow, S. Simulation of the isotopic composition of stratospheric water vapour - part 1: Description and evaluation of the EMAC model. *Atmos. Chem. Phys.*, 15:5537–5555, 2015a. doi: 10.5194/acp-15-5537-2015. (Cited on pages 3, 25, 26, 28, 30, 88, 99, 101, 102, 104, 106, 107, 109, 132, 134, 147 and 149.)

[Eichinger et al. 2015b]   Eichinger, R., Jöckel, P., and Lossow, S. Simulation of the isotopic composition of stratospheric water vapour - part 2: Investigation of HDO / H_2O variations. *Atmos. Chem. Phys.*, 15(12):7003–7015, 2015b. doi: 10.5194/acp-15-7003-2015. URL http://www.atmos-chem-phys.net/15/7003/2015/. (Cited on pages 26 and 101.)

[Eiler 2007]   Eiler, J. M. "clumped-isotope" geochemistry - the study of naturally-occurring, multiply-substituted isotopologues. *Earth and Planetary Science Letters*, 262(3):309–327, 2007. doi: 10.1016/j.epsl.2007.08.020. URL http://www.sciencedirect.com/science/article/pii/S0012821X07005109. (Cited on page 15.)

[Elshorbany et al. 2012]   Elshorbany, Y. F., Kleffmann, J., Hofzumahaus, A., et al. HOx budgets during HOxComp: A case study of HOx chemistry under NOx-limited conditions. *J. Geophys. Res. Atmos.*, 117(D3), 2012. doi: 10.1029/2011JD017008. URL http://dx.doi.org/10.1029/2011JD017008. D03307. (Cited on page 33.)

[Enghag 2004]   Enghag, P. *Encyclopedia of the Elements*. WILEY-VCH Verlag GmbH & Co. KGaA, 2004. ISBN 9788578110796. doi: 10.1017/CBO9781107415324.004. ISBN 3-527-30666-8. (Cited on page 15.)

[Espinosa-Garcia and Garcia-Bernáldez 2000]   Espinosa-Garcia, J. and Garcia-Bernáldez, J. C. Analytical potential energy surface for the $CH_4 + O(^3P) \longrightarrow CH_3 + OH$ reaction. thermal rate constants and kinetic isotope effects. *Phys. Chem. Chem. Phys.*, 2:2345–2351, 2000. (Cited in Appendix E.)

[Etiope et al. 2008]   Etiope, G., Milkov, A. V., and Derbyshire, E. Did geologic emissions of methane play any role in quaternary climate change? *Global and Planetary Change*, 61(1):79–88, 2008. doi: 10.1016/j.gloplacha.2007.08.008. URL `http://www.sciencedirect.com/science/article/pii/S0921818107001300`. (Cited on page 68.)

[Eyring et al. 2013]   Eyring, V., Lamarque, J.-F., Hess, P., et al. Overview of IGAC/SPARC chemistry-climate model initiative (CCMI) community simulations in support of upcoming ozone and climate assessments. 2013. URL `http://www.sparc-climate.org/fileadmin/customer/6_Publications/Newsletter_PDF/40_SPARCnewsletter_Jan2013_web.pdf`. (last access: 23 November 2017). (Cited on page 39.)

[Eyring et al. 2016]   Eyring, V., Righi, M., Lauer, A., et al. ESMValTool (v1.0) – a community diagnostic and performance metrics tool for routine evaluation of Earth system models in CMIP. *Geosci. Model Dev.*, 9(5):1747–1802, 2016. doi: 10.5194/gmd-9-1747-2016. URL `https://www.geosci-model-dev.net/9/1747/2016/`. (Cited on page 35.)

[Feilberg et al. 2004]   Feilberg, K. L., Johnson, M. S., and Nielsen, C. J. Relative reaction rates of HCHO, HCDO, DCDO, H^{13}CHO, and HCH^{18}O with OH, Cl, Br, and NO$_3$ radicals. *J. Phys. Chem. A*, 108(36):7393–7398, 2004. ISSN 10895639. doi: 10.1021/jp048329k. (Cited on page 19.)

[Feilberg et al. 2008]   Feilberg, K. L., Gruber-Stadler, M., Johnson, M. S., Mühlhäuser, M., and Nielsen, C. J. ^{13}C, ^{18}O, and D fractionation effect in the reactions of CH$_3$OH isotopologues with Cl and OH radicals. *J. Phys. Chem.*, 112:11099–11114, 2008. doi: 10.1021/jp805643x. (Cited on page 19.)

[Finlayson-Pitts and Pitts 2000]   Finlayson-Pitts, B. J. and Pitts, J. N. *Chemistry of the Upper and Lower Atmosphere.* Academic Press, Inc., 2000. (Cited on pages 21 and 33.)

[Fiore et al. 2006]   Fiore, A. M., Horowitz, L. W., Dlugokencky, E. J., and West, J. J. Impact of meteorology and emissions on methane trends, 1990–2004. *Geophys. Res. Lett.*, 33:L12809, 2006. doi: 10.1029/2006GL026199. (Cited on pages 1, 20, 34, 50, 60, 129 and 130.)

[Fiore et al. 2009]   Fiore, A. M., Dentener, F. J., Wild, O., et al. Multimodel estimates of intercontinental source-receptor relationships for ozone pollution. *J. Geophys. Res.*, 114(D4), 2009. doi: 10.1029/2008JD010816. D04301. (Cited on page 68.)

[Fletcher et al. 2004]   Fletcher, M., E., S., Tans, P. P., et al. CH$_4$ sources estimated from atmospheric observations of CH4 and its ^{13}C/^{12}C isotopic ratios: 2. inverse modeling of CH$_4$ fluxes from geographical regions. *Glob. Biogeochem. Cycles*, 18(4):1–15, 2004. ISSN 08866236. doi: 10.1029/2004GB002224. (Cited on pages 2, 14, 16, 61, 62 and 89.)

[Flocke et al. 1998]   Flocke, F., Atlas, E., Madronich, S., et al. Observations of methyl nitrate in the lower stratosphere during STRAT: implications for its gas phase production mechanisms. *Geophys. Res. Lett.*, 25:1891–1894, 1998. doi: 10.1029/98GL01417. (Cited in Appendix E.)

[Forster and Shine 1999]   Forster, P. M. d. F. and Shine, K. P. Stratospheric water vapour changes as a possible contributor to observed stratospheric cooling. *Geophys. Res. Lett.*, 26:3309–3312, 1999. URL `https://doi.org/10.1029/1999GL010487`. (Cited on page 21.)

[Frank et al. 2018]   Frank, F., Jöckel, P., Gromov, S., and Dameris, M. Investigating the yield of H$_2$O and H$_2$ from methane oxidation in the stratosphere. *Atmos. Chem. Phys. Discuss.*, 2018:1–29, 2018.

doi: 10.5194/acp-2018-170. URL `https://www.atmos-chem-phys-discuss.net/acp-2018-170/`. (Cited on page 109.)

[Frankenberg et al. 2011] Frankenberg, C., Aben, I., Bergamaschi, P., et al. Global column-averaged methane mixing ratios from 2003 to 2009 as derived from SCIAMACHY: Trends and variability. *J. Geophys. Res. Atmos.*, 116(4):1–12, 2011. ISSN 01480227. doi: 10.1029/2010JD014849. (Cited on page 11.)

[Fry 2006] Fry, B. *Stable isotope ecology.* Springer, 2006. ISBN 0470016175. doi: 10.1002/9780470015902.a0021231. (Cited on pages 12, 13, 15 and 17.)

[Fueglistaler and Haynes 2005] Fueglistaler, S. and Haynes, P. H. Control of interannual and longer-term variability of stratospheric water vapor. *J. Geophys. Res.*, 110:D24108, 2005. URL `https://doi.org/10.1029/2005JD006019`. (Cited on pages 5, 21, 22 and 102.)

[Fung et al. 1991] Fung, I., John, J., Lerner, J., et al. Three-dimensional model synthesis of the global methane cycle. *J. Geophys. Res.*, 96(D7):13033–13065, 1991. ISSN 0148-0227. doi: 10.1029/91jd01247. (Cited on page 1.)

[Garton et al. 2003] Garton, D. J., Minton, T. K., Troya, D., Pascual, R., and Schatz, G. C. Hyperthermal reactions of O(^{3}P) with alkanes: Observations of novel reaction pathways in crossed-beams and theoretical studies. *J. Phys. Chem. A*, 107:4583–4587, 2003. doi: 10.1021/jp0226026. (Cited in Appendix E.)

[Gat 2010] Gat, J. R. *ISOTOPE HYDROLOGY A Study of the Water Cycle*, volume 6 of *Environmental Science and Management.* Imperical College Press, 2010. ISBN 9781860940354. (Cited on pages 15 and 17.)

[Gerst and Quay 2000] Gerst, S. and Quay, P. The deuterium content of atmospheric molecular hydrogen: Method and initial measurements. *J. Geophys. Res. Atmos.*, 105(D21):26433–26445, 2000. (Cited on page 101.)

[Gerst and Quay 2001] Gerst, S. and Quay, P. Deuterium component of the global molecular hydrogen cycle. *J. Geophys. Res. Atmos.*, 106(D5):5021–5031, 2001. doi: 10.1029/2000JD900593. (Cited on page 101.)

[Giorgetta et al. 2002] Giorgetta, M. A., Manzini, E., and Roeckner, E. Forcing of the quasi-biennial oscillation from a broad spectrum of atmospheric waves. *Geophys. Res. Lett.*, 29(8):86–1–86–4, 2002. doi: 10.1029/2002GL014756. URL `http://dx.doi.org/10.1029/2002GL014756`. (Cited on page 25.)

[Gola et al. 2005] Gola, A. A., D'Anna, B., Feilberg, K. L., et al. Kinetic isotope effects in the gas phase reactions of OH and Cl with CH_3Cl, CD_3Cl, and $^{13}CH_3Cl$. *Atmos. Chem. Phys.*, 5(9):2395–2402, 2005. ISSN 1680-7324. doi: 10.5194/acp-5-2395-2005. URL `http://www.atmos-chem-phys.net/5/2395/2005/`. (Cited on page 19.)

[Gosh et al. 2015] Gosh, A., Patra, P. K., Ishijima, K., et al. Variations in global methane sources and sinks during 1910-2010. *Atmos. Chem. Phys.*, 15:2595–2612, 2015. doi: 10.5194/acp-15-2595-2015. (Cited on pages 2, 21, 33, 34, 60 and 129.)

[Grewe 2006]   Grewe, V. The origin of ozone. *Atmos. Chem. Phys.*, 6:1495–1511, 2006. doi: 10.5194/acp-6-1495-2006. URL `https://www.atmos-chem-phys.net/6/1495/2006/`. (Cited on page 25.)

[Grewe et al. 2001]   Grewe, V., Brunner, D., Dameris, M., et al. Origin and variability of upper tropospheric nitrogen oxides and ozone at northern mid-latitudes. *Atmos. Environ.*, 35(20):3421–3433, 2001. (Cited on page 25.)

[Griffith et al. 2013]   Griffith, S. M., Hansen, R. F., Dusanter, S., et al. OH and HO_2 radical chemistry during PROPHET 2008 and CABINEX 2009 - part 1: Measurements and model comparison. *Atmos. Chem. Phys.*, 13(11):5403–5423, 2013. doi: 10.5194/acp-13-5403-2013. URL `https://www.atmos-chem-phys.net/13/5403/2013/`. (Cited on page 5.)

[Gromov 2014]   Gromov, S. *Stable isotope composition of atmospheric carbon monoxide: a modelling study*. PhD thesis, Johannes Gutenberg University Mainz, 2014. URL `http://ubm.opus.hbz-nrw.de/volltexte/2014/3747/`. (Cited on pages 30 and 87.)

[Gromov et al. 2010]   Gromov, S., Jöckel, P., Sander, R., and Brenninkmeijer, C. A. M. A kinetic chemistry tagging technique and its application to modelling the stable isotopic composition of atmospheric trace gases. *Geosci. Model Dev.*, 3:337–364, 2010. doi: 10.5194/gmd-3-337-2010. URL `www.geosci-model-dev.net/3/337/2010/`. (Cited on pages 4, 25, 29, 30, 87, 111 and 131.)

[Gromov et al. 2017]   Gromov, S., Brenninkmeijer, C. A. M., and Jöckel, P. Uncertainties of fluxes and $^{13}C/^{12}C$ ratios of atmospheric reactive-gas emissions. *Atmos. Chem. Phys.*, 17:8525–8552, 2017. URL `https://doi.org/10.5194/acp-17-8525-2017`. (Cited on pages 30 and 87.)

[Gros et al. 2004]   Gros, V., Brenninkmeijer, C. A. M., Jöckel, P., et al. Use of isotopes. Emissions of Atmospheric Trace Compounds, 2004. (Cited on pages 11 and 14.)

[Gurney et al. 2000]   Gurney, L., K., R., P., Rayner, and Denning, A. TransCom 3 experimental protocol. Technical Report Paper No. 707, Department of Atmospheric Science, Colorado State University, USA, 2000. (Cited on page 62.)

[Hall et al. 2016]   Hall, E. G., Jordan, A. F., Hurst, D. F., et al. Advancements, measurement uncertainties, and recent comparisons of the NOAA frost-point hygrometer. *Atmos. Meas. Tech.*, 9(9):4295–4310, 2016. doi: 10.5194/amt-9-4295-2016. URL `https://www.atmos-meas-tech.net/9/4295/2016/`. (Cited on pages 21 and 22.)

[Heard and Pilling 2003]   Heard, D. E. and Pilling, M. J. Measurement of OH and HO_2 in the troposphere. *Chem. Rev.*, 103(12):5163–5198, 2003. doi: 10.1021/cr020522s. URL `http://dx.doi.org/10.1021/cr020522s`. (Cited on page 33.)

[Hein et al. 1997]   Hein, R., Crutzen, P. J., and Heimann, M. An inverse modeling approach to investigate the global atmospheric methane cycle. *Glob. Biogeochem. Cycles*, 11:43–76, 1997. (Cited on pages 1, 2, 14, 34, 44, 60, 61 and 87.)

[Henne 2018]   Henne, S. Extensions of the lagrangian model FLEXPART. pers. comm., 2018. (Cited on page 62.)

[Holden 1990]   Holden, N. E. Total half-lives for selected nuclides. *Pure Appl. Chem.*, 62(5):941–958, 1990. URL `http://dx.doi.org/10.1351/pac199062050941`. (Cited on page 15.)

[Holmgren 2006]   Holmgren, P. Global land use area change matrix. Working Paper 134, Forest Resources Assessment Programme, Food and Agriculture Organization of the United Nations, 2006. (Cited on page 18.)

[Holton et al. 1995]   Holton, J. R., Haynes, P. H., McIntyre, M. E., et al. Stratosphere-troposphere exchange. *Rev. Geophys.*, 33(4):403–439, 1995. doi: 10.1029/95RG02097. URL `http://dx.doi.org/10.1029/95RG02097`. (Cited on page 22.)

[Houweling et al. 1999]   Houweling, S., Kaminski, T., Dentener, F., Lelieveld, J., and Heimann, M. Inverse modeling of methane sources and sinks using the adjoint of a global transport model. *J. Geophys. Res.*, 104(D21):26137–26160, 1999. doi: doi:10.1029/1999JD900428. (Cited on pages 62 and 68.)

[Houweling et al. 2017]   Houweling, S., Bergamaschi, P., Chevallier, F., et al. Global inverse modeling of CH_4 sources and sinks: an overview of methods. *Atmos. Chem. Phys.*, 17(1):235–256, 2017. doi: 10.5194/acp-17-235-2017. URL `https://www.atmos-chem-phys.net/17/235/2017/`. (Cited on page 61.)

[Hu et al. 2012]   Hu, H., Dibble, T. S., Tyndall, G. S., and Orlando, J. J. Temperature-dependent branching ratios of deuterated methoxy radicals ($CH_2DO\cdot$) reacting with O_2. *J. Phys. Chem. A*, 116(24):6295–302, 2012. ISSN 1520-5215. doi: 10.1021/jp211873w. URL `http://www.ncbi.nlm.nih.gov/pubmed/22432871`. (Cited on pages 20 and 88.)

[Hurst et al. 1999]   Hurst, D., Dutton, G., Romashkin, P., et al. Closure of the total hydrogen budget of the northern extratropical lower stratosphere. *J. Geophys. Res. Atmos.*, 104:8191–8200, April 1999. (Cited on pages 109, 110, 126, 127 and 133.)

[Hynes and Wine 1996]   Hynes, A. J. and Wine, P. H. The atmospheric chemistry of dimethylsulfoxide (DMSO) kinetics and mechanism of the OH + DMSO reaction. *J. Atmos. Chem.*, 24:23–37, 1996. (Cited in Appendix E.)

[IPCC 2013]   IPCC. *Climate Change 2013: The Physical Science Basis. Contribution of Working Group I to the Fifth Assessment Report of the Intergovernmental Panel on Climate Change.* Cambridge University Press, Cambridge, United Kingdom and New York, NY, USA, 2013. doi: 10.1017/CBO9781107415324. URL `www.climatechange2013.org`. (Cited on pages 1, 2, 7, 8, 9, 10, 16, 39, 43, 61 and 130.)

[Jacob et al. 2016]   Jacob, D. J., Turner, A. J., Maasakkers, J. D., et al. Satellite observations of atmospheric methane and their value for quantifying methane emissions. *Atmos. Chem. Phys.*, 16 (22):14371–14396, 2016. doi: 10.5194/acp-16-14371-2016. URL `https://www.atmos-chem-phys.net/16/14371/2016/`. (Cited on pages 11 and 61.)

[Jöckel et al. 2000]   Jöckel, P., Brenninkmeijer, C. A. M., and Lawrence, M. G. Atmospheric response time of cosmogenic ^{14}CO to changes in solar activity. *J. Geophys. Res. Atmos.*, 105(D5): 6737–6744, 2000. ISSN 2156-2202. doi: 10.1029/1999JD901140. URL `http://dx.doi.org/10.1029/1999JD901140`. (Cited on page 141.)

[Jöckel et al. 2002]   Jöckel, P., Brenninkmeijer, C. A. M., Lawrence, M. G., Jeuken, A. B. M., and van Velthoven, P. F. J. Evaluation of stratosphere-troposphere exchange and the hydroxyl radical distribution in three-dimensional global atmospheric models using observations of cosmogenic ^{14}CO. *J. Geophys. Res.*, 107(D20):4446, 2002. doi: 10.1029/2001JD001324. (Cited on pages 33 and 55.)

[Jöckel et al. 2003]   Jöckel, P., Brenninkmeijer, C. A. M., Singh, H. B., and Crutzen, P. J.   Investigation of the global atmospheric oxidation efficiency and its trends: A proposal to initiate IGAC-GHOST (global HO systematic tests). IGACtivities Newsletter 28, May 2003. URL `http://www.igacproject.org/sites/default/files/2016-07/Issue_28_May_2003.pdf(lastaccess27Nov2017)`. (Cited on page 33.)

[Jöckel et al. 2006]   Jöckel, P., Tost, H., Pozzer, A., et al. The atmospheric chemistry general circulation model ECHAM5/MESSy1: consistent simulation of ozone from the surface to the mesosphere. *Atmos. Chem. Phys.*, 6:5067–5104, 2006. doi: 10.5194/acp-6-5067-2006. (Cited on pages 25, 34, 40, 43 and 59.)

[Jöckel et al. 2008]   Jöckel, P., Kerkweg, A., Buchholz-Dietsch, J., et al. Technical note: Coupling of chemical processes with the modular earth submodel system (MESSy) submodel TRACER. *Atmos. Chem. Phys.*, 8(6):1677–1687, 2008. doi: 10.5194/acp-8-1677-200. URL `https://www.atmos-chem-phys.net/8/1677/2008/`. (Cited on pages 23, 25 and 143.)

[Jöckel et al. 2010]   Jöckel, P., Kerkweg, A., Pozzer, A., et al. Development cycle 2 of the modular earth submodel system MESSy2. *Geosci. Model Dev.*, 3:717–752, 2010. doi: 10.5194/gmd-3-717-2010. Manual. (Cited on pages 3, 23, 25, 29, 44 and 62.)

[Jöckel et al. 2016]   Jöckel, P., Tost, H., Pozzer, A., et al. Earth system chemistry integrated modelling (ESCiMo) with the modular earth submodel system (MESSy) version 2.51. *Geosci. Model Dev.*, 9:1153–1200, 2016. doi: 10.5194/gmd-9-1153-2016. URL `http://www.geosci-model-dev.net/9/1153/2016/gmd-9-1153-2016.html`. (Cited on pages 23, 25, 26, 29, 33, 34, 35, 36, 111, 130 and 157.)

[Johnston and Kinnison 1998]   Johnston, H. and Kinnison, D. Methane photooxidation in the atmosphere: Contrast between two methods of analysis. *J. Geophys. Res.*, 103(D17):21967–21984, sep 1998. (Cited on pages 1 and 110.)

[Kalman 1960]   Kalman, R. E. A new approach in linear filtering and prediction problems. *ASME–Journal of Basic Engineering*, 82(Series D):35–45, 1960. (Cited on page 62.)

[Kalnay et al. 1996]   Kalnay, E., Kanamitsu, M., Kistler, R., et al. The NCEP/NCAR 40-Year Reanalysis Project. *Bull. Amer. Meteor. Soc.*, 77(3):437–472, 1996. doi: 10.1175/1520-0477(1996)077<0437:TNYRP>2.0.CO;2.   URL `https://doi.org/10.1175/1520-0477(1996)077<0437:TNYRP>2.0.CO;2`. (Cited on page 35.)

[Karlsdóttir and Isaksen 2000]   Karlsdóttir, S. and Isaksen, I. S. A. Changing methane lifetime: Possible cause for reduced growth. *Geophys. Res. Lett.*, 27(1):93–96, 2000. doi: 10.1029/1999GL010860. URL `http://dx.doi.org/10.1029/1999GL010860`. (Cited on pages 1 and 34.)

[Kaye 1992]   Kaye, J. A. Isotope effects in gas-phase chemistry. In Kaye, J. A., editor, *ACS Symposium Series*. American Chemical Society, 1992. ISBN 0841224714. (Cited on page 20.)

[Kerkweg et al. 2006a]   Kerkweg, A., Buchholz, J., Ganzeveld, L., et al. Technical note: An implementation of the dry removal processes DRY DEPosition and SEDimentation in the modular earth submodel system (MESSy). *Atmos. Chem. Phys.*, 6(12):4617–4632, 2006a. doi: 10.5194/acp-6-4617-2006. URL `https://www.atmos-chem-phys.net/6/4617/2006/`. (Cited on page 25.)

[Kerkweg et al. 2006b]   Kerkweg, A., Sander, R., Tost, H., and Jöckel, P. Technical note: Implementation of prescribed (OFFLEM), calculated (ONLEM), and pseudo-emissions (TNUDGE) of chemical species in the modular earth submodel system (MESSy). *Atmos. Chem. Phys.*, 6(11):3603–3609, 2006b. doi: 10.5194/acp-6-3603-2006. URL `https://www.atmos-chem-phys.net/6/3603/2006/`. (Cited on pages 24, 25, 27 and 143.)

[Kern 2013]   Kern, B. *Chemical interaction between ocean and atmosphere*. PhD thesis, Johannes Gutenberg-Universität Mainz, 2013. URL `http://publications.ub.uni-mainz.de/theses/volltexte/2014/3732/pdf/3732.pdf`. (Cited on page 25.)

[Kiemle et al. 2014]   Kiemle, C., Kawa, S. R., Quatrevalet, M., and Browell, E. V. Performance simulations for a spaceborne methane lidar mission. *J. Geophys. Res. Atmos.*, 119(7):4365–4379, 2014. ISSN 2169-8996. doi: 10.1002/2013JD021253. URL `http://dx.doi.org/10.1002/2013JD021253`. 2013JD021253. (Cited on page 11.)

[King 1997]   King, G. Responses of atmospheric methane consumption by soils to global climate change. *Global Change Biology*, 3(4):351–362, 1997. doi: 10.1046/j.1365-2486.1997.00090.x. URL `http://dx.doi.org/10.1046/j.1365-2486.1997.00090.x`. (Cited on page 10.)

[Kirschke et al. 2013]   Kirschke, S., Bousquet, P., Ciais, P., et al. Three decades of global methane sources and sinks. *Nature Geoscience*, 6:813–823, 2013. doi: 10.1038/ngeo1955. URL `https://www.nature.com/articles/ngeo1955#supplementary-information`. (Cited on page 8.)

[Kiyosu 1983]   Kiyosu, Y. Hydrogen isotopic compositions of hydrogen and methane from some volcanic areas in northeastern Japan. *Earth and Planetary Science Letters*, 62(1):41–52, 1983. ISSN 0012821X. doi: 10.1016/0012-821X(83)90069-9. (Cited on pages 16 and 89.)

[Krol and Lelieveld 2003]   Krol, M. and Lelieveld, J. Can the variability in tropospheric OH be deduced from measurements of 1,1,1-trichloroethane (methyl chloroform)? *J. Geophys. Res. Atmos.*, 108(D3), 2003. doi: 10.1029/2002JD002423. URL `http://dx.doi.org/10.1029/2002JD002423`. 4125. (Cited on page 33.)

[Krol et al. 1998]   Krol, M., van Leeuwen, P. J., and Lelieveld, J. Global OH trend inferred from methylchloroform measurements. *J. Geophys. Res.*, 103(D9):10697–10711, 1998. (Cited on page 34.)

[Krol et al. 2008]   Krol, M. C., Meirink, J. F., Bergamaschi, P., et al. What can [14]CO measurements tell us about OH? *Atmos. Chem. Phys.*, 8(16):5033–5044, 2008. doi: 10.5194/acp-8-5033-2008. URL `https://www.atmos-chem-phys.net/8/5033/2008/`. (Cited on pages 33 and 55.)

[Kuze et al. 2016]   Kuze, A., Suto, H., Shiomi, K., et al. Update on GOSAT TANSO-FTS performance, operations, and data products after more than 6 years in space. *Atmos. Meas. Tech.*, 9 (6):2445–2461, 2016. doi: 10.5194/amt-9-2445-2016. URL `https://www.atmos-meas-tech.net/9/2445/2016/`. (Cited on page 11.)

[Lawrence et al. 2001]   Lawrence, M. G., Jöckel, and von Kuhlmann, R. What does the global mean OH concentration tell us? *Atmos. Chem. Phys.*, 1:37–49, 2001. URL `www.atmos-chem-phys.org/acp/1/37/`. (Cited on pages 20, 34, 45, 51 and 59.)

[le Texier et al. 1988]   le Texier, H., Solomon, S., and Garcia, R. R. The role of molecular hydrogen and methane oxidation in the water vapour budget of the stratosphere. *Quart. J. Roy. Meteor. Soc.*, 114(480):281–295, 1988. ISSN 00359009. doi: 10.1002/qj.49711448002. (Cited on pages 26, 107, 109, 110, 126 and 133.)

[Lehmann 2004]   Lehmann, R. An algorithm for the determination of all significant pathways in chemical reaction systems. *J. Atmos. Chem.*, 47(1):45–78, Jan 2004. doi: 10.1023/B:JOCH. 0000012284.28801.b1. (Cited on page 30.)

[Lelieveld et al. 2002]   Lelieveld, J., Peters, W., Dentener, F. J., and Krol, M. C. Stability of tropospheric hydroxyl chemistry. *J. Geophys. Res. Atmos.*, 107(D23):1–11, 2002. ISSN 21698996. doi: 10.1029/2002JD002272. (Cited on pages 33 and 50.)

[Lelieveld et al. 2004]   Lelieveld, J., Dentener, F. J., Peters, W., and Krol, M. C. On the role of hydroxyl radicals in the self-cleansing capacity of the troposphere. *Atmos. Chem. Phys.*, 4: 2337–2344, 2004. URL `www.atmos-chem-phys.org/acp/4/2337/`. (Cited on page 20.)

[Lelieveld et al. 2006]   Lelieveld, J., Brenninkmeijer, C. A. M., Jöckel, P., et al. New directions: Watching overtropospheric hydroxyl (OH). *Atmos. Environ.*, 40:5741–5743, 2006. doi: 10.1016/j. atmosenv.2006.04.008. (Cited on page 33.)

[Lelieveld et al. 2008]   Lelieveld, J., Butler, T. M., Crowley, J. N., et al. Atmospheric oxidation capacity sustained by a tropical forest. *Nature*, 452:737–740, 2008. doi: 10.1038/nature06870. (Cited on page 33.)

[Lelieveld et al. 2016]   Lelieveld, J., Gromov, S., Pozzer, A., and Taraborrelli, D. Global tropospheric hydroxyl distribution, budget and reactivity. *Atmos. Chem. Phys. Discuss.*, 1(March):1–25, 2016. ISSN 1680-7375. doi: 10.5194/acp-2016-160. URL `http://www.atmos-chem-phys-discuss.net/ acp-2016-160/`. (Cited on pages 20 and 34.)

[Löffler et al. 2016]   Löffler, M., Brinkop, S., and Jöckel, P. Impact of major volcanic eruptions on stratospheric water vapour. *Atmos. Chem. Phys.*, 16:6547–6562, 2016. doi: 10.5194/ acp-16-6547-2016. URL `www.atmos-chem-phys.net/16/6547/2016/`. (Cited on pages 35 and 102.)

[Lossow et al. 2011]   Lossow, S., Steinwagner, J., Urban, J., et al. Comparison of HDO measurements from Envisat/MIPAS with observations by Odin/SMR and SCISAT/ACE-FTS. *Atmos. Meas. Tech.*, 4(9):1855–1874, 2011. doi: 10.5194/amt-4-1855-2011. URL `https://www. atmos-meas-tech.net/4/1855/2011/`. (Cited on pages 101, 104 and 132.)

[MacKay and Khalil 1991]   MacKay, R. and Khalil, M. Theory and development of a one dimensional time dependent radiative convective climate model. *Chemosphere*, 22(3):383–417, 1991. doi: 10.1016/0045-6535(91)90326-9. URL `http://www.sciencedirect.com/science/article/ pii/0045653591903269`. (Cited on page 41.)

[MacKenzie and Harwood 2004]   MacKenzie, I. A. and Harwood, R. S. Middle-atmospheric response to a future increase in humidity arising from increased methane abundance. *J. Geophys. Res.*, 109: D02107, 2004. doi: 10.1029/2003JD003590. (Cited on page 127.)

[Manning et al. 2005]   Manning, M. R., Lowe, D. C., Moss, R. C., Bodeker, G. E., and Allan, W. Short-term variations in the oxidizing power of the atmosphere. *Nature*, 436:1001–1004, 2005. doi: 10.1038/nature03900. (Cited on page 33.)

[Maxfield et al. 2008]   Maxfield, P. J., Evershed, R. P., and Hornibrook, E. R. C. Physical and biological controls on the in situ kinetic isotope effect associated with oxidation of atmospheric CH_4 in mineral soils. *Environ. Sci. Technol.*, 42(21):7824–7830, 2008. doi: 10.1021/es800544q. URL `http://dx.doi.org/10.1021/es800544q`. PMID: 19031867. (Cited on page 18.)

[Maycock et al. 2014]   Maycock, A. C., Joshi, J. M., Shine, K. P., Davis, S. M., and Rosenlof, K. H. The potential impact of changes in lower stratospheric water vapour on stratospheric temperatures over the past 30 years. *Quart. J. Roy. Meteor. Soc.*, 26:2176–2185, 2014. doi: 10.1002/qj.2287. (Cited on page 21.)

[McCalley et al. 2014]   McCalley, C. K., Woodcroft, B. J., Hodgkins, S. B., et al. Methane dynamics regulated by microbial community response to permafrost thaw. *Nature*, 514:478–481, 2014. doi: 10. 1038/nature13798. URL `https://www.nature.com/articles/nature13798`. (Cited on page 19.)

[McCarthy et al. 2004]   McCarthy, M. C., Boering, K. A., Rahn, T., et al. The hydrogen isotopic composition of water vapor entering the stratosphere inferred from high-precision measurements of δDCH_4 and δDH_2. *J. Geophys. Res.*, 109:1–12, 2004. ISSN 0148-0227. doi: 10.1029/2003JD004003. URL `http://www.agu.org/pubs/crossref/2004/2003JD004003.shtml`. (Cited on page 102.)

[McCormack et al. 2008]   McCormack, J. P., Hoppel, K. W., and Siskind, D. E. Parameterization of middle atmospheric water vapor photochemistry for high-altitude NWP and data assimilation. *Atmos. Chem. Phys.*, 8:7519–7532, 2008. doi: 10.5194/acp-8-7519-2008. URL `https://www.atmos-chem-phys.net/8/7519/2008`. (Cited on page 127.)

[McKinney et al. 1950]   McKinney, C. R., McCrea, J. M., Epstein, S., Allen, H. A., and Urey, H. C. Improvements in mass spectrometers for the measurement of small differences in isotope abundance ratios. *The Review of Scientific Instruments*, 21(8):724–730, 1950. doi: 10.1063/1.1745698. (Cited on page 12.)

[McNorton et al. 2016]   McNorton, J., Chipperfield, M. P., Gloor, M., et al. Role of OH variability in the stalling of the global atmospheric CH_4 growth rate from 1999 to 2006. *Atmos. Chem. Phys. Discuss.*, pages 1–24, 2016. ISSN 1680-7375. doi: 10.5194/acp-2015-1029. URL `http://www.atmos-chem-phys-discuss.net/acp-2015-1029/`. (Cited on pages 1, 33, 75 and 130.)

[Meinshausen et al. 2011]   Meinshausen, M., Smith, S. J., Calvin, K., et al. The RCP greenhouse gas concentrations and their extensions from 1765 to 2300. *Clim. Change*, 109(1):213, 2011. doi: 10. 1007/s10584-011-0156-z. URL `https://doi.org/10.1007/s10584-011-0156-z`. (Cited on pages 3 and 39.)

[Meirink et al. 2008]   Meirink, J. F., Bergamaschi, P., and Krol, M. C. Four-dimensional variational data assimilation for inverse modelling of atmospheric methane emissions: method and comparison with synthesis inversion. *Atmos. Chem. Phys.*, 8(21):6341–6353, 2008. doi: 10.5194/acp-8-6341-2008. URL `https://www.atmos-chem-phys.net/8/6341/2008/`. (Cited on page 62.)

[Michener and Lajtha 2007]   Michener, R. H. and Lajtha, K., editors. *Stable isotopes in ecology and environmental science*. Ecological Methods and Cocepts. Blackwell Publishing, 2. edition, 2007. ISBN 9781405126809 (pbk. alk. paper) & 1405126809 (pbk. alk. paper). doi: 10.1899/ 0887-3593-028.002.0516. (Cited on pages 15 and 17.)

[Monge-Sanz et al. 2013]   Monge-Sanz, B. M., Chipperfield, M. P., Untch, A., et al. On the uses of a new linear scheme for stratospheric methane in global models: water source, transport tracer and radiative forcing. *Atmos. Chem. Phys.*, 13(18):9641–9660, 2013. doi: 10.5194/acp-13-9641-2013. URL `https://www.atmos-chem-phys.net/13/9641/2013/`. (Cited on pages 26 and 109.)

[Monteil et al. 2011]   Monteil, G., Houweling, S., Dlugockenky, E. J., et al. Interpreting methane variations in the past two decades using measurements of CH_4 mixing ratio and isotopic composition. *Atmos. Chem. Phys.*, 11:9141–9153, 2011. (Cited on pages 2, 16, 44, 60, 87 and 89.)

[Montzka et al. 2011]   Montzka, S. A., Krol, M., Dlugokencky, E., et al. Small interannual variability of global atmospheric hydroxyl. *Science*, 331:67–69, January 2011. (Cited on pages 20 and 33.)

[Mook 2000]   Mook, W. G. *Environmental Isotopes in the Hydrological Cycle: Volume I*, volume 1. UNESCO, 2000. (Cited on page 15.)

[Mote 1995]   Mote, P. The annual cycle of stratospheric water vapor in a general circulation model. *J. Geophys. Res.*, 100(D4):7363–7379, 1995. doi: 10.1029/94JD03301. URL `http://onlinelibrary.wiley.com/doi/10.1029/94JD03301/pdf`. (Cited on pages 22, 26 and 109.)

[Mote et al. 1996]   Mote, P. W., Rosenlof, K. H., McIntyre, M. E., et al. An atmospheric tape recorder: The imprint of tropical tropopause temperatures on stratospheric water vapor. *J. Geophys. Res. Atmos.*, 101(D2):3989–4006, 1996. doi: 10.1029/95JD03422. (Cited on page 101.)

[Myhre et al. 2007]   Myhre, G., Nilsen, J. S., Gulstad, L., et al. Radiative forcing due to stratospheric water vapour from CH_4 oxidation. *Geophys. Res. Lett.*, 34:L01807, 2007. doi: 10.1029/2006GL027472. (Cited on page 109.)

[Naik et al. 2013]   Naik, V., Voulgarakis, A., Fiore, A. M., et al. Preindustrial to present-day changes in tropospheric hydroxyl radical and methane lifetime from the atmospheric chemistry and climate model intercomparison project (ACCMIP). *Atmos. Chem. Phys.*, 13(10):5277–5298, 2013. doi: 10.5194/acp-13-5277-2013. URL `https://www.atmos-chem-phys.net/13/5277/2013/`. (Cited on pages 20, 34 and 55.)

[Nair et al. 2005]   Nair, H., Summers, M. E., Miller, C. E., and Yung, Y. L. Isotopic fractionation of methane in the martian atmosphere. *ICARUS*, 175:32–35, 2005. doi: 10.1016/j.icarus.2004.10.018. (Cited on page 18.)

[Nicely et al. 2017]   Nicely, J. M., Salawitch, R. J., Canty, T., et al. Quantifying the causes of differences in tropospheric OH within global models. *J. Geophys. Res. Atmos.*, 122:1983–2007, 2017. doi: 10.1002/2016JD026239. (Cited on pages 2, 20, 34, 50, 60, 129 and 131.)

[Nielsen et al. 1991]   Nielsen, O. J., Sidebottom, H. W., Donlon, M., and Treacy, J. Rate constants for the gas-phase reactions of OH radicals and Cl atoms with *n*-alkyl nitrites at atmospheric pressure and 298 K. *Int. J. Chem. Kinetics*, 23:1095–1109, 1991. doi: 10.1002/kin.550231204. (Cited in Appendix E.)

[Nilsson et al. 2007]   Nilsson, E., Johnson, M. S., Taketani, F., et al. Atmospheric deuterium fractionation: HCHO and HCDO yields in the CH_2DO+O_2 reaction. *Atmos. Chem. Phys. Discuss.*, 7(4):10019–10041, 2007. ISSN 16807316. doi: 10.5194/acpd-7-10019-2007. (Cited on page 20.)

[Nilsson et al. 2009]   Nilsson, E. J. K., Bache-Andreassen, L., Johnson, M. S., and Nielsen, C. J. Relative tropospheric photolysis rates of acetaldehyde and formaldehyde isotopologues measured at the European photoreactor facility. *J. Phys. Chem. A*, 113(15):3498–3504, 2009. ISSN 1089-5639. doi: 10.1021/jp811113c. URL `http://pubs.acs.org/doi/abs/10.1021/jp811113c`. (Cited on page 19.)

[Nilsson et al. 2010]   Nilsson, E. J. K., Andersen, V. F., Skov, H., and Johnson, M. S. Pressure dependence of the deuterium isotope effect in the photolysis of formaldehyde by ultraviolet light. *Atmos. Chem. Phys.*, 10(7):3455–3462, 2010. ISSN 1680-7324. doi: 10.5194/acp-10-3455-2010. URL http://www.atmos-chem-phys.net/10/3455/2010/. (Cited on page 19.)

[Nisbet et al. 2016]   Nisbet, E. G., Dlugokencky, E. J., Manning, M. R., et al. Rising atmospheric methane: 2007–2014 growth and isotopic shift. *Glob. Biogeochem. Cycles*, 30:1–15, 2016. doi: 10.1002/2015GB005326.Received. (Cited on pages 1, 2, 7, 14 and 129.)

[Nixon et al. 2012]   Nixon, C. A., Temelso, B., Vinatier, S., et al. Isotopic ratios in titan's methane: measurements and modeling. *The Astrophysical Journal*, 749(2):159, 2012. doi: 10.1088/0004-637X/749/2/159. URL http://stacks.iop.org/0004-637X/749/i=2/a=159. (Cited on page 18.)

[NOAA/ESRL]   NOAA/ESRL. National Oceanic and Atmospheric Administration/Earth System Research Laboratory. contact: Ed Dlugokencky, ed.dlugokencky@noaa.gov. (Cited on page 67.)

[NOAA/NASA 1976]   NOAA/NASA. *U.S. Standard Atmosphere 1976 (NASA-TM-X-74335)*. National Oceanic and Atmospheric Administration / National Aeronautics and Space Administration, 1976. (Cited on page 111.)

[O'Connor et al. 2014]   O'Connor, F. M., Johnson, C. E., Morgenstern, O., et al. Evaluation of the new UKCA climate-composition model – part 2: The troposphere. *Geosci. Model Dev.*, 7(1):41–91, 2014. doi: 10.5194/gmd-7-41-2014. URL https://www.geosci-model-dev.net/7/41/2014/. (Cited on page 34.)

[Ogryzlo et al. 1981]   Ogryzlo, E. A., Paltenghi, R., and Bayes, K. D. The rate of reaction of methyl radicals with ozone. *Int. J. Chem. Kinetics*, 13:667–675, 1981. doi: 10.1002/kin.550130707. (Cited in Appendix E.)

[Owens et al. 1982]   Owens, A. J., Steed, J. M., Filkin, D. L., Miller, C., and Jesson, J. P. The potential effects of increased methane on atmospheric ozone. *Geophys. Res. Lett.*, 9(9):1105–1108, 1982. doi: 10.1029/GL009i009p01105. URL http://dx.doi.org/10.1029/GL009i009p01105. (Cited on page 41.)

[Patra et al. 2011]   Patra, P. K., Houweling, S., Krol, M., et al. TransCom model simulations of CH_4 and related species: Linking transport, surface flux and chemical loss with CH_4 variability in the troposphere and lower stratosphere. *Atmos. Chem. Phys.*, 11(24):12813–12837, 2011. ISSN 16807316. doi: 10.5194/acp-11-12813-2011. (Cited on page 55.)

[Patra et al. 2014]   Patra, P. K., Krol, M. C., Montzka, S. A., et al. Observational evidence for interhemispheric hydroxyl-radical parity. *Nature*, 513:219–223, 2014. doi: 10.1038/nature13721. (Cited on pages 33 and 55.)

[Paulot et al. 2011]   Paulot, F., Wunch, D., Crounse, J. D., et al. Importance of secondary sources in the atmospheric budgets of formic and acetic acids. *Atmos. Chem. Phys.*, 11:1989–2013, 2011. doi: 10.5194/acp-11-1989-2011. (Cited in Appendix E.)

[Petit et al. 1999]   Petit, J. R., Jouzel, J., Raynaud, D., et al. Climate and atmospheric history of the past 420,000 years from the Vostok ice core, Antarctica. *Nature*, 399:429–436, 1999. doi: 10.1038/20859. URL http://dx.doi.org/10.1038/20859. (Cited on pages 1 and 6.)

[Pieterse et al. 2009]   Pieterse, G., Krol, M. C., and Röckmann, T. A consistent molecular hydrogen isotope chemistry scheme based on an independent bond approximation. *Atmos. Chem. Phys.*, 9(21):8503–8529, 2009. ISSN 1680-7375. doi: 10.5194/acpd-9-5679-2009. URL `http://www.scopus.com/inward/record.url?eid=2-s2.0-70450228352{&}partnerID=40{&}md5=e579dc603651588c1734b1e179fa4c5b`. (Cited on page 89.)

[Ploeger et al. 2013]   Ploeger, F., Günther, G., Konopka, P., et al. Horizontal water vapor transport in the lower stratosphere from subtropics to high latitudes during boreal summer. *J. Geophys. Res. Atmos.*, 118(14):8111–8127, 2013. doi: 10.1002/jgrd.50636. URL `http://dx.doi.org/10.1002/jgrd.50636`. (Cited on page 22.)

[Poberaj 2015]   Poberaj, C. S. planned publication, pers. comm. with Dominik Brunner, 2015. (Cited on page 63.)

[Ponater et al. 1999]   Ponater, M., Sausen, R., Feneberg, B., and Roeckner, E. Climate effect of ozone changes caused by present and future air traffic. *Climate Dyn.*, 15(9):631–642, Sep 1999. doi: 10.1007/s003820050306. URL `https://doi.org/10.1007/s003820050306`. (Cited on page 43.)

[Poulter et al. 2017]   Poulter, B., Bousquet, P., Canadell, J. G., et al. Global wetland contribution to 2000–2012 atmospheric methane growth rate dynamics. *Environ. Res. Lett.*, 12(9):094013, 2017. URL `http://stacks.iop.org/1748-9326/12/i=9/a=094013`. (Cited on page 2.)

[Pozzer et al. 2006]   Pozzer, A., Jöckel, P., Sander, R., et al. Technical note: The MESSy-submodel AIRSEA calculating the air-sea exchange of chemical species. *Atmos. Chem. Phys.*, 6(12):5435–5444, 2006. doi: 10.5194/acp-6-5435-2006. URL `https://www.atmos-chem-phys.net/6/5435/2006/`. (Cited on page 25.)

[Pozzer et al. 2011]   Pozzer, A., Jöckel, P., Kern, B., and Haak, H. The atmosphere-ocean general circulation model EMAC-MPIOM. *Geosci. Model Dev.*, 4(3):771–784, 2011. doi: 10.5194/gmd-4-771-2011. URL `https://www.geosci-model-dev.net/4/771/2011/`. (Cited on page 24.)

[Prather et al. 2012]   Prather, M. J., Holmes, C. D., and Hsu, J. Reactive greenhouse gas scenarios: Systematic exploration of uncertainties and the role of atmospheric chemistry. *Geophys. Res. Lett.*, 39(9), 2012. ISSN 00948276. doi: 10.1029/2012GL051440. (Cited on pages 1, 34 and 129.)

[Prinn et al. 2005]   Prinn, R. G., Huang, J., Weiss, R. F., et al. Evidence for variability of atmospheric hydroxyl radicals over the past quarter century. *Geophys. Res. Lett.*, 32(7):1–4, 2005. ISSN 00948276. doi: 10.1029/2004GL022228. (Cited on pages 33 and 34.)

[Prinn et al. 2016]   Prinn, R. G., Weiss, R., Krummel, P., et al. The ALE / GAGE AGAGE network, 2016. Carbon Dioxide Information Analysis Center (CDIAC), Oak Ridge National Laboratory (ORNL), U.S. Department of Energy (DOE). (Cited on pages 10 and 67.)

[Quay et al. 1999]   Quay, P., Stutsman, J., Wilbur, D., et al. The isotopic composition of atmospheric methane. *Glob. Biogeochem. Cycles*, 13(2):445–461, 1999. (Cited on pages 14, 15, 16, 44, 60, 89 and 91.)

[Rahn et al. 2002a]   Rahn, T., Eiler, J. M., Kitchen, N., Fessenden, J. E., and Randerson, J. T. Concentration and δD of molecular hydrogen in boreal forests: Ecosystem-scale systematics of atmospheric H_2. *Geophys. Res. Lett.*, 29(18):35–1–35–4, 2002a. doi: 10.1029/2002GL015118. 1888. (Cited on page 101.)

[Rahn et al. 2002b]   Rahn, T., Kitchen, N., and Eiler, J. D/H ratios of atmospheric H_2 in urban air: results using new methods for analysis of nano-molar H_2 samples. *Geochim. Cosmochim. Acta*, 66 (14):2475–2481, 2002b. doi: 10.1016/S0016-7037(02)00858-X. URL `http://www.sciencedirect.com/science/article/pii/S001670370200858X`. (Cited on page 101.)

[Rahn et al. 2003]   Rahn, T., Eiler, J. M., Boering, K. a., et al. Extreme deuterium enrichment in stratospheric hydrogen and the global atmospheric budget of H_2. *Nature*, 424(August):918–921, 2003. ISSN 0028-0836. doi: 10.1038/nature01917. (Cited on pages 101, 109 and 133.)

[Rayner et al. 2003]   Rayner, N. A., Parker, D. E., Horton, E. B., et al. Global analyses of sea surface temperature, sea ice, and night marine air temperature since the late nineteenth century. *J. Geophys. Res. Atmos.*, 108(D14), 2003. doi: 10.1029/2002JD002670. 4407. (Cited on page 43.)

[Revell et al. 2016]   Revell, L., Stenke, A., Rozanov, E., et al. The role of methane in projections of 21st century stratospheric water vapour. *Atmos. Chem. Phys.*, 16(July):13067–13080, 2016. ISSN 1680-7375. doi: 10.5194/acp-16-13067-2016. URL `www.atmos-chem-phys.net/16/13067/2016/`. (Cited on pages 1 and 21.)

[Revell et al. 2012]   Revell, L. E., Bodeker, G. E., Huck, P. E., et al. The sensitivity of stratospheric ozone changes through the 21st century to N_2O and CH_4. *Atmos. Chem. Phys.*, 12:11309–11317, 2012. doi: 10.5194/acp-12-11309-2012. URL `www.atmos-chem-phys.net/12/11309/2012/`. (Cited on page 21.)

[Rhee et al. 2006]   Rhee, T. S., Brenninkmeijer, C. a. M., Braß, M., and Brühl, C. Isotopic composition of H_2 from CH_4 oxidation in the stratosphere and the troposphere. *J. Geophys. Res.*, 111(D23):D23303, 2006. ISSN 0148-0227. doi: 10.1029/2005JD006760. URL `http://doi.wiley.com/10.1029/2005JD006760`. (Cited on page 101.)

[Rice et al. 2010]   Rice, A., Quay, P., Stutsman, J., et al. Meridional distribution of molecular hydrogen and its deuterium content in the atmosphere. *J. Geophys. Res. Atmos.*, 226(D12), 2010. doi: 10.1029/2009JD012529. D12306. (Cited on page 101.)

[Rice et al. 2016]   Rice, A. L., Butenhoff, C. L., Teama, D. G., et al. Atmospheric methane isotopic record favors fossil sources flat in 1980s and 1990s with recent increase. *Proc. Natl. Acad. Sci. USA*, 113(39):10791–10796, 2016. doi: 10.1073/pnas.1522923113. URL `http://www.pnas.org/content/113/39/10791.full`. (Cited on page 1.)

[Ridal and Siskind 2002]   Ridal, M. and Siskind, D. E. A two-dimensional simulation of the isotopic composition of water vapor and methane in the upper atmosphere. *J. Geophys. Res. Atmos.*, 107 (D24):ACH 24–1–ACH 24–8, 2002. ISSN 2156-2202. doi: 10.1029/2002JD002215. URL `http://dx.doi.org/10.1029/2002JD002215`. 4807. (Cited on page 30.)

[Rigby et al. 2012]   Rigby, M., Manning, A. J., and Prinn, R. G. The value of high-frequency high-precision methane isotopologue measurements for source and sink estimation. *J. Geophys. Res.*, 117(D12):D12312, jun 2012. doi: 10.1029/2011JD017384. (Cited on pages 2, 16, 87 and 89.)

[Rigby et al. 2017]   Rigby, M., Montzka, S. A., Prinn, R. G., et al. Role of atmospheric oxidation in recent methane growth. *Proc. Natl. Acad. Sci. USA*, 2017. URL `www.pnas.org/cgi/doi/10.1073/pnas.1616426114`. (Cited on pages 2, 33, 129 and 130.)

[Righi et al. 2015]   Righi, M., Eyring, V., Gottschaldt, K.-D., et al. Quantitative evaluation of ozone and selected climate parameters in a set of EMAC simulations. *Geosci. Model Dev.*, 8:733–768, 2015. doi: 10.5194/gmd-8-733-2015. (Cited on pages 34, 37 and 60.)

[Rind et al. 1990]   Rind, D., Suozzo, R., Balachandran, N. K., and Prather, M. J. Climate change and the middle atmosphere part I: The doubled CO_2 climate. *American Meterological Society*, 47: 475–494, 1990. (Cited on page 41.)

[Roble 1995]   Roble, R. G. Energetics of the mesosphere and thermosphere. In Johnson, R. M. and Killeen, T. L., editors, *The upper Mesosphere and Lower Thermosphere: A Review of Experiment and Theory, Geophysical Monograph 87*, pages 1–23. American Geophysical Union, Washington, DC, USA, 1995. (Cited in Appendix E.)

[Röckmann et al. 2003]   Röckmann, T., Rhee, T. S., and Engel, A. Heavy hydrogen in the stratosphere. *Atmos. Chem. Phys.*, 3:2015–2023, 2003. (Cited on page 101.)

[Röckmann et al. 2010]   Röckmann, T., Walter, S., Bohn, B., et al. Isotope effect in the formation of H_2 from H_2CO studied at the atmospheric simulation chamber SAPHIR. *Atmos. Chem. Phys.*, 10:5343–5357, 2010. doi: 10.5194/acp-10-5343-2010. (Cited on page 19.)

[Röckmann et al. 2011]   Röckmann, T., Brass, M., Borchers, R., and Engel, A. The isotopic composition of methane in the stratosphere: high-altitude balloon sample measurements. *Atmos. Chem. Phys.*, 11(24):13287–13304, 2011. ISSN 16807316. doi: 10.5194/acp-11-13287-2011. (Cited on pages 15, 18, 97, 98, 99, 100, 132 and 174.)

[Röckmann et al. 2016a]   Röckmann, T., Eyer, S., van der Veen, C., et al. In situ observations of the isotopic composition of methane at the Cabauw tall tower site. *Atmos. Chem. Phys.*, 16(16): 10469–10487, 2016a. doi: 10.5194/acp-16-10469-2016. URL https://www.atmos-chem-phys.net/16/10469/2016/. (Cited on page 15.)

[Röckmann et al. 2016b]   Röckmann, T., Popa, M. E., Krol, M. C., and Hofmann, M. E. G. Statistical clumped isotope signatures. *Scientific Reports*, 6, 2016b. doi: 10.1038/srep31947. (Cited on page 15.)

[Roeckner et al. 2006]   Roeckner, E., Brokopf, R., Esch, M., et al. Sensitivity of simulated climate to horizontal and vertical resolution in the ECHAM5 atmosphere model. *American Meterological Society*, 19:3771–3791, 2006. (Cited on pages 23 and 25.)

[Rohs et al. 2006]   Rohs, S., Schiller, C., Riese, M., et al. Long-term changes of methane and hydrogen in the stratosphere in the period 1978-2003 and their impact on the abundance of stratospheric water vapor. *J. Geophys. Res. Atmos.*, 111(14):1–12, 2006. ISSN 01480227. doi: 10.1029/2005JD006877. (Cited on page 109.)

[Ruppel and Kessler 2017]   Ruppel, C. D. and Kessler, J. D. The interaction of climate change and methane hydrates. *Rev. Geophys.*, 55(1):126–168, 2017. doi: 10.1002/2016RG000534. (Cited on pages 1 and 8.)

[Sander et al. 2005]   Sander, R., Kerkweg, A., Jöckel, P., and Lelieveld, J. Technical note: The new comprehensive atmospheric chemistry module MECCA. *Atmos. Chem. Phys.*, 5:445–450, 2005. (Cited on pages 28, 29 and 111.)

[Sander et al. 2011a]   Sander, R., Baumgaertner, A., Gromov, S., et al. The atmospheric chemistry box model CAABA/MECCA-3.0. *Geosci. Model Dev.*, 4:373–380, 2011a. doi: 10.5194/gmd-4-373-2011. (Cited on pages 3, 25, 59, 110, 111 and 141.)

[Sander et al. 2014]   Sander, R., Jöckel, P., Kirner, O., et al. The photolysis module JVAL-14, compatible with the MESSy standard, and the JVal preprocessor (JVPP). *Geosci. Model Dev.*, 7:2653–2662, 2014. doi: 10.5194/gmd-7-2653-2014. URL `www.geosci-model-dev.net/7/2653/2014/`. (Cited on pages 10, 25, 29, 111 and 112.)

[Sander et al. 2018]   Sander, R., Baumgaertner, A., Cabrera, D., et al. The atmospheric chemistry box model CAABA/MECCA-4.0. *Geosci. Model Dev. Discuss.*, 2018. (in prep.). (Cited on page 29.)

[Sander et al. 2011b]   Sander, S. P., Abbatt, J., Barker, J. R., et al. Chemical kinetics and photochemical data for use in atmospheric studies, evaluation no. 17. JPL Publication 10-6, Jet Propulsion Laboratory, 2011b. URL `http://jpldataeval.jpl.nasa.gov/`. (Cited on pages 10, 29 and 112.)

[Sanderson 1996]   Sanderson, M. G. Biomass of termites and their emissions of methane and carbon dioxide: A global database. *Glob. Biogeochem. Cycles*, 10(4):543–557, 1996. doi: 10.1029/96GB01893. (Cited on page 68.)

[Sandu and Sander 2006]   Sandu, A. and Sander, R. Technical note: Simulating chemical systems in fortran90 and matlab with the Kinetic PreProcessor KPP-2.1. *Atmos. Chem. Phys.*, 6(1):187–195, 2006. doi: 10.5194/acp-6-187-2006. URL `https://www.atmos-chem-phys.net/6/187/2006/`. (Cited on page 29.)

[Saueressig et al. 1995]   Saueressig, G., Bergamaschi, P., Crowley, J. N., and Fischer, H. Carbon kinetic isotope effect in the reaction of CH_4 with Cl atoms. *Geophys. Res. Lett.*, 22(10):1225–1228, 1995. (Cited on page 18.)

[Saueressig et al. 1996]   Saueressig, G., Bergamaschi, P., Crowley, J., and Fischer, H. D/H kinetic isotope effect in the reaction $CH_4 + Cl$. *Geophys. Res. Lett.*, 23(24):3619–3622, 1996. ISSN 00948276. (Cited on page 18.)

[Saueressig et al. 2001]   Saueressig, G., Crowley, J. N., Bergamaschi, P., et al. Carbon 13 and D kinetic isotope effects in the reactions of CH_4 with $O^1(D)$ and OH: New laboratory measurements and their implications for the isotopic composition of stratospheric methane. *J. Geophys. Res.*, 106 (D19):23127–23138, October 2001. (Cited on page 18.)

[Saunois et al. 2016a]   Saunois, M., Bousquet, P., Poulter, B., et al. The global methane budget 2000–2012. *Earth Syst. Sci. Data*, 8(2):697–751, 2016a. doi: 10.5194/essd-8-697-2016. URL `https://www.earth-syst-sci-data.net/8/697/2016/`. (Cited on pages 2, 6, 8, 9, 72 and 130.)

[Saunois et al. 2016b]   Saunois, M., Jackson, R. B., Bousquet, P., Poulter, B., and Canadell, J. G. The growing role of methane in anthropogenic climate change. *Environ. Res. Lett.*, 11(12):120207, 2016b. URL `http://stacks.iop.org/1748-9326/11/i=12/a=120207`. (Cited on page 2.)

[Schaefer et al. 2016]   Schaefer, H., Fletcher, S. E. M., Veidt, C., et al. A 21st century shift from fossil-fuel to biogenic methane emissions indicated by $^{13}CH_4$. *Science (New York, N.Y.)*, 352(6281): 80–84, 2016. ISSN 1095-9203. doi: 10.1126/science.aad2705. URL `http://science.sciencemag.org/content/352/6281/80.abstract`. (Cited on pages 2, 14 and 129.)

[Schlager and Scheibe 2011]   Schlager, H. and Scheibe, M. Institute of Atmospheric Physics, German Aerospace Center, Germany, 2011. 2011–2016. (Cited on page 84.)

[Schultz et al. 2008]   Schultz, M. G., Heil, A., Hoelzemann, J. J., et al. Global wildland fire emissions from 1960 to 2000. *Glob. Biogeochem. Cycles*, 22(2), 2008. doi: 10.1029/2007GB003031. GB2002. (Cited on page 68.)

[Schwietzke et al. 2016]   Schwietzke, S., Sherwood, O. A., Bruhwiler, L. M. P., et al. Upward revision of global fossil fuel methane emissions based on isotope database. *Nature*, 538:88–91, 2016. doi: 10.1038/nature19797. URL `http://dx.doi.org/10.1038/nature19797`. (Cited on page 2.)

[Seinfeld and Pandis 2006]   Seinfeld, J. H. and Pandis, S. N. *Atmospheric Chemistry and Physics.* John Wiley & Sons, Inc., second edition, 2006. (Cited on pages 5 and 21.)

[Shang et al. 2015]   Shang, L., Liu, Y., Tian, W., and Zhang, Y. Effect of methane emission increases in East Asia on atmospheric circulation and ozone. *Advances in Atmospheric Sciences*, 32(12):1617–1627, 2015. doi: 10.1007/s00376-015-5028-4. URL `https://doi.org/10.1007/s00376-015-5028-4`. (Cited on page 41.)

[Sherwood et al. 1994]   Sherwood, S. C., Ramanathan, V., Barnett, T. P., Tyree, M. K., and Roeckner, E. Response of an atmospheric general circulation model to radiative forcing of tropical clouds. *J. Geophys. Res. Atmos.*, 99(D10):20829–20845, 1994. doi: 10.1029/94JD01632. URL `http://dx.doi.org/10.1029/94JD01632`. (Cited on page 37.)

[Sigmond et al. 2004]   Sigmond, M., Siegmund, P. C., Manzini, E., and Kelder, H. A simulation of the separate climate effects of middle-atmospheric and tropospheric CO_2 doubling. *J. Climate*, 17(12): 2352–2367, 2004. ISSN 08948755. doi: 10.1175/1520-0442(2004)017<2352:ASOTSC>2.0.CO;2. (Cited on page 41.)

[Smith et al. 2006]   Smith, S. C., Lee, J. D., Bloss, W. J., et al. Concentrations of OH and HO_2 radicals during NAMBLEX: measurements and steady state analysis. *Atmos. Chem. Phys.*, 6: 1435–1453, 2006. doi: 10.5194/acp-6-1435-2006. URL `https://www.atmos-chem-phys.net/6/1435/2006/`. (Cited on page 33.)

[Snover and Quay 2000]   Snover, A. and Quay, P. Hydrogen and carbon kinetic isotope effects during soil uptake of atmospheric methane and a temperate grassland. *Glob. Biogeochem. Cycles*, 14(1):25–39, 2000. (Cited on pages 16, 18 and 89.)

[Sokolov et al. 1999]   Sokolov, O., Hurley, M. D., Ball, J. C., et al. Kinetics of the reactions of chlorine atoms with CH_3ONO and CH_3ONO_2. *Int. J. Chem. Kinetics*, 31:357–359, 1999. (Cited in Appendix E.)

[Solomon et al. 2010]   Solomon, S., Rosenlof, K. H., Portmann, R. W., et al. Contributions of stratospheric water vapor to decadal changes in the rate of global warming. *Science*, 327:1219–1223, May 2010. doi: 10.1126/science.1182488. (Cited on page 21.)

[Sonnemann and Grygalashvyly 2014]   Sonnemann, G. R. and Grygalashvyly, M. Global annual methane emission rate derived from its current atmospheric mixing ratio and estimated lifetime. *Ann. Geophys.*, 32(3):277–283, 2014. ISSN 14320576. doi: 10.5194/angeo-32-277-2014. (Cited on page 1.)

[Spahni et al. 2011]   Spahni, R., Wania, R., Neef, L., et al. Constraining global methane emissions and uptake by ecosystems. *Biogeosciences*, 8(6):1643–1665, 2011. ISSN 17264170. doi: 10.5194/bg-8-1643-2011. (Cited on page 68.)

[Spivakovsky et al. 2000]   Spivakovsky, C. M., Logan, J. A., Montzka, S. A., et al. Three-dimensional climatological distribution of tropospheric OH: Update and evaluation. *J. Geophys. Res. Atmos.*, 105(D):8931–8980, 2000. ISSN 0148-0227. doi: 10.1029/1999JD901006. (Cited on page 20.)

[Steinwagner et al. 2007]   Steinwagner, J., Milz, M., von Clarmann, T., et al. HDO measurements with MIPAS. *Atmos. Chem. Phys.*, 7(10):2601–2615, 2007. doi: 10.5194/acp-7-2601-2007. URL `https://www.atmos-chem-phys.net/7/2601/2007/`. (Cited on pages 104 and 132.)

[Steinwagner et al. 2010]   Steinwagner, J., Fueglistaler, S., Stiller, G., et al. Tropical dehydration processes constrained by the seasonality of stratospheric deuterated water. *Nature Geoscience*, 3: 262–266, 2010. doi: 10.1038/NGEO822. (Cited on page 101.)

[Stenke and Grewe 2005]   Stenke, A. and Grewe, V. Simulation of stratospheric water vapor trends: impact on stratospheric ozone chemistry. *Atmos. Chem. Phys.*, 5:1257–1272, 2005. URL `www.atmos-chem-phys.org/acp/5/1257/`. (Cited on page 21.)

[Stohl et al. 2005]   Stohl, A., Forster, C., Frank, A., Seibert, P., and Wotawa, G. Technical note: The Lagrangian particle dispersion model FLEXPART version 6.2. *Atmos. Chem. Phys.*, 5(9): 2461–2474, 2005. doi: 10.5194/acp-5-2461-2005. URL `https://www.atmos-chem-phys.net/5/2461/2005/`. (Cited on page 62.)

[Stolper et al. 2014]   Stolper, D., Sessions, A., Ferreira, A., et al. Combined C–D and D–D clumping in methane: Methods and preliminary results. *Geochim. Cosmochim. Acta*, 126:169–191, 2014. doi: 10.1016/j.gca.2013.10.045. URL `http://www.sciencedirect.com/science/article/pii/S0016703713006170`. (Cited on page 15.)

[Stowasser et al. 1999]   Stowasser, M., Oelhaf, H., Wetzel, G., et al. Simultaneous measurements of HDO, H_2O, and CH_4 with MIPAS-B: Hydrogen budget and indication of dehydration inside the polar vortex. *J. Geophys. Res.*, 104(D16):19213–19225, August 1999. (Cited on pages 106 and 109.)

[Strahan and Douglass 2018]   Strahan, S. E. and Douglass, A. R. Decline in Antarctic ozone depletion and lower stratospheric chlorine determined from aura microwave limb sounder observations. *Geophys. Res. Lett.*, 2018. doi: 10.1002/2017GL074830. URL `http://dx.doi.org/10.1002/2017GL074830`. (Cited on page 5.)

[Sussmann et al. 2012]   Sussmann, R., Forster, F., Rettinger, M., and Bousquet, P. Renewed methane increase for five years (2007–2011) observed by solar FTIR spectrometry. *Atmos. Chem. Phys.*, 12 (11):4885–4891, 2012. doi: 10.5194/acp-12-4885-2012. URL `https://www.atmos-chem-phys.net/12/4885/2012/`. (Cited on page 2.)

[Tanalski 2017]   Tanalski, F. Untersuchung von Klimaveränderungen durch extreme Methanemissionen. Master's thesis, Universität Duisburg-Essen, september 2017. (Cited on pages 41, 43, 50 and 52.)

[Taylor 2001]   Taylor, K. E. Summarizing multiple aspects of model performance in a single diagram. *J. Geophys. Res. Atmos.*, 106(D7):7183–7192, 2001. doi: 10.1029/2000JD900719. (Cited on page 69.)

[Tost 2006] Tost, H. *Global Modelling of Cloud, Convection and Precipitation Influences on Trace Gases and Aerosols*. PhD thesis, University of Bonn, Germany, 2006. URL `http://hss.ulb.uni-bonn.de/2006/0731/0731.htm`. (Cited on page 25.)

[Tost et al. 2006a] Tost, H., Jöckel, P., Kerkweg, A., Sander, R., and Lelieveld, J. Technical note: A new comprehensive SCAVenging submodel for global atmospheric chemistry modelling. *Atmos. Chem. Phys.*, 6(3):565–574, 2006a. doi: 10.5194/acp-6-565-2006. URL `https://www.atmos-chem-phys.net/6/565/2006/`. (Cited on page 25.)

[Tost et al. 2006b] Tost, H., Jöckel, P., and Lelieveld, J. Influence of different convection parameterisations in a GCM. *Atmos. Chem. Phys.*, 6(12):5475–5493, 2006b. doi: 10.5194/acp-6-5475-2006. URL `https://www.atmos-chem-phys.net/6/5475/2006/`. (Cited on pages 25 and 29.)

[Tost et al. 2007] Tost, H., Jöckel, P., and Lelieveld, J. Lightning and convection parameterisations - uncertainties in global modelling. *Atmos. Chem. Phys.*, 7(17):4553–4568, 2007. doi: 10.5194/acp-7-4553-2007. URL `https://www.atmos-chem-phys.net/7/4553/2007/`. (Cited on page 25.)

[Tsuruta et al. 2017] Tsuruta, A., Aalto, T., Backman, L., et al. Global methane emission estimates for 2000–2012 from CarbonTracker Europe-CH_4 v1.0. *Geosci. Model Dev.*, 10(3):1261–1289, 2017. doi: 10.5194/gmd-10-1261-2017. URL `https://www.geosci-model-dev.net/10/1261/2017/`. (Cited on pages 62 and 72.)

[Tsutsumi et al. 2009] Tsutsumi, Y., Mori, K., Hirahara, T., Ikegami, M., and Conway, T. J. Technical report of global analysis method for major greenhouse gases by the world data center for greenhouse gases. Technical Report 1473, World Meteorological Organization Global Atmosphere Watch, 2009. URL `http://library.wmo.int/pmb_ged/wmo-td_1473_en.pdf`. (Cited on pages 78 and 83.)

[Turner et al. 2017] Turner, A. J., Frankenberg, C., Wennberg, P. O., and Jacob, D. J. Ambiguity in the causes for decadal trends in atmospheric methane and hydroxyl. *Proc. Natl. Acad. Sci. USA*, 2017. URL `www.pnas.org/cgi/doi/10.1073/pnas.1616020114`. (Cited on pages 2, 6 and 33.)

[Umezawa et al. 2012] Umezawa, T., MacHida, T., Ishijima, K., et al. Carbon and hydrogen isotopic ratios of atmospheric methane in the upper troposphere over the western pacific. *Atmos. Chem. Phys.*, 12(17):8095–81113, 2012. ISSN 16807316. doi: 10.5194/acp-12-8095-2012. (Cited on page 95.)

[van der Werf et al. 2010] van der Werf, G. R., Randerson, J. T., Giglio, L., et al. Global fire emissions and the contribution of deforestation, savanna, forest, agricultural, and peat fires (1997–2009). *Atmos. Chem. Phys.*, 10(23):11707–11735, 2010. doi: 10.5194/acp-10-11707-2010. URL `https://www.atmos-chem-phys.net/10/11707/2010/`. (Cited on page 68.)

[Volk et al. 1997] Volk, C. M., Elkins, J. W., Fahey, D. W., et al. Evaluation of source gas lifetimes from stratospheric observations. *J. Geophys. Res.*, 102(D21):25543–25564, 1997. doi: 10.1029/97JD02215. URL `http://dx.doi.org/10.1029/97JD02215`. (Cited on page 53.)

[von Kuhlmann 2001] von Kuhlmann, R. *Tropospheric Photochemistry of Ozone, its Precursors and the Hydroxyl Radical: A 3D-Modeling Study Considering Non-Methane Hydrocarbons*. PhD thesis, University of Mainz, Germany, 2001. (Cited on page 34.)

[Voulgarakis et al. 2013]   Voulgarakis, A., Naik, V., Lamarque, J.-F., et al. Analysis of present day and future OH and methane lifetime in the ACCMIP simulations. *Atmos. Chem. Phys.*, 13: 2563–2587, 2013. doi: 10.5194/acp-13-2563-2013. (Cited on pages 34, 50, 60 and 129.)

[Wahlen 1993]   Wahlen, M. The global methane cycle. *Annual Review of Earth and Planetary Science*, 21(1):407–426, 1993. doi: 10.1146/annurev.ea.21.050193.002203. URL `https://doi.org/10.1146/annurev.ea.21.050193.002203`. (Cited on pages 6 and 7.)

[Wallington et al.]   Wallington, T. J., Ammann, M., Cox, R. A., et al. IUPAC task group on atmospheric chemical kinetic data evaluation. URL `http://iupac.pole-ether.fr`. (Cited in Appendix E.)

[Wang et al. 2015]   Wang, D. T., Gruen, D. S., Lollar, B. S., et al. Nonequilibrium clumped isotope signals in microbial methane. *Science (New York, N.Y.)*, 348(6233):428–431, 2015. ISSN 1095-9203. doi: 10.1126/science.aaa4326. URL `http://www.sciencemag.org/content/348/6233/428`. (Cited on page 15.)

[White et al. 2016]   White, J., Vaughn, B., and Michel, S. University of Colorado, Institute of Arctic and Alpine Research (INSTAAR), Stable Isotopic Composition of Atmospheric Methane (^{2}H) from the NOAA ESRL Carbon Cycle Cooperative Global Air Sampling Network, 2005-2009, version: 2016-04-26, 2016. URL `ftp://aftp.cmdl.noaa.gov/data/trace_gases/ch4h2/flask/`. (Cited on page 93.)

[White et al. 2017]   White, J., Vaughn, B., and Michel, S. University of Colorado, Institute of Arctic and Alpine Research (INSTAAR), Stable Isotopic Composition of Atmospheric Methane (^{13}C) from the NOAA ESRL Carbon Cycle Cooperative Global Air Sampling Network, 1998-2016, version: 2018-01-31, 2017. URL `ftp://aftp.cmdl.noaa.gov/data/trace_gases/ch4c13/flask/`. (Cited on page 93.)

[Whitehill et al. 2017]   Whitehill, A. R., Joelsson, L. M. T., Schmidt, J. A., et al. Clumped isotope effects during OH and Cl oxidation of methane. *Geochim. Cosmochim. Acta*, 196:307–325, 2017. doi: 10.1016/j.gca.2016.09.012. URL `http://www.sciencedirect.com/science/article/pii/S0016703716305269`. (Cited on page 15.)

[Whiticar and Schaefer 2007]   Whiticar, M. and Schaefer, H. Constraining past global tropospheric methane budgets with carbon and hydrogen isotope ratios in ice. *Philosophical transactions, Series A*, 365(1856):1793–1828, 2007. ISSN 1364-503X. doi: 10.1098/rsta.2007.2048. (Cited on pages 14, 16 and 89.)

[WMO 2017]   WMO. WMO greenhouse gas bulletin. Technical Report 13, World Meteorological Organization, 2017. (Cited on page 77.)

[Wuebbels and Hayhoe 2002]   Wuebbels, D. J. and Hayhoe, K. Atmospheric methane and global change. *Earth-Science Reviews*, 57:177–210, 2002. (Cited on pages 1, 6, 7, 8 and 129.)

[Wunch et al. 2011]   Wunch, D., Toon, G. C., Blavier, J.-F. L., et al. The total carbon column observing network. *Philosophical Transactions of the Royal Society of London A: Mathematical, Physical and Engineering Sciences*, 369(1943):2087–2112, 2011. doi: 10.1098/rsta.2010.0240. URL `http://rsta.royalsocietypublishing.org/content/369/1943/2087`. (Cited on page 11.)

[Xiong et al. 2008]   Xiong, X., Barnet, C., Maddy, E., et al. Characterization and validation of methane products from the atmospheric infrared sounder (AIRS). *J. Geophys. Res. Biogeosci.*, 113 (G3):n/a–n/a, 2008. ISSN 2156-2202. doi: 10.1029/2007JG000500. G00A01. (Cited on page 11.)

[Xiong et al. 2013]   Xiong, X., Barnet, C., Maddy, E. S., et al. Mid-upper tropospheric methane retrieval from IASI and its validation. *Atmos. Meas. Tech.*, 6(9):2255–2265, 2013. doi: 10.5194/amt-6-2255-2013. URL `https://www.atmos-meas-tech.net/6/2255/2013/`. (Cited on page 11.)

[Zahn et al. 2006]   Zahn, a., Franz, P., Bechtel, C., Grooß, J.-U., and Röckmann, T. Modelling the budget of middle atmospheric water vapour isotopes. *Atmos. Chem. Phys.*, 6:2073–2090, 2006. ISSN 1680-7324. doi: 10.5194/acp-6-2073-2006. (Cited on page 19.)

[Zazzeri et al. 2015]   Zazzeri, G., Lowry, D., Fisher, R. E., et al. Plume mapping and isotopic characterisation of anthropogenic methane sources. *Atmos. Environ.*, 110:151–162, 2015. ISSN 18732844. doi: 10.1016/j.atmosenv.2015.03.029. (Cited on pages 16 and 89.)

[Zellner et al. 1988]   Zellner, R., Hartmann, D., Karthäuser, J., Rhäsa, D., and Weibring, G. A laser photolysis/LIF study of the reactions of O(^{3}P) atoms with CH_3 and CH_3O_2 radicals. *J. Chem. Soc. Faraday Trans. 2*, 84:549–568, 1988. doi: 10.1039/f29888400549. (Cited in Appendix E.)

[Zellweger et al. 2016]   Zellweger, C., Emmenegger, L., Firdaus, M., et al. Assessment of recent advances in measurement techniques for atmospheric carbon dioxide and methane observations. *Atmos. Meas. Tech.*, 9(9):4737–4757, 2016. doi: 10.5194/amt-9-4737-2016. URL `https://www.atmos-meas-tech.net/9/4737/2016/`. (Cited on page 10.)

Data Acknowledgments

Danksagungen

An dieser Stelle möchte ich mich bei Professor Martin Dameris bedanken, zum einen für die Unterstützung bei der Anfertigung dieser Doktorarbeit und zum anderen für den unvergesslichen Einsatz um diese Stelle zu schaffen.

Ebenfalls bedanken möchte ich mich bei Professor Bernhard Mayer, der sich bereit erklärte das Zweigutachten zu übernehmen und meiner Arbeit mit viel Geduld und Interesse begegnet ist.

An Professor Robert Sausen und Professor Markus Rapp geht mein Dank für die Förderung und Wertschätzung meines Themas. Ich danke auch für die Unterstützung während meiner Tätigkeiten in der Doktorandenvertretung.

Unvergleichbar ist außerdem die Hilfe die ich von meinem Betreuer Dr. Patrick Jöckel erhalten habe. Ich danke ihm vielmals für den wertvollen Rat und die vielen Stunden die nötig waren alle versteckten Programmierfehler zu finden. Er beantwortete mir jede Frage fachkundig und geduldig, selbst wenn ich sie zum wiederholten Male stellte. Ohne seinen Beistand wäre diese Doktorarbeit nicht möglich gewesen.

Ebenso möchte ich mich bei Dr. Sergey Gromov für die vielen hilfreichen und interessanten Diskussionen am Telefon, bei den persönlichen Treffen und bei den Abendessen bedanken, bei denen sogar Quittungen als Notizmöglichkeit genutzt werden mussten.

Besonderer Dank geht an Professor Veronika Eyring, die mich immer sehr unterstützte und motivierte. Ohne sie hätte ich die Doktorandenstelle wahrscheinlich nie angetreten. Dieser Dank gilt auch allen Mitgliedern ESMValTool Gruppe von deren Arbeit und Hilfe ich während meines Praktikums und meiner Doktorarbeit profitieren konnte.

Nicht unerwähnt bleiben sollen auch meine Kollegen in Abteilung für Erdsystemmodellierung. Die geselligen Kaffeerunden und Mittagessen haben mir viel Freude bereitet und ich bedanke mich sehr, dass mir jeder ein offenes Ohr schenkte, wenn ich an dessen Tür klopfte. Ich möchte nicht verheimlichen, dass ich wahrscheinlich in keiner anderen Umgebung diese Arbeit hätte fertig stellen können. Erwähnung finden sollen unter anderem Mattia, meinem NCL Guru, Christopher, der mir Emacs näher brachte, Roland, auf dessen Arbeit mein Thema aufbaute und der mir bei Fragen immer hilfsbereit zur Seite gestanden hat, Daniel, der in unserem gemeinsamen Büro mein Sorgentelefon spielte, Sabine, die mir nicht nur bei meinen Rechenzeitanträgen half und Mariano und Frauke, mit denen ich jetzt hoffentlich öfter Konzerte erleben kann.

Ganz gewiss niemals zustande gekommen wäre diese Arbeit jedoch ohne die Unterstützung meiner Familie. Meine Eltern haben nie in Frage gestellt, wie ich meinen Lebensweg beschreite. Sie haben mir die Freiheit gelassen meine Erfahrungen selbst zu machen und waren immer an meiner Seite wenn dies nötig war. Ein simples Dankeschön wäre für ihren Anteil an dieser Arbeit schlichtweg zu wenig. Genauso möchte ich meine lieben Schwestern erwähnen, die einfach da waren und vieles verstehen was andere nicht tun, und natürlich meine Großmutter, mit deren Segen so manches leichter ging.

Auch meinen Freundinnen, Veri, Lisa und Katrin sei gedankt, für ihre liebevollen, ehrlichen und aufmunternden Worte, wenn ich das Gefühl hatte es würde gar nichts mehr voran gehen.

Die letzten Worte seien einer weiteren Person gewidmet, aber "Old Mister Webster could never define...".